Elucidation of changes in food grains due to spoilage in bulk storage using advanced imaging for post-harvest management

by

Navnath S. Indore

A Thesis submitted to the Faculty of Graduate Studies of

the University of Manitoba

in partial fulfilment of the requirement for the degree of

DOCTOR OF PHILOSOPHY

Department of Biosystems Engineering

University of Manitoba

Winnipeg, Canada

ABSTRACT

Different varieties within a class of a grain type exhibit distinct behaviors that impact their end use quality during storage. Until now, high-resolution imaging data for both dry and spoiled cereal grains have not been available. Therefore, a pioneering effort was made to generate 3D data for a better understanding of seed structure and changes due to spoilage, focusing on the selected crops (wheat and barley). In the first preliminary experiment, durum wheat varieties (AAC Spitfire, CDC Defy, and AAC Stronghold) and spring wheat varieties (AAC Starbuck, AAC Brandon, Faller) were stored for 5 wk at 17% moisture content (wet basis (wb)). Both control (dry) and stored high-moisture seeds were analyzed for structural, and nutritional changes using synchrotron techniques, including phase-contrast micro-computed tomography (SR-μCT), bulk X-ray fluorescence imaging (SR-XRF), X-ray fluorescence imaging (SR-XFI), and mid-infrared spectroscopy (mid-IR) at the Canadian Light Source (CLS), Saskatoon, SK. Seeds were also stored in a freezer (-18°C) for further scanning to study any additional changes in the microstructure of seeds due to freezing. In this experiment, operational parameters were standardized for data acquisition for SR-μCT (20 keV, 3.6μ resolution, and 5 cm propagation distance), SR-XRF/XFI (15 keV, 5μ resolution, and 100 ms dwell time), and mid-IR (900–4000 cm^{-1} range at 4 cm^{-1} resolution). Image processing revealed changes in the microstructure of wheat with spoilage at the end of the 5-wk storage, and this remained unaltered after freezing in stored wheat. Bulk XRF demonstrated the impact of storage time on variations in available nutrients. The SR-XFI revealed significant changes ($p<0.05$) in nutritional distributions at the micron scale in thin section maps within stored durum wheat seeds. Changes in nutritional features (protein, lipids, and carbohydrates) due to spoilage during storage were determined using mid-IR spectroscopy. Durum varieties AAC Spitfire and CDC Defy exhibited maximum changes in microstructural and nutritional composition compared to AAC Stronghold, and all spring wheat varieties performed better than durum wheat varieties.

In the second experiment, eight wheat varieties, each representing distinct wheat classes, were included: Canada Prairie Spring Red (CPSR) cultivar ‘AAC Penhold’, Canada Prairie Spring White (CPSW) cultivar ‘AC Vista’, Canada Western Extra Strong (CWES) cultivar ‘Burnside’, Canada Western Hard White Spring (CWHWS) cultivar ‘AC Snowstar’, Canada Western Red Winter (CWRW) cultivar ‘AAC Wildfire’, Canada Northern Hard Red (CNHR) cultivar ‘Prosper’, Canada Western Special Purpose (CWSP) cultivar ‘Aldoren’, and Canada Western Soft White Spring (CWSWS) cultivar ‘AC Andrew’. Additionally, four barley classes were

considered: Tradition (Six-row), AB Cattlelac (Six-row hulless), Esma (Two-row), and AC Metacalf (Two-row hulless), each representing four different western malt barley classes. These grains were stored for 8 wk at 17% moisture content (wb). Data acquisition for both control (wheat and barley) and 8-wk stored grains (wheat and barley) was carried out using standardized operational parameters for SR-μCT, SR-XFI, and mid-IR. Characterization of wheat based on changes in the microstructure of selected wheat classes became possible. The wheat classes that performed better in storage were CNHR, CWRW, CWSP, and CPSW, compared to classes CWHWS, CPSR, CWSWS, and CWES. The existing condition of the kernel microstructure strongly influenced the performance of wheat in storage, representing a major outcome of this work. Mid-IR analysis of wheat data showed variations among nutritional components, while SR-XFI revealed nutrient distribution gradients before and after storage. Hulled barley varieties exhibited more deterioration in microstructure than hulless varieties of barley, establishing a direct correlation between microstructural changes and alterations in nutritional content. The initial condition of the grain structure of control samples (air spaces beneath the husk and cracks) strongly influenced the storage life of wheat and barley during the short-term storage of 8 wek The high-resolution information generated for selected barley varieties will be useful in the development of real-time decision support systems and planning post-harvest storage.

ACKNOWLEDGEMENTS

I take this opportunity to express my sincere gratitude towards my advisor, Dr. Digvir S. Jayas, for his support, motivation, enthusiasm, and immense knowledge. I heartily thank him for being a great source of inspiration and providing me opportunity to learn and work on novel high-resolution imaging techniques application in my research. With his constant support, I can complete my research as per the planned timeline.

I express my warm thanks to my co-advisor, Dr. Chithra Karunakaran, for her guidance, support, and constructive criticism during my research work at the Canadian Light Source, Saskatoon. The time and effort offered by her to help me accomplish my research objectives during my study are invaluable.

I wish to express my heartfelt gratitude to my honorable committee members, Dr. Jitendra Paliwal, Dr. Trust Beta, and Dr. C. B. Singh for their valuable feedback, evaluation, and improvements in my research project over time.

I would like to acknowledge my funding agencies; ICAR Netaji International fellowship for funding my Ph.D. program and Natural Sciences Engineering Research Council of Canada for funding my research project expenses and publications. I want to acknowledge the Director ICAR-CIPHET, Ludhiana and Ministry of Agriculture & Farmers Welfare, government of India for support and study leave permission.

I would like to acknowledge the Canadian Light Source, Saskatoon staff, Jarvis Stobbs, Miranda Vu, Viorica F. Bondici, Gosia Korbas, Omar Marinos, Arash Panahifar, David Muir, and Kaiyang Tu, for supporting my work at CLS in sample preparation, data acquisition, and processing images after collection.

I sincerely thank Dale Bourns, Marcel Lehmann, Matt McDonald, Vincent Hervet, and Mudassir Chaudhry for their technical support and Heather Innis, Mandy Tanner and for their administrative support. I extend my thanks to my department friends, Rahul Tripathi, Rahul Kumar, Abhinav Tiwari, Anukiruthika Thangarasu, Vimala Bharathi, Chithra Sivakumar, Rajbir Kaur, Shubham Sharma, Sheena Mhalotra, and Aanchal Pandey for their assistance at various stages of the study. Finally, I express my genuine gratitude towards my wife Deepa, daughter Shyla, nephew Shivansh, my parents, parents-in- laws, brother Goraksh, for their encouragement, moral support, and inspiration to succeed.

TABLE OF CONTENT

LIST OF FIGURES

LIST OF TABLES

Chapter 1. INTRODUCTION

1.1 Scope of research

In 2023, the global production of total cereal food grains reached approximately 2.82 billion tonnes (Gt), with wheat alone contributing 789 million tonnes (Mt) (FAO, 2023). Canada, during the same year, is estimated to have produced 89 Mt of cereal grain, representing 3.1% of the global food grain production (Statistics Canada, 2023).Wheat and barley are pivotal food grain crops in Canada, not only contributing significantly to the Canadian economy but also playing a crucial role in the global food supply chain. In 2023, Canada produced 33.82 Mt of wheat and 9.98 Mt of barley, maintaining a consistent supply in the international market owing to their high quality (Statistics Canada, 2023). The grains produced undergo storage at various points along the food chain, whether for a short or long period before consumption. Effective grain storage management is essential to minimize post-harvest losses. These losses can range from 1% in well-managed systems to as high as 50% in poorly managed systems (Jayas & White, 2003). In some cases, an entire unit of storage can experience complete spoilage, resulting in 100% loss in that unit (Jayas, 2012).

Food grain seeds exhibit distinctive structures and compositional, nutritional, and functional characteristics, or a combination thereof, leading to their classification into different classes. In Canada, wheat varieties are categorized into classes based on functional characteristics, with the Canadian Grain Commission (CGC) defining ten classes for western Canadian wheat and seven for eastern Canadian wheat. Similarly, barley is divided into eight classes, comprising four western and four eastern classes. Quantitative losses result from direct consumption of grains by insects and other vertebrates (though not very common), while quality losses arise from contamination by insect parts, excreta, mites, and fungi. Sound or undamaged food grains possess inherent defense mechanisms against spoilage. A study by Sayed et al. (2006) on 12 wheat varieties found that one variety, Mehran-89, demonstrated the highest resistance to storage insects. In the case of wheat, durum varieties are more susceptible to spoilage than other wheat classes (Nithya et al., 2011). Wheat, barley, rye, maize, and oilseeds are particularly susceptible to fungi and their metabolites (mycotoxins), with strict allowable limits (5–10 ppb) necessitating measures to prevent fungal growth during storage (González-Torralba et al., 2013). Understanding the distinctions among these classes is crucial for characterizing different food grains in response to spoilage under unfavorable storage conditions. A study

focusing on the microstructural and nutritional profiles of wheat and barley using a non-destructive and efficient approach is essential. Synchrotron techniques, as reviewed by Indore et al. (2022), emerge as powerful scientific tools for such studies.

The synchrotron, invented in the late 1960s, has undergone considerable improvements since its inception. Its application for sample characterization across various disciplines, including biology, materials science, and the design of semiconductor and nano-devices, gained significant momentum globally after 1974 (Winick and Bienenstock, 1978). Conventional X-ray systems have inherent limitations such as low resolution, extended scanning time, beam hardening, low energy or photon flux, and nonselective wavelength. In response to these limitations, synchrotron X-ray imaging techniques have witnessed accelerated adoption in the last two decades and are now utilized by researchers worldwide. Previous studies utilizing synchrotron imaging to unveil cellular-level details of grain seeds were summarized in the context of applications in agriculture and food sciences (Indore et al., 2022). The application of synchrotron high-resolution imaging holds the potential to offer structural and nutritional insights into food grains at the micron scale. This qualitative data could contribute to the development of more effective post-harvest management systems for grain storage than those presently in use.

1.2 Objectives

i. Characterize ten classes of Canadian wheat and four classes of malt barley based on changes in microstructure due to spoilage in storage using synchrotron phase contrast micro CT (SR-μCT),

ii. Determine changes in nutritional minerals and their distribution in grains due to spoilage during storage by Synchrotron X-ray fluorescence bulk imaging (SR-XRF) and X-ray fluorescence imaging (SR-XFI), and

iii. Determine changes in nutritional features (protein, lipid, and carbohydrate) due to spoilage during storage using mid-infrared (mid-IR) spectroscopy.

1.3 Hypothesis

Food grains exhibit variations in structural features, nutritional composition, and distribution, which can influence their behavior during post-harvest spoilage in storage. Synchrotron X-ray imaging techniques offer a means to quantify changes in internal structures (X-ray phase contrast micro-computed tomography), nutritional features (mid-IR spectroscopy), and nutritional minerals (X-ray fluorescence bulk imaging and X-ray fluorescence imaging) resulting from spoilage during storage.

1.4 References

FAO. 2023. Food and Agriculture Organization of the United Nations. https://www.fao.org/faostat/en/#data/QCL.

González-Torralba, J., S. Arazuri, C. Jarén and L.M. Arregui. 2013. Influence of temperatureand r.h. during storage on wheat bread making quality. *Journal of Stored Products Research* 55: 134–144. https://doi.org/10.1016/j.jspr.2013.10.002.

Indore, N.S., C. Karunakaran and D.S. Jayas. 2022. Synchrotron tomography applications in agriculture and food sciences research: a review. *Plant Methods* 18(1): 101. https://doi.org/10.1186/s13007-022-00932-9.

Jayas, D.S. 2012. Storing Grains for Food Security and Sustainability. *Agricultural Research* 1(1): 21–24. https://doi.org/10.1007/s40003-011-0004-4.

Jayas, D.S. and N.D.G. White. 2003. Storage and drying of grain in Canada: Low cost approaches. *Food Control* 14(4): 255–261. https://doi.org/10.1016/S0956-7135(03)00014-8.

Nithya, U., V. Chelladurai, D.S. Jayas and N.D.G. White. 2011. Safe storage guidelines for durum wheat. *Journal of Stored Products Research* 47(4): 328–333. https://doi.org/10.1016/j.jspr.2011.05.005.

Sayed, T.S., F.Y. Hirad and G.H. Albro. 2006. Resistance of different stored wheat varieties to khapra beetle, *Trogoderma granarium* (Everest) and lesser grain borer, *Rhizopertha dominica* (Fabricus). *Pakistan Journal of Biological Sciences* 9(8): 1567–1571. https://doi.org/10.3923/pjbs.2006.1567.1571.

Statistics Canada. 2023. Model-based principal field crop estimates.

https://www150.statcan.gc.ca/n1/daily-quotidien/220914/dq220914b-eng.htm.

Winick, H. and A. Bienenstock. 1978. Synchrotron radiation research. *Annual Review of Nuclear and Particle Science* 28(1): 33–113. https://doi.org/10.1146/annurev.ns.28.120178.000341.

Chapter 2. LITERATURE REVIEW

2.1 Synchrotron Tomography Applications in Agriculture and Food Sciences Research – a Review (Published in Plant methods)

NAVNATH S. INDORE[1], CHITRA KARUNAKARAN[1,2] and DIGVIR S. JAYAS[1]*

[1]Biosystem Engineering, University of Manitoba, Winnipeg MB R3T 5V6, Canada;
[2]Canadian Light Source Inc., Saskatoon, SK S7N 2V3, Canada
**Corresponding author's email: digvir.jayas@umanitoba.ca*

2.1.1 Abstract

Synchrotron imaging is widely used for research in many scientific disciplines. This article introduces the characteristics of synchrotron X-ray imaging and its applications in agriculture and food science research. The agriculture and food sector are a vast area that comprises of: plants, seeds, animals, food and their products; soils with thriving microbial communities; and natural resources such as water, fertilizers, and organic matter. These entities have unique internal features, structures and compositions which differentiate them from each other in varieties, species, grades, and types. The use of a bright and tuneable monochromatic source of synchrotron imaging techniques enables researchers to study the internal features and compositions of plants, seeds, soil and food in a quick and non-destructive way to enhance their use, conservation and productivity. Synchrotron's different X-ray imaging techniques offer a wide domain of applications, which make them perfect to enhance the understanding of structures of raw and processed food products to promote food safety and security. Therefore, this paper summarizes the results of major experiments carried out with seeds, plants, soil, food and relevant areas of agricultural sciences with more emphasis on two synchrotron X-ray imaging techniques: absorption and phase-contrast imaging and computed tomography.

Keywords: Synchrotron X-ray , X-ray absorption, X-ray phase-contrast, microcomputed tomography, plant imaging, seed imaging, soil-root medium imaging, food imaging.

2.1.2 Introduction

Agriculture has made many advancements after the 19th century to ensure food security for the world's ever-increasing population with the help of high-yielding varieties, integrated farming, post-harvest management, mechanization, and sustainable use of natural resources. Agriculture inputs (seeds, soil, and fertilizers) and produced food (plants, fruits, grains have unique internal

features, structures, and compositions that differentiate them from each other in varieties, species, grades, and types. Every entity of agriculture is adapted and suited to local conditions by altering their internal structures, composition, and features, either naturally or by the intervention of human skills. The study of these internal features at the micro to nanoscale level is vital to study species and composition for addressing several questions. Therefore, many studies have been carried out for decades using tools like optical light microscopy, transmission electron microscopy, scanning electron microscopy, and histology to gather vital microscopic information. Although these techniques were able to provide information, they had certain limitations like destructive sample preparation, sampling area, accuracy of sample location, less number of samples, and extensive sample preparation protocols, all of which can make data interpretation more difficult [1]. Even methods like histology cannot give reliable visualization of small cellular interspaces or indicate the existence of networks of spaces [2]. Therefore, to overcome these challenges, the applications of X-ray imaging have been started since 1980 in agriculture and food sciences with applications in cotton [3], lettuce [4], pine [5], tomato [6], rice [7], wheat [8,9], pecan [10], fruits [11–13], plant leaves [14], and soils[15]. A detailed review was carried out on the use of X-ray computed tomography (CT) in agriculture and food applications [16] with recommendations on the requirement of more advanced X-ray techniques and applications in these areas and the development of commodity-specific algorithms for image processing like those found in the medical imaging field. These conventional X-ray CT systems have certain limitations like low resolution, more scanning time, beam hardening, low energy or photon flux, and nonselective wavelength. Therefore, synchrotron X-ray imaging techniques have gained pace in the last two decades and researchers across the globe have started their use in studies such as: 1. dynamic processes like water or nutrient flow in live plants [14,17–26], internal structural information in seeds [2,27–31], fruits [13,20], wood [24,32–34], and soil root medium [25,35–44]; 2. development of innovative nutritional foods [45–50], and 3. disease management in plants and animals [51–54]. These studies have been carried out using non-invasive synchrotron X-ray imaging methods and are summarized in this article. There are a few questions that require answering on what made synchrotron a popular tool among agriculture and food scientists. This article highlights the unique capabilities of two synchrotron X-ray techniques; absorption micro-CT and phase contrast micro-CT over conventional X-ray imaging methods used in agriculture and food sciences. Paper has also summarized all synchrotron machine parameters used till date in agriculture and food science studies, which will be very useful in planning of new experiment

2.1.3 Synchrotron X-rays

A unique electromagnetic spectrum is created by bending the path of electrons traveling at the speed of light in a synchrotron [55]. During this process, synchronous addition of energy to the electron beam in the ring takes place by changing the energy of electrons or adding energy to the beam without changing the orbit of electrons. This powerful scientific tool was invented back in the late 1960s, and the first-generation multi-GeV storage ring became operational in 1974 at Stanford Synchrotron Laboratory [56]. The synchrotron (SR) generation facility can be very large, the small one equivalent to a football field size. To date, around 67 synchrotron facilities are operational, among the 86 established synchrotron facilities across the world [57] and these establishments themselves explain the importance of technology in research and development across the world.

The facility of the Canadian Light Source (CLS), Saskatoon is taken as an example to briefly describe the layout of a synchrotron imaging facility (Fig. 2.1): it consists of 1. an electron gun, 2. linear accelerator, 3. booster ring, 4. high vacuum storage ring, 5. insertion devices (such as bending magnets, wigglers, and undulators), 6. beamlines with monochromators, 7. optical hutch (slits, filters, mirrors), 8. experimentation hutch (sample loading), and 9. workstations (data acquisition and processing).

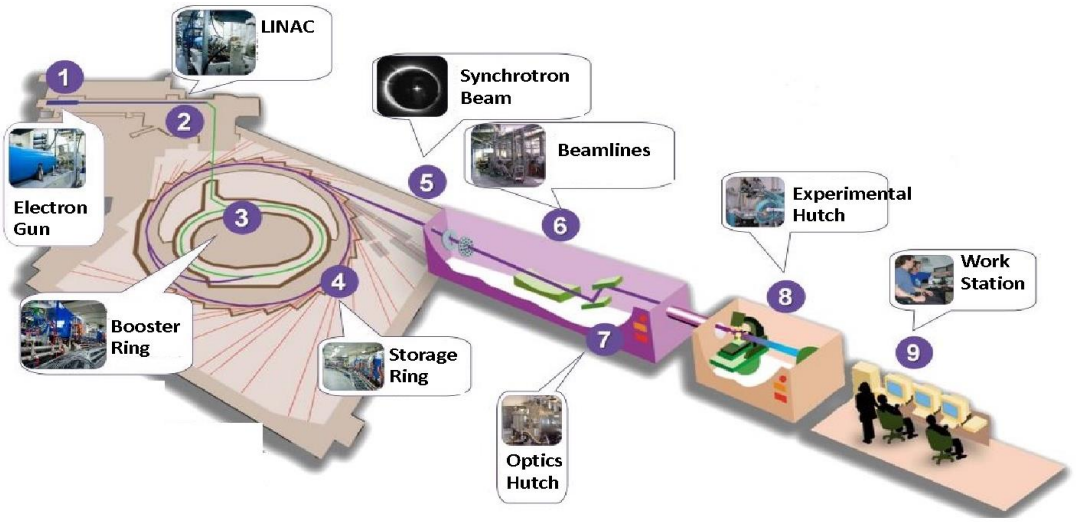

Figure 2.1 Major components of a synchrotron X-ray imaging beamline system (Source: Canadian Light Source, Saskatoon; www.lightsource.ca).

2.1.4 Properties of synchrotron light and interaction

The X-rays generated from synchrotrons generally are of three types: soft, tender, and hard. X-rays are categorized as soft X-rays when generated at or less than 2 keV, tender X-rays at 2-6 keV energy, and hard X-rays at greater than 6 keV [58]. Synchrotron X-rays have unique properties such as high flux density, coherent, and selective wavelength/monochromatic. The developed synchrotron facilities around the world have ring energy (1.7 – 9.0 GeV), ring current (0.010- 0.5 A), ring size (198- 2304 m), emittance (1 nm radx10pm rad to 6 nm rad x 100 nm rad) and brilliance (10^{18}-$10^{23}\, ph.s^{-1}mm^{-2}mr^{-2}0.1\%bw^{-1}$) [59,60]. More details about the brilliance for other cases could be found elsewhere [60,61]. This paper has covered absorption and phase-contrast synchrotron imaging techniques, where SR X-ray is attenuated by photo absorption and elastic (Thomson) scattering processes and their detailed interactions with the material can be found in the literature [60,62,63].

Synchrotron imaging methods are used either in two-dimensional (2D) or three-dimensional (3D) imaging. The tomography and microcomputed tomography are the focus of this review paper. In 2D imaging, a set of two-dimensional images are acquired using a monochromatic source just like radiographs, hence the beam-hardening issues are avoided that are more common in polychromatic beam [64]. The contrast in images is driven by a combination of absorption or density differences, and phase or small density variations of the sample components. The 3D computed tomography makes use of computer-processed combinations of many X-ray projections (2D images or radiographs) taken from different angles of a sample in absorption or phase contrast imaging, then produces cross-sectional (tomographic) images of specific areas of the sample.

2.1.4.1 Synchrotron absorption tomography or micro-computed tomography (SR-µCT):

The general procedure of imaging in SRXTM or µCT consists of (Fig. 2.2): 1. selection of photon energy and flux of desired wavelength by use of a monochromator, 2. sample rotation about an axis from 0-180° in different step sizes in CT, 3. acquisition of images by a set of detectors, and 4. image processing and segmentation. The contrast in imaging is driven by absorption differences and density differences. There is no beam-hardening with this technique, which causes an inaccurate portrayal of the true X-ray absorption of the specimen and inaccurate measurements, and digital sections are more difficult to segment in image processing [65]. Synchrotron X-ray tomography has proven to be an excellent imaging system

for the study of the fossil as well as modern plants [20]. The SR-µCT analysis is based on transmission images after the material attenuates the incoming X-ray beam either by absorption or by scattering (Eq.1). The correlation between the incident or transmitted beam intensity and the material properties can be related through the Lambert-Beer law [32,66]:

$$I = I_0 e^{-\mu.t} \quad (1)$$

where I is transmitted beam, I_0 is incident beam, µ is linear absorption coefficient, and t is the material thickness [59].

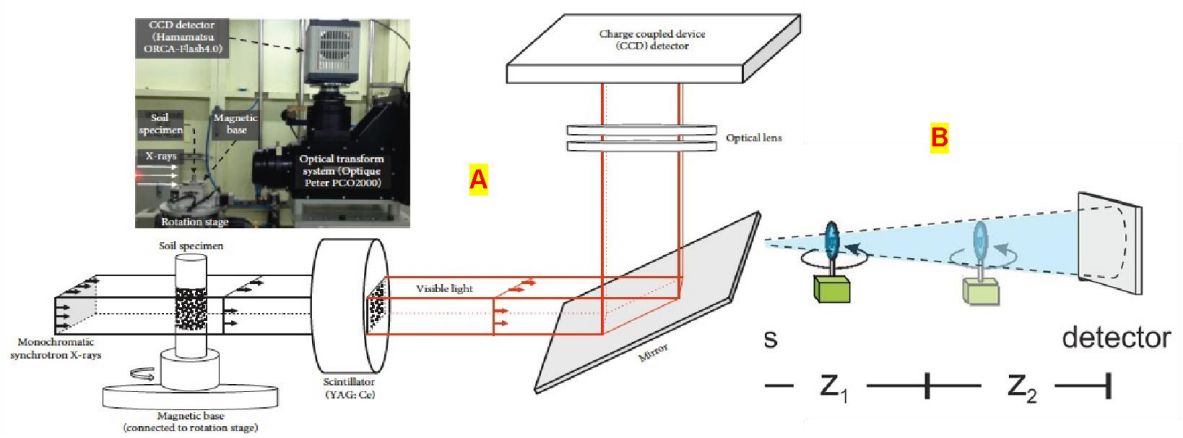

Figure 2.2 (A) Basic layout of synchrotron X-ray micro-CT [35] and (B) Setup of phase contrast micro-CT where sample to detector distance is adjustable [37,67]

2.1.4.2 Synchrotron phase-contrast imaging or microtomography (SRP-µCT)

The imaging setup is very similar to SR-absorption based µCT imaging, the only difference is that rather than placing the detector close to the sample, it is located at some variable distance which gives rise to Fresnel fringes [68] (Fig.2.3). Sample to detector distance is set in a such a way that it always less than sample to source distance [54]. The technique makes use of the refraction of X-rays by the sample and highlights the edges and internal boundaries of a sample, therefore, low-density materials (soft plant parts) can also be imaged, which do not absorb X-rays sufficiently to form a distinct absorption X-ray image [69]. Phase-contrast imaging method is most sensitive to small changes in the refractive index (Eq. 2&3), which creates edge enhancement and increases the contrast of the edges of structures or material boundaries [70]. Fresnel diffraction, resulting from an adjustment of distance, allows for control of the edge enhancement effect which is the key feature of phase-contrast imaging [17,71,72]. It is a

powerful tool to obtain quantitative data from biological samples because of the significant difference in electron density between air, biological tissues, and water [26].

The refractive index of matter can be defined as [54],

$$n = 1 - \delta + i\beta \tag{2}$$

where δ is the decrement in part of the refractive index, which is the phase shift term, and β is the attenuation term for absorption.

The total phase shift ∅ can be related to δ as, ∅ = δkz and the absorption term β can be related to k and z as $\mu' = \mu.t = 2\beta k.t$ (3)

where μ is the absorption coefficient, k is the wavenumber, and t is the object thickness. The detailed theory about SR- μCT and SRP-μCT concepts, working and synchrotron interactions is available [54,61]. A comparison in working principles of both absorption and phase contrast imaging is illustrated in Fig. 3.

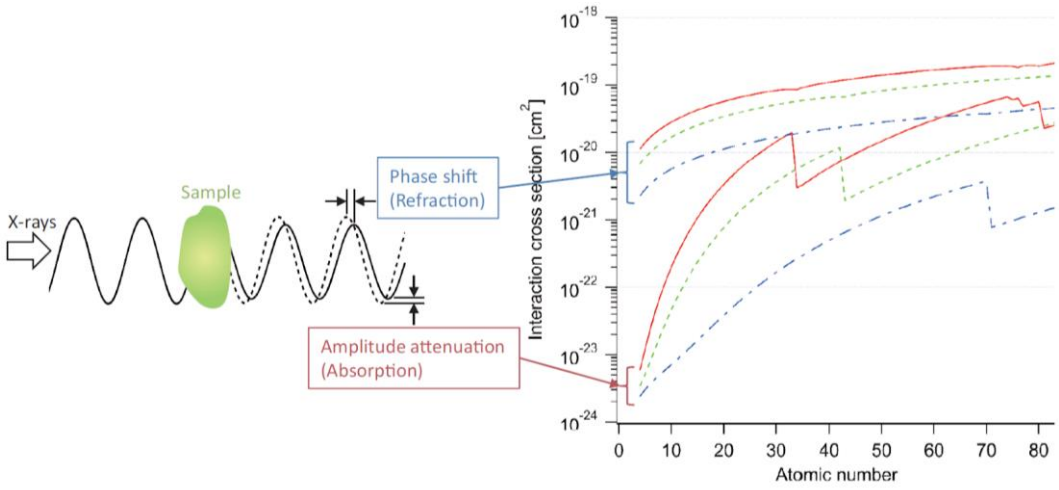

Figure 2.3 Schematic diagram of how X-rays pass through object. Dashed line shows X-ray wave without object, and solid with object. Upper curves: cross section corresponding to X-ray phase shift. Lower curves: cross section corresponding to X-ray absorption [73]

2.1.4.3 Image processing used in agriculture and food sciences studies

It is an important step in the analysis of acquired data which is in pixel form with associated grayscale value. In computed tomography, grayscale values represent the X-ray absorption/phase values, where higher (brighter) grayscale values indicate higher absorption and lower (darker) indicate lower absorption [55]. The acquired raw projections in both mentioned imaging methods are sometimes noisy and associated with artifacts like rings, and motion streaks, which can be caused due to motion, imaging system, and sample conditions. These artifacts can be removed by reconstruction of images, which can be achieved by dedicated software like PITRE, UFO-KIT, Recon., PyHST, Octopus 8.3, SYRMEP TomoProject, VG Studio Max, and DAWN [17,24,35,67,71,74–78]. Initial normalization can be done by subtracting flat (images taken with a beam and without sample) and dark (images taken with beam off) images from radiographs (Fig. 4) by any software like PITRE [71]. Preliminary reconstruction of tomographic images is done using filter back projections and non-iterative phase retrieval algorithms (like Paganin) to produce images with less noise and artifacts [16]. Reviewed studies have used modern approaches like Fourier transform filtered backprojection [2], correction of sinograms, phase retrieval and ring removal by filters and improved signal-to-noise ratio [67,74]. The reconstructed data are then further processed for improving contrast, segmentation and thresholding by either one of the software; ImageJ plugins (Polar transformer) or AVIZO [22,24,40,75] or Dragonfly [79], Pore3D [48], 3dma, and customized Matlab program [78]. It is important to select X-ray energy that is appropriate for the material under testing to optimize both spatial resolution and contrast sensitivity, so an adequate signal-to-noise ratio could be obtained [43]. The sequence of steps involved in the reconstruction and processing of images in detail is discussed (Fig. 2.4) as an example here, starting from flat and dark field correction, reconstruction of acquired projections by PITRE then to segmentation and thresholding in 3D by Avizo [37]. Applications of advanced approaches like machine learning to acquired data [40,80] and deep learning for phase retrieval [81,82] are limited (only a few like local thickness analysis for pore space characterization [39]) in reviewed studies, which means conducted studies were not able to harness the full potential of synchrotron imaging unlike in material science and medical imaging. It has been found that most of the studies processed 8-bit datasets except in a few studies where (16-bit scale of 0–65,535) datasets were used [54] and one group has used the statistical tool of fisher ratio index for enhancing contrast in reconstructed images [27].

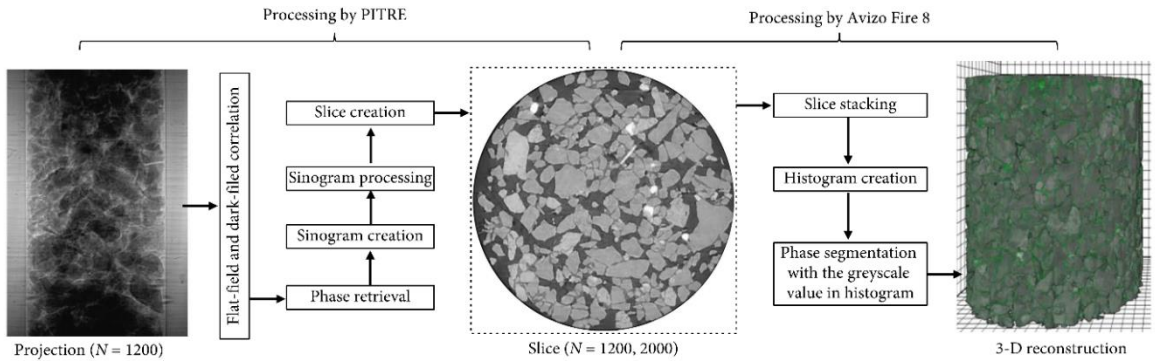

Figure 2.4 . Phase retrieval, slice creation, and 3D reconstruction of a soil sample [37]

2.1.5 Applications in Agriculture

Synchrotron X-ray imaging is already a well-established technique and has many applications in medical and materials sciences. It has been developed for several decades but only in the last two decades, SR has been used in plant science experiments [83,84]. Published research has demonstrated that SR-μCT and SRP-μCT were extensively used for creating three-dimensional images which have enabled researchers to look at different virtual slices of samples and visualize internal micro-structures of plants, soil, and seeds without sample destruction [27].

2.1.5.1 Seeds

Seeds are an integral part of the plant ecosystem which store vital information, food, and energy. The study of modern and ancient seed structures at micro-level is important to conduct their evaluation for vigor, dormancy and other characteristics. Seed growth and physiology are actually dependent on several microscopic features, including cell shape, cellular water potential and the presence of intercellular voids [79]. The structure and composition of cell corners in a dry seed are tissue-dependent and vary with plant development [2]. Synchrotron X-ray imaging is a perfect tool for studying these details in seeds at a cellular level, hence it was used to find links between modern and fossil seeds [20], seed coat thinning [30], developmental stages during germination [27], intercellular void network [2,13]. Paleobotanical studies depend on the recognition and accurate identification of extinct species of plants. The archaeological samples are precious and require non-invasive approach. Traditionally, histology was the only method which involved differential staining to reveal differential tissue and cell wall chemistry, but with synchrotron, differences can be highlighted by varying X-ray absorption. Therefore, Smith et al. [20] carried out successful digital visualization of different components of modern and fossil fruit seeds (Table 1) and visualized

chemically distinct materials of preserved specimens differentially because of a difference in X-ray absorption values. Traditional sectioning does not infiltrate well due to hardness of herbarium specimens, but it can be addressed by digital segmentation and dissection of data in 3D of synchrotron X-ray images for creating virtual infills for simulating taphonomic effects [20]. A similar study was reported dealing with the study of ancient seed grains [30] and documented the evidence of seed coat thinning (from 23.2 to 10.6 µm) in horse gram seed of archaeological and modern seed samples (Table 1). Synchrotron was used extensively for fossil plants, cretaceous flowers [76], and seeds imaging and contributed dramatically to expanding the level of information available for studying diverse fossil plants [85].

Earlier, conventional histology only was used to study the developmental stages of crop seeds which is a skilful and time-consuming job, but Rousseau et al. [27] team had imaged for the first time the development stages of maize (Table 1) seeds after days of pollination (DAP - 7, 9, 12 and 21). The results were compared with conventional histology and demonstrated a good match for the estimation of the length of different components of the seed. The simple thresholding was used to quantitatively segment maize seed into four components of the seed (embryo, endosperm, nucellus, and pericarp) from 7 to 21 DAP (Fig. 2.25). The lack of cellular resolution as compared to conventional histology can be overcome by higher spatial resolution by imaging a small part of the sample in a local tomography mode inside the same type of seeds [27]. Use of statistical tool of fisher ratio as a contrast index in their experiment enhanced the quality of the images and segmentation strategy.

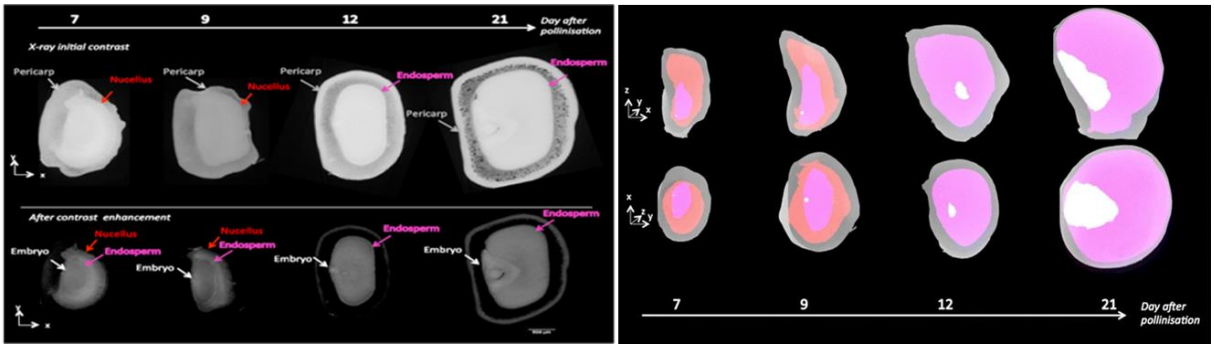

Figure 2.5 Left: X-ray images and Right: 3D segmentation of maize seeds at four different developmental stages corresponding to 7, 9, 12 and 21 days after pollination [27]

A seed is a living entity, which means it respires even after harvest or in storage and can retain its germination. Gases like oxygen are required for support of life and trapped gases inside seed structure or components might play important role in germination. Therefore, Cloetens et al. [2] had used synchrotron (Table 1) X-ray imaging of Arabidopsis seeds and concluded that

intercellular void network provides a transport system for easy gas exchange in embryos and storage space for the oxygen. Produced results were a 3D representation of the local electron density which is directly proportional to the refractive index of material for hard X-rays [2]. The investigation also claims that stored oxygen plays an important role in the onset of germination, during imbibition (Fig. 2.6). Dhondt et al. [86] had also scanned different *Arabidopsis* plants until 13 d after sowing at a spatial resolution of 10.4 µm like Cloetens et al. study [2], (Table 1) and revealed many detailed morphological features such as furrows in the hypocotyls, branching of trichomes, the pollen sacs on the anthers, and the stigma on the flower style. Seeds like rapeseed are small and may appear homogeneous at the macroscopic scale, but their growth and physiology are dependent on several microscopic features, including cell shape, cellular water potential and the presence of intercellular voids [87]. SR-µCT has provided evidence for the existence of voids (Fig. 2.6) and its spatial and geometric complexity has a strong influence on endogenous gas transport and flux, and so may affect the local respiratory activity and seed growth [88]. Seed structural characteristics may responsible for gas exchange and it can be occur through corner cavities located in dry seeds [2].

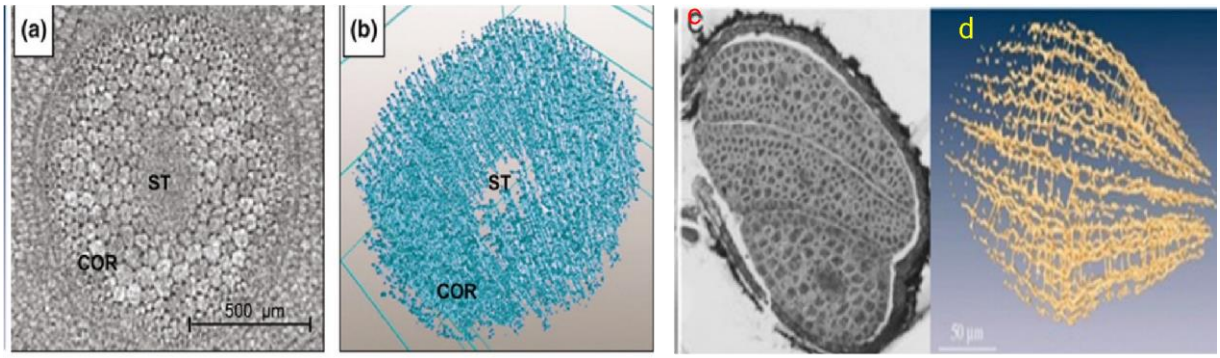

Figure 2.6 3D model of void spaces (a,b) in the hypocotyl of a developing rape seed (Brassica napus) [87] Copyright (2006). National Academy of Sciences and Virtual slice (c,d) of Arabidopsis seeds, void network and reconstructed voids in phase contrast imaging [2]

2.1.5.2 Plants

The living plants have unique internal features to transport water and nutrient from roots to a body of plant (leaves and fruit). The complex water and gas transport phenomena that occur in plant tissues were studied in detail using SR by mapping porosity, microstructure arrangement and the connectivity of the vascular systems. The cellular level information could be gathered easily without any need for additional preparations of samples in plants for analysis [2,30,40].

2.1.5.3 Structural, composition and dynamic process

Synchrotron absorption and phase contrast imaging have been used extensively to study structure-function relationship and dynamic processes in plants [14,17,28,40], vessel networks [11,32,52,87,89], diffusion of gases (CO_2) in leaves [26,86,90], vascular function in live plants (sunflower, oak, redwood, walnut, grapevines and maple) [40], occurrence of xylem cavitation in rice and bamboo [18], and stress physiology [91].

The differential X-ray attenuation is responsible for visualizing the difference between water, and air, and this property makes synchrotron X-rays perfect to study how water refills xylem vessels in plants [92]. As mentioned earlier phase contrast imaging is best suited for soft tissues because it has lower absorption for X-rays, therefore it was compared with SR-μCT (Table 1) by one group at a Canadian light source and revealed microstructural details of the canola stem such as cavitation and surrounding tissues of the vessels [1]. Phase contrast imaging was found best to generate better contrast in images to reveal finer details (Fig.2. 8) and the xylem water refilling process. Whole canola plants were scanned during this experiment, so X-ray energy optimization was carried out and fixed at one energy 18 keV for above ground portion, and two energies 24 keV (clay soil medium) and 38 keV (sandy clay loam medium) below ground portion [17]. A group from Shanghai also carried out a similar study and found (Table 1) that water refilling process is not the same throughout all parts, because cavitation occurs to different degrees under different dehydration conditions [18]. Similar kinds of studies were reported for study of drought-induced embolism in stems (Table 1) of grapevines [22,34,93], sunflower [21], wood microstructure [89], and coast redwood [24]. The purpose of these studies was to quantify resistance to embolism in plants, which is important for understanding their drought response [34] and whether plants can rapidly refill or not, in embolized conduits during recovery from drought stress, which is an important component of their survival in a rapidly changing climate [24]. Embolism affects long-distance water transport through plant xylem which often coincides with drought. Researchers were able to study the dynamics of drought-induced embolism in plants (grapevines) and produced three-dimensional, high-resolution, time-lapse observations of embolism spread (Fig.2.7). High-resolution time-lapse SR-μCT images of embolism removal in plant have improved understanding of the final stages of a biophysical process that plays a critical role in drought recovery of plants [24]. X-ray induced damage of about 25% was also reported by one of the groups during SR-μCT scanning of sunflower plants [21]. Choat et al. [24] were examined spatial patterns of xylem embolism in saplings of a conifer species coast redwood during cycles of drought and rewatering. They did not find any evidence for embolism refilling in tracheids after drought up to few weeks in

their study on basis of SR-CT data and provided a reason that, conifer species lack an active refilling mechanism. Also, another reason is that their xylem lacks the specialization in cell function necessary for such a process, which can be observed in angiosperms. On the basis of these salient findings, several experiments could be run at synchrotrons, ranging from the characterization of drought resistance of different crop species to the evaluation of different treatments on species hydraulics.

The novelty of synchrotron imaging was proven when it was used (Table 1) for the first time for the characterization of gas film retained on superhydrophobic leaves of submerged plants, which revealed how wetland species can survive in submerged conditions [11] and such kind of studies have opened the new area for its application. The generated data could be used for study of structural changes in the cuticle that occur with a time of submergence and then how these changes affect hydrophobicity and the capacity to retain a gas film under water [11].

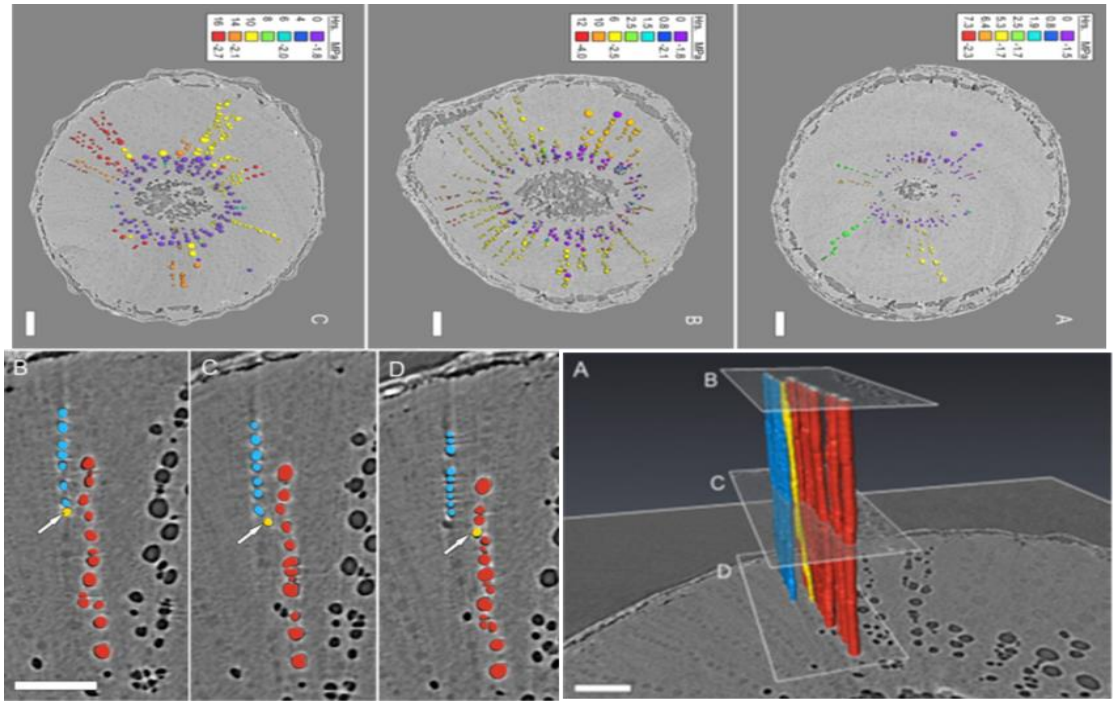

Figure 2.7 Transverse high resolution CT micrographs of grapevine stems showing the radial, sectored spread of embolisms during the simulated drought experiments. Vessel lumen colour denotes the time point (hours) at which gas was first observed inside the vessel. Top:. Bars = 1 mm. Bottom: volume renderings of grapevine vessels showing a pathway for embolism spread between sectors and (B to D) Vessels in the red sector embolized first and then spread through a vessel (yellow) that drifted tangentially from the red sector to the blue sector [93].

Manufacturing good structural and utility-based wood is important for any industry, therefore being a natural resource, the study of its structure is of prime importance. The synchrotron has

been used in a study of wood structural components, environment stress, and fungal decay at the micro level [32,33,89]. The detection of boundary surfaces between neighbouring cells and interconnectivity in wood specimens was challenging with conventional scanning electron microscopy (SEM) and light microscopy [71], but SR-μCT made it possible (Table 1) to map those components. The acquired data were used in the estimation of volumes of water transported in vessel cells and visualized vessel networks in wood samples to understand the effects of wounding and environmental stresses on the xylem structure and water transport system in wood. Forsberg et al. [33] used a novel application combining SR-μCT and digital volume correlation for the deformation analysis of wood under bending stress (Table 1) and developed a methodology for study of fresh plant tissue fracture in structural timber. This was one of the first attempts to use synchrotron to study the influence of anatomical features on the fracture behavior of wood and quantification of deformations during in situ micromechanical experiments.

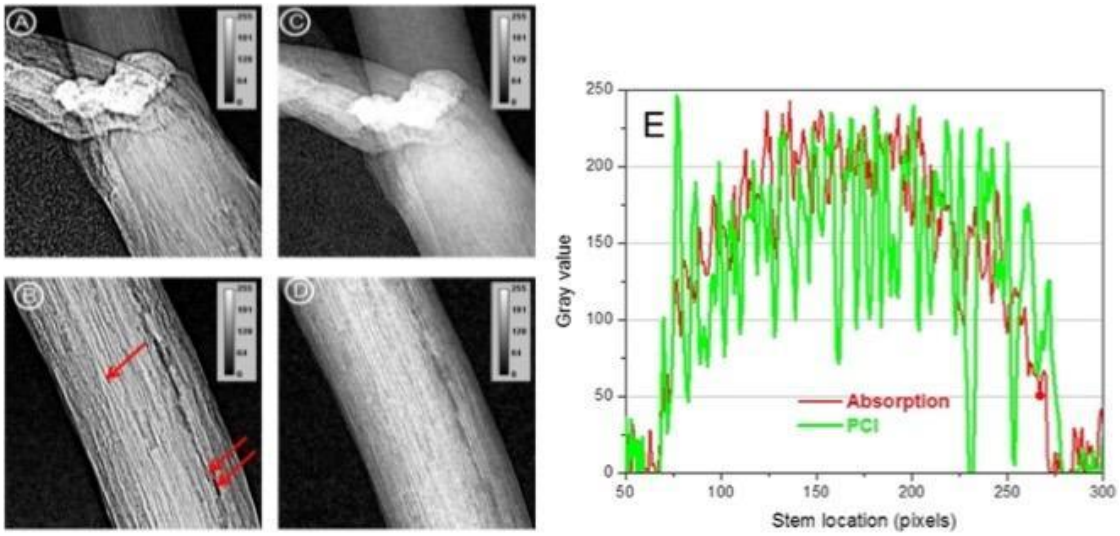

Figure 2.8 The 3D images showing internal details of canola plant in SRPμCT (A,B) of plants and SR-μCT (C,D). Histogram of gray values for absorption and phase contrast are given in E [1]

The high-resolution imaging data generated by synchrotron imaging can be used in validation of developed models like light propagation, CO_2 diffusion, and photosynthesis simulation, therefore, Ho et al. [90] and Verboven et al. [88] imaged tomato leaves (Table 1) to visualize micro leaf structure for gas exchange and related them to leaf optical properties for validation of developed models. Radiation dose in synchrotron imaging is dependent on photon energy, attenuation coefficient, and density of a material, therefore soft tissues are susceptible to damage by X-rays [28]. Therefore, to minimize the radiation doses, Matsushima et al. [28] used three photon energies 30, 40, and 50 keV in scans of three varieties of rose peduncles. In the

selected photon energy ranges, linear absorption was negligible for soft plant tissues. Both SR-μCT and SRP-μCT methods (Table 1) were used in this experiment. In SRP-μCT due to edge enhancement, the cell walls of each single cell were distinctly depicted and clear discrimination was achieved between fully intact cells containing cytoplasm and water-filled cells and air filled objects [28]. The tissue damage was observed for one variety due to more exposure time at 30 keV and 40 keV energies as compared to 50 keV, where effective surface dose was less. It was clarified from the results that the involvement of distinct structural differences in a vascular bundle and typical peduncle pith structure was responsible for the evaluation of different vase life for the selected rose varieties.

2.1.5.4 Infection and disease detection

Capabilities of synchrotron imaging were assessed for disease and infection detection in live plants in a non-invasive way, like visualizing changes in internal features of plants, for detection of fungal infection or decay in the wood [32], fusarium resistance characterization in wheat [52,54], and understanding insect anatomy for control management practices [51]. Fusarium is one of the five top priority diseases of wheat in Canada, which not only reduces yield but destroys protein content and results in toxin accumulation in grain [54]. Synchrotron imaging was found useful in studying plant-pathogen interactions, especially in determining the role of cell wall structural characteristics in response to fungal infection [52]. Therefore, Lahlali et al. [51] mapped structural differences in spikelets of wheat, because it plays a significant role in resistance to Fusarium. Differences in mass densities and phase contrast signals between healthy and infected spikelets are clearly visible (Fig. 2.9). In one cultivar (Muchmore) structure of rachis was altered and became more transparent to synchrotron X-rays which was a sign of infection. Wheat typically has resistance to pathogens, based on which wheat is classified into five types (Type-I to Type-V). High-resolution X-ray images can be used in the characterization of wheat into five categories on basis of resistance. Brar et al. [54] scanned seven genotypes of wheat using SRP-μCT (Table 1) for detection of changes in voids, volume fraction, and voxel intensity due to infection of *Fusarium graminearum*. Their results revealed that rachilla and rachis nodes together provide significant resistance to pathogen spread because inoculated spikes had higher void space fraction and lower X-ray attenuation compared with controls. They also stated that a pathogen can still invade internodes, but this structural reinforcement significantly impedes disease progress. The disintegration of host tissue was observed due to infection and failure of the ovary to develop in the infected floret were observed in the images. They had also developed Python-based scripts and produced

histograms with voxel intensity for each ROI (voxels ranging from 99 to 145 million). They found that one genotype (*CDC Alsask*) which was more susceptible to FHB *(Fusarium graminearum)* had higher void space volume among seven genotypes. As discussed earlier, structural integrity is important in wood used in any industry, therefore it is usually treated for better resistance to decay and more service life. Changes to wood structure at micron lever under fungal decay is of prime importance. Hence, synchrotrons have been found useful in mapping changes in the wood structure under fungal infection. Gilani et al. [31] used SR-µCT (Table 1) for wood at the micro-scale level and evaluated alterations in density distribution after incubation of samples with two white-rot fungi. They were able to develop an algorithm for quantitative study of the density changes in the wood cell walls after different stages of fungal decay and mapped internal changes to establish relationships to describe variations in porosity and density.

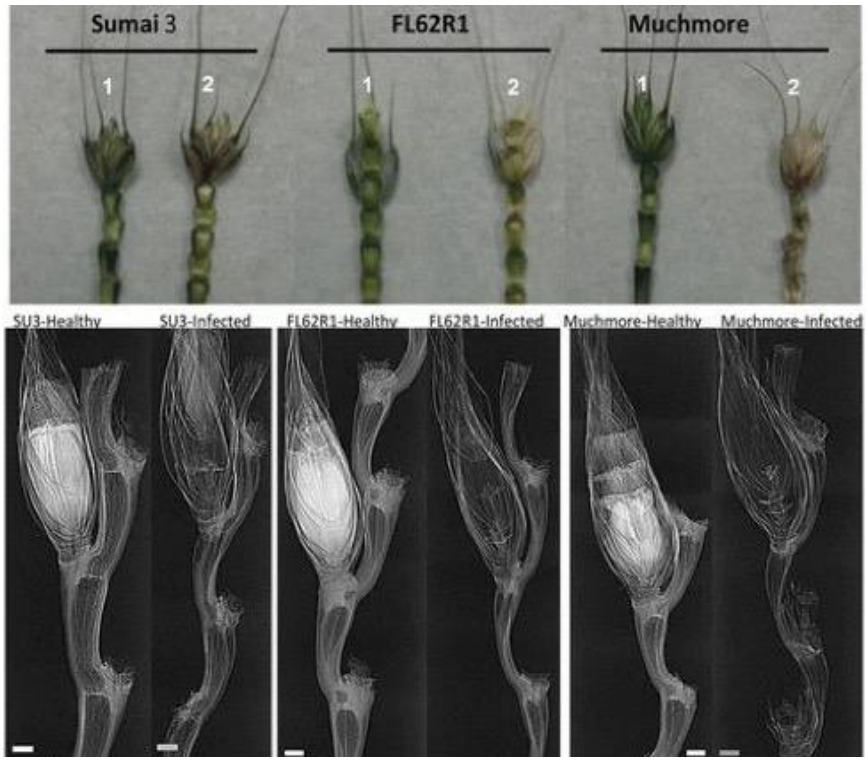

Figure 2.9 Phase contrast X-ray images of healthy (1) and infected rachis (2) of wheat cultivars at four days after inoculation with FHB [91]

2.1.5.5 Soil medium and roots

Good soil structure is essential for supporting plant life to provide essential nutrients and ensure sustainable agriculture. The quantification of pore network, microstructure properties and their relationships are required to enhance our ability to predict changes in soil ecosystems [94]. The hard X-rays of synchrotron have been used to investigate and characterize pore networks,

arrangement of particles, the effect of organic and inorganic matter, root hairs, and soil state under alternate dry-wet conditions [25,35,39,43,44,72,77,95–97]. All the experiments reviewed in soil application were carried out at higher X-ray energies up to 78 keV and high resolutions (0.65,1.0 μm) in comparison to experiments with plants, fruits, and foods [25,37,77].

2.1.5.6 Internal structures of soil aggregates

Study of internal arrangement of soil aggregates is important because soil structure provides pathways for the transport of water, nutrients, gases, and habitats, therefore, it is a fundamental property of soil fertility and quality [98]. The synchrotron absorption imaging and computed tomography were used to investigate the arrangement of soil aggregates and changes in soil pore network due to fertilizer application [96], porosity due to dynamic change in water content [95], and effects of type of soil on water flow and behavior under physical force on structure [39,77]. Soil erosion is a major problem across the globe, where native grassland is converted as farmland for growing food crops. In recent years, a lot of efforts were made to improve the health of these eroded land by growing natural vegetation. In the semi-arid region of China similar efforts were made for stabilizing abandoned croplands with natural vegetation for different lengths of time. One of the aims of a study was to investigate whether natural revegetation on abandoned cropland could improve the stability of soil aggregates, and whether their microstructure could become more connected during natural revegetation. Zhou et al., [35] used SR-CT for quantification of complex aggregate microstructure in soil and its relationship to vegetative restoration. It was found that aggregate microstructure was modified substantially during the vegetative succession and the porosity of the aggregates increased from 9.2 to 45.9% for samples of selected cropland sites. In this study, pore sizes and shapes were expressed based on equivalent diameters and shape factor (F=0.2- 0.5) and classified into four size classes (<30 μm, 30–75 μm, 75–100 μm, and >100 μm) and three shapes (regular, irregular, elongated). It was concluded from the results that aggregate microstructures were more at abandoned cropland sites than at active cropland sites.

Soil micro aggregates microstructure plays an essential role in chemical heterogeneities, microorganism distributions, origin and development of hot spots in soils [39]. Hence quantification of soil aggregates has become of prime importance. The analysis protocol for the morphometric characterization of complete soil micro aggregates had been developed (Table 1) for two distinct soil types of regions; one from Kansas, primarily composed of inorganic particles, and one from Barrow (Alaska) dominated by plant fragments (Fig. 2.10).

In the study they found that the use of local thickness analysis, commonly used in medical imaging for porous material characterization was good approach. Local thickness can be defined for a voxel as mean diameter of the maximum inscribed sphere in the structure that contains the voxel [39]. The Kansas sample had shown typical interstitial pore space, created by the aggregation of rounded mineral particles and aggregates. whereas, a more complex microstructure was found in the Barrow sample with a strong organic component which was verified by variation in attenuation values, due to the high percentage of plant fragments. The Morphometric analysis revealed that Barrow aggregate had high porosity (81%) as compared to Kansas aggregate (43%) which typically has granular composites.

The long-term use of fertilization practices can improve soil aggregation through associated increases in organic matter over time, but organic and inorganic fertilization have different influences on aggregate structures [35]. The aggregate stability under organic and inorganic fertilizer application can be studied using synchrotron [94]. They did analyzed soil samples treated with NPK (chemical fertilizer) + OM (organic matter) and NPK and CK (no fertilizer) (Table 1) at Shanghai synchrotron facility. They had used open-source platform Imagej for reconstruction with a polar transformer plugin and a Matlab program for ring artifacts removal by masking the Fourier transformed image. Use of algorithms like morphological erosion based on the algorithm (LKC algorithm) was found in their study for pore–throat-network construction (Fig. 2.11). Measurement of porosity, nodal pore-size distribution (PSD), pore throat size distribution (TSD), effective throat/pore radii ratio, path length distribution, and tortuosity (ratio between the path length and the straight distance between the ends of the path) were also determined by developed methodology of image processing. Pores were classified into macropores (> 500 μm) and mesopores (≤ 500 μm) according to their equivalent diameters in their study [35]. The results of image analysis revealed that microstructural pore properties were almost the same for NPK and CK treatments. The number of pores, number of pore throats, and number of paths between adjacent nodal pores were all significantly decreased by the NPK + OM treatment relative to the NPK and CK treatments. X-ray attenuation coefficients of organic matter fall between water and air, hence the mineral matrix, making phase separation problematic [77]. Therefore, Peth et al. [77] used monochromatic SR- μCT at photon energies above the absorption edge (78 keV) and photon energy below the absorption edge (70 keV) to locate soil organic matter in the stained soil aggregate samples in relation to soil structure, where attenuation contrast is optimal for distinguishing other soil constituents.

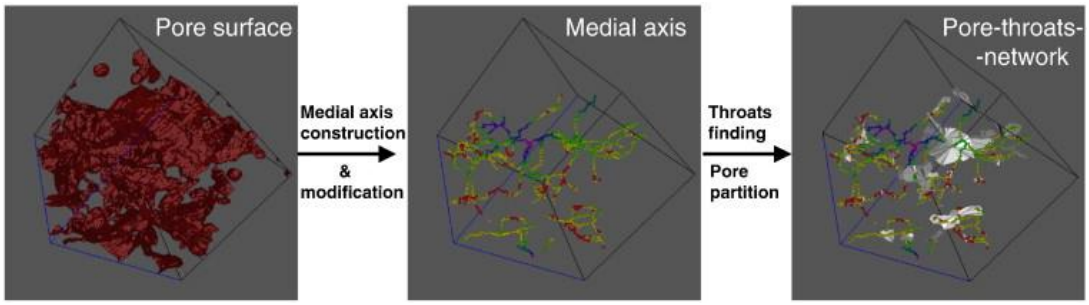

Figure 2.10 Schematic sequential diagram of the pore–throat network construction [35]

As discussed earlier, vegetation has significant impact over soil aggregate structure, similarly wetting and drying of soils is also responsible for changes in aggregation and soil structure [36], hence there is good scope to enhance understanding of changes in topsoil microstructure due to above phenomena. The soil aggregates of 3–5 mm were scanned with an SR-μCT at the same beamline (Table 1) and revealed that wet aggregate stability and tensile strength were closely associated with the pore characteristics. The pore characteristics (pore space larger than 75 μm) and soil clay content accounted for as much as 99% of the variation in both wet aggregate stability and tensile strength [36]. The pore-space geometry of soil aggregates determines the transport of water, gases, and nutrients [77], therefore, 3D visualization and quantification (Table 1) were carried out on two distinct soil samples which went through different management practices (tilled and grassland). In the study, sample structure was quantified on basis of pore-size distributions (PSDs), throat-area distributions, effective throat, frequency distributions of pore channel lengths, widths, and flow path tortuosity. It was determined that the soil aggregate of the tilled site showed more gas and water transport limiting micromorphological features compared to grassland management system. In continuation to this, even agriculture management operations like tillage have an influence on the microstructure of soil aggregate. The study of such mechanical forces has become necessary, therefore, conditions like compaction were been simulated on beads, natural sand, and clay and data acquisition on them was carried out [37]. Two photon energies were used 18 and 20 keV during image acquisition for quick determination of the water distribution in the selected material. Quantification of water (10.2 and 9.3%, for glass beads and sand, respectively) from image segmentation at 0.65 μm/pixel was obtained which was comparable with those measured by the oven-drying method (9.7 and 9.4% for the glass beads and sand, respectively). Contrast agent iodine was used in this study and it was stated that addition of 20% by weight of iodine-based contrast medium can increase the greyscale value of the liquid

and enhance the air-water contrast which contributes to (semi) automatic segmentation of water phase.

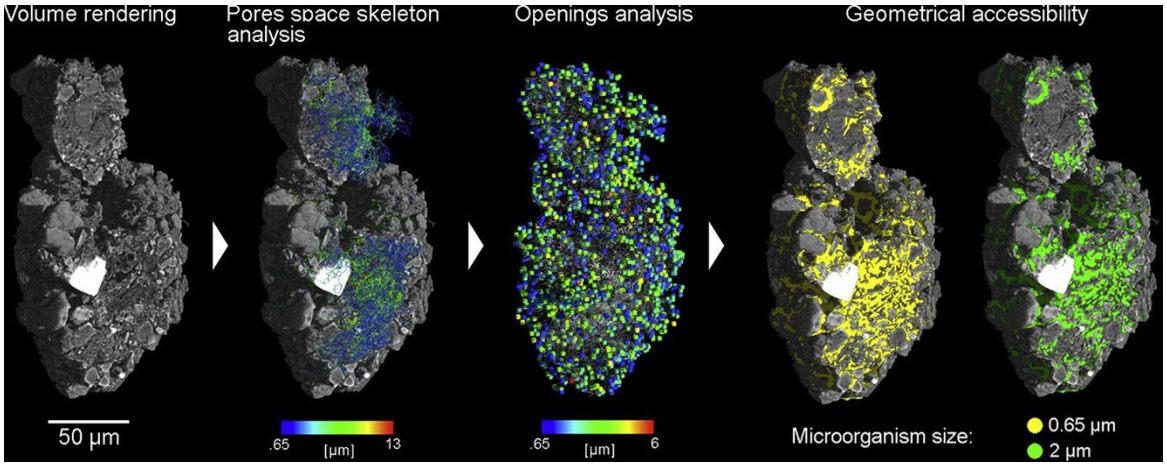

Figure 2.11 Steps involved in image processing of soil aggregate from left; volume rendering, pore space analysis, opening analysis and geometrical accessibility [39]

2.1.5.7 Soil-root interactions and dynamic process

The soil ecosystem contains microbes, roots, nutrients, and water that supports plant life, therefore, synchrotron X-rays were used to study soil root interaction, dynamic uptake process, drainage [43], root hair and aggregate orientation [25,42], and water distribution in compacted soil [37]. The role of root hairs in plant and soil science remains poorly understood, which limits the targeted selection of root hair traits, particularly for enhanced nutrient acquisition in the field [25]. Root hairs play important role in the uptake of sparingly soluble nutrients, especially in nutrient-deficient soils. An earlier study of root hairs has been conducted in artificial hydroponic gel systems, by destructive washing of roots from soil, and a non-destructive approach to this problem was necessary. Therefore, synchrotron X-ray imaging was used by Keyes et al. [25] to uncover the three-dimensional interactions of root hairs (Fig 2.12. *A,B*) in soil. They had investigated phosphate uptake by root hairs based on the geometry of hairs and associated soil pores, which was accomplished by the finite element (FE) method using COMSOL(ScanIP). This study has improved the understanding of how root hairs can be modelled at the plant and crop scale, and indicated that previous modelling studies should be re-visited using imaging based (like synchrotron), multi-scale homogenization approach. They recommended that roots and hairs both equally contribute to phosphate uptake. Similarly, image based mathematical modelling approach was used to provide importance of root hairs on pore structure development at the root–soil interface during the early stage of crop establishment [42] and found that root hairs had a significant effect on soil structure (Fig 2.12*C*)

formation and influenced porosity and connectivity for the pores (≥ 5 μm) visualised with synchrotron imaging (Table 1).

Reviewed studies have shown how structural features of soil aggregate structure influence functional characteristics. Similarly, drainage property is associated with physical characteristics of soil. Agricultural drainage not only check the water table but also maintain healthy root zone ecosystem around the crops. Fast acquisition of synchrotron images made it possible to visualize dynamic behaviour, pattern and quantitative analysis of flow processes in a sand [43]. In this study image acquisition was carried out at two beamline operation parameters (Table 1) for two conditions (fast and slow drainage). Nearest neighbour analysis was carried out for quantitative analysis on air phase distribution and found differences in drainage pattern. In fast drainage condition air bubble tend to be few and far apart, whereas closely packed smaller bubbles were found in slow flow condition [44]. The drainage occurs through well connected large pores initially than finer pores, and drainage can occur through finer pores only under high air phase pressure near boundaries. It was also found that greater pore structure formation presents away from the root for the plants with root hairs [42].

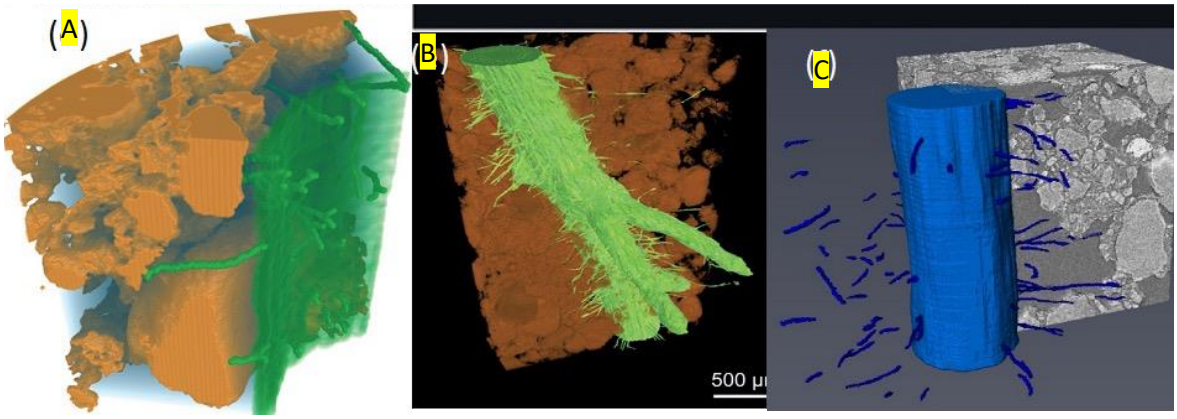

Figure 2.12 (A) 3D volume mesh is generated, with root hairs, soil, root surface and water, (B) section of a seminal root including lateral roots and root hairs and (C) 3D rendered barley root and hairs showing the surrounding soil [25,42]

2.1.6 Applications in Food

Use of synchrotron imaging tools have gained the momentum in area of food science like agriculture science. Conventional X-ray sources have been used extensively in study of food microstructures and product development as reviewed by Schoeman et al. [99]. The access to synchrotron technology is limited, lack of awareness about advantages of the technology and associated cost might be other reasons why synchrotron was not used extensively in the past. But, now due to increasing number of facilities around the globe, researchers have been able to conduct studies for understanding microstructure of foods and its role in improving food quality particularly its texture and taste. Many food products contain a cellular foam structure, such as ice cream, mousses, sponge cake, biscuits and bread, which needs to be characterized in order to determine the relationships between the structure of the product and its mechanical and organoleptic properties [47]. The microstructure of food products is highly correlated to their physical and sensory properties, which are important to evaluate the consumers acceptance of food [100]. Synchrotron experiments were carried out to map changes in structure of food like bread, noodle dough bubbles [45,47,78,101,102], cracking of chocolate [48,49], microstructure changes due to gas exchange in product [13,99,103], ice cream stability under varying conditions [46,104,105], air pathways in pome fruits [75,87] and in fish [104]. Food science involves many processing or unit operations which may involve addition or removal of heat, application of pressure and mechanical shear. These unit operations used in food processing have significant impact on food product structural properties and quality attributes. Study of these changes using synchrotron imaging are discussed here and summarized in (Table 1).

2.1.6.1 Processed food

Cereal based food products are consumed in the form of bread, noodles and in puffed form across the world which is a staple food to most of the people. Bread is the most common processed product of cereal wheat and its quality depends on dough quality. Tabletop X-rays have been widely used for studying 3D structure of bread and other stable food products in the past, but these studies have certain limitation and were not able to map rapid bubble formations. The microstructure of dough is challenging because dough is opaque, and the bubbles in dough are extremely fragile and change very rapidly [78]. Study of bubble distribution, size and formation with time is critical, hence has been studied using synchrotron in bread and noodle dough [45,47,78,101,102]. Babin et al. [45] studied bubble growth and foam setting during breadmaking (Table 1) and revealed that development of gas cell structures during

fermentation was critical in breadmaking. The generated 3D image data sets were used successfully in validation of numerical models of bubble growth, and they found clear evidence of bubble formation with time (Fig. 2.13). The development of gas cell structures during fermentation depends on a critical time initially then coalescence prevails rapidly, and leads to a heterogeneous structure. It was stated that the minor components present in flour may play an essential role in obtaining a desirable bread texture. Their study recommends that synchrotron can be used for the study of rheological properties of doughs and the temperature dependent changes of wheat flour biopolymers which govern the bread baking. Similarly, Koksel et al. [78] investigated bubble size distribution and its evolution in non-yeasted wheat flour doughs (Table 1) and found higher bubble number densities compared to previously reported studies carried out with conventional imaging. Bubble distribution was monitored and measured by customized algorithm developed in MATLAB, and found that distribution had a median bubble radius of 22.1 ± 0.7 μm at 36 min and at the end of mixing around 162 min, the size was increased to 27.3 ± 0.7 μm. This mapped dynamic trend of bubble distribution was indicative of transport of gas in the dough due to disproportionation (a phenomenon by which smaller bubbles disappear and larger bubbles remain or continue to enlarge within the semi-homogenous viscous dough). Results of both studies have contributed significantly to bakery industry in standardization of dough constituents. In continuation to previous studies, Guillermic et al. [102] did rapid characterization of bubbles in noodle dough (Table1). This non-destructive study of bubbles in wheat-flour noodle dough provided a more complete knowledge of the dough sheet's internal structure, and how it originates during processing, and its effect on the overall quality of Asian noodles. Analysis of images revealed that gradient in concentration of bubbles within the dough sheet was present from the core to the sheet edges. Extrusion processed food products or puffed products are fibrous and porous in nature. Extrusion has a significant effect on food product texture, which is an important quality attribute. The cellular structure of a cereal food is an important feature that involves sensory aspects and carries information about the processing and composition of the recipe, therefore, Chevallier et al. [46] studied cellular structure of two products, an extruded breakfast cereal and a short dough biscuit with SR-μCT (Table 1), and also compared results with conventional X-ray CT. In this study, image acquisition was carried out at four different resolutions: 6.5, 7.5, 16.2 and 25.8 μm, because their aim was to find out right resolution for determination of quantitative measurements such as densities and thicknesses

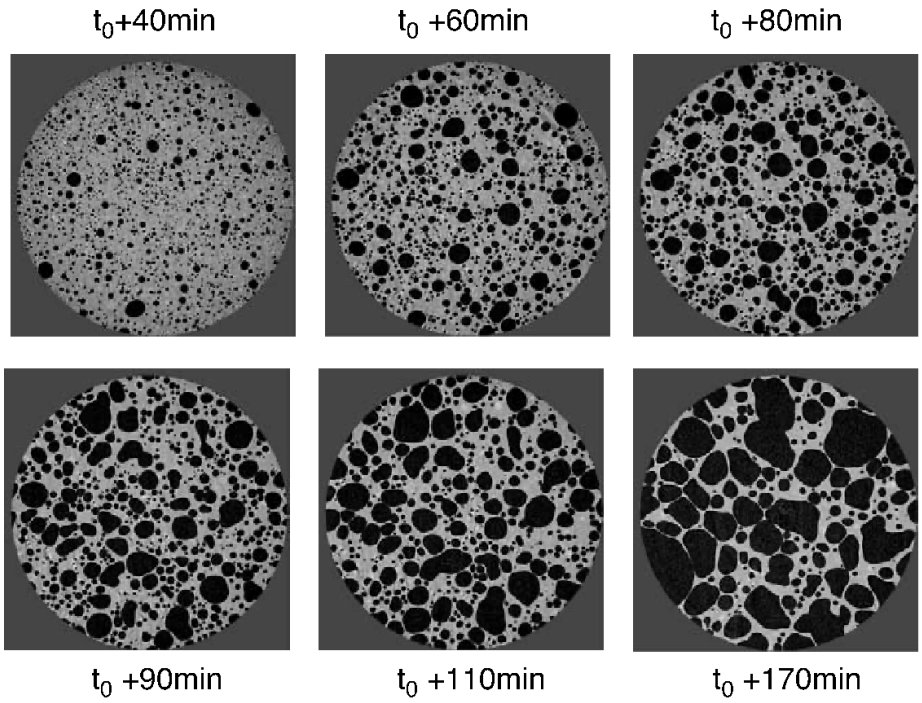

Figure 2.13 Dynamic bubble growth at increasing time period in dough in reconstructed synchrotron 3D X-ray images slices [45]

The SR-μCT produced less noisy images with shorter acquisition time, which is important and compatible with dynamic studies. Both products exhibited quite different cellular structures, Biscuit had lower porosity, with smaller cell sizes, thinner cell walls compared to extrudate snack. The cell density of biscuit was found to be ten times higher than the extrudate snack. Roasting is one of the most common unit operations in food processing, where addition of heat is involved. In coffee processing, roasting is an important step in which green beans are subjected to temperatures up to 250°C as per desired degree of roasting. The heat-induced reactions have significant effect on changes in the chemical, physical, and structural properties of the raw bean, which, in turn, affect the sensory and texture characteristics of the roasted coffee. Pittia et al. [47] used SR-μCT (Table 1) to investigate morphology and the inner microstructural properties of coffee beans as well as the effects of the roasting on it and found that roasted coffee beans had a higher and more uniformly

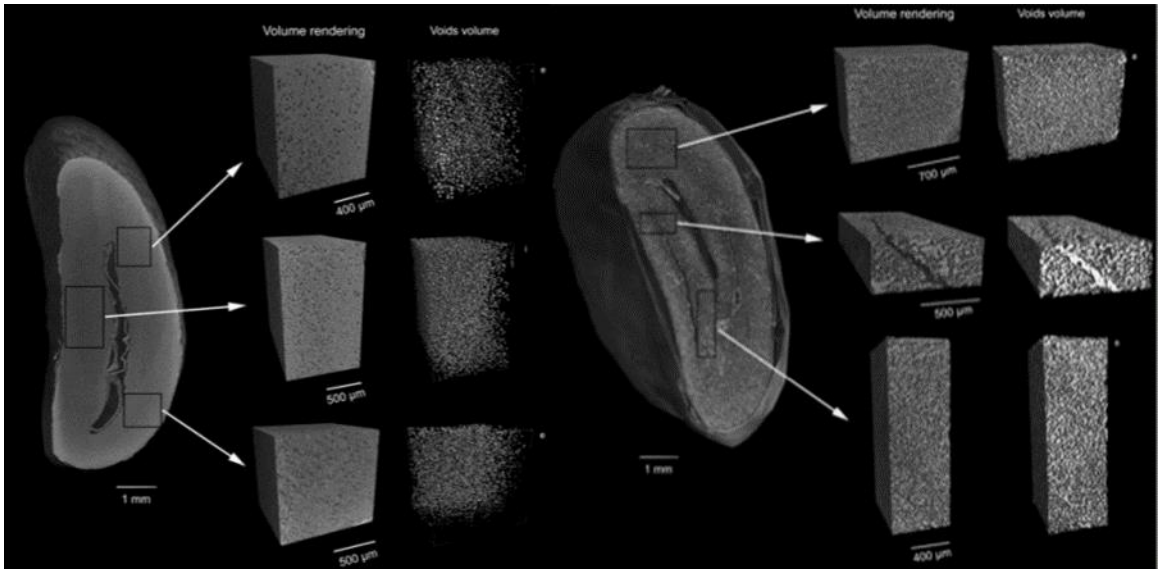

Figure 2.14 The virtual cut of 3D synchrotron X-ray images, where porosity in non-roasted (left set) is lower than roasted coffee bean (right set) [48]

distributed porosity in the order of 40% as compared to green beans 6% (Fig. 2.14). This type of study has opened the possibility to investigate effect of process parameters on the porosity evolution during roasting and to relate the results with those obtained with other conventional and non-destructive imaging.

Like addition of heat, removal of heat in unit operations such as freezing also alters the structural properties of foods, mostly in dairy products. Textural properties of ice-cream products depend on its structure, but cooling cycles may affect its structure due to crystal formation. Therefore, Guo et al. [45] were used SR-µCT (Table 1) to determine the temperature dependence of ice-cream's microstructural evolution. Results of the study revealed that melting-recrystallization mechanism is responsible for the evolution of ice crystal size and morphology during thermal cycling between −15 and −5°C. The coalescence of air cells was the dominant coarsening mechanism controlling air bubble size and interconnectivity in the ice cream. Synchrotron X-ray imaging provided sufficient evidence that unfrozen matrix plays role in microstructural stability and the complex interactions between ice crystals and air structures. Similarly, SR X-rays were used with iodine as a contrast agent at 10 keV, 30 keV and 75 keV to measure the three-dimensional distribution of the three main phases (air, unfrozen sugar solution, and ice crystals) of ice cream (Table 1). Quantification of microstructural evolution in ice cream was carried out (Table 1), which revealed that the growth of ice crystals almost ceases after seven thermal cycles, when they approach the size of the walls between air cells, where air cells continue to coarsen, forming interconnected channels [106]

Chocolate blooming is the major problem in the confectionery industry [49] and many studies have been carried out in the past using non-destructive methods, but due to low resolution and high scanning times failed to provide evidence to resolve the blooming issue. Reinke et al. [49] analysed chocolate using SR-μCT (Table 1) and concluded that the convective flow of liquid-lipid fractions in the solid cocoa butter matrix played a significant role as a transport mechanism responsible for fat blooming. This mechanism was validated by the formation of cracks (width of some microns and a length of up to several 100 μm) propagating through the whole chocolate sample (Fig. 2.15). The imperfections, which arise during the manufacturing process, might act as migration pathways since they propagate throughout the entire chocolate.

2.1.6.2 Fruits and vegetables

Post-harvest storage of perishables is one of the important areas where non-destructive approach is required to study changes during storage. It was reviewed earlier that the current state of the art in modelling tissue microstructures was not sufficient [75] for modelling the 3D configuration of cells, cell walls and intercellular spaces in fruit tissues. Mebatsion et al. [75] applied synchrotron imaging to study post-harvest disorders in pome fruits: apple and pear (Table 1). They have used ANSYS for finite element modelling for quantification and MATLAB programmed algorithms (tessellation algorithm) which yielded smaller apple parenchyma porosity and larger pear parenchyma porosity besides having small sample size. They concluded that multiscale modelling of transport phenomena and mechanical deformation of scanned fruits enhanced the knowledge about fruit environment interactions, and evolution of physiological disorders and can be used to improve cold storage design and control. The connectivity of the voids is essential for mass transfer, and it also determines the tortuosity of the void channels, which are the main pathways for gas exchange. Another research team had generated high-contrast 3D absorption images of in vivo fruit tissues of high moisture content (Table 1), which enabled visualization of individual cell morphology, cell walls, and entire void networks that were previously unknown for understanding spoilage in post-harvest storage [13]. Both reviewed synchrotron methods (phase and absorption contrast imaging) can be used depending on the X-ray energy and sample properties in food product analysis [107].

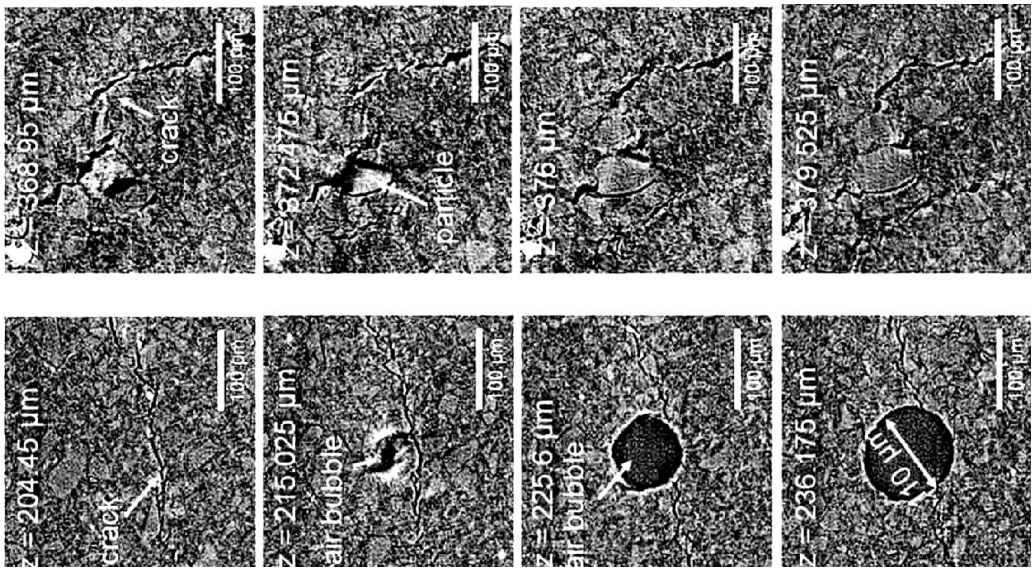

Figure 2.15 Synchrotron X-ray image slices of different layers showing voids and cracks in chocolate samples [49]

2.1.7 Conclusion

The synchrotron X-ray imaging facilities around the world are growing and well established due to their unique properties and application domain. Synchrotron based non-destructive methods enabled researchers engaged in agricultural and food sciences to study structural changes in the material through virtual slicing, as well as on the surface. Phase contrast imaging has great scope for imaging biological materials in harder surrounding matrix, where materials with low X-ray attenuation of interest are located and have differences in refractive index. Researchers were able to find answers to many questions in modern and ancient plants through synchrotron imaging, and mapped for the first time the development of seed and fat blooming of chocolate in food science. The study of quick and dynamic processes in plant sciences like absorption of nutrients, and in food science like bubble formation was made possible due to the intervention of synchrotron imaging. The hard SR X-rays were the best for soil medium imaging.

Present studies do not reflect much on the effect of dose on living things (plants and seeds) in terms of germination, viability, the economic feasibility of methods, and tissue damage except a few. The radiation damage in SR imaging is still lower than in conventional systems due to fast imaging and monochromatic beams. SRP-µCT has potential to address problems of tissue damage in SR-µCT, but knowledge of the possible impact of the X-ray dose was not yet assessible. Sample heating and protein denaturation may be caused which may lead to the

redistribution of cellular components and experimental artifacts. The reconstruction step requires some prior knowledge of the samples which is accessible in material science but rarely in plant and food science. In SR-μCT high photon fluxes and energy are necessary for high-resolution imaging, but plant tissues may be severely damaged, and this can limit the use of this method in a continuous investigation in plant science. There is a good scope for harnessing synchrotron imaging's full potential using approaches like machine learning and deep learning methods for agriculture applications. The future scope of applications may include in post-harvest management of agriculture produce, standardization of engineering parameters of SR imaging such as energy, like the use of not only high spatial resolution but also high density resolution, optimizing dose and development of computer vision methodology or machine learning algorithms for image processing**.**

Abbreviations: SR: Synchrotron, SR-μCT: Synchrotron absorption micro computed tomography, SRP-μCT: Synchrotron phase contrast micro computed tomography, SR-XTM: Synchrotron X-ray absorption tomography, HXRTM: High resolution X-ray tomography, SR-PCI: Synchrotron phase contrast imaging

Acknowledgment: The authors acknowledge the Netaji Subhash Chandra fellowship from the Indian Council of Agriculture Research for the first author and the Natural Sciences and Engineering Research Council of Canada for supporting the student research via a grant no. RGPIN-2018-04420 to Dr. Jayas.

Authors' contributions: NI prepared an outline, first draft, and content of whole paper by reviewing literature. CK who is expert in application of synchrotron imaging in agriculture have edited draft and provided valuable technical inputs and provided literature support for preparation of draft. DJ conceptualized the study, is corresponding author and contributed to overall editing, examination, and finalization of paper drafts. All authors read and approved the final manuscript

Table 2.1 Synchrotron imaging operation parameters used in agriculture and food science research

Technique	Material	Purpose/ findings	Beamline & beam size (H, mm x V, mm)	Energy (keV)	Resolution (μm)	No of Projection or Increment angle(°)	Exposure per image/ total time (s/min)	Field of view mm x mm	Detector /detector pixel	Voxel (mm/ μm)	Source to detector(Sr/d) and sample to detector distance (Sl/d), cm	Reference
Plants and fruits												
SR-XTM	Modern & Fossil plants	Internal structure	TOMCAT, Swiss (50 x 4)	9.9	0.35	1,500	0.42/ 10.5	1x1.4	2560 x 2160	400x 400 x 400 μm	100(Sl/d)	[20]
SRPC-μCT	Canola plant	Water and nutrient transport	BMIT- Canadian light source (40 x 5)	18, 24	4.3	1800, 5001	1 / 83	4x 10	4000 x 2600	0.7x 0.7 x 0.7 mm	80, 60(Sl/d)	[17]
SR-μCT				18	8.75	1800	2.3 / 69				8.5(Sl/d)	
SR-PCI	Wheat	Fusarium disease detection		18	8.75	*-	1s/-		4000 x 2600	1x 1 x 1 mm	80(Sl/d)	[91]
SRP-TM	Live vines of plant	Plant xylem network	ALS, Berkeley CA USA (40x 4.6)	10-18	4.5	720/ 0.25^0	0.1-1/40	8.3x 18	4006x 2672	5 x 5 x 5 μm	1000 (Sr/d)	[24]
SR-μCT	Rose peduncles	Effect of SR-X-ray and residence time on quality	BESSY II, Germany	30, 40, 50	4.56	1500 / 0.12^0	1.4, 1.2, 3/ 35	10x1 3	512 x 512	4.56x 4.56x 4.56 μm	3500(Sr/d)	[28]

			(200 × 100) µm									
SR-µCT	Wood	Microstructure changes under force and stress	DORIS III, DESY (20 x 3)	9	2	720/ 0.25^0	-	1x 1	1536x1024	1 mm^3	-	[89]
SR-µCT	Wood		TOMCAT, SLS	11	2.15	720/ 0.25^0	0.3/ 12	3.58 x 1.2	2048x 2048	1.7x 1.7x 1.7 µm	0.7 (Sr/d)	[33]
SR-µCT	Wood	Microstructural decay due to fungi	TOMCAT, Swiss	15	20	2001	0.13/ 4.2	1650 x1650 µm	1560x2160	0.65x0.65x 0.6 µm	0.5 (Sl/d)	[32]
SRP-µCT	Wheat	Host Interactions	BMIT-CLS, SK	20		1800	0.8 / 24	1 x 1		13.12μm^3	20 (Sl/d)	[54]
SR-µCT	Tomato leaves	3D laminography	ID19 of ESRF, France (60x 15)	18	0.75	1200	0.5/ 10	1.54 x 1.54	2048 x 2048	750x 750x 750 nm	35 (Sl/d)	[87]
		CO_2 gas exchange in leaf		20.5	0.75	-	-	150x 150	-	1.4x 1.4x 1.4 µm	3, 4.5, 10.5, 21.5 (Sl/d)	[90]
SR-µCT	coast redwood samplings	Embolism In the xylem	ALS, Berkeley	15	4.5	720/ 0.25°	12 min	5 x 5	4006 x 2672	175x 175x 500 µm	-	[24]
SR-µCT	Ggrapevine	Xylem vessel refilling		24	0.65	1025	60 min	1.7 x 1.7	-	0.65 µm3	-	[108]
SR-µCT	Sunflower	Drought-induced	SYRMEP Trieste (120 x 4)	22	2.0	2048/1º	250 ms/ 6 min	-	-	-	10 (sl/d)	[21]

		embolism in stems										
SR-µCT	Ggrapevine	Visualizations of Drought-Induced Embolism	ALS, Berkeley (251 x 8) µm	15	4.5	720/ 0.25°	25 min	-	4006 x 2672	-	-	[22]
SRP-µCT	Submerged leaves	visualise gas films on submerged leaves of common cordgrass	TOMCAT	12	0.375	2001	10 min		2048 x 2048	0.375 x 0.375 x 0.375 µm	1.4-4.0(sl/d)	[26]
SR-PCI	Woody herbaceous plant leaves	With iodine contrast agent	APS,IL USA 207 x 15 µm	7 - 20	1.66	-	0.4/-	5 x 5	2048x2048	-	5500 (Sr/d) 1-10 (Sl/d)	[109]
				10- 60	3.56	-	1.7/-		1392 x 1040	-	5500 (Sr/d) 1-20 (Sl/d)	
						Seeds						
SR-inline phase TM	Maize	Internal changes in feature	ID19, ESRF (60x 15) µm	17.6	5	1000	50 s/ 20 min	-	2048x2048	5x5x5 µm	100 (Sl/d)	[27]
SR-XTM	Arabidopsis	Intercellular void network		21	0.3	800/ 0.225°	2 s/ 26 min	0.6 x 0.6	-	5x5x5 µm	14500(Sr/d)and 1.3, 3.3, 6.3, 10.3(Sl/d)	[2]
HXRTM	Fossils & modern horse gram	Seed coat thinning with time	I132 of DLS UK	15	-	4000	0.15, 0.2, 0.25 s/ 16 min	-	5120 x 5120	1x 1x 1 mm	0.5	[31]

			(14.5×19) µm									
SRP-µCT	Rapeseeds	Distribution of storage oils	ESRF, Grenoble (200 x 200) µm	19	0.75	1200	0.1 s/ 2 min	-	-	0.74 µm^3	9 (Sl/d)	[87]
SR-XTM	Fossil seeds	Internal features of fossil flowers	TOMCAT, Swiss	10, 12	0.37, 0.65, 0.74	570-660	-	0.85x 30.7	10x 20 µm	0.65x 0.65x 0.65 µm	-	[85]
SRP-µCT	Fossil flowers	Cretaceous fossil inflorescence	BM05 ESRF	20	0.75	4000	1.2s/80m in		FReLoN 8.8 µm		2(Sl/d)	[76]
SRP-nCT	Fossil flowers	Cretaceous fossil inflorescence	ID22-NI ESRF	29.5	0.76	2000	0.8s		FReLoN 20 µm		4.7, 4.8, 5.2, 6.2 (Sl/d)	[76]
						Soil and roots						
SRP-µCT	Barley root hair in soil	Importance of root hairs on pore structure development at the root-soil interface	I13 DLS UK (1.7 x 1.7)	15 to 21	1.6	1601	0.15 s/ 4 min	4 9 x 3.5	2560 x 2560	2x2x1 mm	6.35(Sl/d)	[42]
SR-µCT	soil aggregation	Soil aggregation in an Ultisol	BL13W1, SSRF, Shanghai	28	9	430	-	2.70 ×3.2	1052 × 1052	9×9×9 µm	-	[35]

SR-µCT	Ultisol under Wetting & drying	Intra-aggregate microstructure	(50 x 5)	24	3.7	1300/ 0.10°	1.8/ 39	-	1700 x 1700	541x541x541	-	[36]
SR-µCT	Quantification of aggregate	Effect of vegetation on strcture		24	3.25	550	30s		2048 x 2048	3.25 x3.25 x 3.25	12 (sr/sl)	[96]
SR-µCT	Two soil types of states USA	Characterization of soil microaggregates	ALS, Berkeley (251 µm x 8 µm)	11	20	1800	1 / 30	-	-	325 nm	0.8 (Sl/d)	[39]
SR-µCT	Soil	Flow of sand	APS, 6.0 (50x5)	33.70	17.1	720/0.25° two pass	1.4/ 16	11.1x 3.6	1317x 1335	650 x 650 x 211 mm	-	[43,44]
			APS 1.5 (1.5 x 1) & (200 x 40) µm	33.69	6.7		5/ 60	4.39 x 3.45	1300x 1330	658x 658 x 517 mm	-	
SR-µCT (KI contras)	Sand	Water content on compaction	BL13W1 SSRF	20	0.65	1200	-/ 150	13 x 13	2048 x 2048	0.65x 0.65x 0.65 µm	-	[37]
SR-µCT at K-edge	Soil	Locate organic matter	HARWI II, Germany (50 x 10)	30, 70, 78	9.77	-	-	-	4.89 µm	3.8x 3.5x 3.30 mm	-	[110]
SR-µCT	Two soil types	3D pore network of grassland and tilled soil	DESY, Germany	Tilled: 21.5, grassland: 24	3.2, 5.4	0.5°	-	-	1536 x 1024	400x 400 x 400	-	[77]
SR-XTM	Soil-root	Growth of wheat root hairs	TOMCAT	20	1.0	1501		-		500x 500x 500	-	[25]

Food											
HRXTM	Soft cereal foods	Impact of protein reinforcement on the deformation	BM05, ESRF, Grenoble	19	11x11	-	2 s	11 x 22 5 x10 1 x 2	2016 x 2016	11 µm 5.5 µm 1.1 µm	-	[103]
SR-XTM	Bread	Bubble growth and foam setting		18	-	400	0.02/ 0.13			628 x 628 x 256 mm		[45]
SR-XTM	Pome Fruits (apple, pear)	Gas network architecture	ID15 EPSRF (3.2 x 3.2)	25	2.5	900	1/ 0.5		2048×2048	1.9 μm^3	3800(Sr/d)	[111]
SR-PCI		Characterization of fruit tissue	ID19 , EPSRF	18	-	700	-	0.7x 0.5x 1 mm^3	-	0.95 μm^3	20.7	[75]
SR-µCT, SRP-µCT		Gas exchange pathways		18	1.4, 5.1 PCI: 0.7	1200	0.5/ 10	1.43 x 1.43	2048 x 2048	712 nm	10000 (Sr/d), 3.5 (Sl/d)	[87]
SR-µCT	Extruded cereal & biscuit	Internal structure		17.6	6.5, 7.5, 16.2, 25.8	2000-5000	0.2/ 15	-	2048 x 2048	7.5 µm (2048 x 2048x 1024)	-	[47]
SR-µCT	Noodle dough	Characterization of bubbles	BMIT CLS	25	8.75	600/ 0.3^0	0.04/1.10	-	4000 × 248 pixels	10-97 voxel	80 (Sl/d)	[102]

SR-µCT	Ice cream	Temp dependence microstructure	(I13-2) DLS, U.K	15 to 30	0.8	900	0.1/1.5	-	2560×2160 pixel	2k × 2k × 2k	3.5 (Sl/d)	[46]
SRP-µCT				15 to 30		3601	0.1/ 6	-				[106]
SR-µCT	Wheat flour	Bubble size distribution in dough	BMIT-BM 05B1-1 CLS, SK 40 x 5 mm	18	8.75	350/ 1.5°	0.2/ 2	-	530 × 2530	7-25 voxels	147 (Sl/d) 2620 (Sr/d)	[78]
SR-µCT	Coffee Beans	Voids/pore volume distribution of green and roasted coffee beans	SYRMEP, Trieste (Italy).	19, 20	4.5	1440/ 0.125^0	-	18×12	4008 × 2672	1 mm^3	20 (Sl/d)	[48]
SR-µCT	Chocolate	Migration pathways through cracks and voids	(DESY) Hamburg	13	1.0	1800	1/ 20	1.8 x 1.8 mm	3056 x 3056	100 µm	-	[49]
SRP-µCT	Fish	Histology	APS, ANL USA	13.8, 16.2	1.43	2048	20/ 20	-	-	0.743 $µm^3$	3 (Sl/d)	[104]

Sl/d: sample to detector, Sr/d: source to detector distance, µCT: micro computed tomography and TM: tomography

2.1.8 References

1. Karunakaran C, Lahlali R, Zhu N, Webb AM, Schmidt M, Fransishyn K, et al. Factors influencing real time internal structural visualization and dynamic process monitoring in plants using synchrotron-based phase contrast X-ray imaging. Sci Rep [Internet]. 2015;5:12119. Available from: http://www.nature.com/articles/srep12119

2. Cloetens P, Mache R, Schlenker M, Lerbs-Mache S. Quantitative phase tomography of Arabidopsis seeds reveals intercellular void network. Proc Natl Acad Sci [Internet]. 2006;103:14626–30. Available from: http://www.pnas.org/cgi/doi/10.1073/pnas.0603490103

3. Hughs SE, Wakelyn PJ, Rousselle MA, Columbus EP. Chemical composition of cotton gin external emissions: Proximate and elemental analysis. Trans Am Soc Agric Eng. 1997;40.

4. D. H. Lenker, P. A. Adrian (deceased). Field Model of an X-Ray System for Selecting Mature Heads of Crisphead Lettuce. Trans ASAE. 1980;23.

5. Oja J, Wallbäcks L, Grundberg S, Hägerdal E, Grönlund A. Automatic grading of Scots pine (Pinus sylvestris L.) sawlogs using an industrial X-ray log scanner. Comput Electron Agric. 2003.

6. Haff RP, Slaughter DC, Jackson ES. X-Ray based stem detection in an automatic tomato weeding system. Appl Eng Agric. 2011;27.

7. J. Matthews, J. I. Wadsworth, J. J. Spadaro. Rough-Rice Breakage in Relation to Kernel Thickness for Hand- and Combine-Harvested Rice. Trans ASAE. 1981;24.

8. Karunakaran C, Jayas D, White N. Soft X-ray image analysis to detect wheat kernels damaged by Plodia interpunctella (Lepidoptera: Pyralidae). Sci Aliments [Internet]. 2003;23:623–31. Available from: http://sda.revuesonline.com/article.jsp?articleId=2466

9. Neethirajan S, Karunakaran C, Symons S, Jayas DS. Classification of vitreousness in durum wheat using soft X-rays and transmitted light images. Comput Electron Agric. 2006;53.

10. Kotwaliwale N, Weckler PR, Brusewitz GH. X-ray Attenuation Coefficients using Polychromatic X-ray Imaging of Pecan Components. Biosyst Eng. 2006;94.

11. Mendoza F, Verboven P, Mebatsion HK, Kerckhofs G, Wevers M, Nicolaï B. Three-dimensional pore space quantification of apple tissue using X-ray computed microtomography. Planta [Internet]. 2007;226:559–70. Available from: http://link.springer.com/10.1007/s00425-007-0504-4

12. Herremans E, Verboven P, Defraeye T, Rogge S, Ho QT, Hertog MLATM, et al. X-ray CT for quantitative food microstructure engineering: The apple case. Nucl Instruments Methods

Phys Res Sect B Beam Interact with Mater Atoms. 2014;324:88–94.
13. Verboven P, Kerckhofs G, Mebatsion HK, Quang TH, Temst K, Wevers M, et al. Three-dimensional gas exchange pathways in pome fruit characterized by synchrotron X-ray computed tomography. Plant Physiol. 2008;147:518–27.
14. Mathers AW, Hepworth C, Baillie AL, Sloan J, Jones H, Lundgren M, et al. Investigating the microstructure of plant leaves in 3D with lab-based X-ray computed tomography. Plant Methods [Internet]. 2018;14:99. Available from: https://plantmethods.biomedcentral.com/articles/10.1186/s13007-018-0367-7
15. Tollner EW, Verma BP. X-ray CT for quantifying water content at points within a soil body. Trans Am Soc Agric Eng. 1989;32.
16. Mathanker SK, Weckler PR, Bowser TJ. X-ray applications in food and agriculture: A review. Trans ASABE. 2013;56.
17. Karunakaran C, Lahlali R, Zhu N, Webb AM, Schmidt M, Fransishyn K, et al. Factors influencing real time internal structural visualization and dynamic process monitoring in plants using synchrotron-based phase contrast X-ray imaging. Sci Rep [Internet]. Nature Publishing Group; 2015;5:12119. Available from: http://www.nature.com/articles/srep12119
18. Xue Y, Xiao T, Du G, Tong Y, Liu H, Deng B, et al. Observation of cavitation and water-refilling processes in plants with X-ray phase contrast microscopy. Nucl Sci Tech. 2013;24.
19. Willick IR, Stobbs J, Karunakaran C, Tanino KK. Phenotyping Plant Cellular and Tissue Level Responses to Cold with Synchrotron-Based Fourier-Transform Infrared Spectroscopy and X-Ray Computed Tomography. Methods Mol Biol [Internet]. 2020. p. 141–59. Available from: http://link.springer.com/10.1007/978-1-0716-0660-5_11
20. Smith SY, Collinson ME, Rudall PJ, Simpson DA, Marone F, Stampanoni M. Virtual taphonomy using synchrotron tomographic microscopy reveals cryptic features and internal structure of modern and fossil plants. Proc Natl Acad Sci [Internet]. 2009;106:12013–8. Available from: http://www.pnas.org/cgi/doi/10.1073/pnas.0901468106
21. Savi T, Miotto A, Petruzzellis F, Losso A, Pacilè S, Tromba G, et al. Drought-induced embolism in stems of sunflower: A comparison of in vivo micro-CT observations and destructive hydraulic measurements. Plant Physiol Biochem. 2017;120.
22. Brodersen CR, McElrone AJ, Choat B, Lee EF, Shackel KA, Matthews MA. In Vivo Visualizations of Drought-Induced Embolism Spread in Vitis vinifera. Plant Physiol [Internet]. 2013;161:1820–9. Available from: https://academic.oup.com/plphys/article/161/4/1820/6110618
23. Guk BK, Yae JY, Tae JS, Hwa SY, Yong SG, Sang JL. X-ray imaging of various biological

samples using a phase-contrast hard X-ray microscope. Microsc Res Tech. 2008;71:639–43.
24. Choat B, Brodersen CR, Mcelrone AJ. Synchrotron X-ray microtomography of xylem embolism in Sequoia sempervirens saplings during cycles of drought and recovery. New Phytol. 2015;205.
25. Keyes SD, Daly KR, Gostling NJ, Jones DL, Talboys P, Pinzer BR, et al. High resolution synchrotron imaging of wheat root hairs growing in soil and image based modelling of phosphate uptake. New Phytol [Internet]. 2013;198:1023–9. Available from: https://onlinelibrary.wiley.com/doi/10.1111/nph.12294
26. Lauridsen T, Glavina K, Colmer TD, Winkel A, Irvine S, Lefmann K, et al. Visualisation by high resolution synchrotron X-ray phase contrast micro-tomography of gas films on submerged superhydrophobic leaves. J Struct Biol. 2014;188.
27. Rousseau D, Widiez T, Di Tommaso S, Rositi H, Adrien J, Maire E, et al. Fast virtual histology using X-ray in-line phase tomography: application to the 3D anatomy of maize developing seeds. Plant Methods [Internet]. 2015;11:55. Available from: http://www.plantmethods.com/content/11/1/55
28. Matsushima U, Graf W, Zabler S, Manke I, Dawson M, Choinka G, et al. 3D-analysis of plant microstructures: advantages and limitations of synchrotron X-ray microtomography. Int Agrophysics [Internet]. 2013;27:23–30. Available from: http://archive.sciendo.com/INTAG/intag.2013.27.issue-1/v10247-012-0064-0/v10247-012-0064-0.pdf
29. DeVore ML, Kenrick P, Pigg KB, Ketcham RA. Utility of high resolution X-ray computed tomography (HRXCT) for paleobotanical studies: An example using London Clay fruits and seeds. Am J Bot [Internet]. 2006;93:1848–51. Available from: http://doi.wiley.com/10.3732/ajb.93.12.1848
30. Murphy C, Fuller DQ. Seed coat thinning during horsegram (Macrotyloma uniflorum) domestication documented through synchrotron tomography of archaeological seeds. Sci Rep [Internet]. 2017;7:5369. Available from: http://www.nature.com/articles/s41598-017-05244-w
31. Fuller DQ, Murphy C. The origins and early dispersal of horsegram (Macrotyloma uniflorum), a major crop of ancient India. Genet Resour Crop Evol. 2018;65:285–305.
32. Sedighi Gilani M, Boone MN, Mader K, Schwarze FWMR. Synchrotron X-ray micro-tomography imaging and analysis of wood degraded by Physisporinus vitreus and Xylaria longipes. J Struct Biol [Internet]. 2014;187:149–57. Available from: https://linkinghub.elsevier.com/retrieve/pii/S1047847714001397
33. Forsberg F, Mooser R, Arnold M, Hack E, Wyss P. 3D micro-scale deformations of wood

in bending: synchrotron radiation muCT data analyzed with digital volume correlation. J Struct Biol [Internet]. 2008;164:255–62. Available from: https://linkinghub.elsevier.com/retrieve/pii/S1047847708002207
34. Pratt RB, Castro V, Fickle JC, Madsen A, Jacobsen AL. Factors controlling drought resistance in grapevine (Vitis vinifera , chardonnay): application of a new micro CT method to assess functional embolism resistance. Am J Bot [Internet]. 2020;107:618–27. Available from: https://onlinelibrary.wiley.com/doi/10.1002/ajb2.1450
35. Zhou H, Peng X, Perfect E, Xiao T, Peng G. Effects of organic and inorganic fertilization on soil aggregation in an Ultisol as characterized by synchrotron based X-ray micro-computed tomography. Geoderma [Internet]. 2013;195–196:23–30. Available from: https://linkinghub.elsevier.com/retrieve/pii/S0016706112003904
36. Ma R, Cai C, Li Z, Wang J, Xiao T, Peng G, et al. Evaluation of soil aggregate microstructure and stability under wetting and drying cycles in two Ultisols using synchrotron-based X-ray micro-computed tomography. Soil Tillage Res [Internet]. 2015;149:1–11. Available from: https://linkinghub.elsevier.com/retrieve/pii/S0167198714002979
37. Li Z-S, Tang L-S. Using Synchrotron-Based X-Ray Microcomputed Tomography to Characterize Water Distribution in Compacted Soils. Adv Mater Sci Eng [Internet]. 2019;2019:1–11. Available from: https://www.hindawi.com/journals/amse/2019/7147283/
38. Perret JS, Al-Belushi ME, Deadman M. Non-destructive visualization and quantification of roots using computed tomography. Soil Biol Biochem [Internet]. 2007;39:391–9. Available from: https://linkinghub.elsevier.com/retrieve/pii/S003807170600321X
39. Voltolini M, Taş N, Wang S, Brodie EL, Ajo-Franklin JB. Quantitative characterization of soil micro-aggregates: New opportunities from sub-micron resolution synchrotron X-ray microtomography. Geoderma [Internet]. 2017;305:382–93. Available from: https://linkinghub.elsevier.com/retrieve/pii/S0016706117300575
40. McElrone AJ, Choat B, Parkinson DY, MacDowell AA, Brodersen CR. Using High Resolution Computed Tomography to Visualize the Three Dimensional Structure and Function of Plant Vasculature. J Vis Exp [Internet]. 2013; Available from: http://www.jove.com/video/50162/using-high-resolution-computed-tomography-to-visualize-three
41. Gregory PJ, Hutchison DJ, Read DB, Jenneson PM, Gilboy WB, Morton EJ. Non-invasive imaging of roots with high resolution X-ray micro-tomography. Plant Soil. 2003. p. 351–9.
42. Koebernick N, Daly KR, Keyes SD, George TS, Brown LK, Raffan A, et al. High-resolution synchrotron imaging shows that root hairs influence rhizosphere soil structure

formation. New Phytol [Internet]. 2017;216:124–35. Available from: https://onlinelibrary.wiley.com/doi/10.1111/nph.14705

43. Wildenschild D, Hopmans JW, Rivers ML, Kent AJR. Quantitative Analysis of Flow Processes in a Sand Using Synchrotron-Based X-ray Microtomography. Vadose Zo J [Internet]. 2005;4:112–26. Available from: http://vzj.scijournals.org/cgi/doi/10.2113/4.1.112

44. Wildenschild D, Rivers ML, Porter ML, Iltis GC, Armstrong RT, Davit Y. Using Synchrotron-Based X-Ray Microtomography and Functional Contrast Agents in Environmental Applications. 2015. p. 1–22.

45. Babin P, Della Valle G, Chiron H, Cloetens P, Hoszowska J, Pernot P, et al. Fast X-ray tomography analysis of bubble growth and foam setting during breadmaking. J Cereal Sci [Internet]. 2006;43:393–7. Available from: https://linkinghub.elsevier.com/retrieve/pii/S0733521005001438

46. Guo E, Kazantsev D, Mo J, Bent J, Van Dalen G, Schuetz P, et al. Revealing the microstructural stability of a three-phase soft solid (ice cream) by 4D synchrotron X-ray tomography. J Food Eng. 2018;237:204–14.

47. Chevallier S, Réguerre A-L, Le Bail A, Della Valle G. Determining the Cellular Structure of Two Cereal Food Foams by X-ray Micro-Tomography. Food Biophys [Internet]. 2014;9:219–28. Available from: http://link.springer.com/10.1007/s11483-014-9336-5

48. Pittia P, Sacchetti G, Mancini L, Voltolini M, Sodini N, Tromba G, et al. Evaluation of Microstructural Properties of Coffee Beans by Synchrotron X-Ray Microtomography: A Methodological Approach. J Food Sci [Internet]. 2011;76:E222–31. Available from: https://onlinelibrary.wiley.com/doi/10.1111/j.1750-3841.2010.02009.x

49. Reinke SK, Wilde F, Kozhar S, Beckmann F, Vieira J, Heinrich S, et al. Synchrotron X-Ray microtomography reveals interior microstructure of multicomponent food materials such as chocolate. J Food Eng [Internet]. 2016;174:37–46. Available from: https://linkinghub.elsevier.com/retrieve/pii/S0260877415300595

50. Sarker TR, Azargohar R, Stobbs J, Karunakaran C, Meda V, Dalai AK. Complementary effects of torrefaction and pelletization for the production of fuel pellets from agricultural residues: A comparative study. Ind Crops Prod. 2022;181.

51. Betz O, Wegst U, Weide D, Heethoff M, Helfen L, Lee WK, et al. Imaging applications of synchrotron X-ray phase-contrast microtomography in biological morphology and biomaterials science. I. General aspects of the technique and its advantages in the analysis of millimetre-sized arthropod structure. J Microsc. 2007;227:51–71.

52. Lahlali R, Song T, Chu M, Karunakaran C, Yu F, Wei Y, et al. Synchrotron-based

spectroscopy and imaging reveal changes in the cell-wall composition of barley leaves in defence responses to Blumeria graminis f. sp. tritici. Can J Plant Pathol [Internet]. 2019;41:457–67. Available from: https://www.tandfonline.com/doi/full/10.1080/07060661.2019.1581662

53. Westneat MW, Socha JJ, Lee WK. Advances in biological structure, function, and physiology using synchrotron X-ray imaging [Internet]. Annu. Rev. Physiol. 2008. p. 119–42. Available from: http://www.annualreviews.org/doi/10.1146/annurev.physiol.70.113006.100434

54. Brar GS, Karunakaran C, Bond T, Stobbs J, Liu N, Hucl PJ, et al. Showcasing the application of synchrotron-based X-ray computed tomography in host-pathogen interactions: The role of wheat rachilla and rachis nodes in Type-II resistance to Fusarium graminearum. Plant Cell Environ [Internet]. 2019;42:509–26. Available from: https://onlinelibrary.wiley.com/doi/10.1111/pce.13431

55. Hofmann A. The Physics of Synchrotron Radiation. Phys. Synchrotron Radiat. 2004.

56. Winick H, Bienenstock A. SYNCHROTRON RADIATION RESEARCH. Annu Rev Nucl Part Sci [Internet]. 1978;28:33–113. Available from: http://www.annualreviews.org/doi/abs/10.1146/annurev.ns.28.120178.000341

57. Holt SA, Le Brun AP, Majkrzak CF, McGillivray DJ, Heinrich F, Lösche M, et al. An ion-channel-containing model membrane: Structural determination by magnetic contrast neutron reflectometry. Soft Matter. 2009.

58. Takahara A, Higaki Y, Hirai T, Ishige R. Application of synchrotron radiation x-ray scattering and spectroscopy to soft matter. Polymers (Basel). 2020.

59. Willmott P. An introduction to synchrotron radiation: Techniques and applications. An Introd. to Synchrotron Radiat. Tech. Appl. 2011.

60. Willmott P. An Introduction to Synchrotron Radiation [Internet]. An Introd. to Synchrotron Radiat. Tech. Appl. Wiley; 2011. Available from: https://onlinelibrary.wiley.com/doi/book/10.1002/9781119970958

61. Als-Nielsen J, McMorrow D. Elements of Modern X-ray Physics: Second Edition. Elem. Mod. X-ray Phys. Second Ed. 2011.

62. Mobilio S, Boscherini F, Meneghini C. Synchrotron radiation: Basics, methods and applications. Synchrotron Radiat. Basics, Methods Appl. 2015.

63. Als-Nielsen J, McMorrow D. X-rays and their interaction with matter. Elem Mod X-ray Phys [Internet]. Wiley; 2011. p. 1–28. Available from: https://onlinelibrary.wiley.com/doi/10.1002/9781119998365.ch1

64. Stonestrom JP, Alvarez RE, Macovski A. A Framework for Spectral Artifact Corrections in X-Ray CT. IEEE Trans Biomed Eng. 1981;BME-28:128–41.
65. Tafforeau P, Boistel R, Boller E, Bravin A, Brunet M, Chaimanee Y, et al. Applications of X-ray synchrotron microtomography for non-destructive 3D studies of paleontological specimens. Appl Phys A Mater Sci Process. 2006;83.
66. Sedigh Rahimabadi P, Khodaei M, Koswattage KR. Review on applications of synchrotron-based X-ray techniques in materials characterization. X-Ray Spectrom. 2020. p. 348–73.
67. Krenkel M, Markus A, Bartels M, Dullin C, Alves F, Salditt T. Phase-contrast zoom tomography reveals precise locations of macrophages in mouse lungs. Sci Rep [Internet]. 2015;5:9973. Available from: http://www.nature.com/articles/srep09973
68. Cloetens P, Barrett R, Baruchel J, Guigay JP, Schlenker M. Phase objects in synchrotron radiation hard x-ray imaging. J Phys D Appl Phys. 1996;29.
69. Cloetens P, Ludwig W, Baruchel J, Van Dyck D, Van Landuyt J, Guigay JP, et al. Holotomography: Quantitative phase tomography with micrometer resolution using hard synchrotron radiation x rays. Appl Phys Lett [Internet]. 1999;75:2912–4. Available from: http://aip.scitation.org/doi/10.1063/1.125225
70. Mayo SC, Stevenson AW, Wilkins SW. In-Line Phase-Contrast X-ray Imaging and Tomography for Materials Science. Materials (Basel). 2012;5:937–65.
71. Chen RC, Dreossi D, Mancini L, Menk R, Rigon L, Xiao TQ, et al. PITRE: Software for phase-sensitive X-ray image processing and tomography reconstruction. J Synchrotron Radiat. 2012;19:836–45.
72. Mooney SJ, Pridmore TP, Helliwell J, Bennett MJ. Developing X-ray computed tomography to non-invasively image 3-D root systems architecture in soil. Plant Soil. 2012. p. 1–22.
73. Yashiro W, Voegeli W, Kudo H. Exploring frontiers of 4D X-ray tomography. Appl. Sci. 2021.
74. Salomé M, Peyrin F, Cloetens P, Odet C, Laval-Jeantet AM, Baruchel J, et al. A synchrotron radiation microtomography system for the analysis of trabecular bone samples. Med Phys. 1999;26:2194–204.
75. Mebatsion HK, Verboven P, Melese Endalew A, Billen J, Ho QT, Nicolaï BM. A novel method for 3-D microstructure modeling of pome fruit tissue using synchrotron radiation tomography images. J Food Eng [Internet]. 2009;93:141–8. Available from: https://linkinghub.elsevier.com/retrieve/pii/S0260877409000193

76. Moreau JD, Cloetens P, Gomez B, Daviero-Gomez V, Néraudeau D, Lafford TA, et al. Multiscale 3D virtual dissections of 100-million-year-old flowers using X-ray synchrotron micro- and nanotomography. Microsc Microanal. 2014;20.
77. Peth S, Horn R, Beckmann F, Donath T, Fischer J, Smucker AJM. Three-Dimensional Quantification of Intra-Aggregate Pore-Space Features using Synchrotron-Radiation-Based Microtomography. Soil Sci Soc Am J [Internet]. 2008;72:897–907. Available from: http://doi.wiley.com/10.2136/sssaj2007.0130
78. Koksel F, Aritan S, Strybulevych A, Page JH, Scanlon MG. The bubble size distribution and its evolution in non-yeasted wheat flour doughs investigated by synchrotron X-ray microtomography. Food Res Int [Internet]. 2016;80:12–8. Available from: https://linkinghub.elsevier.com/retrieve/pii/S0963996915302787
79. Stevenson AW, Mayo SC, Häusermann D, Maksimenko A, Garrett RF, Hall CJ, et al. First experiments on the Australian Synchrotron Imaging and Medical beamline, including investigations of the effective source size in respect of X-ray imaging. J Synchrotron Radiat. 2010;17.
80. Hughes N, Askew K, Scotson CP, Williams K, Sauze C, Corke F, et al. Non-Destructive, high-Content analysis of wheat grain traits using X-ray micro computed tomography. Plant Methods. 2017;13.
81. Qiu X, Zhao W, Yang C, Cheng T, Wang S, Xu B. A single-frame deep learning phase retrieval algorithm based on defocus grating. Hongwai yu Jiguang Gongcheng/Infrared Laser Eng. 2020;49.
82. Yin W, Zhong J, Feng S, Tao T, Han J, Huang L, et al. Composite deep learning framework for absolute 3D shape measurement based on single fringe phase retrieval and speckle correlation. JPhys Photonics. 2020;2.
83. Vijayan P, Willick IR, Lahlali R, Karunakaran C, Tanino KK. Synchrotron Radiation Sheds Fresh Light on Plant Research: The Use of Powerful Techniques to Probe Structure and Composition of Plants. Plant Cell Physiol [Internet]. 2015;56:1252–63. Available from: https://academic.oup.com/pcp/article-lookup/doi/10.1093/pcp/pcv080
84. Lombi E, Susini J. Synchrotron-based techniques for plant and soil science: Opportunities, challenges and future perspectives. Plant Soil. 2009. p. 1–35.
85. Friis EM, Marone F, Pedersen KR, Crane PR, Stampanoni M. Three-dimensional visualization of fossil flowers, fruits, seeds, and other plant remains using synchrotron radiation X-ray tomographic microscopy (SRXTM): new insights into Cretaceous plant diversity. J Paleontol [Internet]. 2014;88:684–701. Available from:

https://www.cambridge.org/core/product/identifier/S0022336000002547/type/journal_article
86. Dhondt S, Vanhaeren H, Van Loo D, Cnudde V, Inzé D. Plant structure visualization by high-resolution X-ray computed tomography. Trends Plant Sci [Internet]. 2010;15:419–22. Available from: https://linkinghub.elsevier.com/retrieve/pii/S1360138510000956
87. Verboven P, Herremans E, Borisjuk L, Helfen L, Ho QT, Tschiersch H, et al. Void space inside the developing seed of Brassica napus and the modelling of its function. New Phytol [Internet]. 2013;199:936–47. Available from: https://onlinelibrary.wiley.com/doi/10.1111/nph.12342
88. Verboven P, Herremans E, Helfen L, Ho QT, Abera M, Baumbach T, et al. Synchrotron X-ray computed laminography of the three-dimensional anatomy of tomato leaves. Plant J [Internet]. 2015;81:169–82. Available from: http://doi.wiley.com/10.1111/tpj.12701
89. Lautner S, Beckmann F. Analysis of wood microstructure by synchrotron radiation-based x-ray microtomography (SRμCT). In: Stock SR, editor. Dev X-Ray Tomogr VIII [Internet]. 2012. p. 85060F. Available from: http://proceedings.spiedigitallibrary.org/proceeding.aspx?doi=10.1117/12.929571
90. Ho QT, Berghuijs HNC, Watté R, Verboven P, Herremans E, Yin X, et al. Three-dimensional microscale modelling of CO 2 transport and light propagation in tomato leaves enlightens photosynthesis. Plant Cell Environ [Internet]. 2016;39:50–61. Available from: http://doi.wiley.com/10.1111/pce.12590
91. Lahlali R, Karunakaran C, Wang L, Willick I, Schmidt M, Liu X, et al. Synchrotron based phase contrast X-ray imaging combined with FTIR spectroscopy reveals structural and biomolecular differences in spikelets play a significant role in resistance to Fusarium in wheat. BMC Plant Biol [Internet]. 2015;15:24. Available from: http://www.biomedcentral.com/1471-2229/15/24
92. Lee SJ, Kim Y. In vivo visualization of the water-refilling process in xylem vessels using x-ray micro-imaging. Ann Bot. 2008;101.
93. Brodersen CR, McElrone AJ, Choat B, Matthews MA, Shackel KA. The Dynamics of Embolism Repair in Xylem: In Vivo Visualizations Using High-Resolution Computed Tomography. Plant Physiol [Internet]. 2010;154:1088–95. Available from: https://academic.oup.com/plphys/article/154/3/1088/6111223
94. Simansky V, Horak J, Juriga M, Srank D. Soil structure and soil organic matter in water-stable aggregates under different application rates of biochar. VIETNAM J EARTH Sci [Internet]. 2018;40:97–108. Available from: http://vjs.ac.vn/index.php/jse/article/view/11090
95. Alves H, Lima I, Assis JT, Geraldes M, Lopes RT. Comparison of pore space features by

thin sections and X-ray microtomography. Appl Radiat Isot [Internet]. 2014;94:182–90. Available from: https://linkinghub.elsevier.com/retrieve/pii/S0969804314003042
96. Zhao D, Xu M, Liu G, Yao X, Tuo D, Zhang R, et al. Quantification of soil aggregate microstructure on abandoned cropland during vegetative succession using synchrotron radiation-based micro-computed tomography. Soil Tillage Res [Internet]. 2017;165:239–46. Available from: https://linkinghub.elsevier.com/retrieve/pii/S0167198716301660
97. De Gryze S, Jassogne L, Six J, Bossuyt H, Wevers M, Merckx R. Pore structure changes during decomposition of fresh residue: X-ray tomography analyses. Geoderma. 2006;134:82–96.
98. Peng X, Horn R, Hallett P. Soil structure and its functions in ecosystems: Phase matter & scale matter. Soil Tillage Res. 2015.
99. Schoeman L, Williams P, du Plessis A, Manley M. X-ray micro-computed tomography (μCT) for non-destructive characterisation of food microstructure. Trends Food Sci Technol [Internet]. 2016;47:10–24. Available from: https://www.sciencedirect.com/science/article/pii/S0924224415300054
100. Barigou M, Douaire M. X-ray micro-computed tomography for resolving food microstructures. Food Microstruct Microsc Meas Model. 2013. p. 246–72.
101. Rokhlenko Y, Zhang K, Gopinadhan M, Larson SR, Majewski PW, Yager KG, et al. Magnetic alignment of block copolymer microdomains by intrinsic chain anisotropy. Lawrence Berkeley Natl Lab [Internet]. 2015;176. Available from: http://arxiv.org/abs/1509.01292
102. Guillermic RM, Koksel F, Sun X, Hatcher DW, Nickerson MT, Belev GS, et al. Bubbles in noodle dough: Characterization by X-ray microtomography. Food Res Int. 2018;105:548–55.
103. Assad-Bustillos M, Guessasma S, Réguerre AL, Della Valle G. Impact of protein reinforcement on the deformation of soft cereal foods under chewing conditions studied by X-ray tomography and finite element modelling. J Food Eng. 2020;286.
104. Mousavi R, Miri T, Cox PW, Fryer PJ. Imaging food freezing using X-ray microtomography. Int J Food Sci Technol. 2007;42:714–27.
105. Pinzer BR, Medebach A, Limbach HJ, Dubois C, Stampanoni M, Schneebeli M. 3D-characterization of three-phase systems using X-ray tomography: Tracking the microstructural evolution in ice cream. Soft Matter. 2012;8:4584–94.
106. Guo E, Zeng G, Kazantsev D, Rockett P, Bent J, Kirkland M, et al. Synchrotron X-ray tomographic quantification of microstructural evolution in ice cream-a multi-phase soft solid. RSC Adv. 2017;7:15561–73.

107. Beckmann F, Herzen J, Haibel A, Müller B, Schreyer A. High density resolution in synchrotron-radiation-based attenuation-contrast microtomography. Dev X-Ray Tomogr VI. 2008.
108. Brodersen CR, Knipfer T, McElrone AJ. In vivo visualization of the final stages of xylem vessel refilling in grapevine (Vitis vinifera) stems. New Phytol [Internet]. 2018;217:117–26. Available from: https://onlinelibrary.wiley.com/doi/10.1111/nph.14811
109. Blonder B, Carlo F, Moore J, Rivers M, Enquist BJ. X-ray imaging of leaf venation networks. New Phytol [Internet]. 2012;196:1274–82. Available from: https://onlinelibrary.wiley.com/doi/10.1111/j.1469-8137.2012.04355.x
110. Peth S, Chenu C, Leblond N, Mordhorst A, Garnier P, Nunan N, et al. Localization of soil organic matter in soil aggregates using synchrotron-based X-ray microtomography. Soil Biol Biochem [Internet]. 2014;78:189–94. Available from: https://linkinghub.elsevier.com/retrieve/pii/S0038071714002648
111. Herremans E, Verboven P, Bongaers E, Estrade P, Verlinden BE, Wevers M, et al. Characterisation of "Braeburn" browning disorder by means of X-ray micro-CT. Postharvest Biol Technol. 2013;75:114–24.

Chapter 3. CHARACTERIZATION OF WHEAT BASED ON CHANGES IN GRAIN MICROSTRUCTURE IN STORAGE DUE TO SPOILAGE

3.1 Characterization of spring and durum wheat during storage using non-destructive synchrotron phase contrast X-ray microtomography for reduction of post harvest losses (Transfer to Nature Science of food, Status: under review)

Navanth S. Indore[1], Chithra Karunakaran[2], Digvir S. Jayas[1,3*], Jarvis Stobbs[2], Miranda Vu[2], Kaiyang Tu[2], Omar Marinos[2],

[1] Biosystems Engineering, University of Manitoba, Winnipeg, MB R3T 5V6, Canada

[2] Canadian Light Source Inc., Saskatoon, SK S7N 2V3, Canada

[3] President's Office, A762 University Hall, University of Lethbridge, Lethbridge, AB T1K 3M4 Canada

*Corresponding author's email: digvir.jayas@umanitoba.ca

3.1.1 Abstract

Post-harvest losses during cereal grain storage are a big concern in both developing and developed countries, where spring and durum wheat are staple food grains. Varieties under these classes behave differently under storage, which affects their end storage life. High resolution imaging data of dry as well as spoiled seed are not available for any class of wheat; therefore, a first attempt was made to generate 3D data for better understanding of seed structure and changes due to spoilage. Six wheat varieties were stored for five weeks at 17% moisture content (wb) before scanning. Seeds were also stored in a freezer (-18°C) for further scanning to study further any changes in the structure of seeds due to freezing. Data could also help plant breeders to develop varieties that do not easily spoil, adjust grain processing techniques, and develop post-harvest recommendations for other wheat varieties.

Keywords: Synchrotron, durum wheat, spring wheat, phase contrast microcomputed tomography, seed spoilage, post harvest loss.

3.1.2 Introduction

The world population is expected to grow up to 9.1 billion by 2050, hence more food is required to feed the growing population. As per FAO, the demand for food (cereals and animal feed) is expected to reach 3 billion tonnes in 2050; therefore, overall food production needs to increase by 70% [1]. Cereals are the main staple food for developing and developed nations. This implies significant increases in the annual cereal production; for instance, it would have to grow by almost one billion tonnes. The soaring food demand may exert more pressure

on currently depleting natural resourses and will be challenging to achieve food security, but prevention or reduction of post harvest losses could be a savior in meeting the food demand, as saved food is equal to food produced. The post-harvest losses are not only limited to physical loss but also quality loss due to fungi (mycotoxins). Presently, post harvest losses in cereals occur around 10-20% in developing and 1-2% in developed countries in storage[2] and it can range from 1% in well-managed systems to 50% in poorly-managed systems[3]. The maximum fraction of all postharvest losses for cereals in developing countries is in storage losses, which negatively affect farmers' livelihoods[4]. The high moisture content leads to the growth of fungi on food grains under favorable temperature. Changes in the quality of wheat during storage due to biotic and abiotic factors have been reported in studies[5–11]. As per a World Bank report, food grains worth about USD 4 billion are lost every year due to post harvest loss[4]. The storage losses are considered most critical in developing countries[4].

Canada produced 33.8 million tonnes (Mt) of wheat in 2022, whereas the production of durum and spring wheat was 6.11 and 19.38 Mt[12], respectively. There is a demand for good quality wheat, and Canada exported about 60.5% of its produced wheat in 2022[12]. Considering post harvest loss of 2% as a developed nation (scientific storage), it would be a loss of 331 million CAD in monetary terms (@490 CAD/metric tonne). Post-harvest losses in wheat that occur during storage are two types: quantitative and qualitative losses. Quantitative loss means loss in dry mass, damage due to insects and fungi, and qualitative loss means loss of nutrition, loss of germination, and infection due to mycotoxins. Wheat is stored after harvesting before consumption. During storage and along the supply chain, moisture content plays an important role in determining its storage life. If the moisture content of grains is higher than the recommended safe storage value, then stored grains are vulnerable to spoilage due to biotic (insect, fungi) and abiotic (temperature, moisture) factors. Wheat grain deterioration is primarily driven by aerobic respiration of fungi because fungi thrive on carbohydrates in the kernel, giving off CO_2, H_2O, and heat. High moisture wheat can produce more respiration heat that leads to hot spots and zones of infestation. Several studies have been carried out at the macroscale to minimize storage losses in wheat. As seed structure also plays a major role in its defense mechanism against spoilage due to unfavorable conditions in storage, it is essential for microscale understanding of wheat seed structures. For instance, existing kernel structure before storage has a major role to play; if the seeds are already cracked or damaged during handling operations, it leads to entry of moisture and insects[13,14]. Therefore, the study of seed

structure becomes an important aspect of grain storage, which is one of the main scopes of this study.

Wheat storage is facing enormous challenges[14]; therefore, numerous studies have been undertaken on macro and micro levels to understand the quality and loss assessment of wheat in grain storage across the world[3,11,13,15–20]. The main scope of these studies is to determine safe storage limits, reduce post harvest loss, assess quality during storage, and develop post harvest storage guidelines suited to local conditions. The microlevel studies or measures include the effect of scientific storage (controlled storage, hermetic) on wheat quality and the interaction of abiotic (moisture, temperature, humidity) and biotic (insects, fungi) factors on grain quality and post harvest losses[21]. These large-scale storage studies require bigger setups and infrastructure for simulating conditions, unlike the microscopic approach. The microscopic method involves destructive and non-destructive approaches, such as the use of X-rays, hyperspectral imaging, and thermal imaging to find defects before loading, during storage, or after unloading. These studies have created useful results in the identification of specific fungi, and macrolevel studies mainly focused on large-scale storage systems where the interaction of biotic and abiotic factors was studied on the quality of food grains[22–26]. Besides these developments in quality evaluation of wheat using microscopic methods, there are limitations in exploring required information from the grain samples due to limitations of the system such as sample preparation, low contrast in imaging, time consumption, low resolution, more scanning time, and non-selective wavelength etc.[27,28]. The conventional X-ray imaging system[23,29–32] used in characterisation of various structural features of wheat was also reported. In wheat seed, crease depth and morphology were found to be responsible for diseases such as black spots that infect grains particularly at the crease[33]. Therefore, the use of high-resolution imaging such as synchrotron X-ray imaging has found promising applications in post harvest storage studies. Applications of synchrotron X-ray imaging were found in understanding seed structure, soil science, and plant systems in agriculture, which were reviewed [27].

To date, there are no high-resolution data available on wheat grain structure that can be used in planning post harvest management strategies, and the present work is the first of its kind, where synchrotron phase contrast imaging was used in a post harvest storage study of wheat. The selection of phase contrast imaging was made over X-ray absorption due to its edge enhancement characteristics of low density materials, because similar applications were found in the characterization of soft tissues, water/nutrient movements and multiphase[27,34–36]. It is difficult to differentiate between spoilage, moisture, and air in absorption X-ray imaging;

therefore, phase contrast imaging has been used due to its edge enhancement characteristics. Grain moisture is a crucial parameter in the post harvest storage of wheat, which can be controlled during all unit operations performed before storage. The objective of this study was to gather structural features information from two popular wheat classes (spring and durum) using phase contrast imaging for the characterization of dry and fungal infected seeds. Another objective was to develop a methodology for testing cereal grains using synchrotron imaging in post-harvest grain storage studies, which can be used for other wheat classes and cereal grains. The results of the study could also help plant breeders to develop varieties that do not spoil easily, adjust grain processing techniques such as milling, and develop post harvest recommendations for other wheat varieties**.**

3.1.3 Material and Methods

3.1.3.1 Wheat

In this study, we procured and used commercially available certified seeds of Canada Western Amber Durum wheat (varieties: CDC Defy, AAC Stronghold, and AAC Spitfire) and Canada Western Spring Wheat (varieties: AAC Starbuck, AAC Brandon and Faller) from a company (SeCan, Niverville, MB).

3.1.3.2 Storage experiment

Five-hundred-gram samples of each variety were conditioned to a moisture content (mc) of 17% wet basis (wb) by adding distilled water in triplicates and then stored in airtight glass jars (volume 1 L), and these procedures were repeated every week up to five weeks. Then glass jars were stored at ambient conditions where storage temperatures were in the range of 22-25ºC. The mc was determined 24 h after conditioning by oven drying of 10 g samples at 130°C for 19 h and the samples were reconditioned, if necessary, to maintain at 17±0.5%[37].

3.1.3.3 Synchrotron X-Ray phase contrast microcomputed tomography (SR-µCT)

3.1.3.3.1 Sample preparation

No specific sample preparation is required for this imaging technique, where samples such as agricultural food grains can be scanned noninvasively. Fifteen to twenty grain kernels of each variety were randomly selected from two replicate jars and placed inside a plastic tube. The grains of the same variety were placed inside the tube with the bottom having replicate 2 and the top having replicate 1 for the identification of acquired image slices (slice number 1 (top)

- slice number 13 (bottom). The tube ends were closed by a reusable adhesive to prevent the dehydration of the seeds during scanning and then placed on the sample stage. The sample was eccentrically aligned perfectly on the stage to keep it in the field of view of the beam, and then the sample was mounted on a rotating stage between the detector and X-ray beam. The rotating stage was used to change the orientation of the sample in 0.06° steps with respect to the incident white beam of 20 keV. The distance between the sample and detector is important in phase contrast imaging for better contrast due to edge enhancement, and the distance was 5 cm (Fig. 3.1). The detailed principles and theory of X-ray phase contrast imaging can be found elsewhere[38–41].

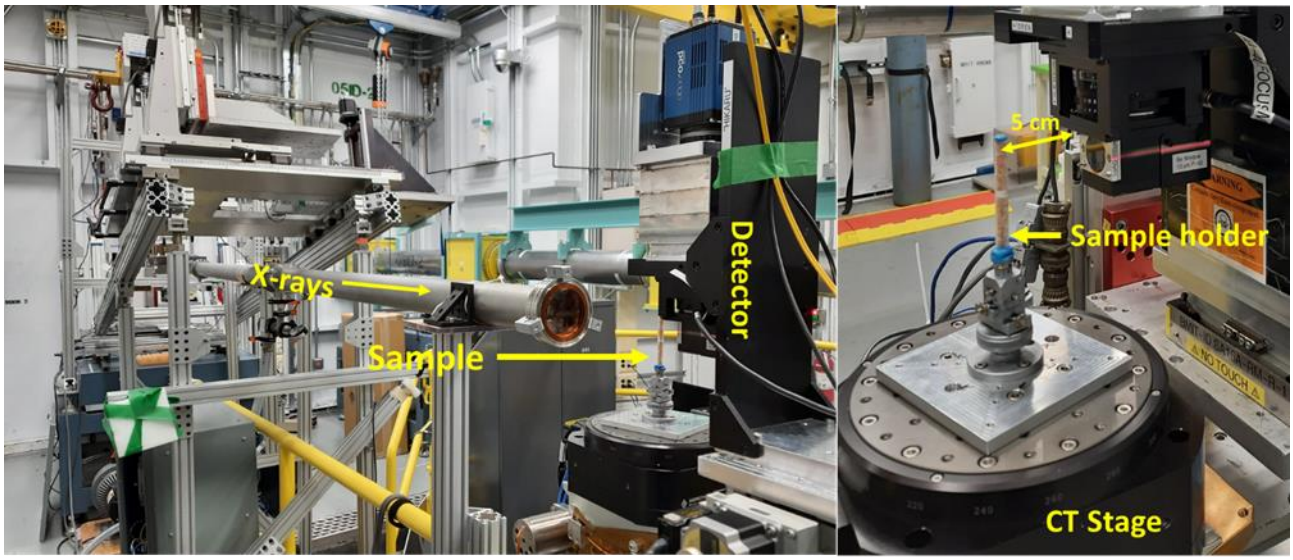

Figure 3.1 Left: SR-µCT beamline and sample setup. Right: enlarged view showing sample and detector.

3.1.3.3.2 Data acquisition and image processing

The SR-µCT imaging of the samples was carried out using a BMIT-BM beamline at the Canadian Light Source (CLS), Saskatoon, Canada. Two filters Al (0.800-mm thick) and Md (0.076 mm) were used before the monochromator to obtain a filtered white beam of energy of about 20.0 keV. The transmitted X-ray images were converted into visible images by a combination of a scintillator (LuAg 500) and a detector (PCO Edge 5.0, AA-40) for 3.6 µm resolution in the study (Fig. 3.1). The collected projection images were corrected for the dark signal from the detector (without X-ray beam) and the flat signal (with X-ray beam and no sample) to account for the imperfections in the beam and inhomogeneity in the scintillator screens. The entire sample was made of 13 slices with each slice consisting of 3000 images.

The images of flat and dark signals were recorded before and after recording the CT images and the average of the flat and dark images was used for normalization[35,42,43]. Phase retrieval was performed from a single phase-contrast image at each projection angle using Paganin's method using the UFO-kit software (Tofu 0.12, Karlsruhe Institute of Technology, Karlsruhe, Germany). Vertical stitching of all 13 slices was carried out after the reconstruction of data using the same software, where all projections were stitched vertically by finding overlap by matching two consecutive data sets using the ez_helper module of the UFO- kit. As the dataset was large and data were binned 4x4 to size (<4 Gb) using Fiji (2.9.0)[44].

Binarization using interactive thresholding was performed for each data set to segment seeds from the air space for further analysis. The thresholded image was then used for morphological operations (opening, closing, and fill holes) to remove unwanted pixels from seed boundaries, which is a prerequisite for performing seed label analysis. The label analysis of Avizo improved the thresholded images that were used to determine: seed volume, size dimensions etc. (Fig. 3.2). The porosity of the seed samples was determined using the volume fraction module of Avizo by analyzing the thresholded seed images. Similar image processing was performed in past studies[35,42,45]. Individual seed segmentation was achieved using a customized ROI tool of the ORS Dragonfly (2021.3, Object Research Systems, Montreal, QC) module by selecting a targeted pixel. Before segmentation, the three most spoiled seeds of each variety were selected as replication by visualizing the collected projection. Three control seeds were randomly selected for segmentation of each variety. In the first step, separate ROIs were created for each component of interest (germ, air space, change in structure/spoilage, and whole seed) in the segmentation editor of the ORS dragonfly. The defined range (global thresholding) based on histogram intensity was used for painting or selection of component pixels, as shown in Fig. 3.2. Labeled pixels were measured by an analysis module for the determination of the volume of each component of the seed.

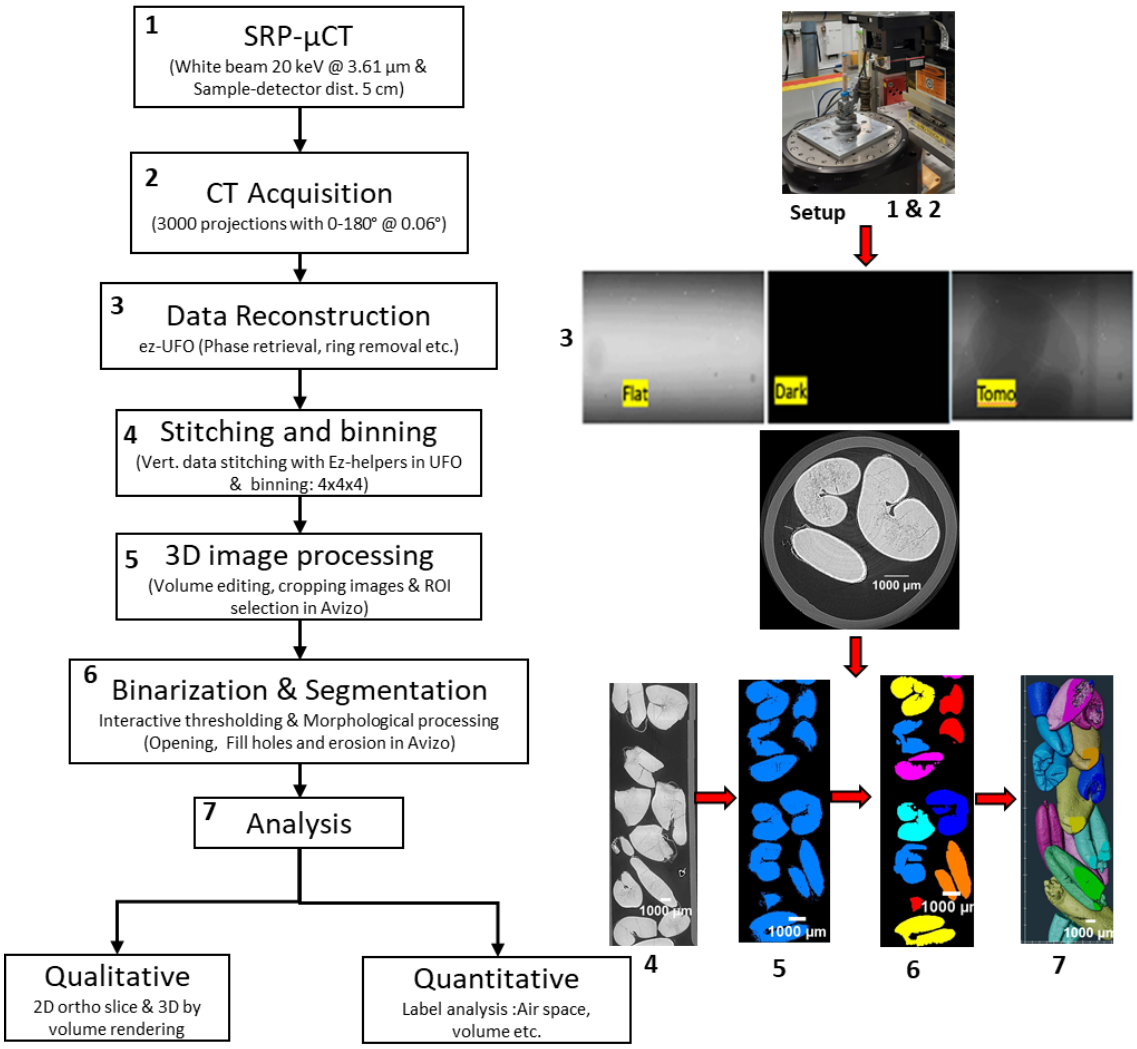

Figure 3.2 Left: Developed image processing pipeline of SR-µCT data using Avizo and right: visualization of Avizo image processing steps

3.1.4 Results and discussion

3.1.4.1 Structural changes

The physical condition of all six varieties stored for 5 weeks was assessed by visual observation. Both durum wheat and spring wheat showed varying levels of deterioration during the visual inspection compared to control samples. Durum wheat showed more deterioration in comparison to spring wheat during the visual inspection of wheat kernels. The fungus was visible on some of the germ parts of the AAC Spitfire variety, followed by CDC Defy and AAC Stronghold. In case of spring wheat, AAC Starbuck and AAC Brandon were found to be more affected during storage, but many of the kernels were found to be sound compared to durum wheat, where almost both replicates of samples of AAC Spitfire and CDC Defy showed

deterioration. The Faller variety did not show major visible deterioration on the surface of grain kernels.

The scanned seeds using SR-μCT have shown promising results and revealed important structural information. The high-resolution data of both wheat classes were visualized in the form of two types of cross sections, as shown in Figs. 3.3 and 3.4 and both durum and spring wheat showed distinctive features in seed structure, size, and shape. The presence of cracks was predominant in all three control samples of durum varieties (Fig 3.3; A1, B1, C1) compared to spring wheat varieties (Fig 3.4; D1, E1, F1). The seed endosperm was found to be more damaged in the AAC Spitfire and CDC Defy than in the AAC Stronghold. In the case of spring wheat, damage or presence of cracks were found but less in comparison to durum wheat. The varieties AAC Starbuck and AAC Brandon had higher anomalies than the Faller variety. Control samples of Faller wheat variety were more sound than the other five varieties of wheat. The seed coat (with aleurone layer) of durum wheat was more affected than spring wheat as storage time increased from one week to five week. The cracks evolved from the crease of the kernel and propagated across the endosperm and even in some cases breached the seed coat, which could be visible from both longitudinal and cross-sections of both dataset in Fig 3.3 and Fig 3.4. These uneven imperfections (cracks, holes) in grain kernel might have made them vulnerable to spoilage during storage and the reasons behind this internal damage could be uneven drying, weathering of crop before harvesting, and grain handling operations[14]. As the storage period progressed from one week to five weeks, an increase in the level of deterioration was found in all cross sections. The change in the structure of kernel due to spoilage could be visualized by differences in the gray values in the cross-section near the germ, crease, and around cracks. The higher deterioration due to fungal infection was clearly visible in durum varieties from 3 weeks (A2, B2, C2) to 5 weeks (A3, B3, C3) of Fig 3.3 and in frozen samples (A4, B4, C4). Also, in spring varieties of 5-week (D2, E2, F2) and frozen (D3, E3, F3) samples, AAC Spitfire and CDC Defy in durum wheat severely spoiled than the AAC stronghold, and we were able to characterize them based on these differences (Fig. 3.4). Similarly, in spring wheat, AAC Brandon and AAC Starbucks deteriorated more than Faller with an increase in storage time. The presence of spoilage due to fungi is visible in dark gray values across damaged seed endosperm in Fig. 3.3 and Fig. 3.4. The fungi *Aspergillus flavus, A. niger, Circinella umbellata, Gliocladium sp., Penicillium frequentans, P. islandicum*, and *Ulocladium atrum* are found in stored wheat in bulk storage[14].

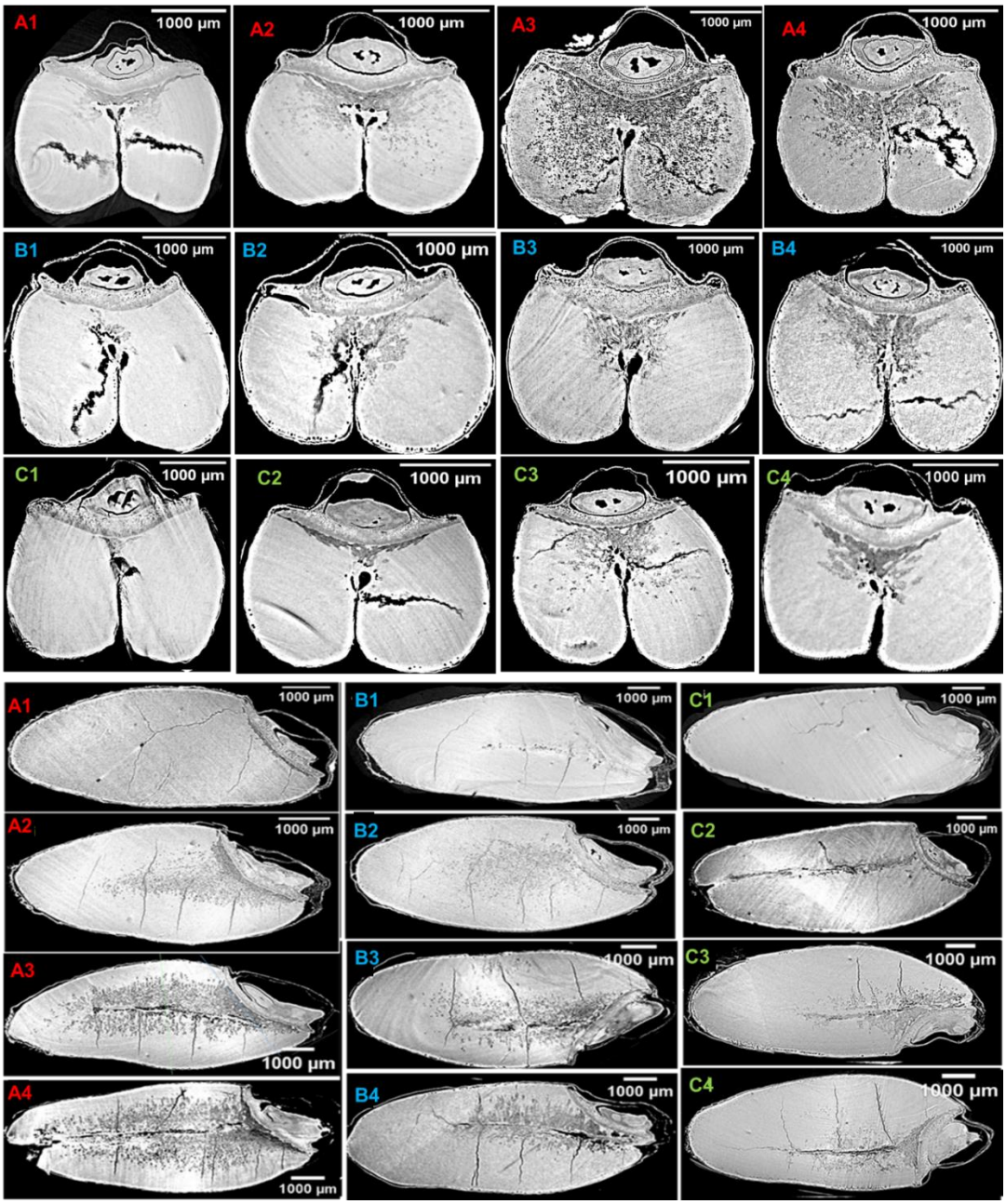

Figure 3.3 Durum wheat SR-µCT data; AAC Spitfire(A), CDC Defy(B), and AAC Stronghold(C) (1: control, 2: 3 week, 3: 5 week, and 4: frozen 5 week)

One change found common in both wheat classes during storage is that deterioration initiated at the crease part of the wheat and then followed the path of the damaged area. Therefore, the crease features (depth, opening) of wheat could have a significant impact on the wheat response to spoilage in storage. It was earlier reported that, wheat seeds affected due to diseases at the crease[29] and the same was verified from our images of both spring and durum wheat in this study. It is evident from the images that moisture could enter from the physically damaged seed surface and across the crease rather than the seed coat, which was the main cause found in the

deterioration of wheat. These observations can be verified from the projections because the best performing spring variety Faller had a tight closed crease along with fewer imperfections in the endosperm (Fig. 3.2, 3.3). The changes in five-week frozen samples of both wheat classes were accessed by visualizing all six projections Fig 3.3 (A4, B4, and C4) and Fig 3.4 (D3, E3 and F3) and there was no further deterioration and our hypothesis hold true that freezing of spoiled samples does not alter structure further. These results also validate the varying spoilage among the varieties of the same class. For the first time changes due to deterioration were mapped using high resolution imaging during post harvest storage in our study.

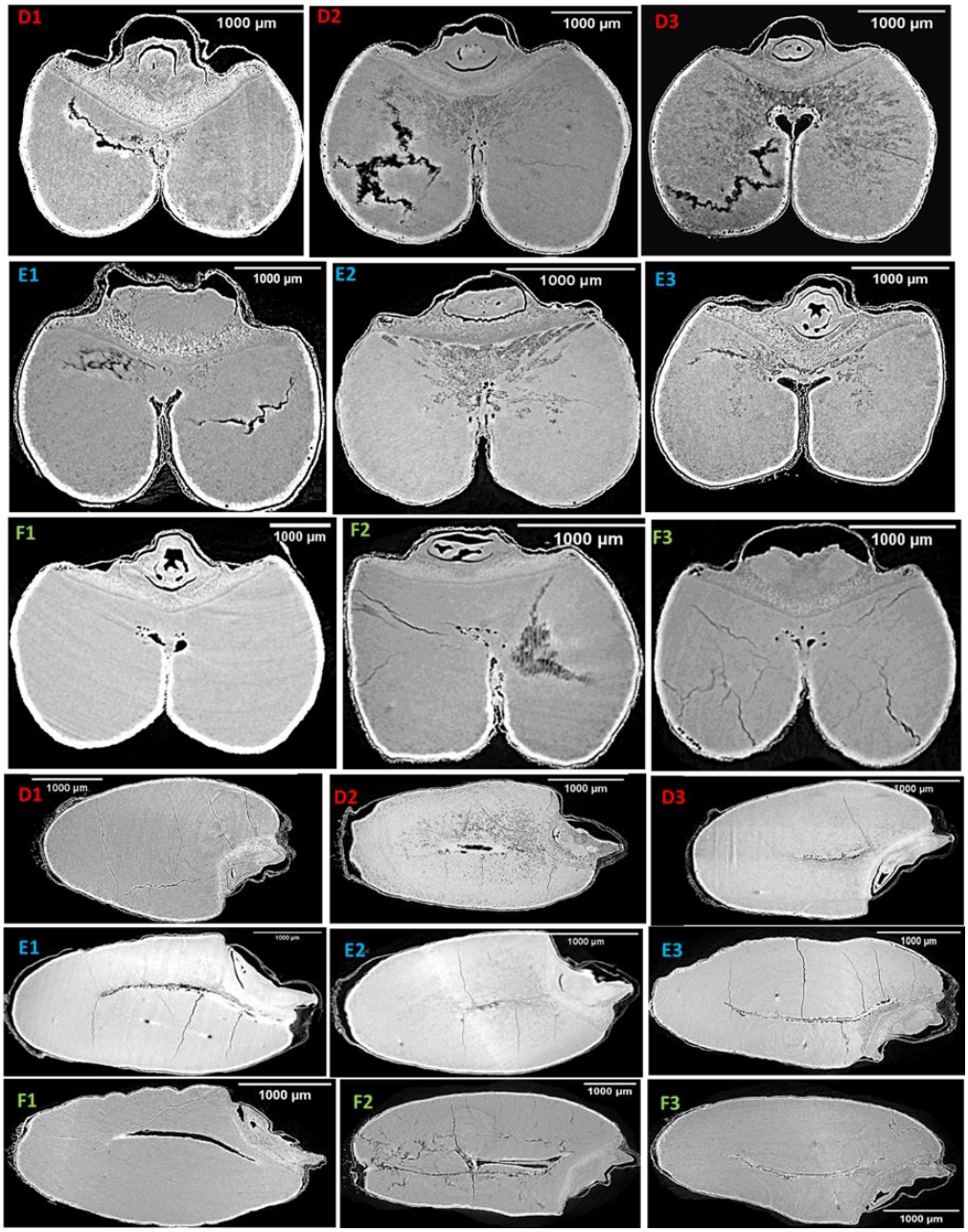

Figure 3.4 Spring wheat SR-µCT data; AAC Brandon(E), AAC Starbuck(D) and Faller(F) (1: control, 2: 5 week and 3: frozen 5 week)

The changes due to spoilage among all varieties were segmented, visualized, and measured as presented in Figs. 3.5 and 3.6. The 3D visualization of damaged areas due to spoilage of two varieties (AAC Spitfire and AAC Brandon), which have shown more deterioration from each class, is presented in Fig. 3.5 (a1, b1). The volume of segmented features was measured for both wheat classes and is shown in Fig 3.35 (a2, b2). All three varieties of durum wheat had shown higher volume of segmented deterioration compared to spring varieties (Fig 3.5 (a2,

b2)). The AAC Spitfire variety had a maximum segmented volume of change due to spoilage followed by CDC Defy and AAC Stronghold. It was also observed that, durum wheat had a comparatively higher germ volume than spring varieties. Most of the deterioration was initiated near the germ and the crease part from early weeks and then spread further. The germ area was the first to be infected with fungal infection and durum had it more than spring which can be one of the reasons of faster spoilage of durum than spring varieties. These findings of measured spoilage volume can be linked to the findings of Fig 3.6 (A), where large variation in seed volume was in durum wheat than spring wheat. CDC Defy had the highest seed volume among all varieties studied whereas, AAC Starbuck had the lowest seed volume. The measured values of air gaps and cracks in seeds are presented in Fig 3.6 (B), where AAC Spitfire had the maximum percentage of air space and Faller had the lowest percentage among all, and the same was verified earlier from 2D projections of both wheat (Fig 3.3 and Fig 3.4) and 3D rendered images from Fig 3.5 (a1, b1). Increase in airspace values along with change in seed volume from control samples to 5-week stored samples could be an indication of spoilage. The measured seed volumes and airspace values of the frozen samples were almost similar to those of the 5-week stored samples and did not show major variation (Fig 3.5 and Fig 3.6).

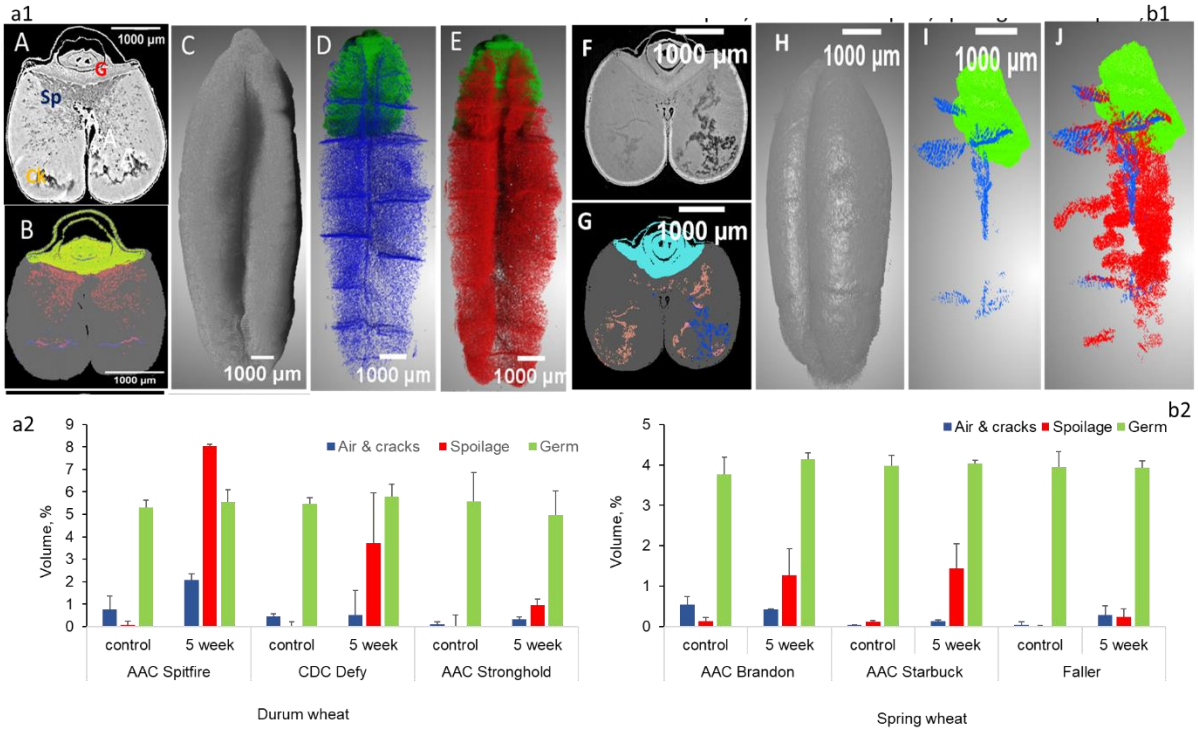

Figure 3.5 Segmented seed features of 5 week-stored AAC Spitfire (a1, Top left; A-E) and AAC Brandon (b1, Top right; F-J). In AAC Spitfire (A: X-ray image and B: labeled image), volume rendered image of labeled voxels (C: Seed, D: germ in green, cracks along with pore in blue, and E: change due to spoilage in red). In AAC Brandon (F: X-ray image

and J: labeled image), volume rendered of labeled voxels (G: Seed, H: cracks along with pores in blue and I: germ and cracks and no change due to spoilage). At the bottom, measured segmented volumes of components for durum wheat (a2) and spring wheat (b2) (n=3)

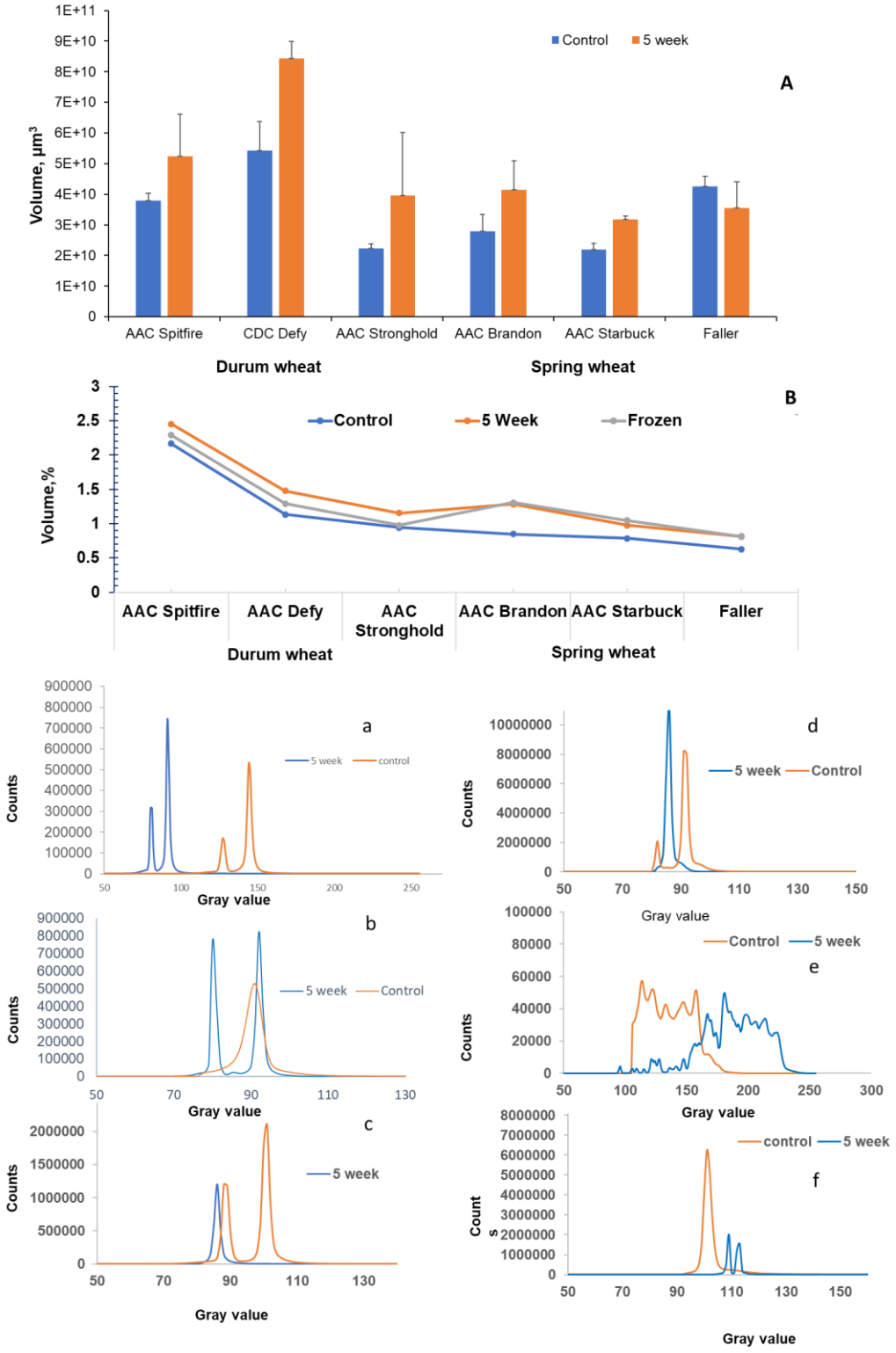

Figure 3.6 Analyzed seed volumes (A) and porosity (B)of durum wheat and spring wheat (A) of control, 5-week and 5-week frozen (n=20). The histogram of 5-week stored wheat

and control (a: AAC Spitfire, b: CDC Defy, c: AAC Stronghold, d: AAC Brandon, e: AAC Starbuck, f: Faller)

All agricultural food grains are inherently variable and cannot have the same size and shape and even internal features, as is obvious from the difference in germ volumes in control samples as well as 5-week stored samples. The wheat germ volume was segmented and calculated for the first time in our study as shown in Fig 3.5 (a2,b2). Image segmentation also revealed that in both classes of wheat, fungal infection starts at the germ area near the crease and spreads or follows the cracks or damages area. This evidently suggests that the germ part of wheat is vulnerable to spoilage during storage of wheat and hence loss of viability of seed. This characterization of varieties based on changes in internal components provides critical information about wheat varieties, indicating that each variety in a class can behave differently in grain storage. The deterioration differed in all six varieties but strongly correlated to the existing condition of control samples. SR-µCT is best to differentiate between phases that have low X-rays such as soft tissue, and in this study, we were able to differentiate and segment change due to spoilage and airspace, which have almost similar X-ray absorption. The histogram of five week stored and control wheat samples were produced and presented in Fig 3.6 (a-f), and the purpose was to check shifts in the peaks of selected varieties that reflect the deterioration. The maximum shift was observed in the AAC Spitfire as shown in Fig 3.6(a), followed by CDC Defy (b) and AAC Stronghold (c). The minimum shifts were observed in spring wheat Fig 3.6 (d, e, f). The shift of histogram in durum wheat was observed, which is a sign of infection due to fungi, where the most affected variety AAC Spitfire showed more shift with respect to the control sample. A similar shift in histogram was first reported for maize seeds in study[46].

Recommendation could be drawn from the study that prior understanding of dry samples using synchrotron X-rays is required before long-term storage. High-resolution data of wheat seed would be helpful in the modeling and planning of long-term storage studies. The post-harvest losses could be high if inferior or damaged seeds were stored or selected for long-term grain storage. It is evident from the image analysis of selected varieties that varieties of the same class behave differently. Earlier there was no evidence of how much deterioration in wheat seed structure could happen during post harvest spoilage at the microscopic level, but our study has shown how much actual level deterioration could happen in wheat if stored at unsafe moisture. The results will have a greater impact on wheat storage because if healthy grain will go into grain storage and storage losses could be reduced significantly, say from 10% to less

than 1%. Similar results were reported in durum wheat storage experiment[9]. Earlier studies of X-ray absorption were unable to differentiate changes due to spoilage inside the wheat, but in this study it was possible due to phase contrast imaging where phase of low density difference can be visualized[28,35]. It was earlier reported that porosity of dry cereal kernel could not be measured in lab due to inaccessibility of air space[47], but in this study it was measured in both classes. Collected high resolution data could be useful in the development of new/improved varieties through breeding programs that have better crease features and less brittle endosperm. Researchers should be able to freeze their samples during long-term storage studies and transport the frozen samples for imaging during the block of time assigned to that study at a synchrotron facility. These data will help post-harvest engineers develop efficient modeling strategies for better storage for wheat and can be correlated with nutrient changes in wheat. The future scope of this work could be the use of machine learning algorithms in extracting information about the opening of crease and crease depth in different classes of Canadian wheat.

3.1.5 Acknowledgment

The authors acknowledge the Netaji Subhash Chandra fellowship from the Indian Council of Agriculture Research via a grant no. ICAR/2019 for the first author and the Natural Sciences and Engineering Research Council of Canada for supporting the student research via a grant no. RGPIN-2018-04420 to Dr Jayas. The authors also acknowledge the Canadian Light Source, Saskatoon for providing beamtime and access to conduct experiments.

3.1.6 Authors' contributions

NI and CK prepared an outline, the first draft, and the content of the whole paper on the basis of experiments. JS, MV, KT, and OM, who are experts in synchrotron imaging at the Canadian light source, edited the draft and provided technical inputs, training, data acquisition, and support for the preparation of the draft. DJ conceptualized the study, is the corresponding author, received funding, and contributed to it through editing, examination, and the finalization of the manuscript drafts. All authors have read and approved the final manuscript**.**

3.1.7 Competing interest statement

The authors declare that there are no competing interests.

3.1.8 Data availability statement

High - resolution imaging data are available on request from the corresponding author.

3.1.9 References

1. Northoff, E. 2050: A third more mouths to feed. *Food Agric. Organ. United Nations* 2022 (2016).
2. Hodges, R. J., Buzby, J. C. & Bennett, B. Postharvest losses and waste in developed and less developed countries: Opportunities to improve resource use. *J. Agric. Sci.* 149, 37–45 (2011).
3. Jayas, D. S. Storing Grains for Food Security and Sustainability. *Agric. Res.* 1, 21–24 (2012).
4. Kumar, D. & Kalita, P. Reducing postharvest losses during storage of grain crops to strengthen food security in developing countries. *Foods* 6, 1–22 (2017).
5. F. Worku, A., K. Kalsa, K., Abera, M. & G. Nigus, H. Effects of storage strategies on physicochemical properties of stored wheat in Ethiopia. *AIMS Agric. Food* 4, 578–591 (2019).
6. Yuan, Q.-S., Yang, P., Wu, A.-B., Zuo, D.-Y., He, W.-J., Guo, M.-W., Huang, T., Li, H.-P. & Liao, Y.-C. Variation in the Microbiome, Trichothecenes, and Aflatoxins in Stored Wheat Grains in Wuhan, China. *Toxins (Basel).* 10, 171 (2018).
7. Zhang, S.-B., Lv, Y.-Y., Wang, Y.-L., Jia, F., Wang, J.-S. & Hu, Y.-S. Physiochemical changes in wheat of different hardnesses during storage. *J. Stored Prod. Res.* 72, 161–165 (2017).
8. Schmidt, M., Horstmann, S., De Colli, L., Danaher, M., Speer, K., Zannini, E. & Arendt, E. K. Impact of fungal contamination of wheat on grain quality criteria. *J. Cereal Sci.* 69, 95–103 (2016).
9. Nithya, U., Chelladurai, V., Jayas, D. S. & White, N. D. G. Safe storage guidelines for durum wheat. *J. Stored Prod. Res.* 47, 328–333 (2011).
10. Schroth, E., Muir, W. E., Jayas, D. S., White, N. D. G. & Abramson, D. Storage limit of wheat at 17% moisture content. *Can. Agric. Eng.* 40, 201–205 (1998).
11. Wallace, H. A. H., Sholberg, P. L., Sinha, R. N. & Muir, W. E. Biological, physical and chemical changes in stored wheat. *Mycopathologia* 82, 65–76 (1983).
12. Statistics Canada. Model-based principal field crop estimates. (2022). -(e)n <https://www150.statcan.gc.ca/n1/daily-quotidien/220914/dq220914b-eng.htm>
13. Neme, K. & Mohammed, A. Mycotoxin occurrence in grains and the role of postharvest

management as a mitigation strategies. A review. *Food Control* 78, 412–425 -(e)n https://doi.org/10.1016/j.foodcont.2017.03.012 (2017(e)ko)

14. Moustafa, S. M. N., Alhaithloul, H. A. S. & Abdelzaher, H. M. A. in *Glob. Wheat Prod.* (2018). doi:10.5772/intechopen.75585
15. Cheyed, S. H. Effect of storage method and period on vitality and vigour of wheat seed. *Indian J. Ecol.* 47, 27–31 (2020).
16. Kibar, H. Influence of storage conditions on the quality properties of wheat varieties. *J. Stored Prod. Res.* 62, 8–15 (2015).
17. Tian, P. P., Lv, Y. Y., Yuan, W. J., Zhang, S. B. & Hu, Y. Sen. Effect of artificial aging on wheat quality deterioration during storage. *J. Stored Prod. Res.* 80, 50–56 (2019).
18. Karunakaran, C., Muir, W. ., Jayas, D. ., White, N. D. . & Abramson, D. Safe storage time of high moisture wheat. *J. Stored Prod. Res.* 37, 303–312 (2001).
19. Moreno-Martínez, E., Rivera, A. & Badillo, M. V. Effect of fungi and fungicides on the preservation of wheat seed stored with high and low moisture content. *J. Stored Prod. Res.* 34, 231–236 (1998).
20. Vimala Bharathi, S. K., Vishnu Priya, V., Eswaran, V., Moses, J. A. & Sujeetha, A. R. P. Insect infestation and losses in stored food grains. *Ecol. Environ. Conserv.* 23, 286–291 (2017).
21. Jian, F. & Jayas, D. S. The Ecosystem Approach to Grain Storage. *Agric. Res.* 1, 148–156 (2012).
22. Jayas, D. S., Paliwal, J., Erkinbaev, C., Ghosh, P. K. & Karunakaran, C. in *Comput. Vis. Technol. Food Qual. Eval.* 385–412 (Elsevier, 2016). doi:10.1016/B978-0-12-802232-0.00016-5
23. Neethirajan, S., Karunakaran, C., Symons, S. & Jayas, D. S. Classification of vitreousness in durum wheat using soft X-rays and transmitted light images. *Comput. Electron. Agric.* 53, 71–78 (2006).
24. Singh, C. B., Jayas, D. S., Paliwal, J. & White, N. D. G. Fungal Damage Detection in Wheat Using Short-Wave Near-Infrared Hyperspectral and Digital Colour Imaging. *Int. J. Food Prop.* 15, 11–24 (2012).
25. Bechtel, D B; Zayas, I; Dempster, R, W. J. D. Size distribution of starch granules isolated from Hard Red Winter and Soft Red Winter wheats. *Cereal Chem.* 70, 238–240 (1993).
26. Narvankar, D. S., Singh, C. B., Jayas, D. S. & White, N. D. G. Assessment of soft X-ray imaging for detection of fungal infection in wheat. *Biosyst. Eng.* 103, 49–56 (2009).

27. Indore, N. S., Karunakaran, C. & Jayas, D. S. Synchrotron tomography applications in agriculture and food sciences research: a review. *Plant Methods* 18, 101 (2022).
28. Karunakaran, C., Lahlali, R., Zhu, N., Webb, A. M., Schmidt, M., Fransishyn, K., Belev, G., Wysokinski, T., Olson, J., Cooper, D. M. L. & Hallin, E. Factors influencing real time internal structural visualization and dynamic process monitoring in plants using synchrotron-based phase contrast X-ray imaging. *Sci. Rep.* 5, 12119 (2015).
29. Le, T. D. Q., Alvarado, C., Girousse, C., Legland, D. & Chateigner-Boutin, A.-L. Use of X-ray micro computed tomography imaging to analyze the morphology of wheat grain through its development. *Plant Methods* 15, 84 (2019).
30. Hughes, A., Askew, K., Scotson, C. P., Williams, K., Sauze, C., Corke, F., Doonan, J. H. & Nibau, C. Non-destructive, high-content analysis of wheat grain traits using X-ray micro computed tomography. *Plant Methods* 13, 76 (2017).
31. Neethirajan, S., Jayas, D. S., White, N. D. G. & Zhang, H. Investigation of 3D geometry of bulk wheat and pea pores using X-ray computed tomography images. *Comput. Electron. Agric.* 63, 104–111 (2008).
32. Karunakaran, C., Jayas, D. & White, N. Soft X-ray image analysis to detect wheat kernels damaged by Plodia interpunctella (Lepidoptera: Pyralidae). *Sci. Aliments* 23, 623–631 (2003).
33. Radchuk, V., Weier, D., Radchuk, R., Weschke, W. & Weber, H. Development of maternal seed tissue in barley is mediated by regulated cell expansion and cell disintegration and coordinated with endosperm growth. *J. Exp. Bot.* 62, 1217–1227 (2011).
34. Lee, S. J. & Kim, Y. In vivo visualization of the water-refilling process in xylem vessels using x-ray micro-imaging. *Ann. Bot.* 101, 595–602 (2008).
35. Brar, G. S., Karunakaran, C., Bond, T., Stobbs, J., Liu, N., Hucl, P. J. & Kutcher, H. R. Showcasing the application of synchrotron-based X-ray computed tomography in host-pathogen interactions: The role of wheat rachilla and rachis nodes in Type-II resistance to Fusarium graminearum. *Plant. Cell Environ.* 42, 509–526 (2019).
36. Lahlali, R., Karunakaran, C., Wang, L., Willick, I., Schmidt, M., Liu, X., Borondics, F., Forseille, L., Fobert, P. R., Tanino, K., Peng, G. & Hallin, E. Synchrotron based phase contrast X-ray imaging combined with FTIR spectroscopy reveals structural and biomolecular differences in spikelets play a significant role in resistance to Fusarium in wheat. *BMC Plant Biol.* 15, 24 (2015).
37. ANSI/ASABE. Moisture Measurement — Unground Grain and Seeds. *ASABE Stand.*

2–4 (2017).

38. Willmott, P. *An Introduction to Synchrotron Radiation*. *An Introd. to Synchrotron Radiat.* (Wiley, 2019). doi:10.1002/9781119280453

39. Cloetens, P., Ludwig, W., Baruchel, J., Van Dyck, D., Van Landuyt, J., Guigay, J. P. & Schlenker, M. Holotomography: Quantitative phase tomography with micrometer resolution using hard synchrotron radiation x rays. *Appl. Phys. Lett.* 75, 2912–2914 (1999).

40. Betz, O., Wegst, U., Weide, D., Heethoff, M., Helfen, L., Lee, W. K. & Cloetens, P. Imaging applications of synchrotron X-ray phase-contrast microtomography in biological morphology and biomaterials science. I. General aspects of the technique and its advantages in the analysis of millimetre-sized arthropod structure. *J. Microsc.* 227, 51–71 (2007).

41. Yashiro, W., Voegeli, W. & Kudo, H. Exploring Frontiers of 4D X-ray Tomography. *Appl. Sci.* 11, 8868 (2021).

42. Karunakaran, C., Lahlali, R., Zhu, N., Webb, A. M., Schmidt, M., Fransishyn, K., Belev, G., Wysokinski, T., Olson, J., Cooper, D. M. L. & Hallin, E. Factors influencing real time internal structural visualization and dynamic process monitoring in plants using synchrotron-based phase contrast X-ray imaging. *Sci. Rep.* 5, 12119 (2015).

43. Cloetens, P., Mache, R., Schlenker, M. & Lerbs-Mache, S. Quantitative phase tomography of Arabidopsis seeds reveals intercellular void network. *Proc. Natl. Acad. Sci.* 103, 14626–14630 (2006).

44. Schindelin, J., Arganda-Carreras, I., Frise, E., Kaynig, V., Longair, M., Pietzsch, T., Preibisch, S., Rueden, C., Saalfeld, S., Schmid, B., Tinevez, J. Y., White, D. J., Hartenstein, V., Eliceiri, K., Tomancak, P. & Cardona, A. Fiji: An open-source platform for biological-image analysis. *Nat. Methods* 9, 676–682 -(e)n https://doi.org/10.1038/nmeth.2019 (2012(e)ko)

45. Xiong, B., Wang, B., Xiong, S., Lin, C. & Yuan, X. 3D morphological processing for wheat spike phenotypes using computed tomography images. *Remote Sens.* 11, 1110 (2019).

46. Rawson, S. D., Maksimcuka, J., Withers, P. J. & Cartmell, S. H. X-ray computed tomography in life sciences. *BMC Biol.* 18, -(e)n https://doi.org/10.1186/s12915-020-0753-2 (2020(e)ko)

47. Chang, C. Measuring density and porosity of grain kernel using gas pycnometer. *Cereal Chem.* 65, 13–15 (1987).

3.2 Application of Synchrotron imaging techniques for study of changes in microstructural and nutritional properties of different wheat classes in storage (Submitted to Scientific Reports in October 2023, Status : under review)

Navnath S. Indore[1], Digvir S. Jayas[1,3*], Chithra Karunakaran[1,2], Jarvis Stobs[2], Viorica F. Bondici[2], Miranda Vu[2], and Kaiyang Tu[2]

[1] Biosystems Engineering, University of Manitoba, Winnipeg, MB R3T 5V6, Canada
[2] Canadian Light Source Inc., Saskatoon, SK S7N 2V3, Canada
[3] President's Office, A762 University Hall, University of Lethbridge, Lethbridge, AB T1K 3M4, Canada
*Corresponding author's email: digvir.jayas@umanitoba.ca

3.2.1 Abstract

Eight wheat varieties of different classes were stored for 8 wk at 17% moisture content (wb) before data acquisition using synchrotron phase contrast micro tomography, synchrotron X-ray fluorescence imaging and mid-IR spectroscopy at the Canadian Light Source, Saskatoon, SK. Differentiation of wheat is possible based on changes in microstructure of selected wheat classes. Minimum changes in microstructure were observed in Canada Northern Hard Red (CNHR), Canada Western Red Winter (CWRW), Canada Western Special Purpose (CWSP), and Canada Prairie Spring White (CPSW) classes of wheat, hence these could perform better in storage. The existing condition of kernel microstructure strongly influences the performance of wheat in storage, which is a significant outcome of this study. The nutrient distribution and biochemical composition were affected at the end of 8 wk storage in deteriorated wheat classes Canada Prairie Spring Red (CPSR), Canada Western Hard White Spring (CWHWS), Canada Western Soft White Spring (CWSWS), and Canada Western Extra Strong (CWES). Data could also help plant breeders to develop varieties that do not easily spoil, improve grain processing techniques, and develop post-harvest recommendations.

3.2.2 Introduction

Wheat is a staple food for 35% of the world's population and Canada stands as one of the world's top wheat producing nations. Canada exports wheat to more than 80 countries and also uses domestically for food, feed and fuel[1] . In Western Canada, different wheat classes serve as the foundation of agriculture. There are sixteen wheat classes in Canada, and the popular

classes are Canada Prairie Spring Red (CPSR), Canada Prairie Spring White (CPSW), Canada Western Extra Strong (CWES), Canada Amber Durum Wheat (CWAD), Canada Western Hard White Spring (CWHWS), Canada Western Red Winter (CWRW), Canada Northern Hard Red (CNHR), Canada Western Special Purpose (CWSP), and Canada Western Soft White Spring (CWSWS) [2].These classes cater to diverse end-users, such as bakeries, pasta manufacturers, and livestock feed producers. The classification system ensures that the right wheat type is cultivated to meet the specific quality standards for various products. The country's vast wheat fields span across the Prairie provinces of Alberta, Saskatchewan, and Manitoba, with smaller scale production in other regions[3]. Each class possesses unique characteristics, such as protein content and gluten strength, making them suitable for processing into different products. The classification system ensures that Canadian wheat meets the precise requirements of global markets, contributing to the country's reputation as a reliable wheat supplier. The wheat industry plays a pivotal role in Canada's economy. Wheat exports generate significant revenue (8.3 billion USD) for the country, contributing to a favorable balance of trade[4].

While Canada boasts robust wheat production, storage losses can pose challenges[5]. Maintaining the quality and quantity of wheat in storage is critical to preserving its market value. Factors like moisture, temperature fluctuations, and pest infestations can lead to spoilage and reduce wheat quality[6,7]. Farmers and storage facilities must employ proper storage techniques and technologies to minimize losses. Addressing these challenges is vital not only for economic reasons but also to ensure a consistent supply of high-quality wheat to meet domestic and international demand. The examination of wheat quality fluctuations during storage is a significant research focus in Canada, given the pivotal role wheat plays as both a vital food source and a cash crop in the country. The changes in quality during storage due to biotic and abiotic factors were reported in studies for wheat [8–14]. The application of advanced imaging techniques; Soft X-rays, hyperspectral imaging, hard X-rays (synchrotron techniques) and infrared spectroscopy to the study grain quality during storage has been a subject of rigorous investigation in the past [15–17]. Synchrotron X-ray imaging has gained popularity as an advanced scientific tool for studying the microstructure of seeds, plants, and food. This is due to its unique properties, including high brilliance, high resolution, rapid scanning capabilities, and non-invasiveness[15]. Therefore, to exploit synchrotron capability, objective of this study are to characterize different classes wheat based on seed internal microstructural information as it relates to spoilage and changes in biochemical and nutritional components in storage.

3.2.3 Methods

3.2.3.1 Wheat

In this study, we procured commercially available certified seeds of CPSR cultivar 'AAC Penhold', CPSW cultivar 'AC Vista', CWES cultivar 'Burnside', CWHWS cultivar 'AC Snowstar', CWRW cultivar 'AAC Wildfire', CNHR cultivar 'Prosper', CWSP cultivar 'Aldoren', and CWSWS. cultivar 'AC Andrew' (Table 1) from a company (SeCan, Niverville, MB)

3.2.3.2 Storage

The experiments were carried out as per procedure described in [18] .The 500 g samples of each cultivar were conditioned, in triplicate, to a moisture of 17% mc (wb) using distilled water and then stored in airtight glass jars (volume 1 L) and these procedures were repeated every week up to 8 wk. Then, glass jars were stored at ambient conditions where temperatures during the storage was in the range of 22-25ºC. The moisture content was determined after 24 h by oven drying method [19].

Table 3.2.3.1 Initial and conditioned moisture content of selected wheat classes during storage

Wheat Class*		Cultivar	Initial mc (WB),%	Conditioned mc (WB), %
a	CNHR	Prosper	12.48	17±0.5
b	CPSR	AAC Penhold	14.74	17±0.5
c	CWES	Burnside	12.07	17±0.5
d	CWHWS	AC Snowstar	13.29	17±0.5
e	CWRW	AAC Wildfire	13.25	17±0.5
f	CWSP	Aldoren	12.60	17±0.5
g	CWSWS	AC Andrew	13.72	17±0.5
h	CPSW	AC Vista	11.51	17±0.5

*CNHR - Canada Northern Hard Red, CPSR - Canada Prairie Spring Red, CWES-Canada Western Extra Strong, CWHWS- Canada Western Hard White Spring, CWRW- Canada Western Red Winter, CWSP- Canada Western Special Purpose, CWSWS- Canada Western Soft White Spring, and CPSW- Canada Prairie Spring White.

The sample preparation, data acquisition and data processing was carried out as per the procedures described in[18,20] and briefly summarized here.

3.2.3.3 Synchrotron phase contrast microtomography (SR-µCT)

The SRP-µCT imaging of wheat samples was carried out at (BMIT-BM, 05B1-1) beam at the Canadian Light Source, Saskatoon, SK (CLS). Ten to twenty grain kernels of each wheat class were randomly selected and used for data acquisition. The operational parameters were standardized for data acquisition in an earlier study[18] and were: energy: 20 keV, resolution 3.6 µm, and sample to detector distance of 5 cm. The data reconstruction, image processing, and visualization were conducted using in house software (UFO), ImageJ[21], and ORS Dragonfly (4.0, Object Research Systems, Montreal, QC).

3.2.3.4 Mid Infrared (mid-IR) Spectroscopy

The selected wheat samples, in pellet form following the previously outlined procedure [20], were used in data collection. The data acquisition was carried out with help of Cary 670 series microscope (Agilent Technologies Inc., Santa Clara, CA). The spectral data were collected within the range of 4000 to 900 cm^{-1}, at a resolution of 4 cm^{-1}. A total of 64 scans were co-added to ensure reliable and accurate data. After data acquisition, the processing and analysis steps (cut, rubber band baseline correction, and vector normalization) were executed using the Quasar software (version 1.5.0)[22].

3.2.3.5 Synchrotron X-ray fluorescence imaging (SR-XFI)

The sample preparation, data acquisition and processing of selected wheat classes were carried out using the previously described procedure[18].

3.2.4 Results and discussion

3.2.4.1 Visual Inspection

The visual inspection of all the selected wheat classes (varieties) was carried out after 8 wk storage period and deterioration was observed in stored wheat samples. The fungal infection was detected in the germ area in dark grey color in (CWHWS, CWES, CWSWS) wheat classes (figure 3.7). The fungal infection was observed on the surface and near crease of wheat of CPSR and CWES classes. The impact of spoilage in storage was prominent, where discoloration of wheat kernel was observed in classes (CNHR, CWES, CPSR, and CWSWS), at the end of 8 wk storage.

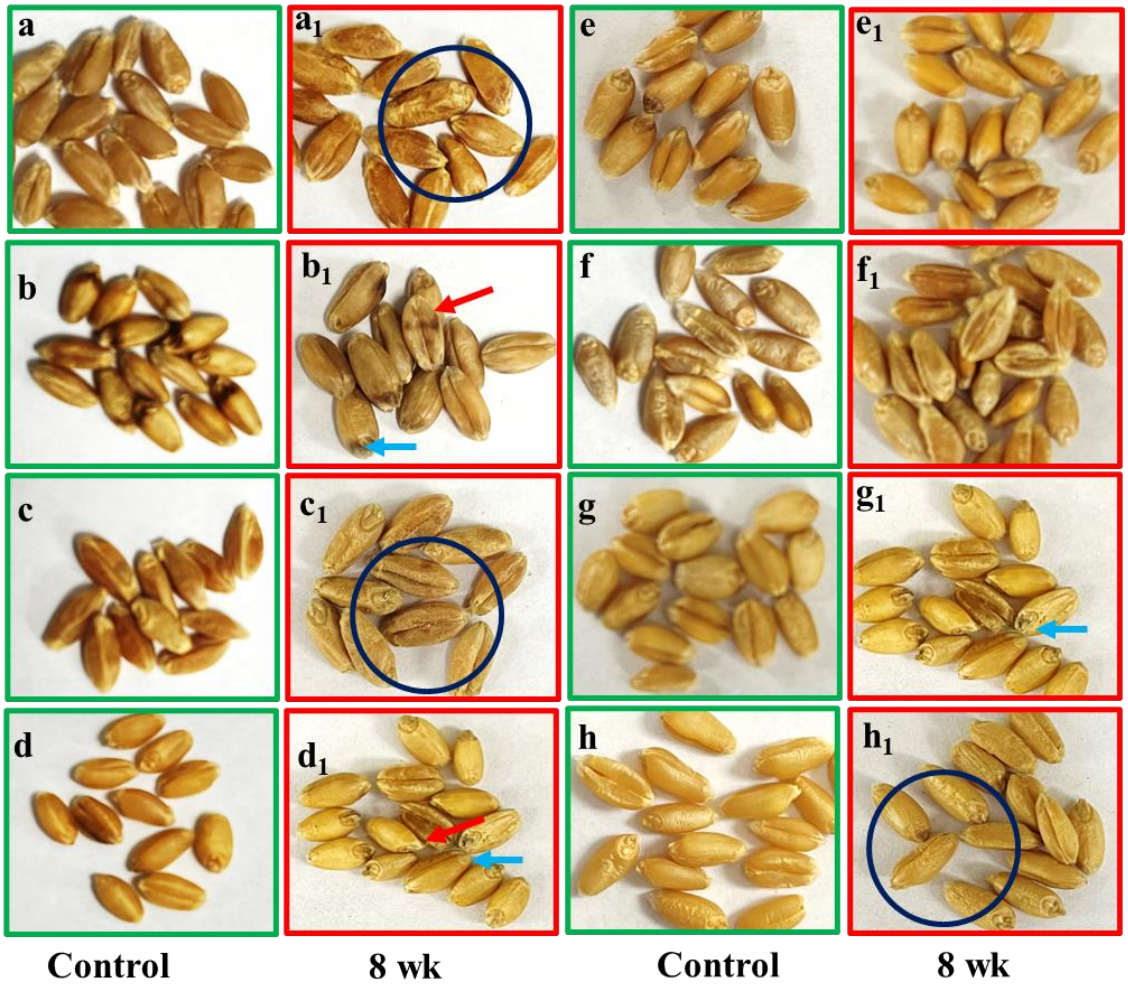

Figure 3.7. The results of visual observation of wheat classes control and 8 wk stored [a: (CNHR) Prosper, b: (CPSR) AAC Penhold, c: (CWES) Burnside, d: (CWHWS) AC Snowstar, e: (CWRW) AAC Wildfire, f: (CWSP) Aldoren, g: (CWSWS) AC Andrew, h: (CPSW) AC Vista]. Arrows denotes deterioration regions (germ: blue, crease: blue) and circles denotes the change in colour in 8 wk stored samples. Full names of the wheat classes are given in Table 1.

3.2.4.2 Synchrotron phase contrast microtomography (SR-µCT)

Reconstructed cross sections of eight wheat classes for both control and 8-wk stored samples from SR-µCT imaging are presented in figures 3.8 and 3.9 The control samples of CNHR, CWRW, CWSP, and CWSWS were healthy and free from any deterioration before storage but remaining samples (CWHWS, CPSR, CWES, and CPSW) showed existing imperfections in microstructure. The cracks were present in control samples of CPSR, CWES, CWHWS and CPSW before storage, these observations are important because the deterioration always starts near these initial damages or cracks as reported in[18]. All selected wheat classes showed varying level of deterioration at the end of 8 wk storage period. The changes due to deterioration were visible due to changes in grey values, this was made possible due to edge enhancement of SR-

μCT[23]. The contrast due to this imaging technique made it possible to visualize changes due to deterioration in selected wheat classes which could not be possible in absorption imaging methods[15,24]. The maximum deterioration was observed in 8-wk stored CPSR where all parts of the seed including germ, endosperm were seriously damaged. Canada Prairie Spring Red (showed deterioration before storage, which might caused extreme microstructural change in it figure3.7(b1). The CWRW and CWSWS (figure 3.8 e_1 and g_1) also showed deterioration in their endosperm, besides having better microstructure before storage unlike CPSR. The wheat classes (CPSR, CWRW, CWHWS, CWSWS) which were physically sound before storage had initial mc (Table 1) above 13% (wb). Among these classes (CPSR, CWRW, CWHWS) observed deterioration in SR-CT data before storage. The one common thing in all wheat classes was that the deterioration started from crease region and then propagated across the endosperm. The microstructural changes in endoderm were dominated in wheat classes that already had presence of cracks. Earlier studies[25,26] also reported that the crease region was more susceptible to spoilage than other regions of wheat. The wheat classes with intact microstructures performed better and showed more tolerance to spoilage during storage at 17% mc (wb). The characterization of wheat classes is possible based on this high-resolution visualization of each wheat class. The wheat class CWSP performed the best after 8 wk storage followed by wheat class CPSW. The wheat classes that might perform better in storage are CNHR CWES, and CWSP based on our visual observations of SR-μCT data.

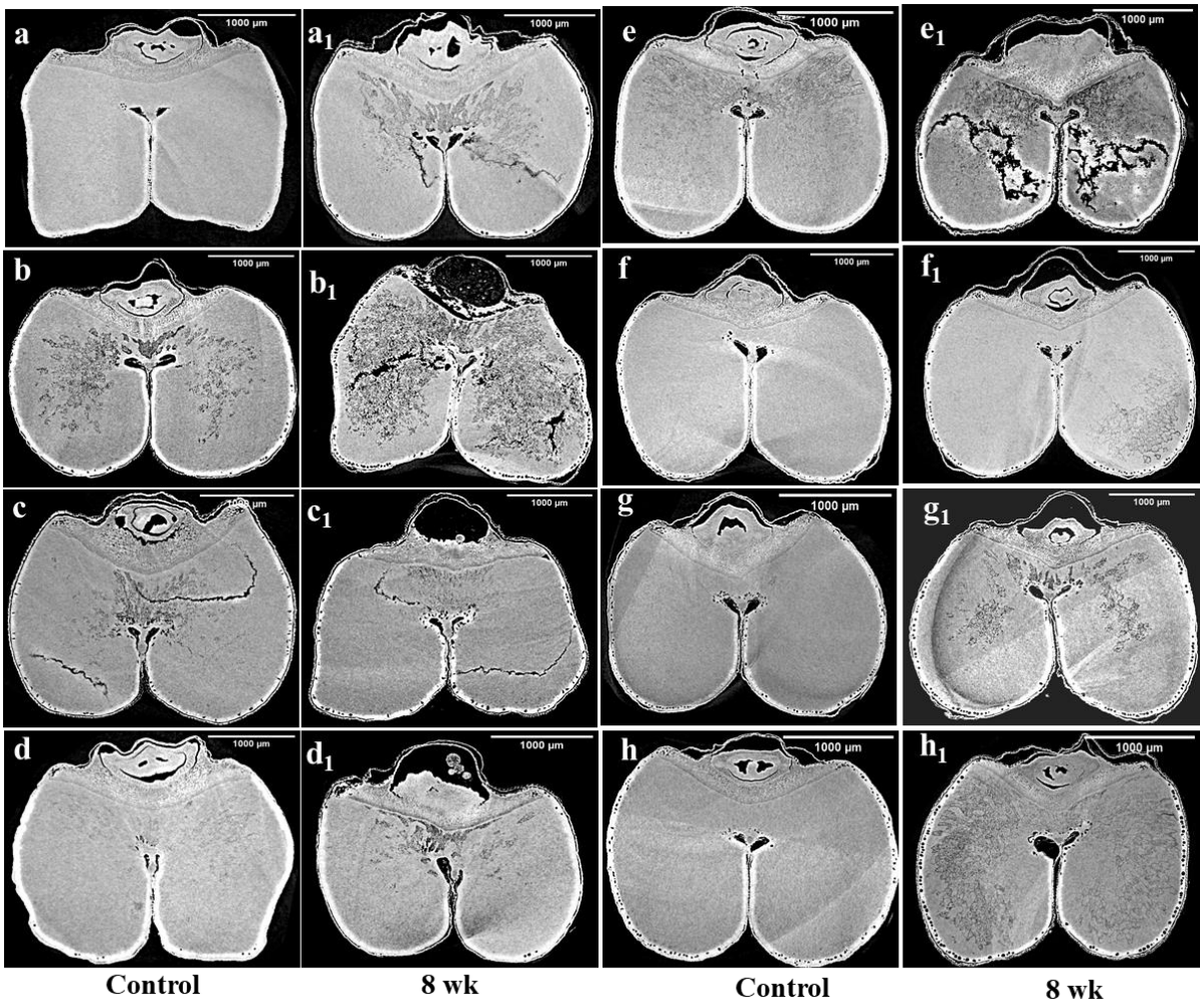

Figure 3.8. The reconstructed cross sections along minor axis (axis perpendicular to the longest dimension) of wheat classes control and 8 wk stored based on Synchrotron phase contrast microtomography (SR-µCT) [a: (CNHR) Prosper, b: (CPSR) AAC Penhold, c: (CWES) Burnside, d: (CWHWS) AC Snowstar, e: (CWRW) AAC Wildfire, f: (CWSP) Aldoren, g: (CWSWS) AC Andrew, h: (CPSW) AC Vista] . Full names of the wheat classes are given in Table 1

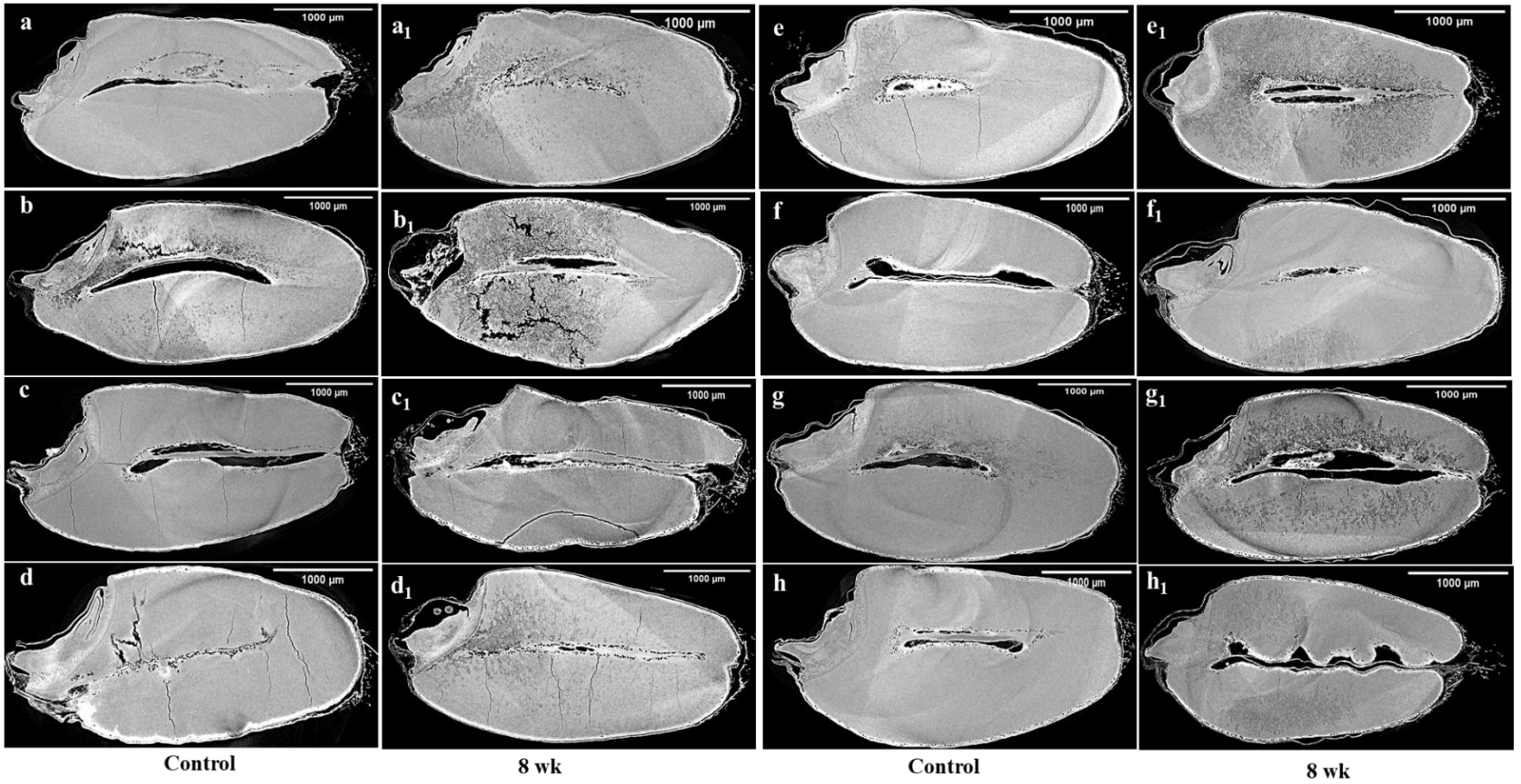

Figure 3.9. The reconstructed longitudinal sections of wheat classes control and 8 wk stored based on Synchrotron phase contrast microtomography (SR-µCT) [a: (CNHR) Prosper, b: (CPSR) AAC Penhold, c: (CWES) Burnside, d: (CWHWS) AC Snowstar, e: (CWRW) AAC Wildfire, f: (CWSP) Aldoren, g: (CWSWS) AC Andrew, h: (CPSW) AC Vista] . Full names of the wheat classes are given in Table 1

The quantification of microstructural properties like kernel air space, density are important, therefore, histograms for wheat classes were plotted (control vs 8 wk) and are presented in figure 4.

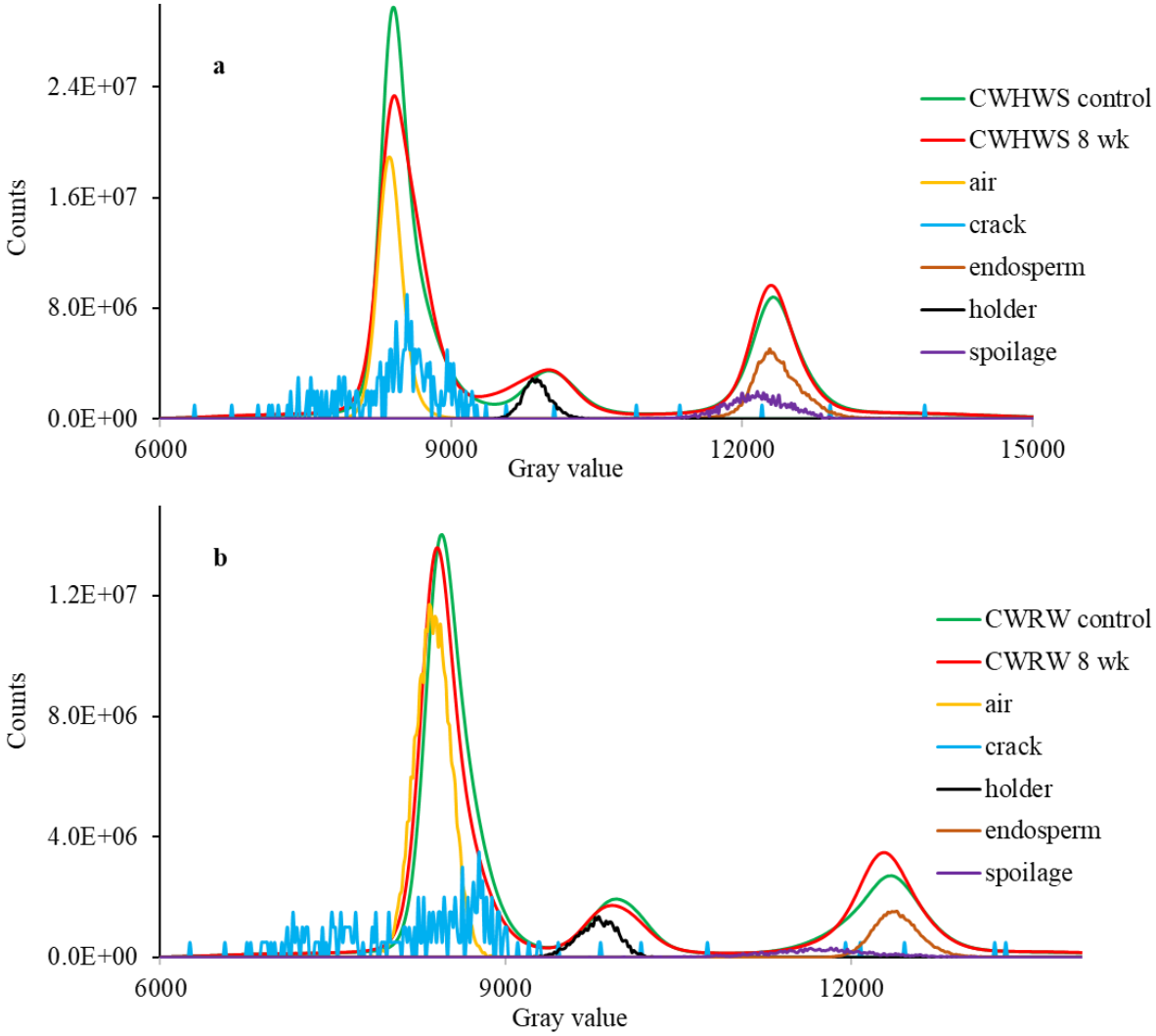

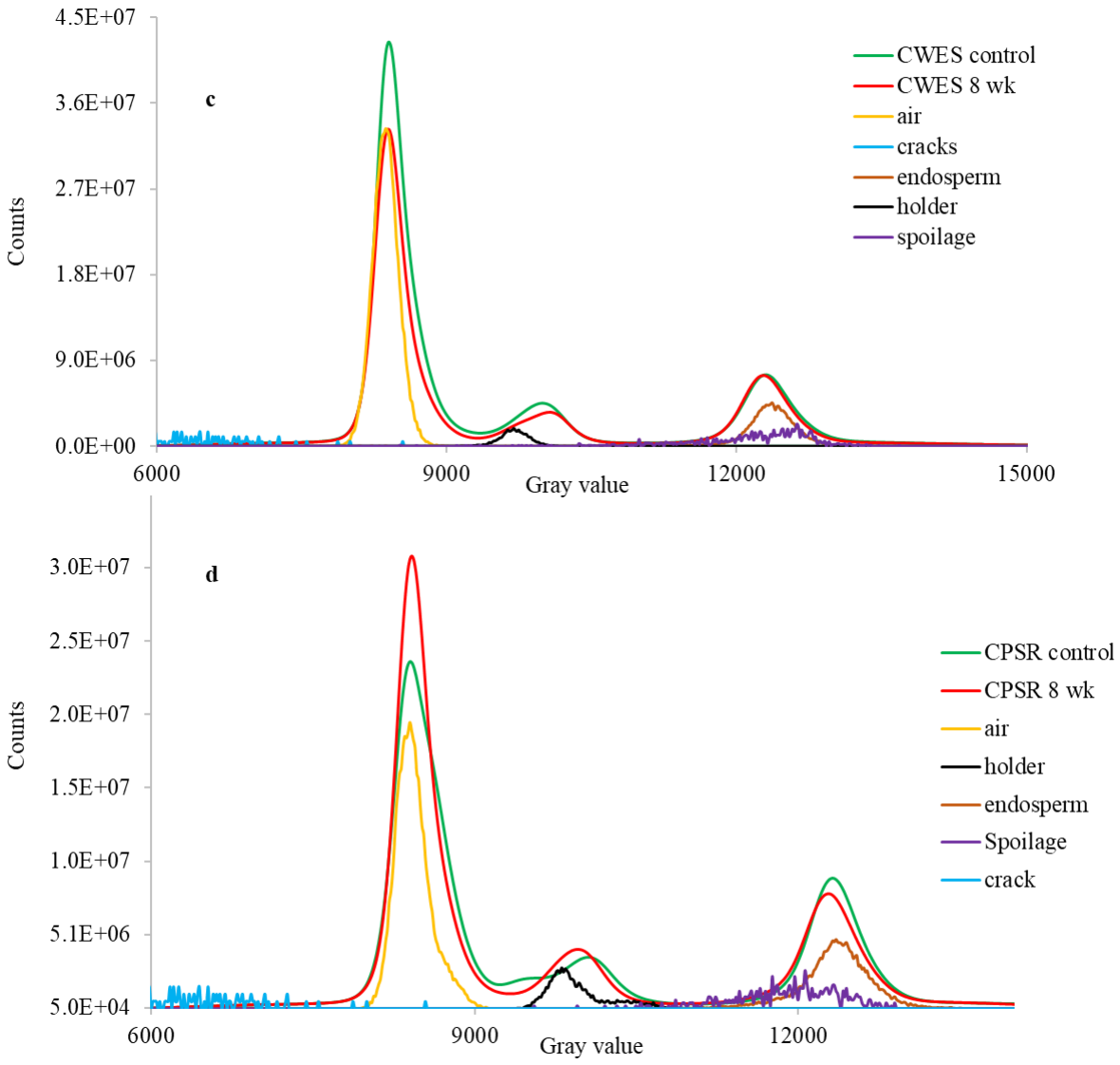
c
Counts
4.5E+07
3.6E+07
2.7E+07
1.8E+07
9.0E+06
0.0E+00
6000
9000
12000
15000
Gray value
CWES control
CWES 8 wk
air
cracks
endosperm
holder
spoilage
d
Counts
3.0E+07
2.5E+07
2.0E+07
1.5E+07
1.0E+07
5.1E+06
5.0E+04
6000
9000
12000
Gray value
CPSR control
CPSR 8 wk
air
holder
endosperm
Spoilage
crack

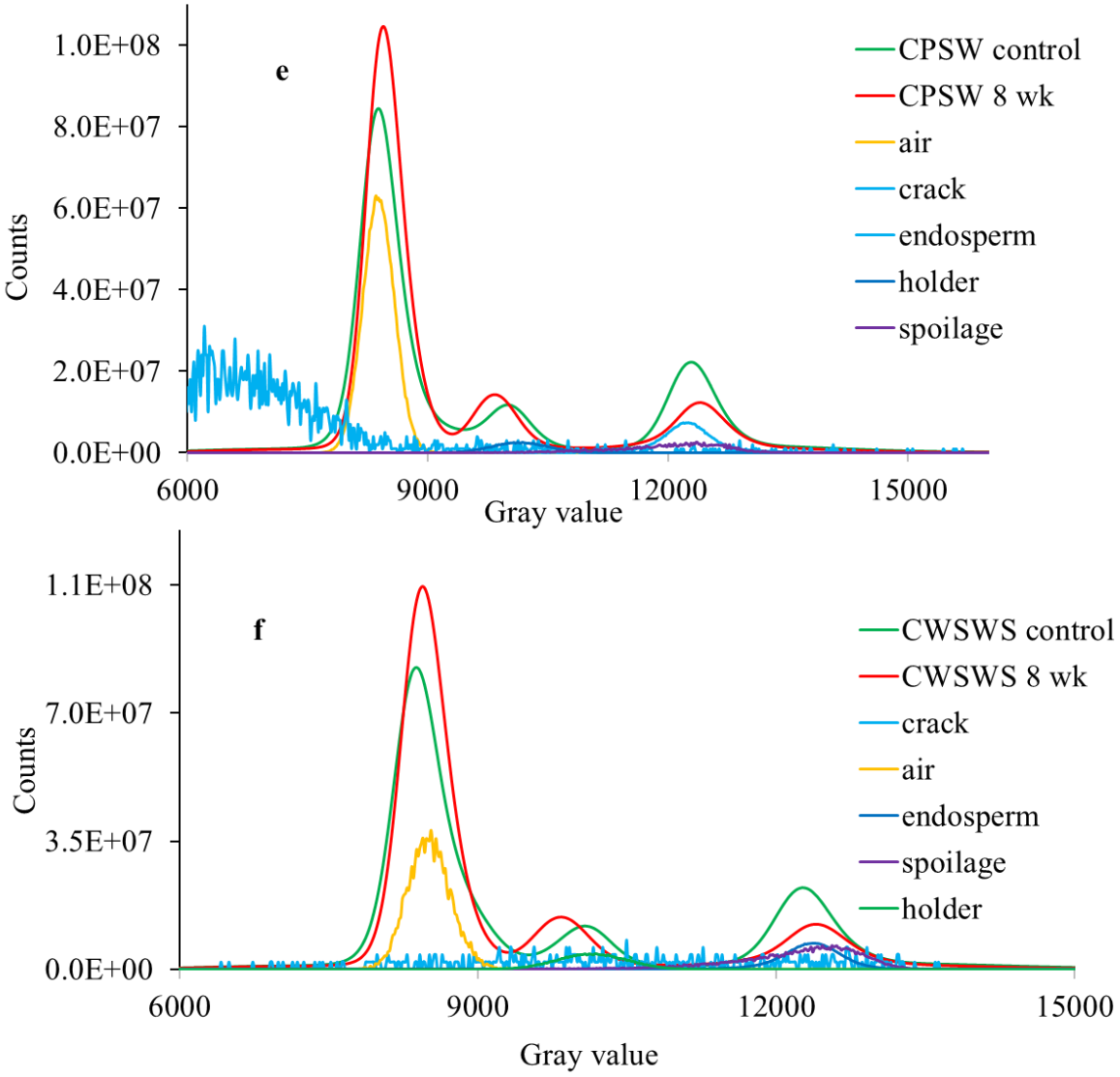
e
1.0E+08
8.0E+07
6.0E+07
4.0E+07
2.0E+07
0.0E+00
Counts
6000
9000
12000
15000
Gray value
CPSW control
CPSW 8 wk
air
crack
endosperm
holder
spoilage
f
1.1E+08
7.0E+07
3.5E+07
0.0E+00
Counts
6000
9000
12000
15000
Gray value
CWSWS control
CWSWS 8 wk
crack
air
endosperm
spoilage
holder

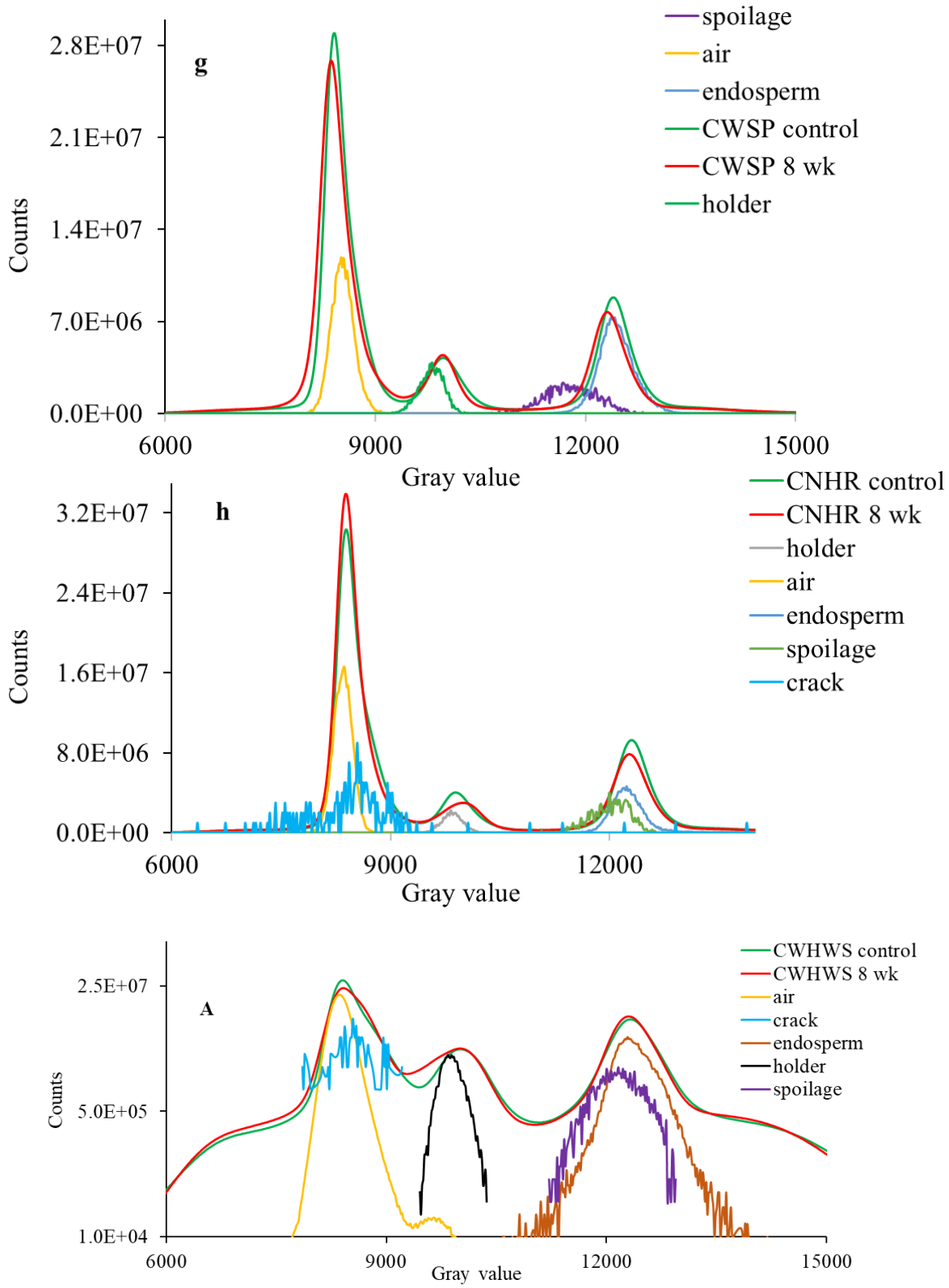

Figure 3.10. Histogram comparison of four wheat classes [top to bottom: CWHWS (a), CWRW (b), CWES (c), CPSR (d), CPSW (e), CWSWS (f), CWSP (g) and CNHR (h)] control and 8-wk stored. A refers to logarithmic scale histogram of CWHWS. Full names of the

wheat classes are given in Table 1. Microstructural features (cracks, spoilage, endosperm, air) and sample holder are deconvoluted in histogram for visualization under peaks. (n=10).

This comparison aimed to examine the shift in peaks and their corresponding positions within the histograms (figure 3.10). Histograms of four wheat classes were plotted and compared here as an example to check the effect of storage on the grain microstructure. In the histograms, the first peak corresponds to air around the wheat, the second peak corresponds to the sample holder and the third peak represent wheat kernel. The third peak in the histogram is an important part of our data analysis, where shift because of spoilage can be traced for comparison. The microstructural features of grain such as cracks, air, endosperm, change because of spoilage were deconvoluted and plotted in the same histogram. Deconvoluted data are helpful in locating their position under the peaks, which could help infer possible results from the peaks. The first two histograms of classes, CWHWS and CWRW, where the shift in peaks of 8-wk stored samples was observed, provides valuable insights into the changes that had occurred due to deterioration[27]. The peak is bent toward the left side in case of 8 wk stored samples along with spoilage peak underneath a reference figure 3.10 (a,b. The cracks were dominated across the analyzed wheat samples and mostly lied in the first peak and rest distributed in the kernel. Similar results were observed for CWES and CPSR class, where a larger shift was observed in the CPSR class in third peak of histogram as compared to CWES class figure 3.10 (c,d). The little change in a left hump of histogram in CWHWS was observed which represents the change in porosity of the kernel at the end of 8 wk storage figure 3.10 (A), where air and cracks deconvoluted peaks located. Counts were found lowered and shifting of peaks occurred in most of the 8 wk stored wheat classes expect CWHWS , CWRW , CWES as visible from the third peak of each histogram figure 3.10(a, b, and c). The observed shifts in peaks substantiated the findings derived from the comprehensive analysis and supported the conclusions drawn regarding the influence of storage on the microstructural changes in the wheat.

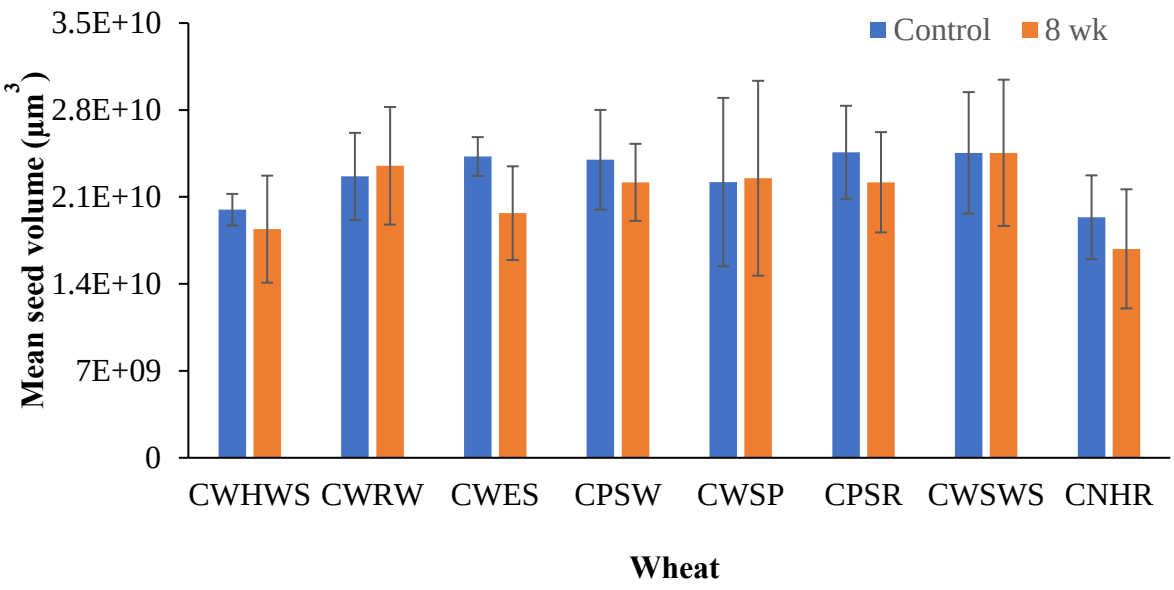

Figure 3.11. Measured mean seed volumes of control and 8-wk stored wheat, [Full names of the wheat classes are given in Table 1] (n=10)

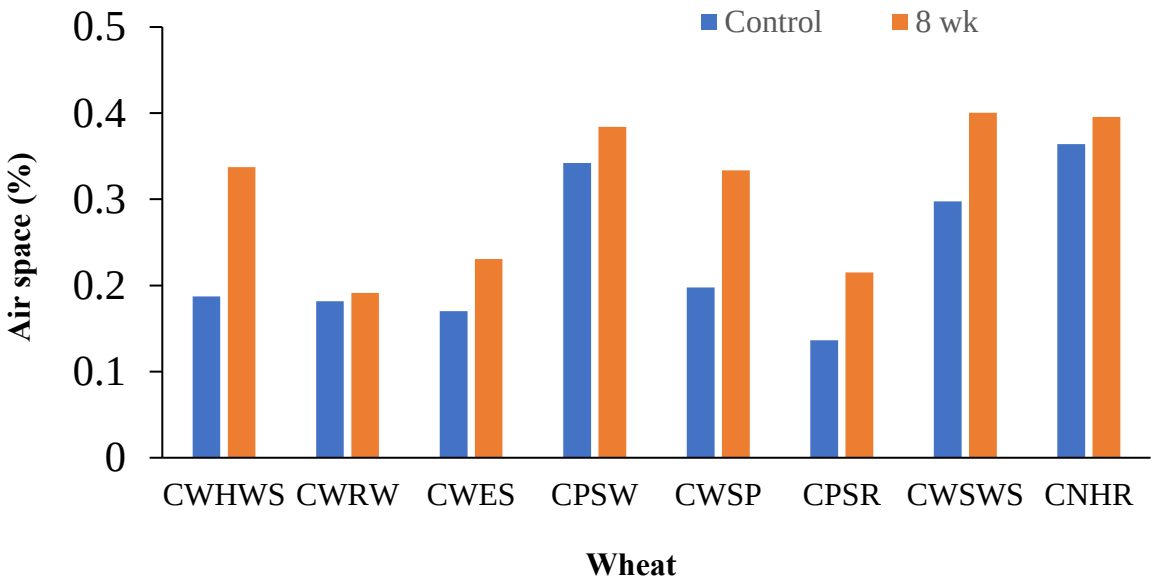

Figure 3.12. Average air space in kernels of control and 8-wk stored wheat, [Full names of the wheat classes are given in Table 1] (n=10)

The results of air space and seed volume measurement are presented in figures 3.11 and 3.12, respectively. The CNHR wheat class showed minimum seed volume and the CPSR class had maximum seed volume before storage (control samples). The change in seed volume was observed

in almost all the wheat classes at the end of 8 wk storage period. In selected wheat classes, seed volume decreased at the end of storage period except for classes CWRW and CWSP. This change in seed volume may be associated with the deterioration of wheat in storage similar to changes in microstructures observed in SR-μCT data. The CNHR wheat class showed maximum kernel air space and CPSR showed minimum air space in control. At the end of 8 wk storage, maximum air space was in classes CWSWS and CWES. But larger change observed in the kernel air space of CWHWS class was observed over control, whereas minimum was observed in CWRW class over control (figure 3.12). As earlier visualized from the SR-μCT data, the presence of cracks was contributing to kernel air space.

3.2.4.3 Mid-IR spectroscopy analysis

The results of the mid-IR spectroscopy analysis are shown in figures 3.13, 3.14, and 3.15. These figures illustrate the changes in protein, carbohydrates, and lipids in 8 wk stored wheat, as compared to their corresponding control samples. The analysis is based on the collected spectra, and the focus lies in evaluating alterations in these key biochemical components due to spoilage at the end of 8 wk of storage. The spectral region ranging from 1800 to 900 cm^{-1}, was used in analysis, as depicted in figure 3.13. This IR region is called the fingerprint region and its range definition can vary from between 1800 – 1500 cm^{-1} to 800-600 cm^{-1}. This region was selected due to its relevance, featuring absorption bands are dominated by contribution from protein, lipid, and carbohydrate content[28,29]. Lipids, proteins, and carbohydrates are marked by distinct absorption peaks at 1740 cm^{-1}, 1657 cm^{-1}, and 1158-1023 cm^{-1}, respectively[30]. These spectral analyses provide qualitative changes relative to each other in the key biochemical constituents over the 8-wk storage duration. The shifts in absorption bands can offer valuable insights into the alterations occurring in the wheat samples composition, thereby aiding in a comprehensive understanding of the effects of storage on their nutritional and biochemical characteristics.

The peaks at 1158, 1081, and 1024 cm^{-1} represents the carbohydrate region. The bands located at 1081 and 1024 cm^{-1} are attributable to starch components, while the band at 1150 cm^{-1} is linked to the stretching vibrations of single C-C, C-O-H, C-O-C bonds within carbohydrates[31]. The control samples exhibited a distinct amount for carbohydrates, which followed the order on basis of peak height (abundance to less): CWRW > CWSWS > CWSP > CPSW>CNHR>CWES>CPSR>CWHWS. However, in the case of 8-wk stored samples, a notable

decrease in absorption at 1080 cm^{-1} for carbohydrates was observed and order changed as (abundance to less): CWHWS >CPSR >CWSP>CWRW>CPSW>CNHR>CWES as shown in figure 3.13. This change in absorption indicated shifts in carbohydrate content due to spoilage after 8-wk storage. The spoiled cereals showed differences in some component (lignin, lipids and cellulose versus the remaining components) as reported in an earlier study[32]. The protein spectra occurs in the regions of 1600–1500 cm^{-1} and 1700–1600 cm^{-1} with amide I at 1650 cm^{-1} and amide II at 1540 cm^{-1} [30].

A distinct pattern emerged in terms of lipid absorption at 1740 cm^{-1} for wheat classes. The lipid peak at 1740 cm^{-1} corresponds to the ester C=O stretching in triglycerides and polyhydroxy aldehydes [33,34]. The shift in peaks and broadening was observed between control and 8 wk stored samples figure 3.13 (a: CNHR (1) vs 2: CPSR (2), b: CWES (3) vs CWHWS (4), and d: CWSWS (7) vs CPSW (8)). No peak shifts or less shifts were observed for classes CWRW and CWSP as shown in figure 7 (c). The lowest absorption (1740 cm^{-1}) for lipids was observed for 8-wk stored CWHWS and the highest absorption was in control CWHWS, which reflects how deterioration could have impacted on certain wheat classes Previous research findings[29,32] align with the present study's observation of shifts in peaks for key biochemical components (carbohydrates, protein, and lipids) in spoiled cereals. The classes CWSP and CWRW did not show variations in 8 wk stored and control samples (figure 3.13c). This peak position shifts during spoilage may arise from changes in metabolic activity, as well as variable defense mechanisms inherent to each wheat class [35]. In deterioration process, fungi can absorb and metabolize a diverse range of soluble carbohydrates, insoluble ones like starches, and cellulose[36]. It was also reported that fungal spoilage of cereals can degrade protein, and carbohydrates by 3-19 % and by 77%, respectively, of their original value[37].

The Principal Component Analysis (PCA) was conducted, and the outcomes were depicted in figures 3.14 and 3.15. The comparison between the principal components for control samples and principal components for 8 wk stored samples is shown in figure 3.15. Principal component analysis is a widely employed technique in IR spectroscopy to visualize the distribution of data points [32,35]. In this context, PCA serves as a valuable tool to find clustering first and then relate to the individual PC. A notable change was observed in spectra of individual PC of control and 8 wk stored in the carbohydrate (1200–900 cm^{-1}) and protein (1700–1500 cm^{-1}) regions as shown in

figure 3.14, it means biochemical changes have taken place due to spoilage in storage. The PCA revealed clusters in control and 8 wk stored wheat samples. In controls PCA, most of the samples were in clusters but placed close to each other, but in PCA of 8 wk stored samples, these clusters showed change in their position and placed little distance apart from each other. In 8 wk stored samples, some of the samples moved from positive region to negative region in the plot. These results are in line with previously reported findings in the context of cereal analysis[32,35].

The principal components of control wheat samples, PC1, PC2, PC3 and PC4 accounted for approximately 51%, 17%, 12% and 6% of the explained variance, respectively. Similarly, PC1, PC2, PC3 and PC4 were plotted for 8 wk stored samples with an explained variance of 45%, 25%, 12%, and 6% respectively. The scores of 8 wk stored wheat in negative region of the plot (Figure 3.15) were CNHR 8 wk, CPSW 8wk, CWSP 8 wk, CWRW 8 wk, CWSWS 8 wk, CPSW control, CPSR control, and CWHWS control. The scores of samples in positive region were CWHWS control, CNHR control, CWES control, CWRW control, CPSW control, and CWSP control. Only samples CWHWS, CWSWS and CPSR controls and 8 wk stored samples were found close to negative region of the plots. The PCA scores of stored samples were situated at the far right, these findings were in line with results of SR-µCT data, where large changes due to deterioration in seed microstructure were observed. By leveraging the observations derived from this study, PCA could prove to be a valuable technique for distinguishing and categorizing different types of spoilage, particularly those associated with fungal infection, based on mid-IR spectroscopy data.

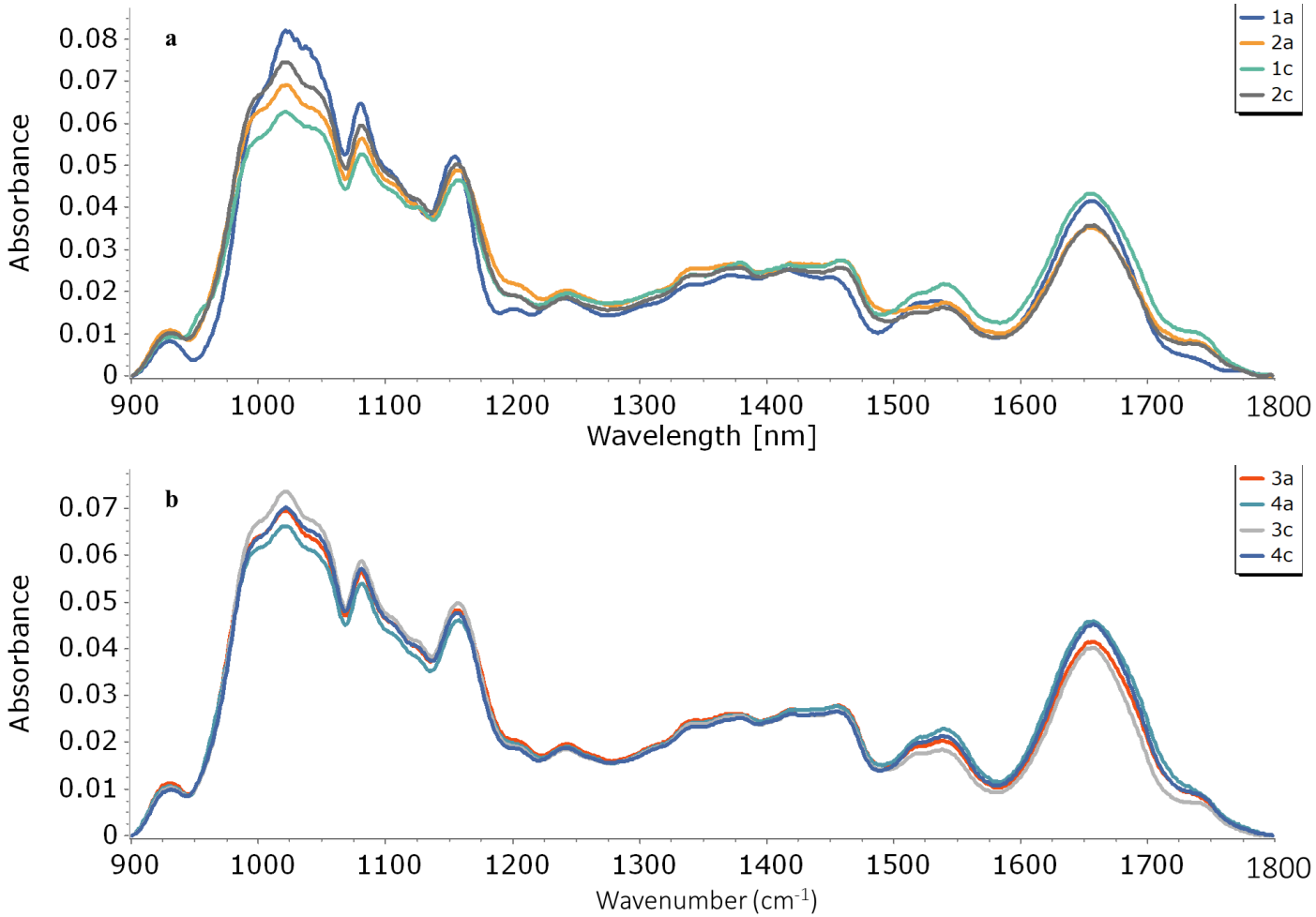
a
1a
2a
1c
2c
Absorbance
0.08
0.07
0.06
0.05
0.04
0.03
0.02
0.01
0
900
1000
1100
1200
1300
1400
1500
1600
1700
1800
Wavelength [nm]
b
3a
4a
3c
4c
Absorbance
0.07
0.06
0.05
0.04
0.03
0.02
0.01
0
900
1000
1100
1200
1300
1400
1500
1600
1700
1800
Wavenumber (cm-1)

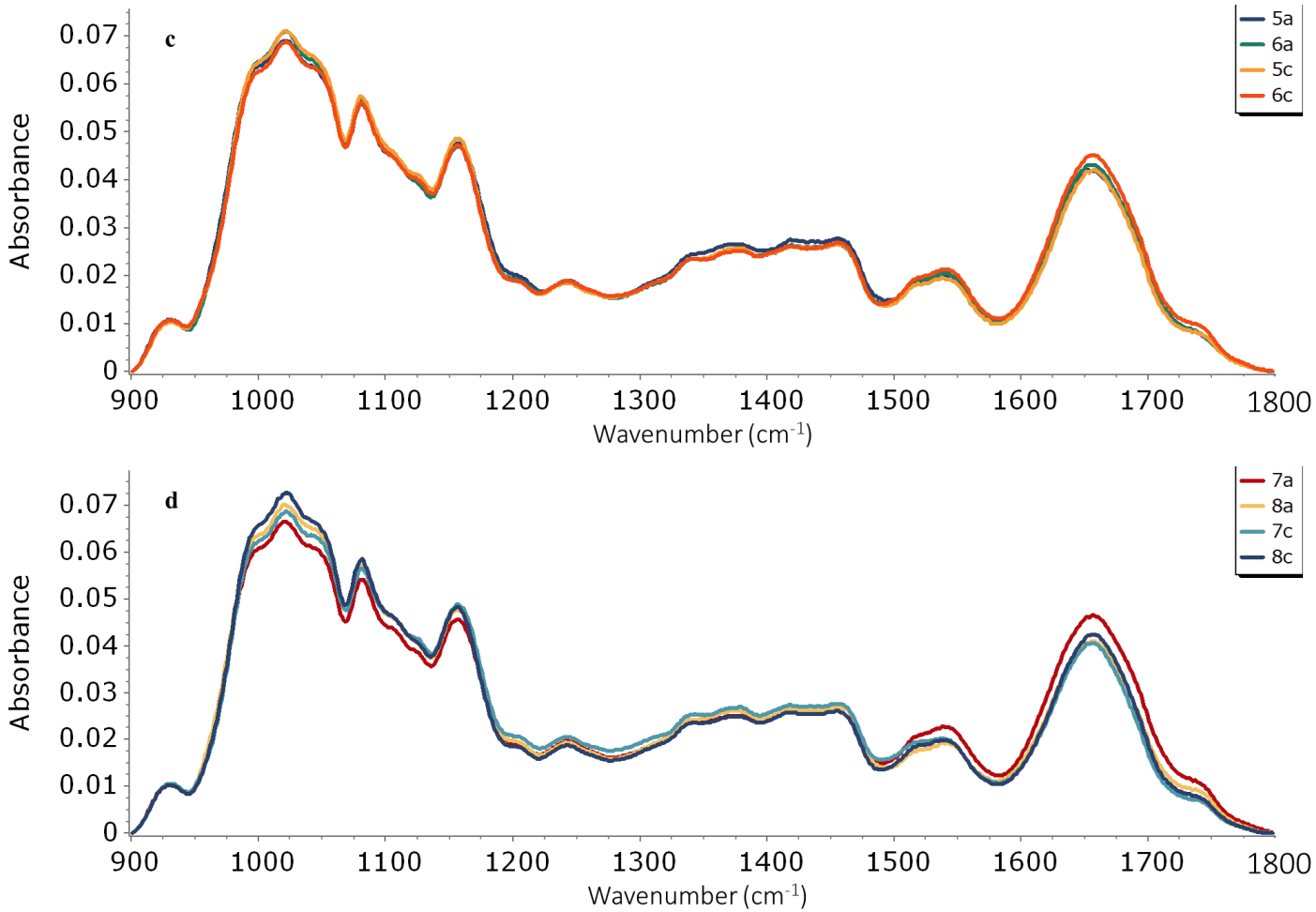

Figure 3.13 Normalized mid-IR spectra of wheat control (c) and 8 wk stored (a) [a: CNHR (1) vs 2: CPSR (2), b: CWES (3) vs CWHWS (4), c: CWRW (5) vs CWSP (6), d: CWSWS (7) vs CPSW (8)] Full names of the wheat classes are given in Table 1 (n=3)

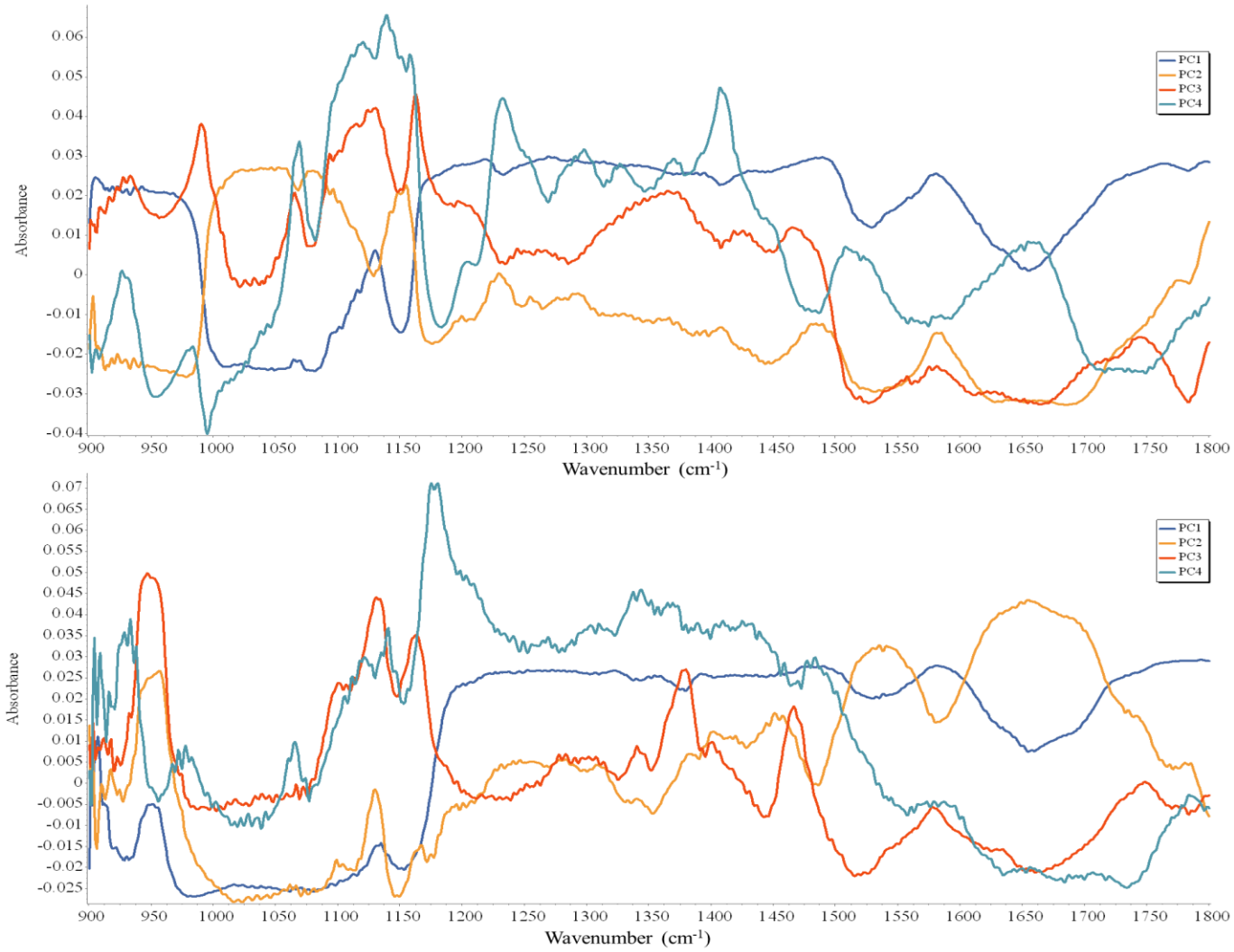

Figure 3.14. Comparisons of spectra data loading points of PC1, PC2, PC3 and PC4 for all wheat classes (top: control wheat and bottom: 8 wk stored wheat) (n=3)

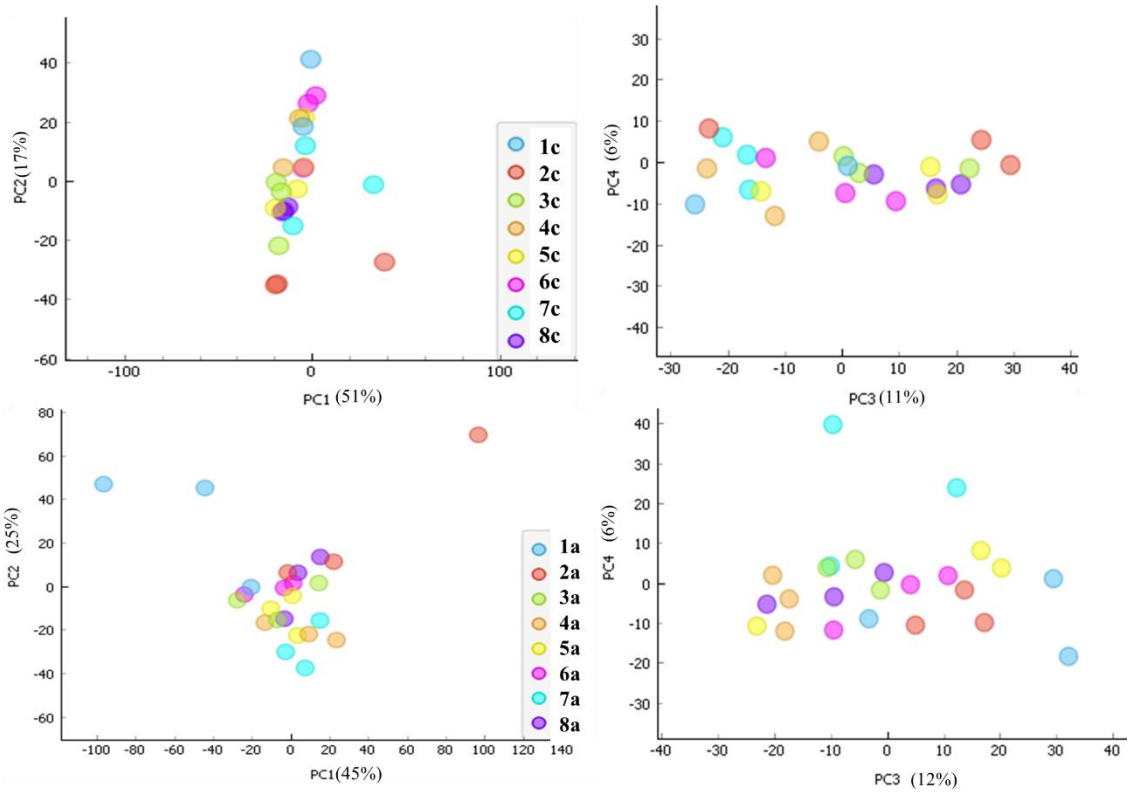

Figure 3.15 Principal component analysis top: (control, c), bottom: (8 wk, a) [1: CNHR, 2: CPSR, 3: CWES, 4: CWHWS, 5: CWRW, 6: CWSP, 7: CWSWS, 8: CPSW] (n=3). Full names of the wheat classes are given in Table 1

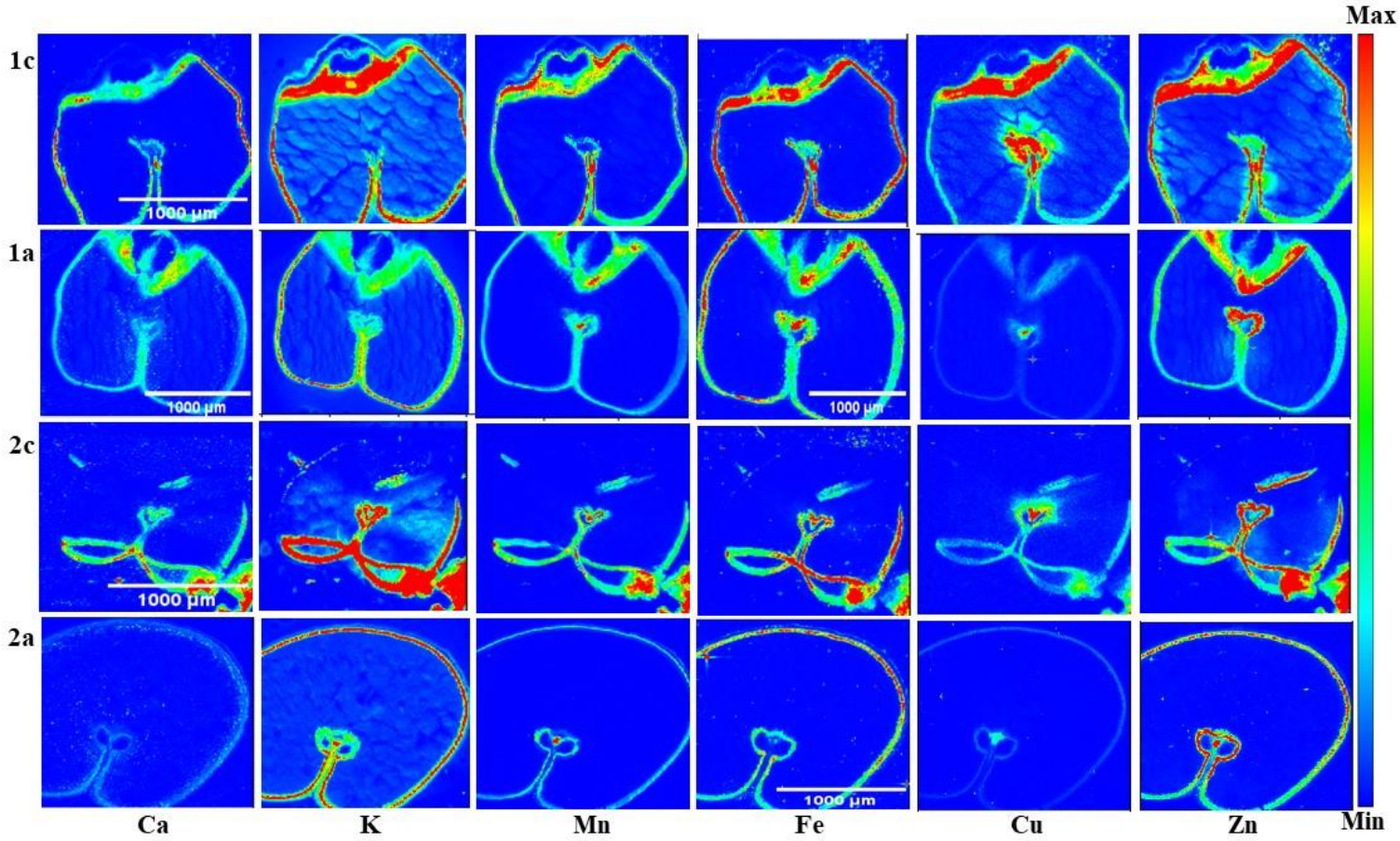

Figure 3.16. Nutrient distribution inside control (c) and 8 wk stored (a) wheat thin sections (1: CWHWS, 2: CWRW)

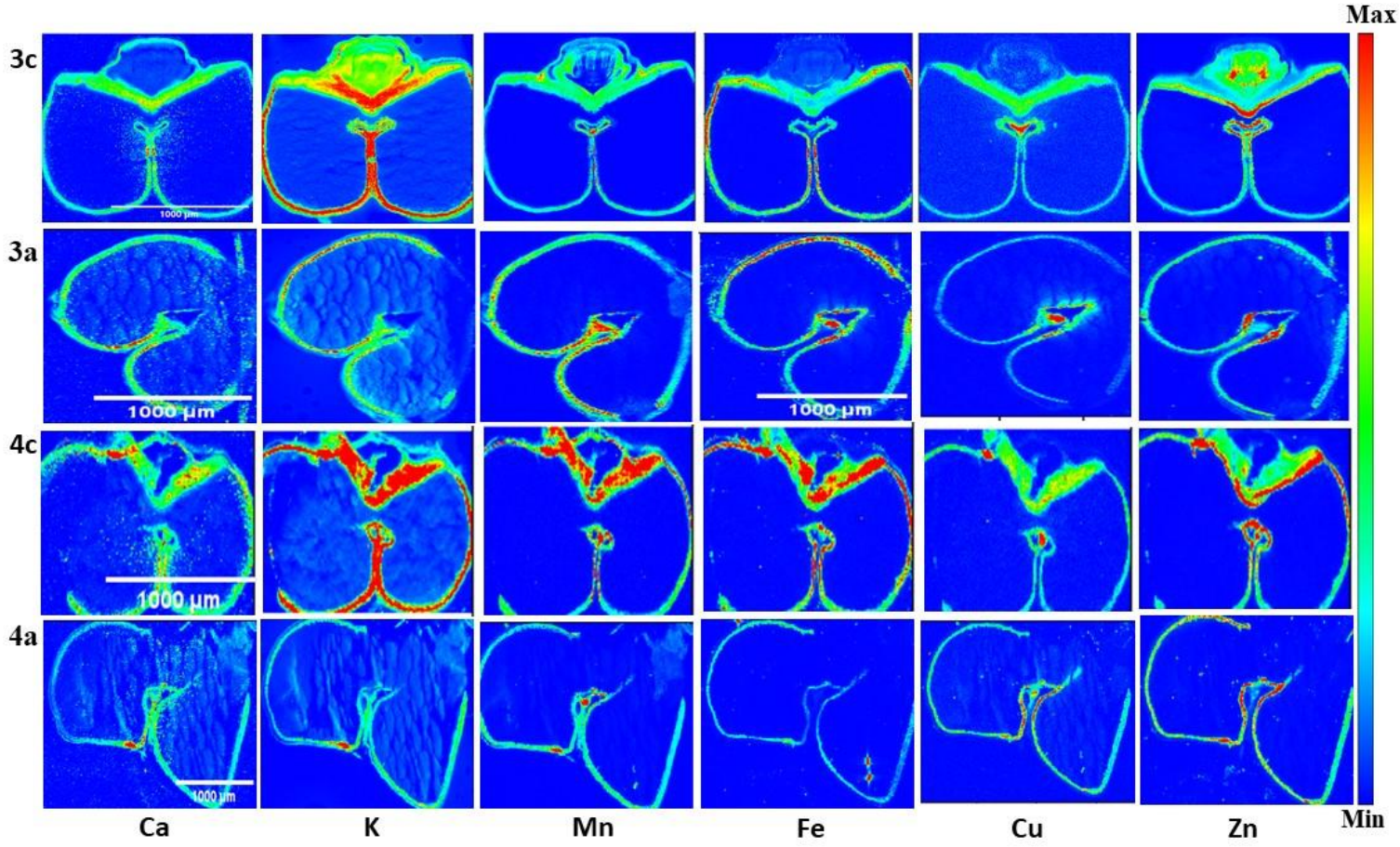

Figure 3.17. Nutrient distribution inside control (c) and 8 wk stored (a) wheat thin sections (3: CWSWS, 4: CWES)

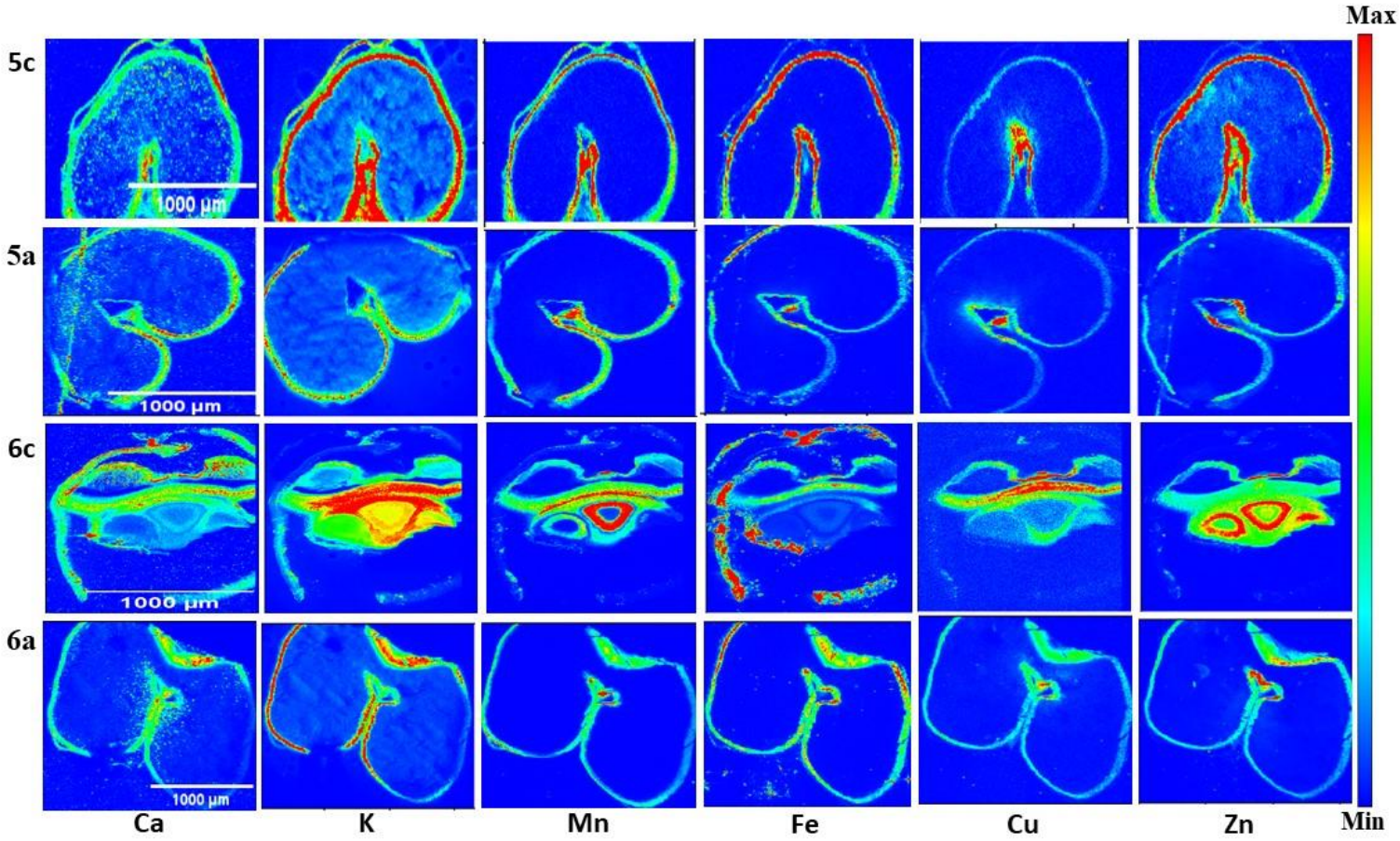

Figure 3.18. Nutrient distribution inside control (c) and 8 wk stored (a) wheat thin sections (5: CPSW, 6: CPSR)

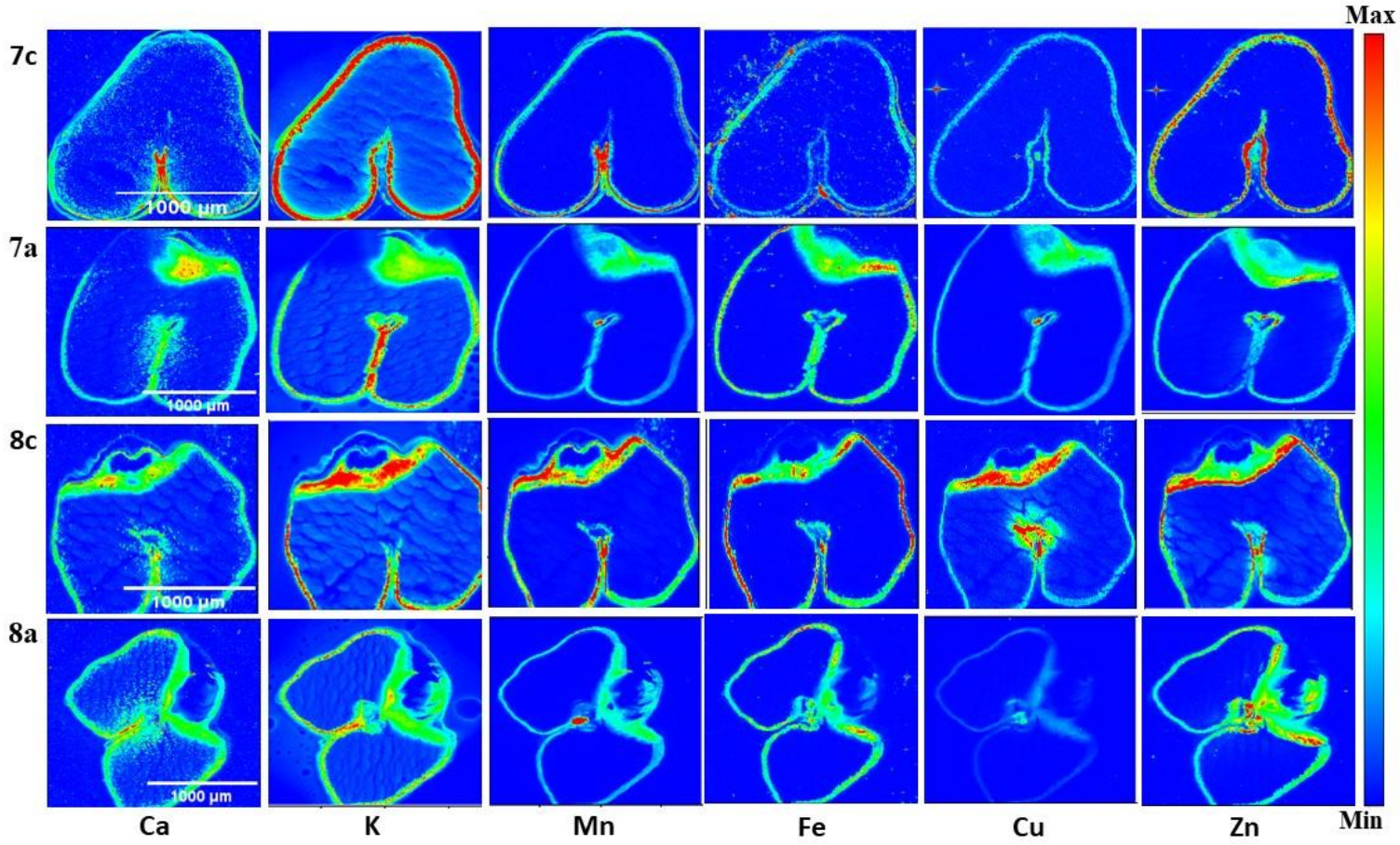

Figure 3.19. Nutrient distribution inside control (c) and 8 wk stored (a) wheat thin sections (7: CNHR, 8: CWSP)

3.2.4.4 XFI nutrient distribution analysis

The nutrient Ca was found in abundance and well distributed in almost all parts of selected wheat classes before storage except class CWRW (figure 3.16). The distribution of Ca was found less affected at the end of 8 wk storage and only little variations was observed in classes CWRW and CNHR (figure 3.17). The nutrient K was found very well distributed in all control samples of selected wheat. It was found concentrated in seed coat with higher intensity and across all the endosperm region (figure 3.16-3.19). Distribution of K was affected at the end of 8 wk storage in wheat classes (CWHWS, CWRW, CWES and CPSW) over control samples. The nutrient Mn distribution was found to be changed in (CWHWS, CWRW, CWES, CWSP, CPSR,) and found unchanged in CPSW and CWSWS over control samples. Nutrients Mn, Fe, and Zn are essential for plant and food crops for defense against pathogens, diseases, or deterioration[38]. The changes in distribution of these nutrients might be sign of fungal infection. In control samples, the nutrient Fe was found concentrated in seed coat (aleurone layer) in all selected wheat classes. The change in distribution of Fe in seed coat region was prominent in CWES, CPSW and CWSP classes at the end of 8 wk storage. The nutrient Zn is next essential element after Mn in plant immune system. The nutrient Cu was found in lower intensities in control samples, but its distribution was not affected after storage except in wheat class CWSP. The nutrient Zn was abundantly available in control samples of the selected wheat classes. The little variation was observed in 8 wk stored samples (CWSWS, CWSP, CWES) for nutrient Zn. The results of distribution of nutrients found in different wheat classes in our study are in line with earlier reported nutritional distribution for wheat[38–40], but the purpose of their study was to map nutrients. In this study novel use of SR-XFI was carried out first time to map changes in major Canadian wheat classes in storage due to spoilage. The nutrients which were in embryo and crease region had diminished intensities like K and Zn were lowered in 8 wk stored samples in comparison to the control. The intensity of nutrients in crease region found to be lowered in 8 wk stored samples, the one reason behind this might be as crease region was reported vulnerable earlier to diseases[26,41] The presence of nutrients essential for germination (Ca, Cu) and defense (Mn, Zn) decreased in CWES, CWHWS, CWSWS, and CPSR classes. The results obtained provide strong evidence that SR-XFI technique, when combined with the SR-μCT technique, can effectively characterize various wheat classes for post-harvest storage purpose.

3.2.5 Conclusion

Based on changes in microstructure of selected wheat classes characterization of wheat is possible. The wheat classes that could perform better in storage are: CNHR, CWRW, CWSP, and CPSW. Existing condition of kernel microstructure strongly influence the performance of wheat in storage which is major outcome of our work. Based on results of short-term storage study and acquired data, machine learning algorithm could be employed to predict and measured actual spoilage in wheat. The mid-IR analysis of wheat data showed the variation among the biochemical component and SR-XFI revealed nutrient distribution gradients before and after storage.

3.2.6 Acknowledgements

The authors acknowledge the Netaji Subhash Chandra fellowship from the Indian Council of Agriculture Research via grant no. ICAR/2019 for the first author and the Natural Sciences and Engineering Research Council of Canada for supporting the student research via grant no. RGPIN-2018-04420 to Dr Jayas. Part of the research described in this paper was performed at the Canadian Light Source, a national research facility of the University of Saskatchewan, which is supported by the Canada Foundation for Innovation (CFI), the Natural Sciences and Engineering Research Council (NSERC), the National Research Council (NRC), the Canadian Institutes of Health Research (CIHR), the Government of Saskatchewan, and the University of Saskatchewan.

3.2.7 Author contributions

DSJ conceptualized the study, is the corresponding author, received funding, and contributed through editing, examination, and finalization of the manuscript drafts. All authors have read and approved the final manuscript. NSI prepared an outline, the first draft, and the content of the whole paper based on the carried-out experiment. CK, MV, KT, JS, and VFB who are experts in synchrotron techniques at the Canadian light source provided technical inputs, and training, helped in data acquisition, and supported revision of the manuscript.

3.2.8 Data availability statement

High-resolution imaging data are available on request to the corresponding author.

3.2.9 References

1. LMC International. *The economic impact of canola on the Canadian economy: 2020 update insights for agribusiness specialist data and analysis for commercial decision-making*. libk. 1 https://cerealscanada.ca/wheat/ (2020).

2. CGC. Canadian wheat classes. https://www.grainscanada.gc.ca/en/grain-quality/grain-grading/wheat-classes.html (2019).

3. FAO. FAOSTAT. *Food and Agriculture Organization of the United Nations* 1–2 https://www.fao.org/faostat/en/#data/QCL (2023).

4. LMC International. The economic impact of canola on the Canadian economy: 2020 update insights for agribusiness specialist data and analysis for commercial decision-making. 1, 1–44 (2020).

5. Jayas, D. S. Storing Grains for Food Security and Sustainability. *Agric. Res.* 1, 21–24 (2012).

6. Nithya, U., Chelladurai, V., Jayas, D. S. & White, N. D. G. Safe storage guidelines for durum wheat. *J. Stored Prod. Res.* 47, 328–333 (2011).

7. Jayas, D. S., White, N. D. G. & Muir, W. . Stored-Grain Ecosystem. *Dry. Technol.* 13, 1045–1046 (1995).

8. F. Worku, A., K. Kalsa, K., Abera, M. & G. Nigus, H. Effects of storage strategies on physicochemical properties of stored wheat in Ethiopia. *AIMS Agric. Food* 4, 578–591 (2019).

9. Miś, A., Grundas, S. & Geodecki, M. Changes in hardness and thickness of wheat grain as a result of its moistening. *Int. Agrophysics* 14, 203–206 (2000).

10. Schmidt, M. *et al.* Impact of fungal contamination of wheat on grain quality criteria. *J. Cereal Sci.* 69, 95–103 (2016).

11. Schroth, E., Muir, W. E., Jayas, D. S., White, N. D. G. & Abramson, D. Storage limit of wheat at 17% moisture content. *Can. Agric. Eng.* 40, 201–205 (1998).

12. Wallace, H. A. H., Sholberg, P. L., Sinha, R. N. & Muir, W. E. Biological, physical and chemical changes in stored wheat. *Mycopathologia* 82, 65–76 (1983).

13. Yuan, Q.-S. *et al.* Variation in the Microbiome, Trichothecenes, and Aflatoxins in Stored

Wheat Grains in Wuhan, China. *Toxins (Basel).* 10, 171 (2018).

14. Zhang, S.-B. *et al.* Physiochemical changes in wheat of different hardnesses during storage. *J. Stored Prod. Res.* 72, 161–165 (2017).

15. Indore, N. S., Karunakaran, C. & Jayas, D. S. Synchrotron tomography applications in agriculture and food sciences research: a review. *Plant Methods* 18, 101 (2022).

16. Karunakaran, C., Jayas, D. & White, N. Soft X-ray image analysis to detect wheat kernels damaged by Plodia interpunctella (Lepidoptera: Pyralidae). *Sci. Aliments* 23, 623–631 (2003).

17. Olakanmi, S. J., Jayas, D. S. & Paliwal, J. Applications of imaging systems for the assessment of quality characteristics of bread and other baked goods: A review. *Comprehensive Reviews in Food Science and Food Safety* libk. 22 1817–1838 -(e)n https://doi.org/10.1111/1541-4337.13131 (2023(e)ko).

18. Navanth S. Indore, Chithra Karunakaran, Digvir S. Jayas, Jarvis Stobbs, Miranda Vu, Kaiyang Tu, O. M. Characterization of spring and durum wheat during storage using non-destructive synchrotron phase contrast X-ray microtomography for reduction of post harvest losses. *Univ. Manitoba, Winnipeg, Manitoba, Canada. 2023, status (manuscript Submitt.* (2023).

19. Joseph, S. Moisture Measurement — Unground Grain and Seeds. *ASABE Stand.* ASAE S352., (2017).

20. Navnath S. Indore, Chithra Karunakarana, Digvir S. Jayasa, Viorica F Bondicib, Miranda VuKaiyang Tu, D. M. Mapping biochemical and nutritional changes in durum wheat due to spoilage during storage. *Univ. Manitoba, Winnipeg, Manitoba, Canada. 2023, status (manuscript Submitt.* (2023).

21. Schindelin, J. *et al.* Fiji: An open-source platform for biological-image analysis. *Nature Methods* libk. 9 676–682 -(e)n https://doi.org/10.1038/nmeth.2019 (2012(e)ko).

22. Demšar, J. *et al.* Orange: Data mining toolbox in python. *J. Mach. Learn. Res.* 14, 2349–2353 (2013).

23. Cloetens, P., Mache, R., Schlenker, M. & Lerbs-Mache, S. Quantitative phase tomography of Arabidopsis seeds reveals intercellular void network. *Proc. Natl. Acad. Sci.* 103, 14626–14630 (2006).

24. Karunakaran, C. *et al.* Factors influencing real time internal structural visualization and dynamic process monitoring in plants using synchrotron-based phase contrast X-ray imaging. *Sci. Rep.* 5, 12119 (2015).

25. Cakmak, I. *et al.* Biofortification and localization of zinc in wheat grain. *J. Agric. Food Chem.* 58, 9092–9102 (2010).

26. Le, T. D. Q., Alvarado, C., Girousse, C., Legland, D. & Chateigner-Boutin, A.-L. Use of X-ray micro computed tomography imaging to analyze the morphology of wheat grain through its development. *Plant Methods* 15, 84 (2019).

27. Yashiro, W., Voegeli, W. & Kudo, H. Exploring Frontiers of 4D X-ray Tomography. *Appl. Sci.* 11, 8868 (2021).

28. Yu, P., McKinnon, J. J., Christensen, C. R. & Christensen, D. A. Using Synchrotron Transmission FTIR Microspectroscopy as a Rapid, Direct, and Nondestructive Analytical Technique to Reveal Molecular Microstructural-Chemical Features within Tissue in Grain Barley. *J. Agric. Food Chem.* 52, (2004).

29. Singh, C. B., Jayas, D. S., Paliwal, J. & White, N. D. G. Fungal Damage Detection in Wheat Using Short-Wave Near-Infrared Hyperspectral and Digital Colour Imaging. *Int. J. Food Prop.* 15, 11–24 (2012).

30. Saxton, R. & McDougal, O. M. Whey Protein Powder Analysis by Mid-Infrared Spectroscopy. *Foods* 10, 1033 (2021).

31. Karunakaran, C. *et al.* High throughput nutritional profiling of pea seeds using Fourier transform mid-infrared spectroscopy. *Food Chem.* 309, 125585 (2020).

32. Singh, C. B., Jayas, D. S., Borondics, F. & White, N. D. G. Synchrotron based infrared imaging study of compositional changes in stored wheat due to infection with Aspergillus glaucus. *J. Stored Prod. Res.* 47, 372–377 (2011).

33. Kaya-Celiker, H., Mallikarjunan, P. K. & Kaaya, A. Mid-infrared spectroscopy for discrimination and classification of Aspergillus spp. contamination in peanuts. *Food Control* 52, 103–111 (2015).

34. Grube, M., Bekers, M., Upite, D. & Kaminska, E. Infrared spectra of some fructans. *Spectrosc. An Int. J.* 16, 289–296 (2002).

35. Lahlali, R. *et al.* Synchrotron based phase contrast X-ray imaging combined with FTIR spectroscopy reveals structural and biomolecular differences in spikelets play a significant role in resistance to Fusarium in wheat. *BMC Plant Biol.* 15, 24 (2015).

36. David moore. Nutrition. *Brittanica* 1–5 https://www.britannica.com/science/fungus/Form-and-function-of-fungi (2022(e)ko).

37. Rosentrater, K. A. Biochemical, functional, and nutritive changes during storage. in *Storage of Cereal Grains and their Products* 443–501 (2022). doi:10.1016/B978-0-12-812758-2.00010-6.

38. De Brier, N. *et al.* Element distribution and iron speciation in mature wheat grains (Triticum aestivum L.) using synchrotron X-ray fluorescence microscopy mapping and X-ray absorption near-edge structure (XANES) imaging. *Plant. Cell Environ.* 39, 1835–1847 (2016).

39. Lombi, E., Scheckel, K. G. & Kempson, I. M. In situ analysis of metal(loid)s in plants: State of the art and artefacts. *Environ. Exp. Bot.* 72, 3–17 (2011).

40. Singh, C. B., Jayas, D. S., Paliwal, J. & White, N. D. G. Fungal detection in wheat using near-infrared hyperspectral imaging. *Trans. ASABE* 50, 2171–2176 (2007).

41. Strange, H., Zwiggelaar, R., Sturrock, C., Mooney, S. J. & Doonan, J. H. Automatic estimation of wheat grain morphometry from computed tomography data. *Funct. Plant Biol.* 42, 452–459 (2015).

3.3 Conclusions Chapters 3

Significant microstructural changes were observed in durum wheat (AAC Spitfire) and spring wheat (AAC Brandon) during the 5-wk storage period. Interestingly, spring wheat exhibited better performance during this storage duration. No discernible variations in microstructure were observed in the frozen samples after 5 wk, indicating that changes during freeze storage do not occur in grains without free moisture. At high moisture (>23% wb for wheat) some water exits as free moisture and due to formation of ice crystals internal microstructure may change. This implies that low to medium moisture samples can be frozen for analysis in the future when beamtime at a synchrotron facility is allocated.

Among the selected classes of wheat, the CWES (Canada Western Extra Strong) Burnside variety demonstrated the best storage performance. Minimal changes in microstructure were observed in CWES, Canada Prairie Spring White (CPSW), Canada Western Hard White Spring (CWHWS), and Canada Western Special Purpose (CWSP) at the end of the 8-wk storage period. Shifts in the peaks of histograms in X-ray images were noted, indicative of changes in microstructure during storage. Structural integrity plays a crucial role, as compromised grains are susceptible to spoilage under unfavorable conditions. Additionally, crease features were identified as influencing the storage performance of wheat classes which showed maximum changes in microstructure**.**

Chapter 4. NUTRITIONAL CHANGES IN WHEAT DUE TO SPOILAGE IN STORAGE

4.1 Mapping biochemical and nutritional changes in durum wheat due to spoilage during storage (Published in Helyion, November 2023)

Navnath S Indore[a], Chithra Karunakaran[a,b], Digvir S. Jayas[a,c*], Viorica F Bondici[b], Miranda Vu[b], Kaiyang Tu[b] , David Muir[b]

[a] Biosystems Engineering, University of Manitoba, Winnipeg, MB R3T 5V6, Canada

[b] Canadian Light Source Inc., Saskatoon, SK S7N 2V3, Canada

[c] President's Office, A762 University Hall, University of Lethbridge, Lethbridge, AB T1K 3M4 Canada

*Corresponding author's email: digvir.jayas@umanitoba.ca

4.1.1 Abstract

Synchrotron X-ray imaging and spectroscopy techniques were used for studying changes during post-harvest storage of food grains. Three varieties (AAC Spitfire, CDC Defy, and AAC Stronghold) of the Canada Western Amber Durum (CWAD) wheat class were stored for five weeks at 17% moisture content (wb). Control (dry) and stored moistened seeds were analyzed for biochemical and nutritional changes using synchrotron bulk X-ray fluorescence spectroscopy (SR-XRF), X-ray fluorescence imaging (SR-XFI), and mid-infrared (mid-IR) spectroscopy at the Canadian Light Source (CLS), Saskatoon, SK. All varieties of durum wheat were spoiled at the end of five week, and AAC Spitfire and CDC Defy varieties were most affected in nutritional composition and their distribution than AAC Stronghold. Variable response to changes in biochemical and nutrition were found in all three spoiled varieties of the same durum wheat class.

Keywords: Synchrotron, durum wheat, X-ray fluorescence spectroscopy, X-ray fluorescence imaging, mid-infrared spectroscopy, post-harvest storage

4.1.2 Introduction

Durum wheat is the 10th most important cereal cultivated worldwide [1] with an annual production of average of 40 million tonnes (Mt). Durum wheat is an important cereal crop of

Canada because Canada leads the export of durum wheat in the world. The total economic impact on Canadian economy from durum wheat sector was 7.5 billion CAD per year during 2018-20 [2]. Canada produced around 6.11 Mt of durum wheat and exported around 2.71 Mt in 2022 [3]. There is a demand for good quality durum wheat, and Canada shares 50% of the world's export of durum wheat [4]. Canadian durum wheat is bright yellow in color with high protein content and semolina yield, making it an excellent choice for making high-quality food products. Durum wheat is a cereal crop and cereal food grains face many challenges during bulk storage. Cereal grains are stored at many points along the food chain for a short or long time before consumption, where sound grain storage management plays an important role in keeping post-harvest losses to a minimum. The post-harvest losses in cereals range from 1% in well managed systems to 50% in poorly managed systems [5]. Sometimes, in a single unit of storage, total grain can be spoiled, making it unsuitable for human consumption, thus resulting in 100% loss [5]. The high moisture content leads to the growth of fungi on food grains under favourable temperatures. It is necessary to study changes in the quality of wheat during storage; therefore many studies had been conducted to develop better post-harvest guidelines [4,6–11]. Food grains have unique internal features, structures, and compositions that differentiate them from each other in classes and varieties. Therefore, the use of non-destructive methods such as X-ray imaging for the study of changes in storage has taken place in the last two decades. The conventional X-ray imaging system for wheat [12–16] was used to determine various structural features for seed characterisation. The wheat seed crease depth and morphology of two wheat lines were compared to reveal diseases such as black spots that infect particularly at the crease [17]. These conventional systems have certain limitations such as low resolution, more scanning time, and non-selective wavelength. Therefore, synchrotron X-ray imaging techniques have gained pace in the last two decades and are used by researchers across the globe.

Soft wheat cultivars have better post-harvest storage tolerance than harder cultivars [18] and durum wheat is hard wheat, hence it has poor storability than other non-durum wheat [4]. The wheat structure and nutritional composition might play an important role in the resistance to deterioration. However, knowledge about changes in nutrients or study on effect of storage on nutrient presence using advanced imaging is limited. Wheat has micro-nutrients: Mn, Fe, Cu, and Zn; and macro-nutrients: Na, Mg, K and Ca [19]. Micro- and macro-nutrients may play a role in fungal pathogen defense for plants or wheat seeds. The roles of micronutrients in plant defense have been documented for Mn, Fe, Cu, and Zn [20–22]. Synchrotron X-ray fluorescence imaging and spectroscopy are widely used in agricultural and medical sciences and have potential for determining nutritional components in seeds. The changes in nutrient presence and mapping using synchrotron X-ray based fluorescence imaging in wheat crops were reported during crop growth stages, and effect of various fertilizer treatments but not visualized in post harvest storage studies. It has been used in pea seeds [23] for bulk nutritional analysis, whole wheat sections [24], and in cereals [24–27].

Wheat has about 78% carbohydrates, 14% protein, 2% lipids, and 2.5% minerals [28] and durum wheat is generally characterized by its high amounts of protein (14.3-15.1%) [29,30]. Fungal infection of wheat seeds can cause significant changes in the biochemical components [31]. The storage protein of wheat has immense importance in determining the quality and end-use properties of the grain, which means it has some role to play during safe storage [32]. Mid-IR spectroscopy was used along with synchrotron imaging techniques for the identification of *Fusarium* resistant wheat variety [33], high nutritional value pea seeds [34], changes in stored wheat due to fungal damage [35], and synchrotron infrared microscopy was also used for analyses of animal feed quality [36]. Therefore, this study was conducted to characterize the durum wheat varieties based on nutritional and biochemical changes in storage due to spoilage. Our study hypothesizes that, spoilage in storage can have an impact on nutritional and

biochemical composition of durum wheat, and each variety under the durum wheat class can behave differently. The generated data for durum wheat can be beneficial for making storage decisions and for the food processing industry. Information about the changes in nutrition using advanced imaging, like synchrotron imaging, is limited in post harvest storage studies of cereals; therefore, this work was undertaken to understand the behaviour of nutritional changes due to spoilage in durum wheat during bulk storage. The objectives of this study were to 1) determine nutrient composition using synchrotron X-ray fluorescence spectroscopy (SR-XRF) and localization using synchrotron X-ray fluorescence imaging (SR-XFI) and 2) determine the biochemical composition by mid-infrared (mid-IR) spectroscopy. The developed methodology of this study can be used for assessing changes in other Canadian wheat classes during storage.

4.1.3 Materials and Methods

4.1.3.1 Wheat

In this study, we procured and used commercially available certified seeds of Canada Western Amber Durum wheat (varieties: CDC Defy, AAC Stronghold, and AAC Spitfire) from a company (SeCan, Niverville, MB).

4.1.3.2 Storage experiment

Five-hundred-gram samples of each variety were conditioned to a moisture content (mc) of 17% (wb) using distilled water in triplicates and then stored in airtight glass jars (volume 1 L) and these procedures were repeated every week for up to five week. Then, glass jars were stored at ambient conditions where storage temperatures were in the range of 22-25ºC. The mc was determined 24 h after conditioning by oven drying of 10 g samples at 130°C for 19 h and the samples were reconditioned, if necessary, to maintain mc at 17±0.5% [37].

4.1.3.3 Bulk X-ray fluorescence spectroscopy

4.1.3.3.1 Sample preparation

Technical replicates were employed during the preparation of samples for bulk X-ray fluorescence (XRF) analyses. The samples were pulled from the three jars for grinding as a whole and three pellets were made as technical replicates. The purpose of using technical replicates was to ensure the reliability and reproducibility of the experimental results by accounting for any variability that might arise during the sample preparation process. The sample was first ground to fine powders using a cryo grinder (GENCO Spex 2010, Metuchen, NJ USA) using liquid nitrogen. Three circular pellets were prepared using a 13-mm diameter stainless steel die in a hydraulic press (PIKE Technologies, Madison, WI, USA) at three pressures (53.93, 34.32, and 14.70 kPa) with a holding of time 3 s for each pressure. The use of pressed pellets gives more accurate results compared to packed powder samples [38]. Ninety-seven milligrams of wheat flour were pressed into pellets of an approximate thickness of 0.2 mm and diameter of 13 mm (Fig. 4.1). The used die was wiped using ethanol after each sample and pellets were stored in the dark in a vacuum desiccator until further use [23].

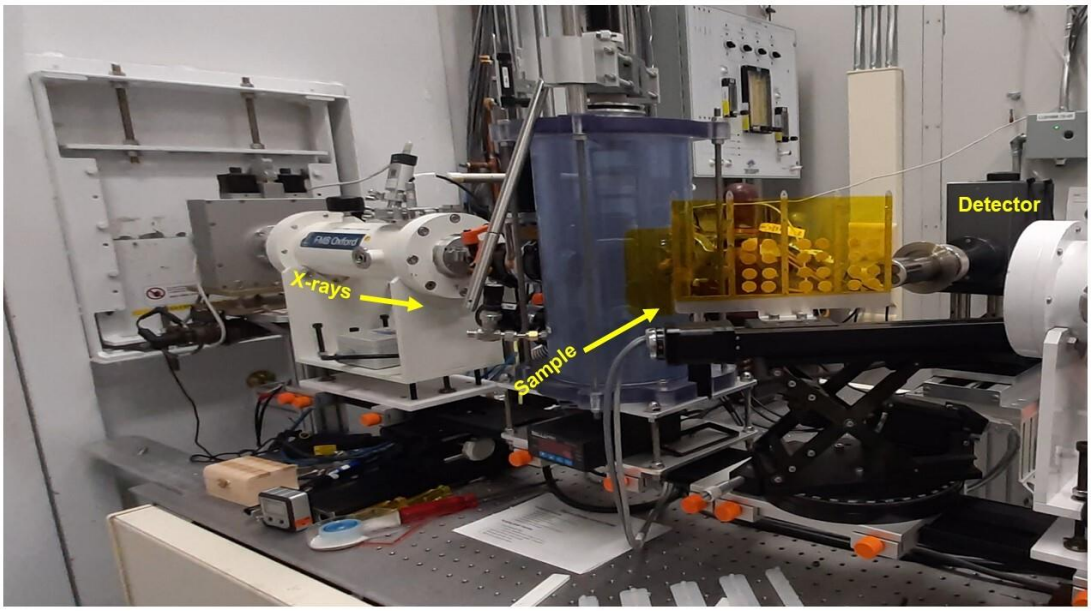

Figure 4.1 The layout of the IDEAS-XRF beamline during data acquisition of Canadian Light Source, Saskatoon

4.1.3.3.2 Data acquisition and analysis

Data acquisition was carried out at the Industry Development Education Applications Students (IDEAS), which is a bending magnet beamline at the Canadian Light Source (CLS) (Figure 1). Incident X-ray of energy of 13.6 keV was used in scanning of sample pellets and scanning was performed as per the procedure established [23]. The sample stage was placed between the source and detector at an angle of 45° and the detector distance from the sample was set to 11 mm. A beam size of 5 mm width and 2 mm height was used for sample scanning. Total of twenty-four sample pellets were mounted on the sample stage using Kapton tape. Three spectra were collected per pellet and each spectrum was completed in 85 s. Data acquisition was carried out using an in-house developed Aquaman software and then further data processing was done using PyMca (5.6.7) software [39]. The configuration and a calibration fit were developed using one representative sample spectrum and the rest of the sample analysis was completed using the batch fitting routine. The statistical analysis (one way ANOVA) was done to check significant differences in fluorescence count of nutrients (Fe, K, Zn, Ca and Mn) in the samples

stored for 1 week, 3 week, 5 week, and control in MS-Excel 2008 and results are discussed in the discussion section.

4.1.3.4 X-ray fluorescence imaging

4.1.3.4.1 Sample preparation

Seeds were embedded in a Leica Cryogel using liquid nitrogen. The seeds were thin-sectioned to 80 µm thickness as per the described procedure [40] using a Leica CM1950 cryostat microtome (Leica Biosystems Inc., Richmond Hill, ON). Thin sections of samples reduce the distortion of the elemental maps caused by the penetrating nature of the X-rays [41]. Multiple sample sections on Kapton tape were placed on the sample holder of the BioXAS-Imaging beamline at the CLS (Fig. 4.2). The microscopic images were collected using digital microscope (Motic DM143, Motic, Kowloon, Hong Kong) before SR-XFI imaging of samples.

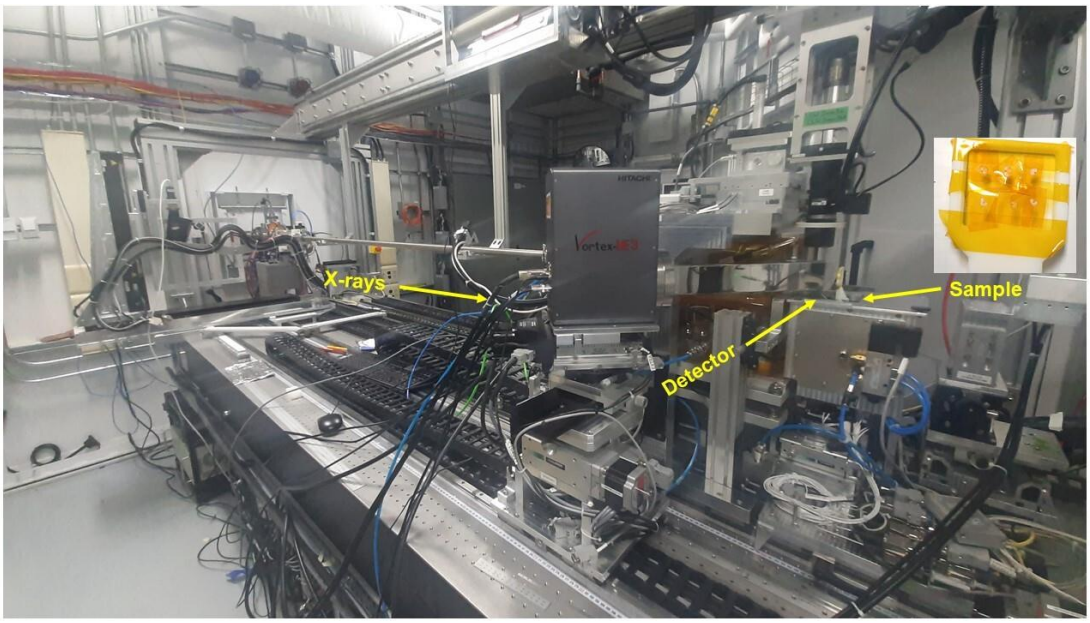

Figure 4.2 BioXAS-imaging beamline and sample setup of Canadian Light Source, Saskatoon.

4.1.3.4.2 Data acquisition and analysis

The X-ray fluorescence imaging data were collected using the BioXAS-Imaging beamline at the CLS. The in-vacuum undulator of the beamline provides a high spectral brightness source for X-rays. In this study, the incident beam energy was set to 15 keV. The focused beam spot size was 5 µm x 5 µm. Data were collected in continuous bi-directional fly-scanning mode with a step size of 5 µm and 100 ms dwell time. Each seed section took about 8 h to scan. The Vortex-ME3 silicon drift X-ray detector (Hitachi High Technologies Science American, Inc. Chatsworth, CA) was at 45° and the samples were in a 90-degree stage configuration to the incident beam. The detector to the sample distance was set to 3.5 cm. Data acquisition was carried out using PyAcq data acquisition software. Calibration of elemental peaks and data fitting was carried out using PyMca (5.6.7) [39]. The batch fitting of data was carried out to generate the distribution of elements and further data were normalized using an RGB calculator of PyMca.

4.1.3.5 Mid Infrared (mid-IR) Spectroscopy

4.1.3.5.1 Sample preparation

Technical replicates were formed by selecting (pooling) wheat seeds from three jars and then grinding these to fine powders using a cryo grinder (GENCO Spex 2010, Metuchen, NJ USA) using liquid nitrogen. Fine flours (4.85 mg) were mixed with 385 mg potassium bromide (KBr) to make three powder pellets. Then, this mixture was ground again using the cryo grinder and then three equal portions of material were pressed using a hydraulic press (PIKE Technologies, Madison, WI, USA) at three pressures (53.93, 34.32, and 14.70 kPa) with holding time 3 s each time to form three pellets (13 mm in diameter) for each sample.

4.1.3.5.2 Data acquisition and analysis

Biochemical components (protein, lipid, and carbohydrates) were determined using mid infrared spectroscopy [34]. The pelleted sample was placed in a sample wheel for FTIR data

collection. Data were collected using Cary 670 series microscope (Agilent Technologies Inc., Santa Clara, CA) equipped with a bulk analysis accessory and thermoelectrically cooled Deuterated Lanthanum α-Alanine doped TriGlycine Sulphate (DLaTGS) detector. The spectra were collected in the 4000-900 cm^{-1} range at 4 cm^{-1} resolution with 64 scans co-added at each raster point. Data processing and analysis were carried out using the Quasar software (version 1.5.0) [42] and OriginPro was used for plotting the spectra. The acquired spectra underwent several preprocessing steps to ensure data quality and reliability. These steps encompassed background correction, normalization based on sample concentration, baseline correction utilizing the rubber band method, and vector normalization in Quasar software (Version 1.5.0). The reshaped combined dataset, comprising both healthy and damaged samples, underwent an application of principal component analysis (PCA) which is a well-established method for data reduction, wherein the dataset is transformed into a smaller number of components that encapsulate most of the original data's information. The initial and secondary principal components (PCs) were of particular interest in this analysis.

4.1.4 Result and Discussion

The physical condition of three varieties stored for 5 week was assessed by visual observation of three replicates and found varying levels of deterioration compared to control samples. The fungus was visible on some of the germ parts of the AAC Spitfire and CDC Defy. Slight discoloration from yellow to faded yellow/blackish was also found on AAC Spitfire and CDC Defy. The AAC stronghold variety showed less deterioration on the surface or near the germ compared with other two varieties. The level of deterioration increased from the first week to fifth week in the selected varieties.

4.1.4.1 Micro and macro-nutrients presence

Bulk analysis of samples using spectroscopy of durum wheat varieties provided an overall picture of how much particular nutrient was present before and after storage and more insight

into whether spoilage has any impact on their presence (Fig. 4.3). The higher photon counts were found for control samples than stored wheat samples for targeted nutrients. Nutrients Ca, K, Mn, Fe, Cu, Zn, and Br were located with peaks in durum samples at photon energies 3660 eV, 3320 eV, 5900 eV, 8000 eV, 8650 eV, and 12000 eV, respectively as shown in Figure 3. The variation in nutrients Ca, K, Mn, Fe, Cu, Zn, and Br peaks was found among the three selected varieties. In control samples, the nutrient Fe was the highest in AAC Spitfire (Fig 4.3A) followed by CDC Defy and the lowest in the AAC Stronghold. The stored samples of AAC Spitfire and CDC Defy showed differences in Fe peaks as compared to control. Maximum reduction of around 40% in Fe fluorescence count was observed in 5 week stored samples over control samples. In case of AAC Stronghold, less variation about 20% in Fe peaks was observed in 5 week stored samples over control. These results agreed with the visual inspection, where more spoilage was observed in AAC Spitfire and CDC Defy. The large variation of nutrient Fe was found in our results and it can be linked to fungal infection. One of the reasons for variation in nutrient Fe can be due to growth of fungus on durum wheat, as per literature fungal infection might strive on plant cells iron for support of their metabolic activities [43]. In fungi, intracellular siderophores can serve as iron storage [44]. One more reason for large variation of Fe element could be linked to deterioration of two durum wheat varieties (AAC Spitfire and CDC defy) where the outermost layer from whole grain was lost in sample preparation (may be damaged due to weak structure) where Fe is distributed. One of the study, stated that whole wheat contains Fe about 3.9 mg/100 g, as compared to wheat flour 0.9 mg/100 g [45], hence due to deterioration the Fe present in outer layers or attached husk, which may have fallen off at the end of 5 week of storage, could not make into wheat flour of pellets. In CDC Defy variety (Fig 4.3B), the steep decline in Fe peak was observed as storage period progressed from 1 week to 5 week. A similar trend was observed in case of nutrient K and Zn in 5 week stored samples of durum wheat and reduction by 15% in photon counts compared to

control. The roles of micro-nutrients in plant defense were documented for Zn [20–22]. Hence from the seed defence point of view degradation of Zn and Mn micronutrients can be sign of deterioration in durum wheat.

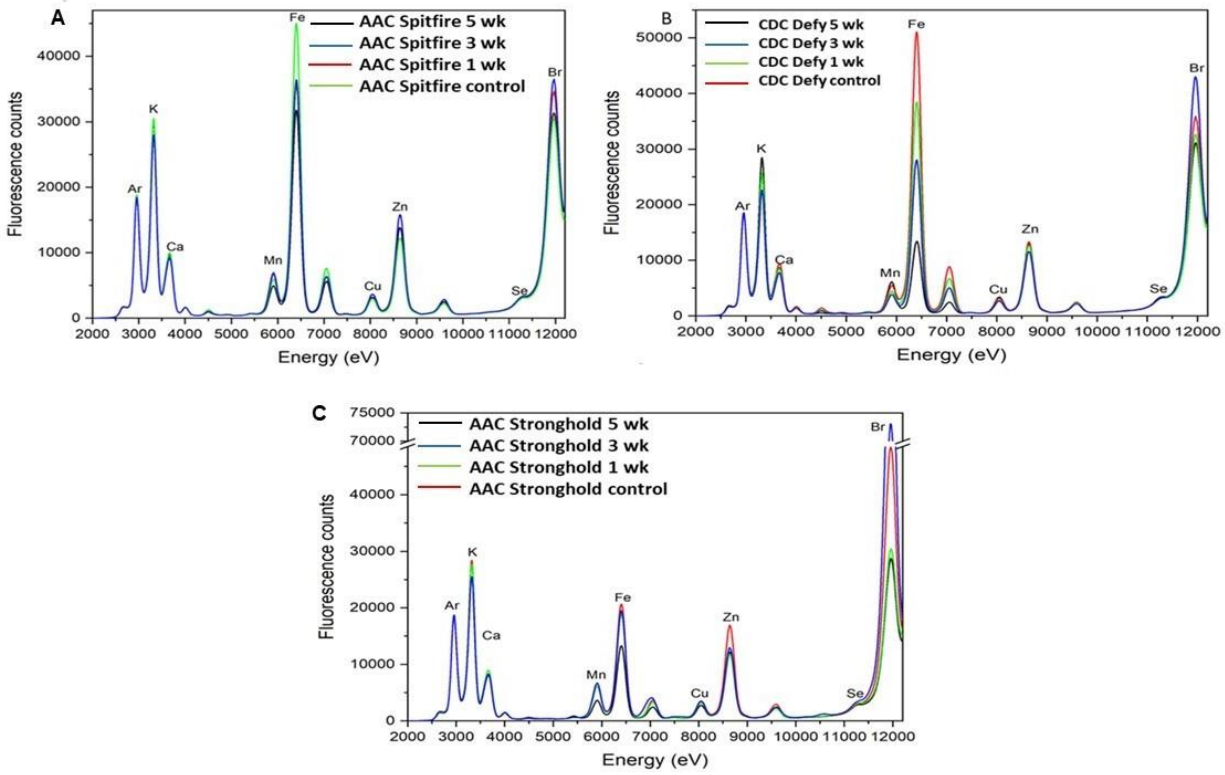

Figure 4.3 XRF bulk spectra of durum wheat (A: AAC Spitfire, B: CDC Defy, and C: AAC Stronghold) in control (dry) and stored at different week at 17% mc (wb)

In all durum varieties, minor degradation of nutrients (Ca, Mn, and Cu) was also observed due to deterioration. The around 8-10% reduction in fluorescence counts was observed for Ca, Mn, and Cu nutrients in spoiled samples of durum wheat. As the storage time increased, it had an observable impact on K, Mn, and Fe, whereas Ca, Zn, and Cu had less variations. Durum wheat variety AAC Stronghold (Fig 4.3C) showed a higher presence of nutrient Br and had variations among the samples stored for different week and remaining other nutrients were least affected or had less variation but showed comparatively higher variation in Zn. The nutrients Fe, Zn and Mn are essential for growth of fungus in cereals [46]. As discussed earlier in case of Fe presence that fungal or mould growth due to unfavorable condition during storage might be

responsible for diminishing of nutrients. As per Bamrah et al. [23] the results obtained using the XRF spectroscopy method are statistically not different from the analytical laboratory methods for seed nutrient analysis, it means observed results in variation of nutrient due to deterioration can be used in further analysis or interpretation. In case of AAC Spitfire and CDC Defy, the decrease in counts or variation in peaks was observed from one-week storage onwards, whereas AAC Stronghold variety did not show reduction in counts until 3 week storage. These observations can be linked to deterioration of samples, where AAC Stronghold performed better in storage and three varieties can be characterised based on changes in macronutrients and micronutrients. All three varieties of durum wheat showed variable response in spectra of available nutrients; hence synchrotron X-ray fluorescence spectroscopy can be used in characterization of wheat varieties for post harvest storage. One-way ANOVA revealed statistically significant differences in means of fluorescence counts ($p<0.05$) in some nutrients. In all selected varieties of durum wheat, the significant changes in ($p<0.05$) nutrient Fe, Zn, and Mn were found during length of storage. The changes in nutrient K was found statistically insignificant ($p>0.05$) in variety AAC Spitfire but was found significant in CDC Defy and AAC Stronghold ($p<0.05$) varieties. The changes in nutrients Ca and Cu were found statistically insignificant at ($p>0.05$) in all durum wheat varieties. The results illustrate that, deterioration of durum wheat had significant impact on its available nutrients at the end of 5 week storage.

4.1.4.2 Changes in nutrient distribution

The results of SR-XFI imaging of 80-micron thin sections of durum wheat (control and 5 week stored) are presented in Fig.4.4. The purpose was to map changes in the distribution of essential nutrients within seed components before and after storage. Gradients in micronutrients and macronutrients were observed between spoiled and control durum wheat samples. The red in the scale represents maximum value and blue represents the minimum value of detected nutrient across wheat sections. In Fig. 4.4, only those sections in which maximum difference in nutrient distribution was observed are presented. Nutrient Fe was abundantly distributed in the seed coat (with aleurone layer) of the durum wheat in control samples in the order CDC Defy > AAC Spitfire > AAC Stronghold as is visible in Fig 4.4 (a1, b1, c1) before storage and after storage in spoiled samples as in order CDC Defy > AAC Stronghold > AAC Spitfire Fig 4.4 (d1, e1, f1). Next to Fe, the nutrient K was well distributed in all control samples of three varieties inside the seed coat and across the endosperm of the seed as shown in Fig 4.4 (a2, b2, and c2). In spoiled samples nutrient K was found in the order CDC Defy > AAC Stronghold > AAC Spitfire as observed from Fig 4.4 (d2, e2, f2). The distribution of K was also lowered in spoiled samples as observed from Fig 4.4 (d2, e2 and f2). The observed distribution of K was lowered in endosperm, but not in the seed coat in durum wheat, this might be due to the deterioration of endosperm due to spoilage in the seed. Larger gradients were observed in Fe, Zn, and K in spoiled samples than controls.

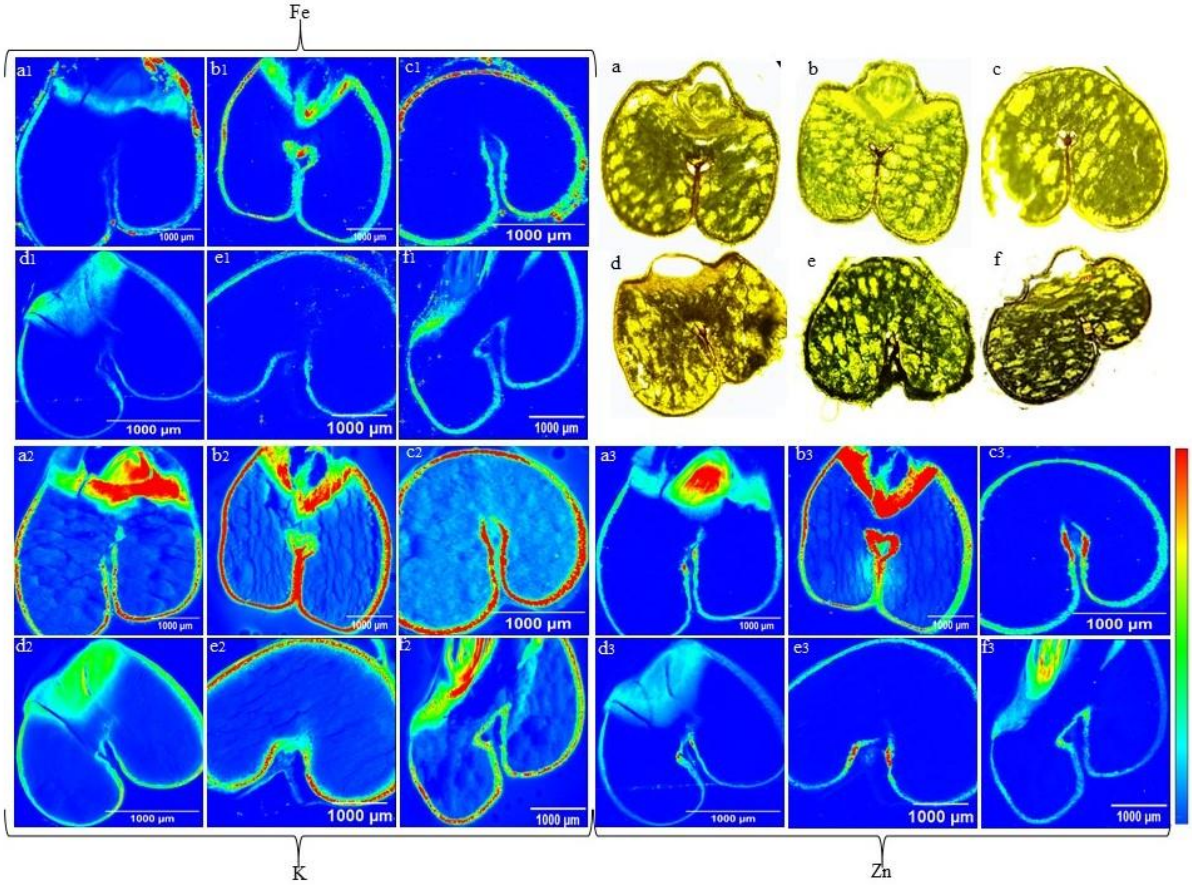

Figure 4.4 The mapping of nutrients in control and 5 week stored durum wheat. Distribution of nutrients Fe (a1, b1, c1, d1, e1, f1), K (a2, b2, c2, d2, e2, f2) and Zn (a3, b3, c3, d3, e3, f3) using SR-XFI. Microscopic images of durum wheat control thin sections (a: AAC Spitfire, b: CDC Defy, c:AAC Stronghold) and 5 week stored (d: AAC Spitfire, e: CDC Defy, f: AAC Stronghold)

Elements Cu, Fe, and Zn are localized in aleurone layer in wheat and large gradients in concentration of elements (Cu, Fe, Zn, Mn) exist between crease and endosperm region [24]. In this study only distribution of elements of interest were mapped not the concentration; however, in previous studies wheat seed components were characterized on the basis of element concentrations [24,47]. The distribution of Fe, Zn, and K was lowered in all spoiled samples as is visible in Fig 4.4. Control samples of AAC Spitfire and CDC Defy showed Zn concentrated in germ and adjoined aleurone layer, but later in spoiled samples the distribution was lowered in all durum wheat samples Fig 4.4 (a3-f3). In CDC Defy, Zn was found to be distributed in aleurone and crease region after 5 week Fig 4.4 (b3); however, lower than control

samples Fig 4.4 (e3). An earlier study also reported that Zn is Associated with aleurone and crease regions [47]. Zinc plays a pivotal function in the plant's response to pests and diseases [48]. The major changes in Fe and K nutrient distribution were observed in scanned spoiled seed samples and these findings agreed with the findings of bulk XRF spectroscopy. As compared to K, Fe, and Zn, a minor variation in the distribution of other nutrients was observed for Ca, Mn, and Cu in the case of all durum varieties. The microscopic images of spoiled samples Fig 4.4(d, e, f) showed deterioration in the endosperm over control samples Fig 4.4(a, b, c). The presence of air gaps and cracks were found in microscopic images of control samples in AAC Spitfire (Fig 4.4a) and CDC Defy (Fig 4.4b). These imperfections may have been caused due to deterioration during storage or sample preparation, where major changes were observed in nutrients in spoiled sections as discussed earlier. The extent of damage was less in both thin sections of the AAC Stronghold as shown in Fig 4.4(c, f).

In our study, we were able to map variations in the distribution of micro- as well as macro-nutrients in durum wheat during post-harvest storage, because, in earlier studies, only effect of field treatments on the presence of nutrients in different cultivars was studied [19,24]. The nutrients Mn, Cu, Fe, and Zn play an important role in plant defense and immune responses [20–22]. Manganese is responsible for the production of phenolic compounds, which assist in plant defense mechanisms [49]. Almost similar trend was observed in decreasing distribution of nutrients in durum wheat cross sections for other nutrients Ca, Mn, and Cu, but gradients were lower than for Fe, Zn, and K. The variety AAC Stronghold performed better than other two varieties, but all durum wheat were affected at 17% mc within 5 week of storage. The spoilage in storage not only affects physical structure, which was found in microscopic images, but also diminishes the nutritive value of durum wheat. The outcomes of nutrient mapping were found to be interconnected with the findings obtained from bulk spectroscopy analysis.

4.1.4.3 Biochemical changes

The changes in biochemical components during storage using mid-infrared spectroscopy analysis are presented in Fig (4.5-4.7). The variations in proteins, lipids, and carbohydrates in durum wheat varieties due to spoilage during storage were assessed and the spectra of control and 5 week stored wheat are presented in Figure 5. The 1800–1100 cm^{-1} region of spectra was used in the analysis because this region has absorption bands related to protein, lipid, and carbohydrates [35]. Control samples of wheat have relatively higher lipids, proteins, and carbohydrates at 1740, 1650, and 1080 cm^{-1} [50]. The region 1200-900 cm^{-1} represent carbohydrates with peaks at 1023, 1080 and 1150 cm^{-1}, in which spectral bands located at 1080 and 1023 cm^{-1} have been attributed to starch and, the band observed at 1150 cm^{-1} can be attributed to the stretching of CC and CO bonds within starch molecules, as suggested by previous studies [34]. The control AAC Spitfire showed maximum absorbance for carbohydrates followed by CDC Defy and AAC Stronghold. Later, at the end of 5 week of storage large gradient was observed in absorbance of carbohydrates for AAC Spitfire compared to other two varieties CDC Defy and AAC Stronghold. The variety CDC Defy showed lower absorption for carbohydrates at the end of 5 week of storage, this illustrates impact of deterioration on biochemical composition and AAC stronghold showed less changes compared to other two varieties. Carbohydrates were degraded mostly may be due to starch degradation compared to lipids and proteins, which can be inferred from normalised spectra of CDC Defy and AAC Spitfire.

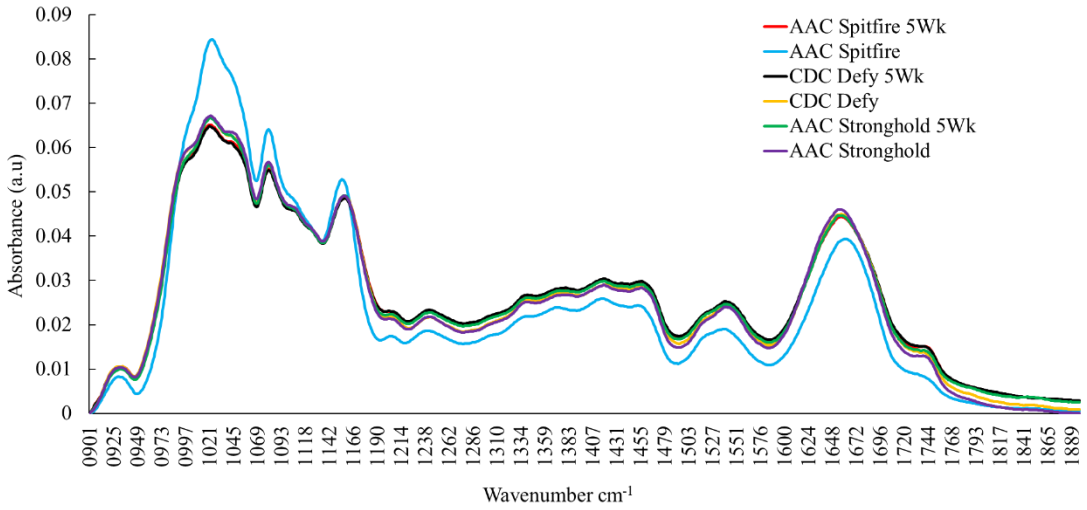

Figure 4.5 Normalized bulk mid-IR spectra of durum wheat varieties; AAC Spitfire, CDC Defy and AAC Stronghold stored for 5 week and control to check biochemical (proteins, lipids, carbohydrates) variation in spectral region 1900-900 cm -1

Durum wheat is called hard wheat due to its high protein content [13], hence it is important to know the impact of deterioration on wheat protein. Mid-IR may help in characterization of selected durum wheat on these changes due to deterioration in storage. Therefore, second derivatives of spectra were plotted for regions 1700-1600 cm^{-1} as shown in Fig 4.6. The band regions at 1600–1500 cm^{-1} and 1700–1600 cm^{-1} represent the protein spectra with amide I at 1650 cm^{-1} (C= O and C–N stretching) and amide II at 1540 cm^{-1} (N–H bending and C–H stretching) [34]. The nature of proteins can be evaluated from Fig. 4.6. The peaks located at 1635 and 1654 cm^{-1} were β-sheets and α-helical secondary protein structures in durum wheat. All observed peaks followed similar pattern, but considerable variation was observed in 5 week stored samples for AAC Spitfire and CDC Defy varieties compared to control. It can be observed protein (1700–1500 cm^{-1}) regions play an important role in the characterization of durum wheat. AAC Spitfire control and 5 week stored wheat showed variation in lipid peaks at 1750 cm^{-1} as presented in the second derivative spectra of Figure 6. Biochemical changes in storage studies wheat and other cereals at unsafe moisture were summarized [51] and found that protein, carbohydrates were decreased in range of 3-19 % after 6 week storage due to

mould growth. Lipids were at 77% of original value in wheat and processed wheat products after end of storage due to fungal infection [51]. The analysis of principal components revealed that the first three principal components (PCs) PC1, PC2 and PC3 collectively showed 73%, 20% and 5% of the explained variance, respectively (Fig 4.7a). By employing the PC scores, a clear distinction was observed between the PC scores generated for control samples and 5 week stored samples. These PC scores were further utilized to create a graphical representation Fig 4.7(b, c). The score of 5 week stored samples are bent to right side than that of control samples which were clustered at left side. In the resulting plot a discernible separation between the PC scores corresponding to control and 5 week stored wheat was evident. The deterioration in seed tends to be non-uniform, hence not all tissues of seed would necessarily experience damage, therefore, some 5 week stored samples showed up in left side with controls in the plot. In summery, more affected varieties due to spoilage were AAC Spitfire and CDC Defy and less affected was the AAC Stronghold. The control sample of AAC Spitfire was in the negative region than the other two varieties, which might reflect its initial condition that it has poor storability. Similar result was reported for fusarium susceptible and resistant wheat varieties [33], where they were able to characterize fusarium resistant varieties of wheat based on FTIR spectra results. The plot revealed that almost all durum wheat showed deterioration as per shifting of scores in negative region. AAC Stronghold was sound before storage but later showed deterioration, but less compared to other two varieties. The kernel texture and biochemical composition, including starch granule texture, and protein content vary among wheat varieties [52] and similar findings were the outcome of this study. In deterioration process, fungi can absorb and metabolize a diverse range of soluble carbohydrates, insoluble ones like starches, cellulose, and hemicelluloses and break down complex hydrocarbons such as lignin [53]. The durum wheat is said to be poor in storage under unfavorable conditions [4]

and in our study using high resolution imaging it was found more susceptible to spoilage in short term storage.

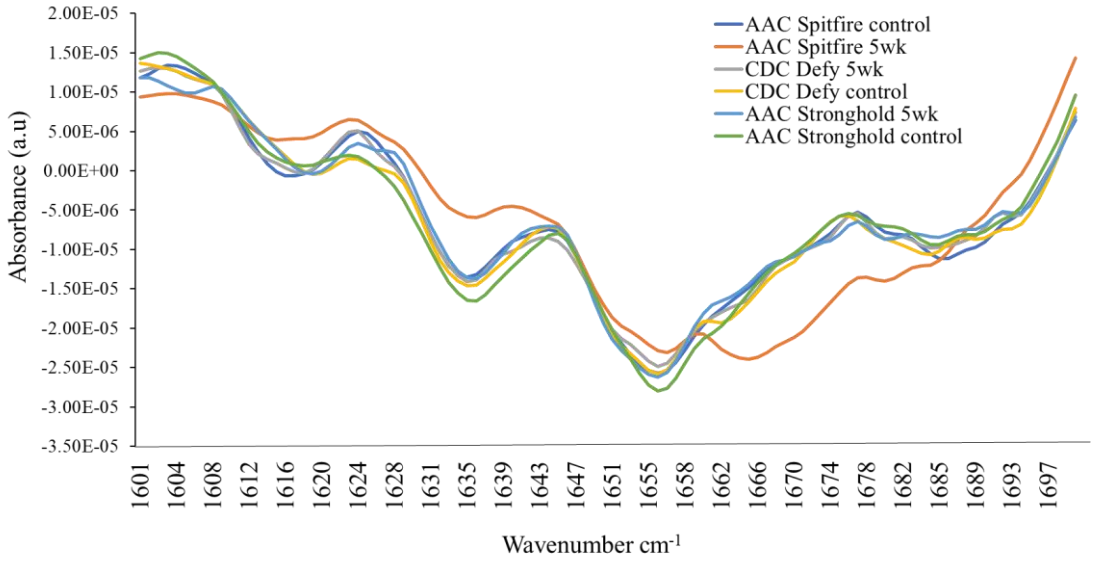

Figure 4.6 The second derivative bulk mid-IR spectra of durum wheat varieties; AAC Spitfire, CDC Defy and AAC Stronghold stored for 5 week and control in spectral region 1700-1600 cm-1 for analysis of changes in protein and its structure

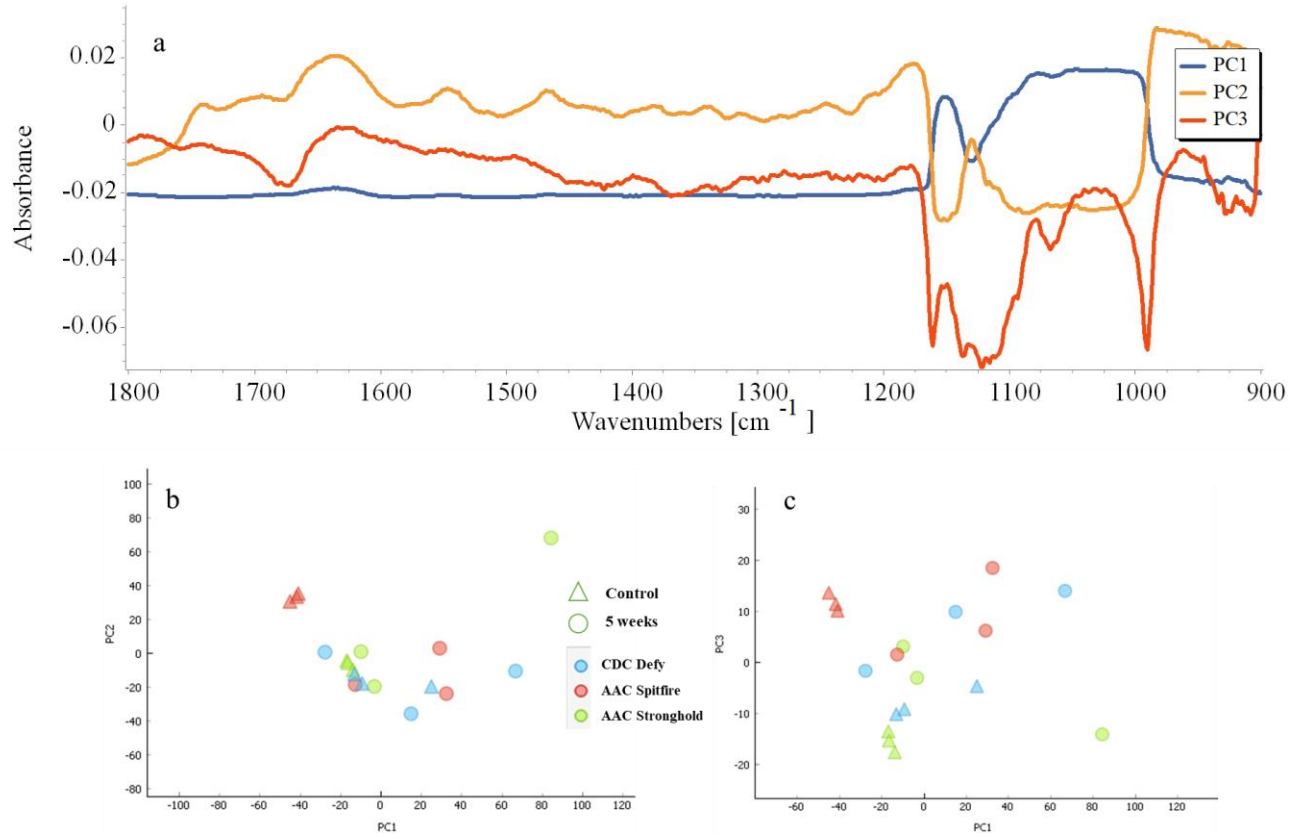

Figure 4.7 Top (a): data loading plots of three principal components (PC1, PC2, PC3) of the data (durum wheat varieties; AAC Spitfire, CDC Defy and AAC Stronghold stored for 5 week and control) in spectral region 1800-900cm-1. Bottom: Principal component analysis (b) (PC1 vs PC2) of durum wheat. Principal component analysis (c) (PC1 vs PC3) of durum wheat varieties.

4.1.5 Conclusion

The SR-XRF analysis revealed the effect of storage time and deterioration on variations in micro and macro nutrients. The SR-XFI imaging revealed changes in nutritional distributions at the micron scale in thin sections in their maps within seed features. The changes in biochemical components (proteins, lipids, and carbohydrates) due to deterioration during storage were determined using mid-infrared (mid-IR) spectroscopy. The AAC Spitfire and CDC Defy varieties showed more deterioration than AAC Stronghold, and all three varieties can be characterized based on variation in nutrient and their distribution with spoilage and storage time. The developed methodology in this study will be useful in the analysis of more

cereal and pulse seeds. There is good scope of linking observed changes in wheat during storage to X-ray microcomputed tomography data (microstructural data) of wheat.

4.1.6 Acknowledgement

The authors acknowledge the Netaji Subhash Chandra fellowship from the Indian Council of Agriculture Research via grant no. ICAR/2019 for the first author and the Natural Sciences and Engineering Research Council of Canada for supporting the student research via a grant no. RGPIN-2018-04420 to Dr Jayas. The authors also acknowledge the Canadian Light Source, Saskatoon for providing beamtime and access to conduct experiments.

4.1.7 Authors' contributions

NSI and CK prepared an outline, the first draft, and the content of the whole paper based on carried out experiments. MV, KT, VB, and DM who are experts in synchrotron imaging at the Canadian Light Source provided technical inputs and training, helped in data acquisition, and supported the preparation of draft. DSJ conceptualized the study, is the corresponding author, received funding and contributed to it through editing, examination, and finalisation of the manuscript drafts. All authors have read and approved the final manuscript.

4.1.8 Competing interest statement

The authors declare that there are no competing interests.

4.1.9 Data availability statement

Data will be made available on request.

4.1.10 References

[1] B.L. Beres, E. Rahmani, J.M. Clarke, P. Grassini, C.J. Pozniak, C.M. Geddes, K.D. Porker, W.E. May, J.K. Ransom, A Systematic Review of Durum Wheat: Enhancing Production Systems by Exploring Genotype, Environment, and Management (G × E × M) Synergies, Front. Plant Sci. 11 (2020) 1–14.

https://doi.org/10.3389/fpls.2020.568657.

[2] LMC International, The economic impact of canola on the Canadian economy: 2020 update insights for agribusiness specialist data and analysis for commercial decision-making, 2020. https://cerealscanada.ca/wheat/.

[3] Statistics Canada, Model-based principal field crop estimates, (2022). https://www150.statcan.gc.ca/n1/daily-quotidien/220914/dq220914b-eng.htm.

[4] U. Nithya, V. Chelladurai, D.S. Jayas, N.D.G. White, Safe storage guidelines for durum wheat, J. Stored Prod. Res. 47 (2011) 328–333. https://doi.org/10.1016/j.jspr.2011.05.005.

[5] D.S. Jayas, Storing Grains for Food Security and Sustainability, Agric. Res. 1 (2012) 21–24. https://doi.org/10.1007/s40003-011-0004-4.

[6] H.A.H. Wallace, P.L. Sholberg, R.N. Sinha, W.E. Muir, Biological, physical and chemical changes in stored wheat, Mycopathologia. 82 (1983) 65–76. https://doi.org/10.1007/BF00437333.

[7] E. Schroth, W.E. Muir, D.S. Jayas, N.D.G. White, D. Abramson, Storage limit of wheat at 17% moisture content, Can. Agric. Eng. 40 (1998) 201–205.

[8] M. Schmidt, S. Horstmann, L. De Colli, M. Danaher, K. Speer, E. Zannini, E.K. Arendt, Impact of fungal contamination of wheat on grain quality criteria, J. Cereal Sci. 69 (2016) 95–103. https://doi.org/10.1016/j.jcs.2016.02.010.

[9] S.-B. Zhang, Y.-Y. Lv, Y.-L. Wang, F. Jia, J.-S. Wang, Y.-S. Hu, Physiochemical changes in wheat of different hardnesses during storage, J. Stored Prod. Res. 72 (2017) 161–165. https://doi.org/10.1016/j.jspr.2017.05.002.

[10] Q.-S. Yuan, P. Yang, A.-B. Wu, D.-Y. Zuo, W.-J. He, M.-W. Guo, T. Huang, H.-P. Li,

Y.-C. Liao, Variation in the Microbiome, Trichothecenes, and Aflatoxins in Stored Wheat Grains in Wuhan, China, Toxins (Basel). 10 (2018) 171. https://doi.org/10.3390/toxins10050171.

[11] A. F. Worku, K. K. Kalsa, M. Abera, H. G. Nigus, Effects of storage strategies on physicochemical properties of stored wheat in Ethiopia, AIMS Agric. Food. 4 (2019) 578–591. https://doi.org/10.3934/agrfood.2019.3.578.

[12] C. Karunakaran, R. Lahlali, N. Zhu, A.M. Webb, M. Schmidt, K. Fransishyn, G. Belev, T. Wysokinski, J. Olson, D.M.L. Cooper, E. Hallin, Factors influencing real time internal structural visualization and dynamic process monitoring in plants using synchrotron-based phase contrast X-ray imaging, Sci. Rep. 5 (2015) 12119. https://doi.org/10.1038/srep12119.

[13] S. Neethirajan, C. Karunakaran, S. Symons, D.S. Jayas, Classification of vitreousness in durum wheat using soft X-rays and transmitted light images, Comput. Electron. Agric. 53 (2006) 71–78. https://doi.org/10.1016/j.compag.2006.03.001.

[14] S. Neethirajan, D.S. Jayas, N.D.G. White, H. Zhang, Investigation of 3D geometry of bulk wheat and pea pores using X-ray computed tomography images, Comput. Electron. Agric. 63 (2008) 104–111. https://doi.org/10.1016/j.compag.2008.01.019.

[15] A. Hughes, K. Askew, C.P. Scotson, K. Williams, C. Sauze, F. Corke, J.H. Doonan, C. Nibau, Non-destructive, high-content analysis of wheat grain traits using X-ray micro computed tomography, Plant Methods. 13 (2017) 76. https://doi.org/10.1186/s13007-017-0229-8.

[16] T.D.Q. Le, C. Alvarado, C. Girousse, D. Legland, A.-L. Chateigner-Boutin, Use of X-ray micro computed tomography imaging to analyze the morphology of wheat grain through its development, Plant Methods. 15 (2019) 84. https://doi.org/10.1186/s13007-

019-0468-y.

[17] V. Radchuk, D. Weier, R. Radchuk, W. Weschke, H. Weber, Development of maternal seed tissue in barley is mediated by regulated cell expansion and cell disintegration and coordinated with endosperm growth, J. Exp. Bot. 62 (2011) 1217–1227. https://doi.org/10.1093/jxb/erq348.

[18] Y. Lv, P. Tian, S. Zhang, J. Wang, Y. Hu, Dynamic proteomic changes in soft wheat seeds during accelerated ageing, PeerJ. 6 (2018) e5874. https://doi.org/10.7717/peerj.5874.

[19] M. Ciudad-Mulero, M.C. Matallana-González, M.J. Callejo, J.M. Carrillo, P. Morales, V. Fernández-Ruiz, Durum and Bread Wheat Flours. Preliminary Mineral Characterization and Its Potential Health Claims, Agronomy. 11 (2021) 108. https://doi.org/10.3390/agronomy11010108.

[20] C. Dordas, Role of nutrients in controlling plant diseases in sustainable agriculture. A review, Agron. Sustain. Dev. 28 (2008) 33–46. https://doi.org/10.1051/agro:2007051.

[21] H. Fones, G.M. Preston, The impact of transition metals on bacterial plant disease, FEMS Microbiol. Rev. 37 (2013) 495–519. https://doi.org/10.1111/1574-6976.12004.

[22] R. Graham, M. Webb, Micronutrients and disease resistance and tolerance in plants, in: Micronutr. Agric., 2018: or. 329–370. https://doi.org/10.2136/sssabookser4.2ed.c10.

[23] R.K. Bamrah, P. Vijayan, C. Karunakaran, D. Muir, E. Hallin, J. Stobbs, B. Goetz, M. Nickerson, K. Tanino, T.D. Warkentin, Evaluation of X-Ray Fluorescence Spectroscopy as a Tool for Nutrient Analysis of Pea Seeds, Crop Sci. 59 (2019) 2689–2700. https://doi.org/10.2135/cropsci2019.01.0004.

[24] N. De Brier, S. V. Gomand, E. Donner, D. Paterson, E. Smolders, J.A. Delcour, E.

Lombi, Element distribution and iron speciation in mature wheat grains (Triticum aestivum L.) using synchrotron X-ray fluorescence microscopy mapping and X-ray absorption near-edge structure (XANES) imaging, Plant. Cell Environ. 39 (2016) 1835–1847. https://doi.org/10.1111/pce.12749.

[25] K. Tanaka, T. Yoshida, Z. Kasai, Distribution of mineral elements in the outer layer of rice and wheat grains, using electron microprobe x-ray analysis, Soil Sci. Plant Nutr. 20 (1974) 87–91. https://doi.org/10.1080/00380768.1974.10433231.

[26] S.P. Singh, K. Vogel-Mikuš, I. Arčon, P. Vavpetič, L. Jeromel, P. Pelicon, J. Kumar, R. Tuli, Pattern of iron distribution in maternal and filial tissues in wheat grains with contrasting levels of iron, J. Exp. Bot. 64 (2013) 3249–3260. https://doi.org/10.1093/jxb/ert160.

[27] S.P. Singh, K. Vogel-Mikuš, P. Vavpetič, L. Jeromel, P. Pelicon, J. Kumar, R. Tuli, Spatial X-ray fluorescence micro-imaging of minerals in grain tissues of wheat and related genotypes, Planta. 240 (2014) 277–289. https://doi.org/10.1007/s00425-014-2084-4.

[28] M. Javid Iqbal, N. Shams, K. Fatima, Nutritional Quality of Wheat, in: Wheat, IntechOpen, 2022. https://doi.org/10.5772/intechopen.104659.

[29] G. Boggini, H. Namoune, J. Abecassis, B. Cuq, Other Traditional Durum-Derived Products, in: Durum Wheat, Elsevier, 2012: or. 177–199. https://doi.org/10.1016/B978-1-891127-65-6.50015-5.

[30] Cereals Canada, Crop Summary Grown in 2022, 2022. https://cerealscanada.ca/wp-content/uploads/2022/11/2022-New_Crop_Summary_FINAL_1122.pdf.

[31] D. Boyacioğlu, N.S. Hettiarachchy, Changes in some biochemical components of wheat

grain that was infected with Fusarium graminearum, J. Cereal Sci. 21 (1995) 57–62. https://doi.org/10.1016/S0733-5210(95)80008-5.

[32] A. Sharma, S. Garg, I. Sheikh, P. Vyas, H.S. Dhaliwal, Effect of wheat grain protein composition on end-use quality, J. Food Sci. Technol. 57 (2020) 2771–2785. https://doi.org/10.1007/s13197-019-04222-6.

[33] R. Lahlali, T. Song, M. Chu, C. Karunakaran, F. Yu, Y. Wei, G. Peng, Synchrotron-based spectroscopy and imaging reveal changes in the cell-wall composition of barley leaves in defence responses to Blumeria graminis f. sp. tritici, Can. J. Plant Pathol. 41 (2019) 457–467. https://doi.org/10.1080/07060661.2019.1581662.

[34] C. Karunakaran, P. Vijayan, J. Stobbs, R.K. Bamrah, G. Arganosa, T.D. Warkentin, High throughput nutritional profiling of pea seeds using Fourier transform mid-infrared spectroscopy, Food Chem. 309 (2020) 125585. https://doi.org/10.1016/j.foodchem.2019.125585.

[35] C.B. Singh, D.S. Jayas, F. Borondics, N.D.G. White, Synchrotron based infrared imaging study of compositional changes in stored wheat due to infection with Aspergillus glaucus, J. Stored Prod. Res. 47 (2011) 372–377. https://doi.org/10.1016/j.jspr.2011.07.001.

[36] P. Yu, D.A. Christensen, C.R. Christensen, M.D. Drew, B.G. Rossnagel, J.J. McKinnon, Use of synchrotron FTIR microspectroscopy to identify chemical differences in barley endosperm tissue in relation to rumen degradation characteristics, Can. J. Anim. Sci. 84 (2004) 523–527. https://doi.org/10.4141/A03-102.

[37] S. Joseph, Moisture Measurement — Unground Grain and Seeds, ASABE Stand. ASAE S352. (2017). http://refhub.elsevier.com/S0022-474X(22)00131-X/sref1.

[38] J.S. Watson, Fast, Simple Method of Powder Pellet Preparation for X-Ray Fluorescence Analysis, X-Ray Spectrom. 25 (1996) 173–174. https://doi.org/10.1002/(SICI)1097-4539(199607)25:4<173::AID-XRS158>3.0.CO;2-Z.

[39] V.A. Solé, E. Papillon, M. Cotte, P. Walter, J. Susini, A multiplatform code for the analysis of energy-dispersive X-ray fluorescence spectra, Spectrochim. Acta - Part B At. Spectrosc. 62 (2007) 63–68. https://doi.org/10.1016/j.sab.2006.12.002.

[40] E. Lombi, K.G. Scheckel, J. Pallon, A.M. Carey, Y.G. Zhu, A.A. Meharg, Speciation and distribution of arsenic and localization of nutrients in rice grains, New Phytol. 184 (2009) 193–201. https://doi.org/10.1111/j.1469-8137.2009.02912.x.

[41] E. Lombi, K.G. Scheckel, I.M. Kempson, In situ analysis of metal(loid)s in plants: State of the art and artefacts, Environ. Exp. Bot. 72 (2011) 3–17. https://doi.org/10.1016/j.envexpbot.2010.04.005.

[42] J. Demšar, T. Curk, A. Erjavec, Č. Gorup, T. Hočevar, M. Milutinovič, M. Možina, M. Polajnar, M. Toplak, A. Starič, M. Štajdohar, L. Umek, L. Žagar, J. Žbontar, M. Žitnik, B. Zupan, Orange: Data mining toolbox in python, J. Mach. Learn. Res. 14 (2013) 2349–2353.

[43] J. Schindelin, I. Arganda-Carreras, E. Frise, V. Kaynig, M. Longair, T. Pietzsch, S. Preibisch, C. Rueden, S. Saalfeld, B. Schmid, J.Y. Tinevez, D.J. White, V. Hartenstein, K. Eliceiri, P. Tomancak, A. Cardona, Fiji: An open-source platform for biological-image analysis, Nat. Methods. 9 (2012). https://doi.org/10.1038/nmeth.2019.

[44] U. Neubauer, B. Nowack, G. Furrer, R. Schulin, Heavy metal sorption on clay minerals affected by the siderophore desferrioxamine B, Environ. Sci. Technol. 34 (2000). https://doi.org/10.1021/es990495w.

[45] B. McKevith, Nutritional aspects of cereals, Nutr. Bull. 29 (2004). https://doi.org/10.1111/j.1467-3010.2004.00418.x.

[46] G.S. Rawla, A note on trace elements for the growth of nigrospora oryzae (b. And br.) Petch, New Phytol. 68 (1969) 941–943. https://doi.org/10.1111/j.1469-8137.1969.tb06493.x.

[47] T. Zhang, H. Sun, Z. Lv, L. Cui, H. Mao, P.M. Kopittke, Using Synchrotron-Based Approaches To Examine the Foliar Application of ZnSO 4 and ZnO Nanoparticles for Field-Grown Winter Wheat, J. Agric. Food Chem. 66 (2018) 2572–2579. https://doi.org/10.1021/acs.jafc.7b04153.

[48] S.K. Gupta, A.K. Rai, S.S. Kanwar, T.R. Sharma, Comparative Analysis of Zinc Finger Proteins Involved in Plant Disease Resistance, PLoS One. 7 (2012) e42578. https://doi.org/10.1371/journal.pone.0042578.

[49] F. Mendoza, P. Verboven, H.K. Mebatsion, G. Kerckhofs, M. Wevers, B. Nicolaï, Three-dimensional pore space quantification of apple tissue using X-ray computed microtomography, Planta. 226 (2007) 559–570. https://doi.org/10.1007/s00425-007-0504-4.

[50] R. Saxton, O.M. McDougal, Whey Protein Powder Analysis by Mid-Infrared Spectroscopy, Foods. 10 (2021) 1033. https://doi.org/10.3390/foods10051033.

[51] K.A. Rosentrater, Biochemical, functional, and nutritive changes during storage, in: Storage Cereal Grains their Prod., 2022. https://doi.org/10.1016/B978-0-12-812758-2.00010-6.

[52] I. Pasha, F.M. Anjum, C.F. Morris, Grain hardness: A major determinant of wheat quality, Food Sci. Technol. Int. 16 (2010) 511–522.

https://doi.org/10.1177/1082013210379691.

[53] David moore, Nutrition, Brittanica. (2022) 1–5. https://www.britannica.com/science/fungus/Form-and-function-of-fungi (eskuratua 2023(e)ko abuztuakaren 29a).

Chapter 5. STUDY CHANGE IN BALREY MICROSTRCTURE AND NUTRITION IN STORAGE

5.1 Study of microstructural, nutritional, and biochemical changes in hulled and hulless barley during storage using X-ray and infrared techniques (Published in MDPI Foods)

Navnath S. Indore[1], Digvir S. Jayas[1,3*], Chithra Karunakaran[1,2], Jarvis Stobs[2], Viorica F. Bondici[2], Miranda Vu[2], Kaiyang Tu[2], Omar Marinos[2]

[1] Biosystems Engineering, University of Manitoba, Winnipeg, MB R3T 5V6, Canada
[2] Canadian Light Source Inc., Saskatoon, SK S7N 2V3, Canada
[3] President's Office, A762 University Hall, University of Lethbridge, Lethbridge, AB T1K 3M4, Canada
*Corresponding author's email: digvir.jayas@umanitoba.ca

5.1.1 Abstract

Four varieties of barley (Esma, AC Metacalf, Tradition, AB Cattlelac), representing four Canadian barley classes, were stored at 17% moisture content (mc) for 8 week. Stored barely was characterized using synchrotron X-ray phase contrast microcomputed tomography, synchrotron X-ray fluorescence imaging, and mid-infrared spectroscopy at the Canadian Light Source, Saskatoon. The deterioration was observed in all the selected varieties of barley at the end of 8 week of storage. Changes due to spoilage over time were observed inside grain microstructure and its nutrient distribution and composition. The study underscores the critical importance of the initial condition of barley grain microstructure in determining its storage life, particularly under unfavorable conditions. The hulled barley varieties showed more deterioration in microstructure than the hulless varieties of barley, where a direct correlation between microstructural changes and alterations in nutritional content was found. All selected barley classes showed changes in distribution of nutrients (Ca, Fe, K, Mn, Cu and Zn), but two row AC Metcalf variety exhibited more substantial variations, in the nutrient distribution (Zn and Mn) than other three varieties during storage. The two row class barley varieties showed more changes in biochemical components (protein, lipids, and carbohydrates) than six row class varieties

Keywords: Synchrotron microcomputed tomography; X-ray fluorescence; mid-IR; Storage of barley; Micro-structure; Nutrition

5.1.2 Introduction

Barley (*Hordeum vulgare L.*) holds significance as a vital cereal crop in Canada and globally. It is cultivated for purposes such as animal feed, malt products, and human

consumption. Globally, 70% of barley production is allocated for animal feed, with the remainder being utilized for human consumption, including malt and food products [1]. Canada, ranks as the fifth-largest producer globally, producing 9.8 million metric tonne (Mt) of barley from an area of 2.8 million hectares in 2022 [2]. Canadian barley can be categorized into two types: hulled (intact husk) and hulless (loosely attached husk), further subdivided into six-row or two-row classes [3]. The malt industry is one of main consumers of barley in Canada and across the world. The barley intended for malt production, a prerequisite of 95% varietal purity is important [4], and Canada excels in producing high-quality barley for the malt export market. Key quality parameters for barley consist of better germination rate, good protein content, and kernel uniformity. Superior-quality barley has less than 5% broken kernels, a protein content ranging from 9 to 12%, and a germination rate of 95% or higher [5,6].

Post-harvest storage of barley, like other cereals, is essential prior to consumption. The losses can occur during grain storage, with the extent of losses spanning from 1 to 50%, depending upon storage conditions and characteristics [4–6]. The storage life of barley is influenced by both biotic factors (insects, fungi) and abiotic factors (temperature, humidity, moisture). Among these, maintaining an appropriate moisture level is paramount. Barley is typically harvested at elevated moisture levels to mitigate harvesting losses. Therefore, drying is required to achieve a storage moisture content of 13% (wb). Elevated moisture levels during barley storage foster mold growth, culminating in post-harvest losses including diminished germination rates, nutrient degradation, weight loss, and toxin contamination [7]. A multitude of studies have been conducted to assess and mitigate quality and post-harvest losses in barley storage, focusing on the interaction of abiotic and biotic factors [8–14]. The average nutritive loss of 2.82% was found in barely stored for 12 months, protein losses were about 2.5%, and losses in fats were minimal. The germination of 14% and above moisture content malting barley are found to be reduced below 95% when stored for five months and high temperature and moisture can reduce barley germination to 0% at the end of nine months. Significant changes can occur in free fatty acid values dur-ing storage of hulless and hulled barley. Most common fungi that affect the quality of malting barley in storage are Aspergillus, Penicillium, and Fusarium [15].

All agricultural food grain seeds possess unique attributes such as physical (size, shape, colour) and composition (nutrients) which serve as distinguishing factors among them [15]. Even within the same category of cereal grains, variations in seed characteristics exist. For instance, Canadian wheat is categorized into sixteen classes, while barley is grouped into eight

classes based on seed attributes. These attributes can play a role in safe storage of cereal grains. The varieties of same grain type or class can exhibit varying degrees of resistance to deterioration within their respective habitats, as evidenced by instances where certain varieties have outperformed others during storage [16]. The inherent structure and properties of the seed might contribute to its defense mechanisms against spoilage under unfavorable conditions. In pursuit of insights, numerous investigations have been conducted to uncover such information concerning seeds, utilizing advanced imaging techniques such as X-ray and hyperspectral imaging [14,17–21]. These techniques have enabled researchers to extract microstructural details of seeds, composition, structural arrangements, and dynamic processes inside the plants, fruits, and seeds [22]. The utilization of synchrotron imaging has gained prominence in agriculture and food science, primarily due to limitations (experiment time, resolution, non-coherent source) as-sociated with conventional imaging methods (X-ray, microscopic, digital imaging). Com-prehensive applications of synchrotron X-rays have been compiled and details can be found in the literature [15,17,25]. Application of synchrotron X-ray microtomography was extensively used in food industries for product development, mapping changes in structure of food like bread, noodle dough bubbles, cracking of chocolate, microstructure changes due to gas exchange in product, ice cream stability under varying conditions, air pathways in pome fruits, and in fish [17]. Synchrotron phase contrast imaging has an edge over normal absorption imaging, because it can work for low density materials like soft tissues of plants and differentiation of dynamic process in tissues. Phase contrast is created by variable propagation distance between sample and detector; therefore, this unique property could be utilized in differentiation in seed features like changes in deterioration, moisture, and air volume which have less density gradients. The more detailed theory and its properties could be found elsewhere [15,23,24].

In a similar vein, the exploration of post-harvest dynamics in malting barley presents a promising avenue for synchrotron imaging. The quest for superior quality malting barley necessitates the presence of robust grain structures coupled with elevated germination potential and vigor [24].. Hence, a hypothesis emerges wherein synchrotron X-ray and mid-infrared technologies might be harnessed to map structural, nutritional, and biochemical changes that occur in barley varieties due to spoilage during post-harvest storage.

5.1.3 Materials and methods

In this study, commercially available and certified seeds of four distinct barley classes were acquired from a private enterprise (SeCan, Niverville, MB). The two barley varieties, namely Esma and AC Metacalf were selected which represent Canada eastern malting two-row hulled (2R) and Canada western malting two-row hulless (2Rhl), respectively. Additionally, two other varieties, Tradition and AB Cattlelac, were selected which belong to Canada western malting six row hulled (6R) and Canada western six row hulless (6Rhl), respectively. Samples of each variety, about 500 g, were conditioned to achieve a moisture content of 17% (wb) using distilled water. Subsequently, these samples were stored within sealed glass jars, each possessing a volume of 1 L under ambient conditions where temperatures ranged between 22 to 25°C. This process of conditioning and storage was recurrently executed every week for a duration spanning 8 week. The moisture content of the samples was evaluated post storage through an oven drying method. Specifically, 10 g samples were subjected to drying at 130°C for 19 h, and the resulting moisture content was determined [25].

5.1.3.1 Synchrotron X-ray phase contrast microcomputed tomography (SR-µCT)

The sample preparation, data acquisition, and data processing were carried out as per the procedures described in [26] and briefly summarized here. The imaging of the selected barley samples was completed at the BMIT-BM beamline at the Canadian Light Source (CLS) in Saskatoon, Canada [26] (Briefly summarized here). For energy filtration, two filters, namely aluminum (Al) with a thickness of 0.800 mm and molybdenum (Md) with a thickness of 0.076 mm, were used. These filters effectively modified the incident X-ray beam into a filtered white beam with an energy level approximating 20 keV. The transmitted X-rays were converted into visible images by using a scintillator (LuAg 500) in combination with a detector (PCO Edge 5.0, AA-40). The acquisitions were carried out at a resolution of 3.6 µm. Fifteen to twenty individual grain kernels were randomly chosen for each variety from the glass jars. These kernels were then placed inside a plastic tube and positioned onto a sample stage, secured with reusable adhesive. The orientation of the sample was carefully adjusted to ensure its eccentric alignment on the stage, guaranteeing its sustained presence within the beam's field of view. Subsequently, the sample was mounted onto a rotating stage positioned between the X-ray detector and the X-ray beam. The rotating stage facilitated a controlled alteration in the sample's orientation, accomplished through increments of 0.06°, relative to the incident beam. A vital parameter in phase contrast imaging, the distance between the sample and the detector, was optimized at 5 cm to enhance contrast through the sample. Around 3000 projection images were captured for 180° rotation of the sample. Before and following the acquisition of the CT

images, reference images of flat and dark signals were captured. The average of these flat and dark images was used for normalization [22,27]. The extraction of phase information was achieved through Paganin's method, performed from a singular phase-contrast image corresponding to each projection angle. This phase retrieval process was facilitated using the UFO-kit [28]. The results of reconstrued data are presented in Figures 1a and 1b, where projections from control, 6-week, and 8-week stored barley samples are shown. The principles and theory of X-ray phase contrast imaging are available elsewhere [29–31].

The reconstructed data were effectively assembled in a vertical manner using the "ez_helper" module, an integral component of the UFO kit. Subsequently, a further binning process of 4x4 was applied to ensure the data size remained below 4 gigabytes. This operation was performed using the software "Fiji" (version 2.9.0), setting the stage for subsequent image processing. To evaluate the properties of the seed, specifically the volume and air space, analysis was conducted on ten individual kernels per sample using a label analysis module in ORS Dragonfly software (2021.3, Object Research Systems, Montreal, QC) for both the control and spoiled samples data. Further segmentation procedures were executed to extract more intricate features from the images, including but not limited to cracks, air gaps (between husk and endosperm/seed coat), seed coat/husk, endosperm, change due to deterioration, and germ. The initial step encompassed the creation of distinct regions of interest (ROIs) for each component of interest, accomplished through the segmentation editor found in the ORS Dragonfly software. This enabled the segmentation of components like the germ, air spaces, and microstructural alterations indicative of spoilage. These analyses were performed to check the effect of storage and spoilage on seed microstructure; therefore, it was performed on control and 8-week stored barley samples. Visualization of these segmented components and measurement for both the control and 8-week stored samples is presented in Fig 5.3 and 5.4, subsequently utilized for a comprehensive characterization of the changes in barley due to spoilage. The results of this analysis are depicted in Fig 5.5. Additionally, the normalized histograms of both control samples and stored samples are plotted and displayed in Fig 5.6. These histograms were prepared by processing 4096 bins with 0 to 65536 image stacks.

5.1.3.2 Synchrotron X-ray fluorescence imaging (SR-XFI)

The sample preparation, data acquisition, and data processing were carried out as per the procedures described in [26] and briefly summarized here. To spatially visualize the distribution of nutrients within barley seeds [32] (briefly summarized here), this method was

used. Randomly selected barley seeds were embedded in a Leica Cryogel using liquid nitrogen. Subsequently, thin sections of these seeds were obtained with a thickness of 80 µm, employing the established procedure [33]. The thin sectioning procedure was executed using a Leica CM1950 cryostat microtome (Leica Biosystems Inc., Richmond Hill, Ontario). The utilization of thin sections is instrumental in minimizing distortions that may arise in nutrient maps due to the penetrative characteristics of X-rays [34]. Multiple thin-sectioned samples were positioned on Kapton tape and arranged on the sample holder. Before acquisition, microscopic images were captured utilizing a digital microscope (Motic DM143, Motic, Kowloon, Hong Kong). Following this preliminary step, the SR-XFI imaging of the samples was performed. Notably, one sample representative of each specific barley class was subjected to SR-XFI analysis to construct nutrient distribution maps of barley sections.

The data were collected at the BioXAS-Imaging beamline at the CLS, Saskatoon. The in-vacuum undulator of the beamline provides a high spectral brightness source for X-rays. In this study, the incident beam energy was set to 15 keV. The Kirkpatrick-Baez (K-B) micro-focusing mirrors were used to micro-focus the monochromatic X-ray beam spot size to 5 µm x 5 µm. Data were collected in continuous bi-directional fly-scanning mode with a step size of 5 µm and 100 ms dwell time. The Vortex-ME3 silicon drift X-ray detector (Hitachi High Technologies Science American, Inc., Chatsworth, CA) was at 45° and the samples were in a 90° stage configuration to the incident beam. The detector to the sample distance was set at 3.5 cm and each seed section took about 6-8 h to scan. Data were acquired using PyAcq (CLS, SK), an in-house developed multi-threaded python based data acquisition software. Calibration of nutrient peaks and data fitting was carried out using PyMca software (5.6.7) [35] and results are presented in Fig 5.7.

5.1.3.3 Mid Infrared (mid-IR) Spectroscopy

The sample preparation, data acquisition, and data processing were carried out as per the procedures described in [26] and briefly summarized here. To quantify the biochemical constituents encompassing protein, lipid, and carbohydrates, mid-infrared (IR) spectroscopy was carried out [36]. For the comprehensive analysis of barley biochemistry on a larger scale, sample sets consisting of 25 to 30 grain kernels were chosen randomly from the storage jars [32] (briefly summarized here). These selected samples were then subjected to cryogenic grinding to produce finely powdered material. Subsequently, these fine flours, amounting to 4.85 mg each, were combined with 385 mg of potassium bromide (KBr), resulting in the

creation of three distinct technical replicates for each sample. The mixture of fine flour and KBr underwent further grinding using the cryo grinder, ensuring homogeneity. From this homogenized mixture, equal portions were extracted, and these portions were subsequently subjected to the pressing process. A hydraulic press (Auto-CrushIR, PIKE Technologies, Madison, WI, USA) was employed for this purpose. Three different pressures were applied during the pressing procedure, specifically 53.93, 34.32, and 14.70 kPa. Each pressure was maintained for 3 s. This sequence of pressing yielded the formation of three individual pellets for each sample. These pellets were standardized in size, measuring 13 mm in diameter.

The samples, now in pellet form following the previously outlined process, were positioned within a sample wheel designed for data collection. For the data acquisition, FTIR microscope (Cary 670, Agilent Technologies Inc., Santa Clara, CA) was employed. This microscope was equipped with a bulk analysis accessory and a Deuterated Lanthanum α-Alanine doped TriGlycine Sulphate (DLaTGS) detector, which was maintained at a low temperature through thermoelectric cooling. The spectral data were collected within the range of 4000 to 900 cm^{-1}, at a resolution of 4 cm^{-1}. A total of 64 scans were co-added to ensure reliable and accurate data. After data acquisition, the processing and analysis steps were executed using the Quasar software (version 1.5.0) [37]. The resulting spectra were visualized and presented by plotting them in Spectragryph (version 1.2.16.1). Principal Component Analysis (PCA) was also performed using Quasar software, and all the results of the mid-IR analysis are presented in Figs 5.8- 5.10. This analytical approach harnessed the capabilities of mid-IR spectroscopy to deduce the content of protein, lipid, and carbohydrates within the pelleted samples, thus contributing to a comprehensive understanding of the barley's biochemical composition during 8-week storage.

5.1.4 Statistical analysis

The paired t test was performed on results of 3D segmentation analysis. It was performed for each pair (control and 8 wk stored) of barley class group to check significant differences for components (husk, germ, volume, air space, change due to spoilage, endosperm, and cracks).

5.1.5 Results and discussion

Upon visual inspection, it was evident that the stored samples of all the selected barley varieties exhibited varying degrees of deterioration by the conclusion of the 8-week storage period. This deterioration was observed after visual inspection of stored barley samples. The fungal infection was detected in the germ area of the stored barley varieties. This observation underscores the adverse impact of storage conditions on the barley, resulting in the growth of fungi. Additionally, the deterioration process was accompanied by the discoloration of the husk in the spoiled samples. The presence of fungal infection and the discoloration of the husk serve as tangible indicators of the spoilage process and the subsequent alteration in the overall quality and condition of the stored barley**.**

5.1.5.1 Microstructural changes

The microstructure of all the chosen barley varieties was subjected to analysis by utilizing the SR-μCT projections that had been gathered. In doing so, the structural features of the seeds were closely examined, revealing notable disparities between control samples and stored barley samples. In figures 1a and 1b, these distinctions are visually depicted. The visual analysis of the X-ray images of control samples unveiled the presence of pre-existing cracks and air gaps within the seed endosperm. Interestingly, these cracks initiated from the crease region of the seed and subsequently propagated throughout the endosperm. This structural attribute was particularly noticeable in the selected barley samples. The shape of the inspected seeds from the same variety was observed to remain relatively consistent during the storage period, as illustrated in Fig 5.1 and Fig 5.2. However, beneath this externally unaltered appearance, significant internal microstructural transformations occurred with storage.

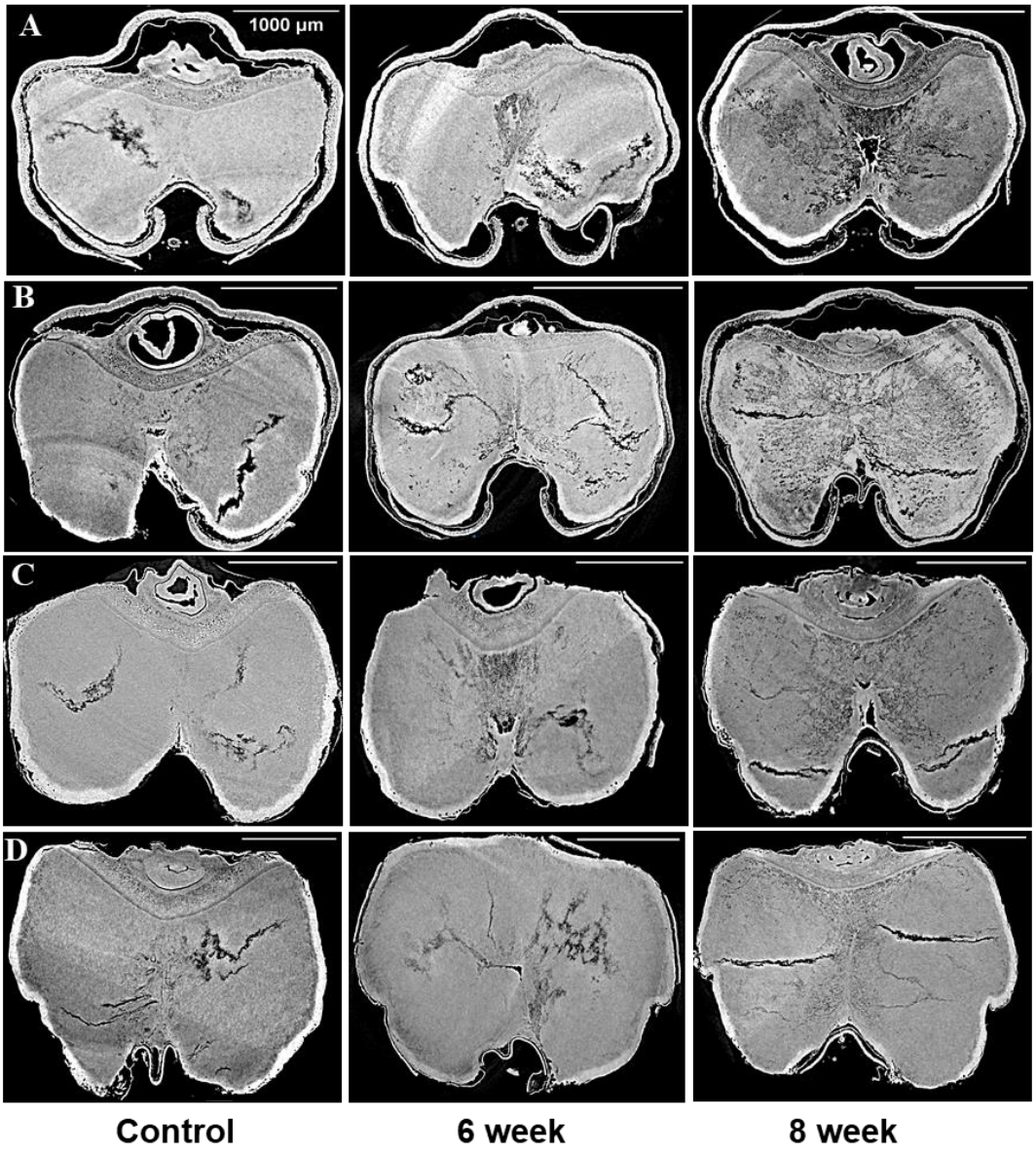

Figure 5.1 Cross sections from images of control and 17% moisture content four barley varieties [A: (6R) Tradition, B: (2R) AC Metacalf, C: (6Rhl) AB Cattlelac, D: 2Rhl) Esma] stored for 6 and 8 week. The white bar in the X-ray projections represent the scalebar of 1000 µm.

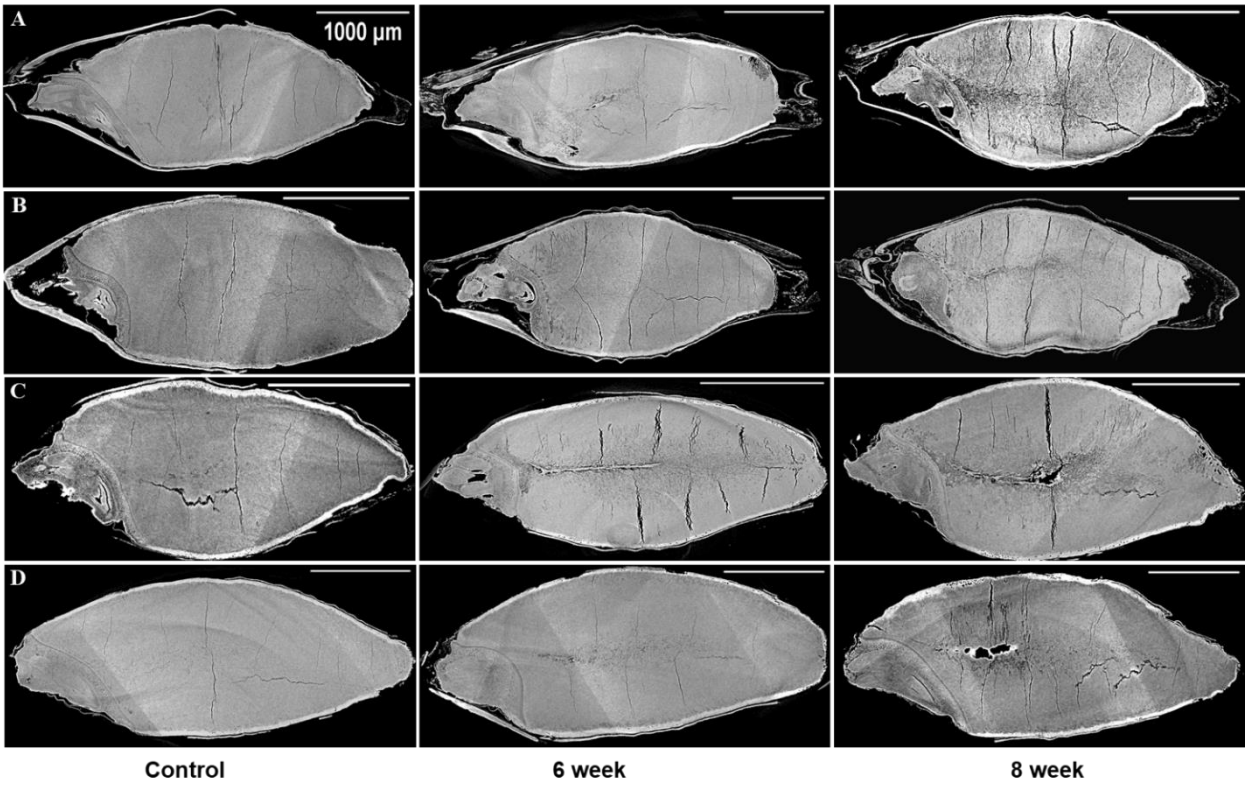

Figure 5.2 Longitudinal sections from 3D images of control and 17% moisture content four barley varieties [A: (6R) Tradition, B: (2R) AC Metacalf, C: (6Rhl) AB Cattlelac, D: 2Rhl) Esma] stored for 6 and 8 week. The white bar in the X-ray projections represent the scalebar of 1000 µm

A novel revelation of this study was the identification of air gaps between the endosperm and the husk, which adheres closely to the seed coat in hulled barley varieties. These air spaces contribute to the overall air space of the kernel, including the presence of cracks and pores. The manifestation of deterioration within the spoiled samples was characterized by shifts in grey values and better contrast with edge enhancement due to SR-µCT. The boundaries of the seed microstructure became more apparent due to the enhanced contrast achieved through phase imaging, as exhibited in Fig 5.1 and Fig 5.2. This capability to visualize structural details is crucial for understanding the mechanisms of spoilage related changes within the seed microstructure. The discernible features observed in both cross sections were subjected to further processing and segmentation, leading to specific measurements aimed at evaluating the extent of spoilage among the different classes of barley (Fig 5.3). Notably, in both the six row and two row hulled varieties, the presence of air space beneath the husk was detected. This structural feature may contribute to spoilage, particularly at unsafe moisture conditions. The changes attributed to deterioration were more pronounced in the hulled varieties belonging to both the six row and two row types of barley. However, among the selected barley **varieties,**

both the six row varieties; hulled variety (6R) Tradition and the hulless variety (6Rhl) AB Cattlelac showed comparatively higher deterioration than two row varieties.

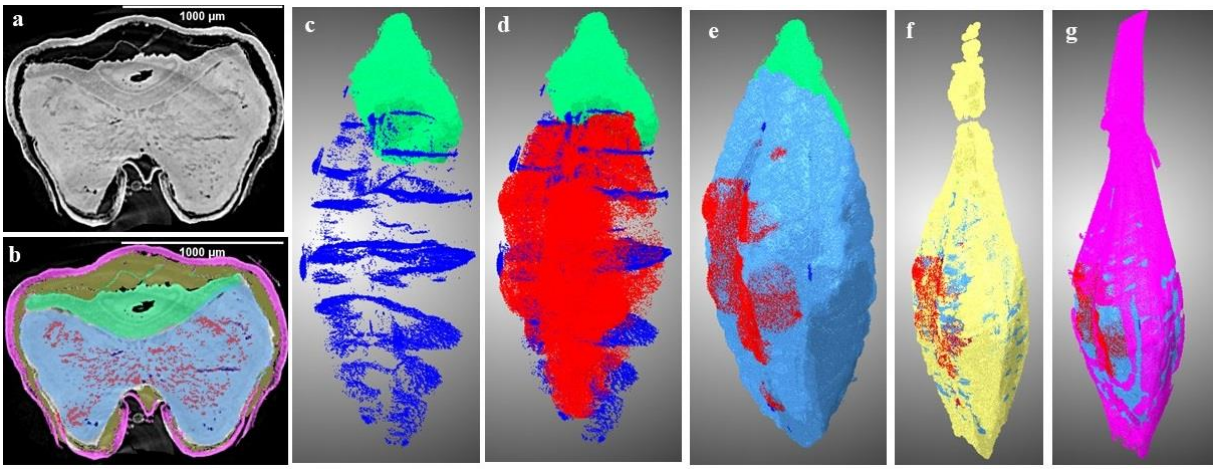

Figure 5.3 3D visualization of segmented components of two row hulled barley (2R: AC Metacalf) stored for 8 week. [a: cross section, b: labelled slice, c: germ (green) & cracks (dark blue), d: c & changes due to deterioration (red), e: d & endosperm (light blue), f: e & husk gap (yellow), and g: f & husk with seed coat (pink)], (n=1)

The measured voxel volumes of segmented components were estimated from the total labelled seed volume voxels as shown in figure 3. The two row AC Metacalf variety emerged as the most affected among the four selected barley varieties, with an estimated change due to deterioration of 8% of total seed volume at the end of 8 week of storage (Fig. 5.4). On the other hand, the two row hulless variety (2Rhl) Esma demonstrated better performance, with only a 2% change due to deterioration over the same duration. This relatively less deterioration was notably linked to the intact microstructure observed in the control samples of the Esma variety. Among the examined characteristics, the (6R) Tradition displayed larger cracks, accounting for approximately 6% of the seed volume, in contrast to 2% for the (2R) AC Metacalf variety. Furthermore, the gap between the endosperm and germ was more substantial in the hulled varieties (6R and 2R) of both classes at 11% and 10%, respectively. Consequently, the six row hulled barley samples exhibited higher kernel air space. The volume of the husk and coat was found higher in six row hulled and hulless varieties (Tradition, AB Cattlelac) than two row hulled and hulless (AC Metacalf, Esma) varieties.

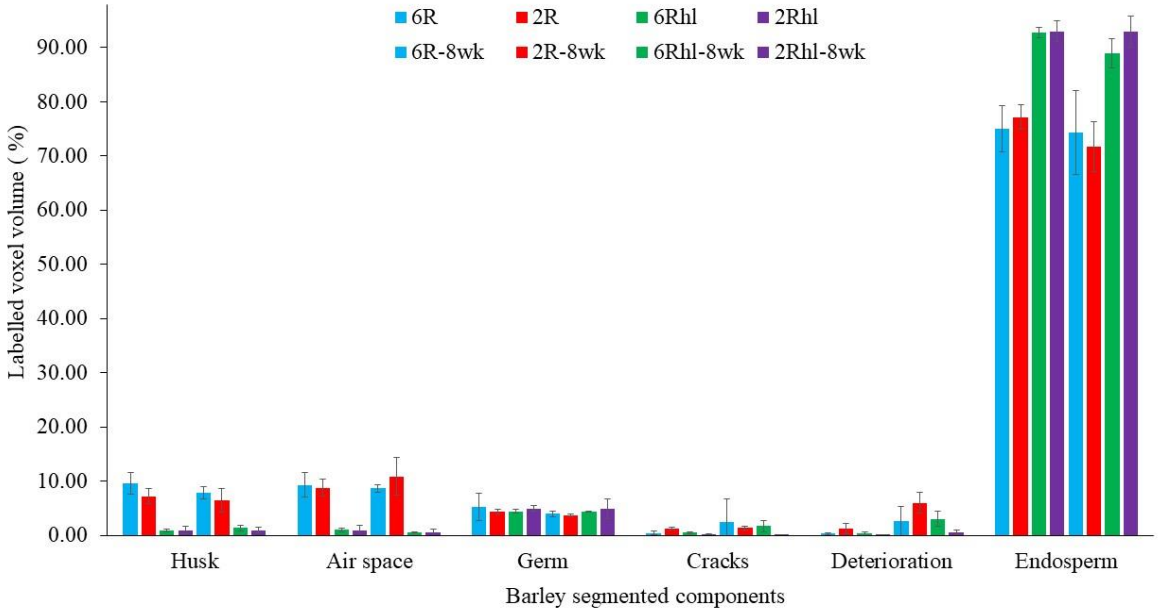

Figure 5.4 Measured labelled volume of control and eight week (8wk) stored barely varieties [(2Rhl) Esma, (2R) AC Metacalf, (6Rhl) AB Cattlelac, and (6R) Tradition)] (n=3)

Maximum and minimum air spaces or gaps were identified within the two row (2R) AC Metacalf and (6R) Tradition varieties both before storage and following an 8-week storage period. This observation highlights the variations in air space presence among the examined barley varieties. In the control samples, existing cracks were detected across all varieties, with the order of crack volume being as follows: (2R) AC Metacalf > (6R) Tradition > (6Rhl) AB Cattlelac > (2Rhl) Esma. These cracks appeared to originate from the crease region of the seeds. The emergence of cracks in this pattern may be attributed to external and internal stresses present within the seed structure due to action of field operations, drying, or other unit operations [38]. These cracks were evident in the 3D segmentation visualization (dark blue). The progression of deterioration (red pixels), was observed to spread around these cracks and near the crease region, a trend that was similarly observed in 2D visualization. The 3D visualization of our data showed how existing irregularities like cracks in seeds widened due to the deterioration of endosperm at the end of storage period. In cereal food grains the infection around the crease region may occur and this region was found vulnerable [39,40]. The germ of all varieties displayed signs of deterioration; a phenomenon demonstrated through 3D visualization. In these visualizations, the red pixels extended within and over the green pixels of germ. This deterioration within the germ could signify a decline in germination potential, ultimately impacting the malting value of the barley. Notably, the size of the germ differed

between hulled and hulless varieties, with hulless varieties having larger germ sizes. Specifically, the germ size of Esma (2Rhl) was approximately 25% larger than that of AB Cattlelac (6Rhl). Although the germ volume remained relatively consistent after the 8-week storage period, slight deviations were observed in the germ volume of hulled varieties in comparison to the control. This deviation could potentially be attributed to the presence of a larger deterioration volume within the segmentation results for these hulled varieties. It was also observed from Fig. 5.5 that, there were changes in seed volume at the end of the 8-week storage period, particularly with respect to spoilage in comparison to control samples. Notably, the six-row varieties exhibited a greater change in volume (i.e., increased over control) compared to the two-row varieties. Air space was observed within the germ outer layer and germ in both hulled varieties of two row and six row over the germ, This could be helpful for germination but may make hulled seeds more susceptible to deterioration and ultimately might affect the seed viability. . Results of the paired-t test indicated that there was a significant difference ($p < 0.001$) be-tween control and 8 wk samples for 6R and 2Rhl barley classes in measured segmented seed volumes, but it was found non-significant for 6Rhl ($p = .353$) and 2R ($p = .057$). Similarly, the results of paired-t test were carried out for microstructural feature cracks, and there was significant differences for 6Rhl ($p=0.009$) and 2R (0.043), but not for 6R ($p=0.193$) and 2Rhl ($p=0.153$) barley classes. In case of change due to spoilage, the significant differences were observed for 2R ($p=0.015$), 2Rhl ($p=0.005$) and 6Rhl ($p= 0.004$), but not for 6R ($p= 0.055$). It was observed from the statistical analysis in case of spoilage, almost all the selected barely classes (four varieties) were found to be affected. Barley class (2R) only showed significant difference ($p=0.03$) for husk content but not other barley classes. Barely classes: 2R ($p= 0.043$) and 6Rhl($p=0.009$) showed significant difference for presence of cracks but other two classes (6R and 2Rhl), had no significant difference. The only barley class that showed a significant difference in endosperm was 2R ($p=0.034$). But in case of features germ and air spaces beneath husk, all the barley classes showed nonsignificant differences between control and 8 week samples.

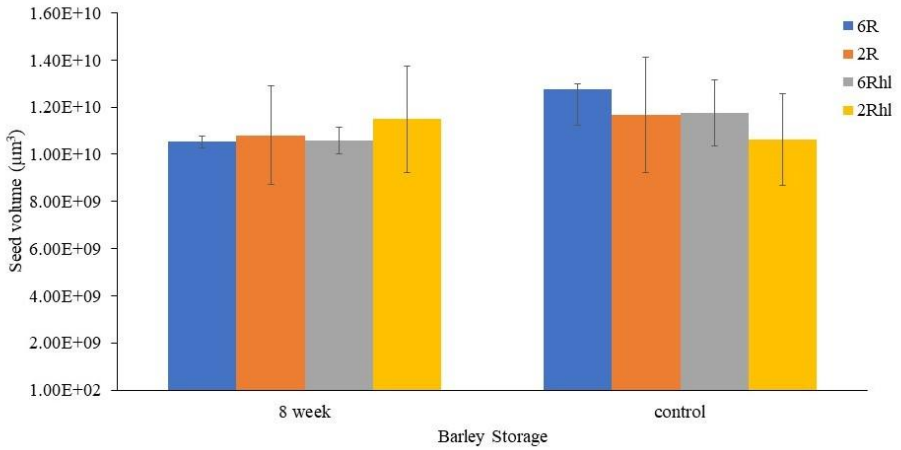

Figure 5.5 Measured seed volume of control and 8-week stored barely varieties [(2Rhl) Esma, (2R) AC Metacalf, (6Rhl) AB Cattlelac, and (6R) Tradition)]. (n=10)

To visually assess and quantify the differences between the control and 8-week stored samples, histograms were plotted for both categories (Fig. 5.6). The data were deconvoluted in each histogram to locate seed features (endosperm, cracks, air, and spoilage) beneath the peaks to show significant changes and support data analysis. This comparison aimed to examine the shift in peaks and their corresponding positions within the histograms. Notably, the shifting of peaks in 8-week stored samples was particularly prominent, meaning the density reduction and provided valuable insights into the changes that had occurred due to deterioration [21]. Among the observed outcomes, the most significant shift in peaks was noted in the 8-week stored six row and two row hulled varieties. This observation served as validation, corroborating the previously noted changes evident in the X-ray images. Third peak of histogram in the logscale histogram (Fig 5.6a) showed change in height along with the shift. The lowering of peak height can be attributed to change in volume and density due deterioration in storage The pronounced shift of peaks in this variety further underscored the considerable impact of deterioration on the microstructure and composition of the barley samples during the storage period. Histogram analysis serve as a quantitative tool to elucidate changes in distribution patterns and provides a direct visual representation of the effects of spoilage on the examined samples. The observed shifts in peaks substantiated the findings derived from the comprehensive analysis and supported the conclusions drawn regarding the influence of storage on the microstructural changes in the barley varieties. In the histograms of barley, the second peak corresponds to the seed endosperm, while the first peak represents the air spaces within the seed. Upon closer examination of all the histograms, a consistent pattern emerged: the grey value of 8-week stored samples decreased progressively. This decline in grey value signified a reduction in the density

of the seed's internal structure (Fig. 5.6). The six row varieties exhibited higher density when compared to their two row counterparts. This relationship between spoilage density alteration with time underscores the dynamic interplay between internal structural changes and the progression of spoilage within barley seeds.

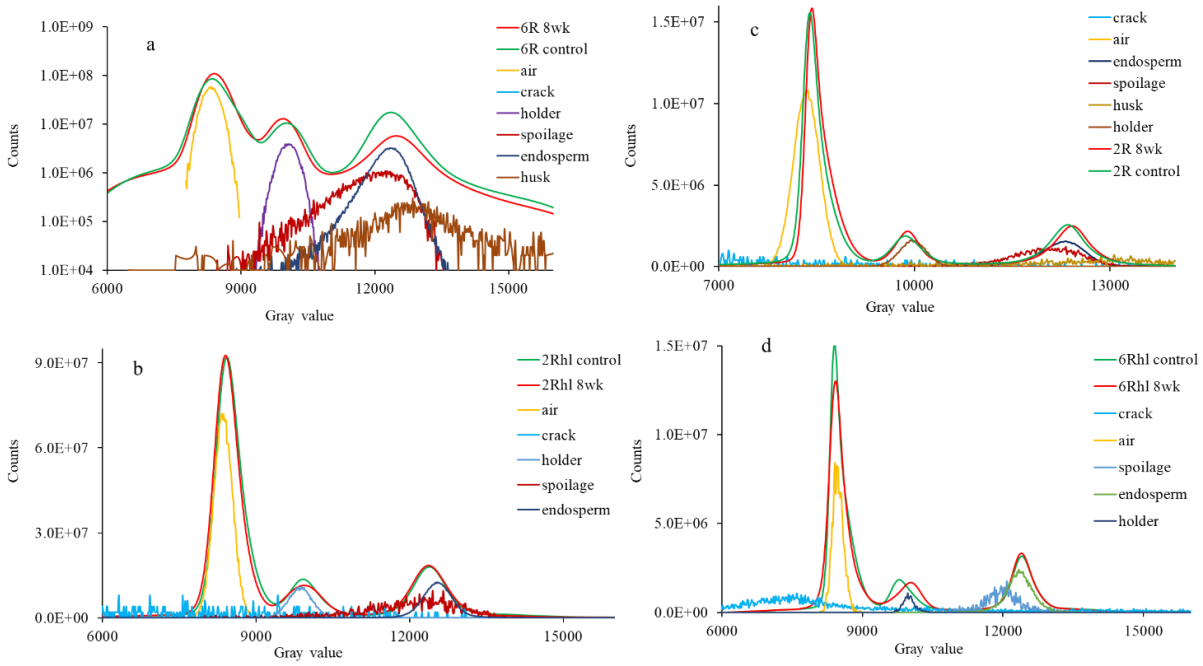

Figure 5.6 Normalized histogram of control and 8-week stored barely varieties [(a:6R) Tradition, (b:2Rhl) Esma, (c:2R) AC Metacalf, and (d:6Rhl) AB Cattlelac)]. Deconvoluted data are shown below the peaks in logplot of (a:6R barley) histogram. (n=10)

5.1.5.2 Changes in nutrient distribution

The outcomes from synchrotron X-ray fluorescence imaging (XFI) are shown in figure 6. The nutrient distribution map of one barley variety (6R) AB Cattlelac (control and 8-week stored samples) is shown as an example in Fig 5.7. It highlights the observed alterations in the distribution of nutrients, including K, Ca, Mn, Fe, Cu and Zn within the 8-week stored barley when compared to the control. The methodology employed for synchrotron XFI results has been verified to yield statistically consistent findings when compared to analytical methods [41]. The colour scales were used for visual representations, which enabled clear visualization of the variations in nutrient distribution across the barley samples. Analyzed images effectively illustrated how the distribution of nutrients within the barley seeds changed due to deterioration. By capturing and presenting these variations, the synchrotron XFI method enhanced our understanding of the impact of spoilage on the nutrient distribution within barley seeds. This information can have broader implications for assessing the nutritional quality of stored barley and making informed decisions regarding post-harvest management strategies.

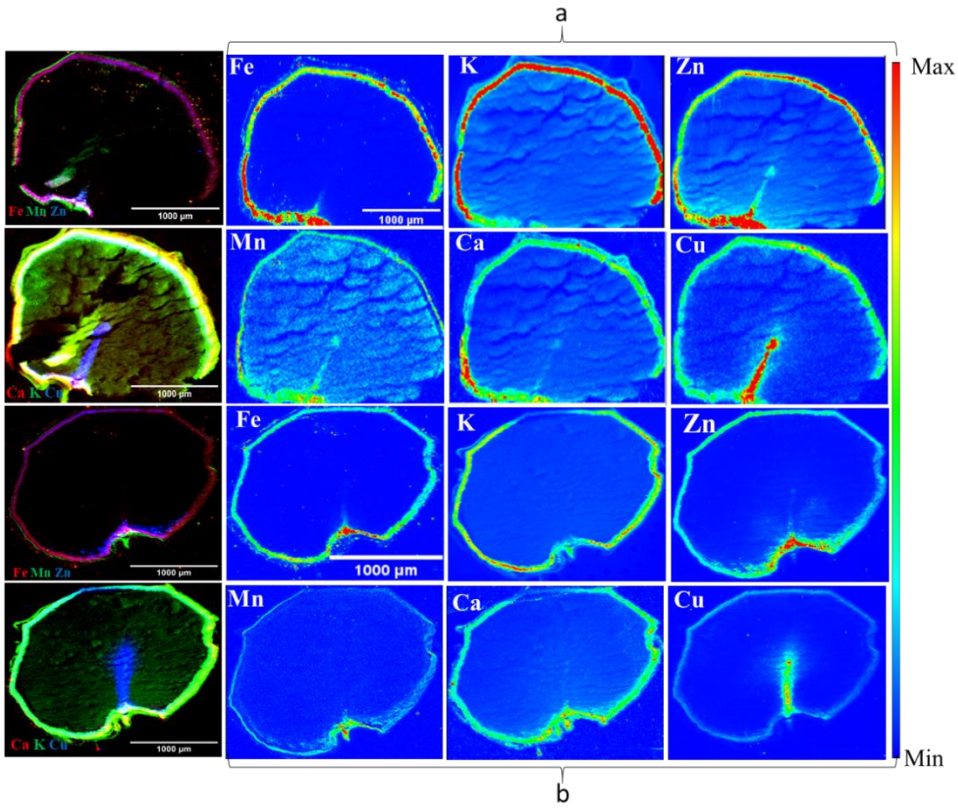

Figure 5.7 X-ray fluorescence images of six row AB Cattlelac barely variety, control (top) and 8-week stored sample (bottom) showing nutrient distributions (left: nutrient in group distribution and right: individual distribution) (n=1)

The nutrient K was observed to be most abundant in all control samples of the selected barley varieties, as depicted in Fig 5.7. It displayed a well distributed presence across all seed components, namely the endosperm, seed coat, and embryo. The distribution sequence (high to low) as per intensity was (6R) AB Cattlelac >(6Rhl) Tradition >(2Rhl) AC Metacalf > (2R) Esma. Previous research has indicated that K tends to concentrate in the scutellum, seed coat, and vascular bundle within cereal grains [42]. However, K was found at lower intensities in the husk of hulled varieties. Our study suggests that the distribution of K was influenced by spoilage. Specifically, in the case of variety AC Metacalf, the impact on K distribution was relatively minor compared to other varieties, as K distribution was found visible in both the seed coat and endosperm regions. In hulled varieties, the distribution of nutrient K in the husk remained unchanged. Interestingly, the distribution of K within the endosperm was reduced near or in region of the endosperm, as depicted in Fig 5.7. This suggests that spoilage induced changes due to moisture resulted in damage to the endosperm region (which was earlier observed in SR-μCT), leading to alterations in K distribution. In hulless varieties, K was found to be present in the seed coat after 8 week of storage. These distribution patterns align with findings from previous studies [33,43,44].

The nutrient iron (Fe) exhibited concentration in the seed coats (aleurone) of all samples, with distinct intensities across them. Control barley samples, i.e., those taken prior to storage, showcased a greater intensity of nutrient Fe distribution within the seed coat in comparison to 8-week stored samples. In the latter scenario, there was a noticeable reduction in the intensity of Fe. This phenomenon can be further substantiated by considering the example of the six row barley variety, as depicted in Fig 5.7. The nutrient Fe was not detected in the husk region of the hulled varieties belonging to both the two row and six row classes. The distribution of Fe abundance based on intensity followed the order: (6Rhl) Tradition > (2Rhl) AC Metacalf > (6R) AB Cattlelac > (2R) Esma. Previous research has reported that Fe is primarily concentrated in the aleurone layer [42,45]. Our study aligns with these findings, as we observed similar results in our analysis, but this holds true for only six row varieties in the study. The two row barley varieties, both hulled and hulless, exhibited the presence of Fe in the endosperm at lower intensity compared to aleurone region. Notably, these varieties displayed the higher disparity in Fe distribution between 8-week stored and control samples.

The subsequently essential nutrients, Mn and Zn were visualized across thin sections of the barley sample. Within control samples, Zn was notably concentrated in the aleurone layer and embryo region more than in the endosperm. In contrast, Mn exhibited a more uniform

distribution across all sections of control samples. It was found that, in the control samples, the distribution of Zn followed the order (most abundant to less); (6R)AB Cattlelac > (2Rhl)AC Metacalf > (2R) Esma > (6Rhl)Tradition, while the distribution of Mn followed the order (2Rhl) AC Metacalf >(6R) AB Cattlelac > (6Rhl) Tradition > (2R)Esma. However, an evident degradation of both Zn and Mn was observed in the 8-week stored samples of the four barley varieties. Comparatively, the degradation of Mn was more pronounced than that of Zn in the stored samples. Among the varieties, AC Metacalf variety exhibited the highest degree of degradation, particularly in the case of Zn, while Esma variety showed the least degradation of Zn. The images revealed that Zn nutrient was also localized in the embryo and crease regions of the barley seeds. These observations align with earlier studies that reported similar distribution patterns of Zn and Mn in barley samples [33,42,44]. Notably, all the stored samples exhibited a lower abundance of Mn compared to Zn at the end of 8-week storage. AC Metcalf variety exhibited more substantial variations, indicating changes in the distribution of Zn and Mn in comparison to the control samples, as compared to the other three varieties.

In the results, degradation of micronutrients was observed due to spoilage with increasing storage period. Micronutrients are considered essential for plant defense to diseases, which have been previously documented for Mn, Cu, Fe, and Zn [46–48]. Mn was found responsible in the production of phenolic compounds which assist in plant defense mechanisms [49] and Zn nutrient has been reported to play a major role in plant immune responses [50]. Both, Zn and Mn were found concentrated in crease region of the four barley control samples but, later after 8 week of storage, their abundance decreased, which might be due to spoilage starting near the crease region of the grain. The crease features of grains have a great impact on their post harvest quality [39]. In hulless varieties, a large gradient was observed between control and 8-week stored barley than hulled varieties. Therefore, hulless varieties under both classes of barley may perform comparatively weak in storage and more susceptible to spoilage than hulled varieties, and similar results were found when hulled and hulless barley were stored for 12 month [13]. The variations that were observed in nutrient distribution due to deterioration could be linked to fungal infection. One of the reasons for variation could be due to growth of fungus on barely seeds, As per literature fungal infection might strive of plant cells iron and other essential nutrients for support of their metabolic activities [51]. In our study, the structural changes were found maximum in hulled varieties than hulless varieties, and this could be due to prior condition of barley grains as discussed earlier. In all hulled and hulless varieties changes or reductions in the distribution of other nutrients (Ca, K, Fe, Cu) were observed in

spoiled samples. These vital nutrients are responsible for healthy grain and growth of barley [52], hence their degradation in storage means loss of germination, and the loss in germination of malting barley below 95% is not recommended if it is used for malt production [24]. The utilization of synchrotron X-ray fluorescence imaging (SR-XFI) proved valuable in accurately mapping the changes occurring during post-harvest storage in barley due to spoilage.

5.1.5.3 Biochemical changes

The outcomes of the mid-IR spectroscopy analysis are shown in figures 7-9. These figures illustrate the changes in protein, carbohydrates, and lipids in 8-week stored barley samples, as compared to their corresponding control samples. The analysis is based on the collected spectra, and the focus lies in evaluating alterations in these key biochemical components due to spoilage at the end of 8 week of storage. The spectral region ranging from 1800 to 900 cm^{-1}, was used in analysis, as depicted in Fig 5.8. This specific region was selected due to its relevance, featuring absorption bands that correspond to protein, lipid, and carbohydrate content [53]. Lipids, proteins, and carbohydrates, which are marked by distinct absorption peaks at 1740 cm^{-1}, 1651 cm^{-1}, and 1080-1023 cm^{-1}, in selected barley varieties control and 8-week stored samples [54]. These spectral analyses provide a means to track and quantify the changes in the key biochemical constituents over the 8-week storage duration. The shifts in absorption bands can offer valuable insights into the alterations occurring in the barley samples composition, thereby aiding in a comprehensive understanding of the effects of storage on their nutritional and biochemical characteristics.

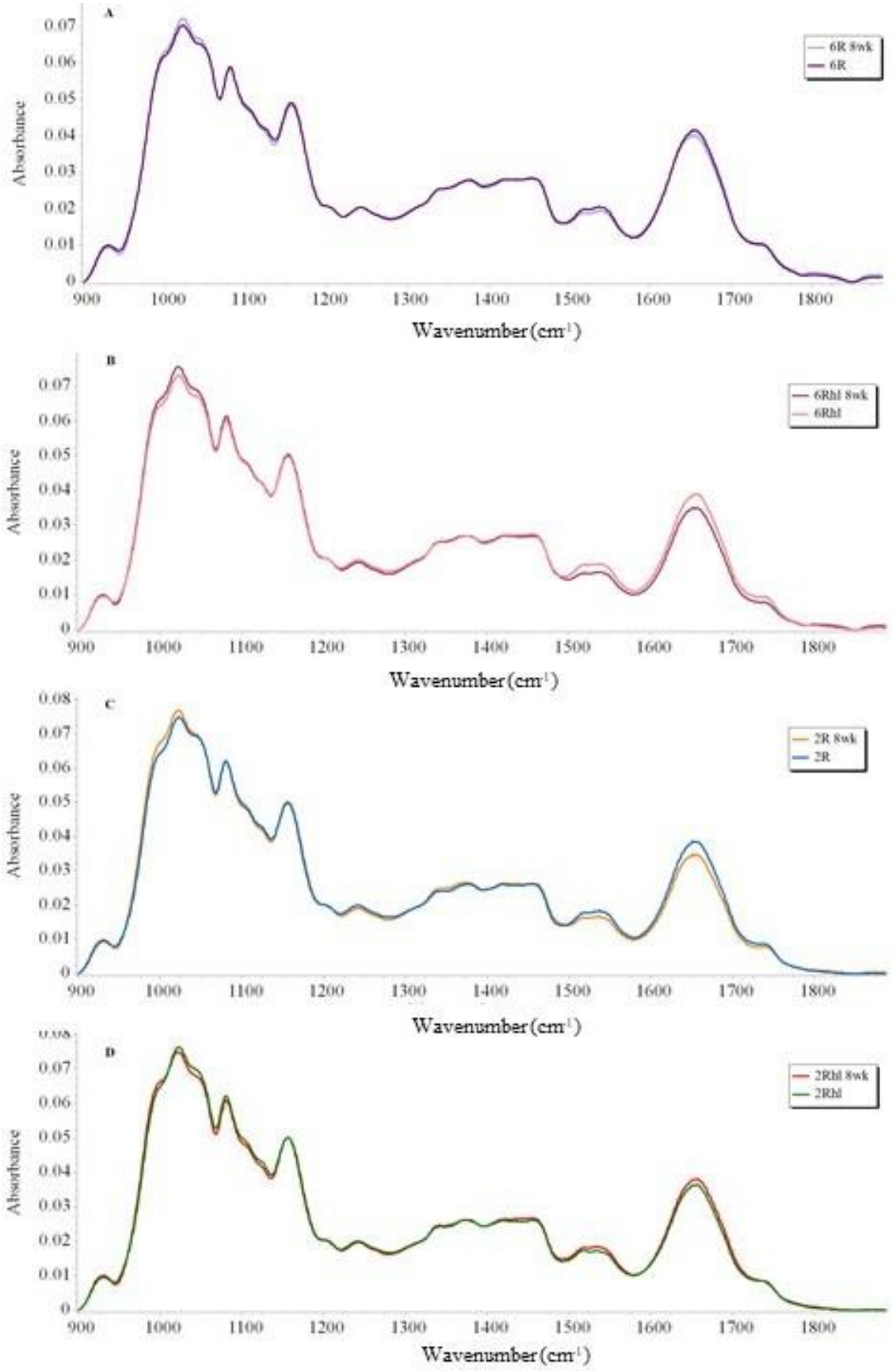

Figure 5.8 Normalized mid-IR spectra of three sample pellets of four barley classes (A: 6R, B: 6Rhl, C: 2R, and D: 2Rhl) control and 8-week stored samples (n=3).

The peaks at 1156, 1081, and 1024 cm^{-1} represents the carbohydrate region. The bands located at 1081 and 1024 cm^{-1} have been attributed to starch components, while the band at 1150 cm^{-1} can be linked to the stretching vibrations of CC and CO within starch molecules [36]. The control samples exhibited a distinct amount for carbohydrates, which followed the order (abundance to less): (2Rhl) Esma > (2R) AC Metacalf > (6Rhl) AB Cattlelac > (6R) Tradition. It means before storage two row barley varieties had higher lipids before storage compared to six row varieties. However, in the case of 8-week stored samples, a notable decrease in absorption at 1080 cm^{-1} for carbohydrates was observed and order changed as: (2R-8wk) AC Metacalf >(6Rhl-8wk)AB Cattlelac >(2Rhl-8wk) Esma>(6R-8wk) Tradition. This change in absorption indicated shifts in carbohydrate content due to spoilage after 8-week storage. The spoiled cereals showed lower absorbance for biochemical components (carbohydrates, protein and lipids) as reported in an earlier study [55]. The protein spectra in the regions of 1600–1500 cm^{-1} and 1700–1600 cm^{-1} were investigated, with amide I at 1650 cm^{-1} and amide II at 1540 cm^{-1} [54]. To evaluate protein structure, second derivatives of the spectra were plotted at 1700-1600 cm^{-1}, as illustrated in figure 8. The β-sheets and α-helical secondary protein structures exhibited peaks at 1636 cm^{-1} and 1656 cm^{-1}, respectively. The selected barley varieties demonstrated almost similar patterns of secondary protein structures, except for the 8-week stored (6R) Tradition and (2Rhl) AC Metacalf barley varieties. There was a considerable variation observed in the normalized absorbance of 8 week stored barley and control in the second derivative spectra, which can be inferred from in-dividual spectra as shown in Fig 5.8 (A, B, C and D). The hulled barley class (6R and 2R) showed lower absorbance for the β-sheets and α-helical secondary protein structures (Fig 5.8 A and C). The selected barley varieties demonstrated almost similar patterns of secondary protein structures, except for the 8-week stored (6R) Tradition and (2Rhl) AC Metacalf barley varieties. This observation signified changes in protein secondary structures due to spoilage. The normalized absorbance displayed considerable variation in both spoiled samples compared to control samples after 8 week of storage, as seen in Fig 5.9. In contrast, control samples exhibited a consistent trend without major variations in peaks, unlike the altered pattern observed in the stored samples as shown in Fig 5.9. This comparison highlights the impact of storage-induced spoilage on the normalized absorbance and spectral characteristics of carbohydrates and proteins in barley varieties.

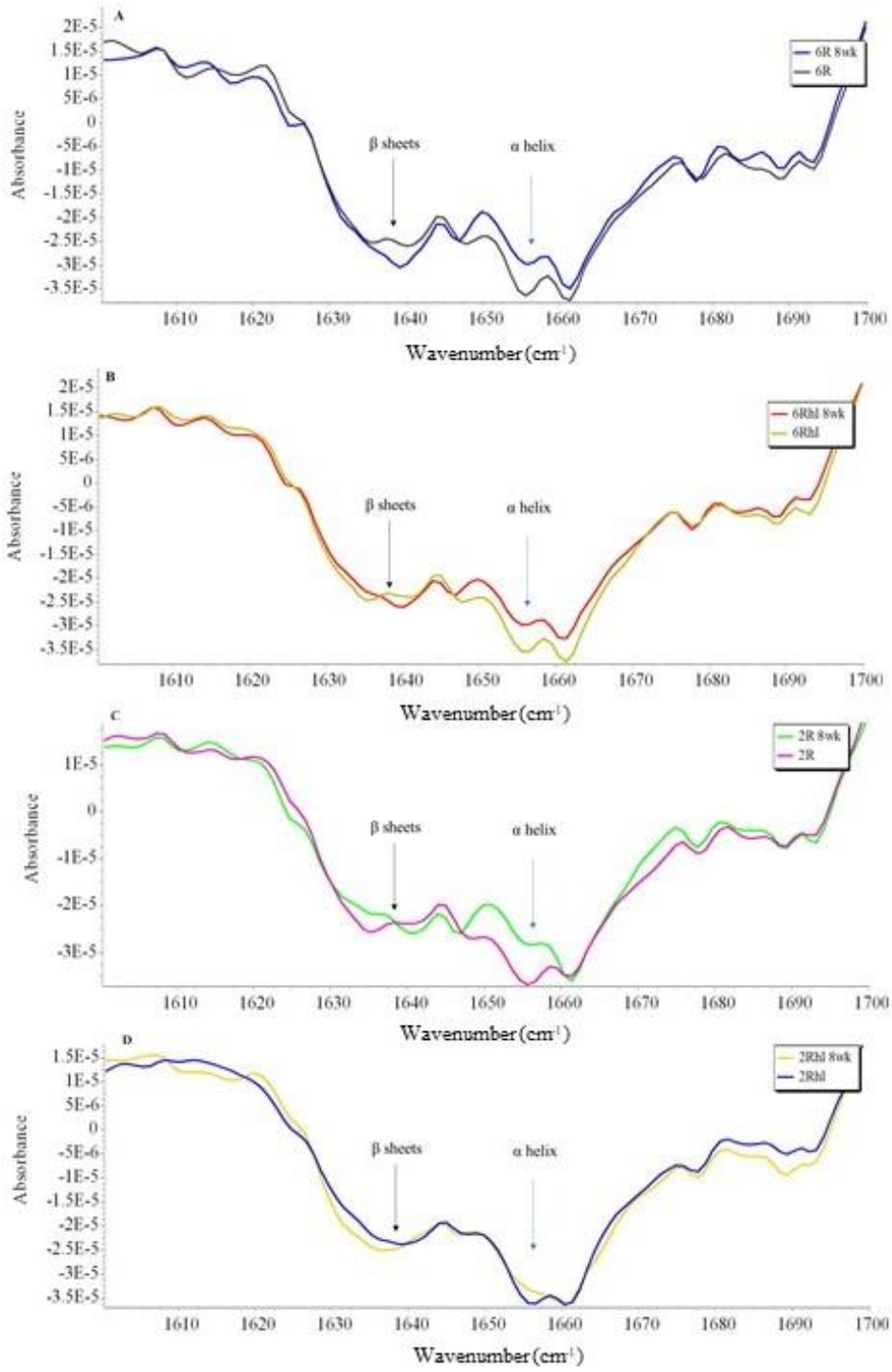

Figure 5.9 Second derivative spectra of control and 8-week stored barley classes (A: 6R, B: 6Rhl, C: 2R, and D: 2Rhl) for analysis of changes in protein structure.

A distinct pattern emerged in terms of lipid absorption at 1740 cm^{-1} for selected barley varieties. The lipid peak at 1740 cm^{-1} corresponds to the ester C=O stretching in triglycerides all polyhydroxy aldehydes [56,57]. This divergence in absorption patterns can be attributed to the unique composition and structure of hulled and hulless barley varieties, influencing the spectral response during spoilage. The lowest absorption (1740 cm^{-1}) for lipids was observed for 8-

week stored (6Rhl) AB Cattlelac variety and the highest absorption was in control (6R) Tradition variety followed by (6Rhl-8wk) Tradition variety. Previous research findings [53,55] align with the present study's observation of lower absorbance for key biochemical components (carbohydrates, protein, and lipids) in spoiled cereals. This shift in peaks during spoilage may arise from changes in metabolic activity, as well as variable defense mechanisms inherent to each barley variety [27]. In deterioration process, fungi can absorb and metabolize a diverse range of soluble carbohydrates, insoluble ones like starches, and cellulose [58]. It was also reported that fungal spoilage of cereals can degrade protein, and carbohydrates by 3-19 % and by 77% of their original value [59].

The Principal Component Analysis (PCA) was conducted, and the outcomes were depicted in Fig 5.10. This figure illustrates the comparison between the PC1 and PC2 scores of control and 8-week stored barley samples. PCA is a widely employed technique in IR spectroscopy to visualize the distribution of data points [27,55]. In this context, PCA serves as a valuable tool to analyze and comprehend the patterns and relationships within the collected spectral data. The first two principal components, PC1 and PC2, accounted for approximately 67% and 14% of the explained variance, respectively. Similarly, PC2 and PC3 were plotted with an explained variance of 74% and 7%, where scores of stored barley and control barley were separated from each other, unlike the first two components. Almost all the stored samples were inclined towards right side as compared to control. These results are in line with previously reported findings in the context of cereal analysis [27,55]. For the Esma and Tradition varieties, PCA scores of stored samples were situated at the far right, these findings were in line with results of SR-μCT data, where large changes due to deterioration in seed microstructure were observed. From the data loading of PC1, PC2 and PC3 showed in Fig 5.10, notable observation can be made in the carbohydrate (1200–900 cm^{-1}) and protein (1700–1500 cm^{-1}) regions. It was used in the differentiation of stored samples and control samples based on biochemical changes. The application of PCA, in conjunction with the identified mid-IR peaks, presents a potential avenue for the characterization of stored grains. By leveraging the observations derived from this study, PCA could prove to be a valuable technique for distinguishing and categorizing different types of spoilage, particularly those associated with fungal infection, based on mid-IR spectroscopy data. This approach offers a promising means to enhance the understanding of spoilage processes and to facilitate the development of strategies for identifying and addressing issues related to food grain quality and safety.

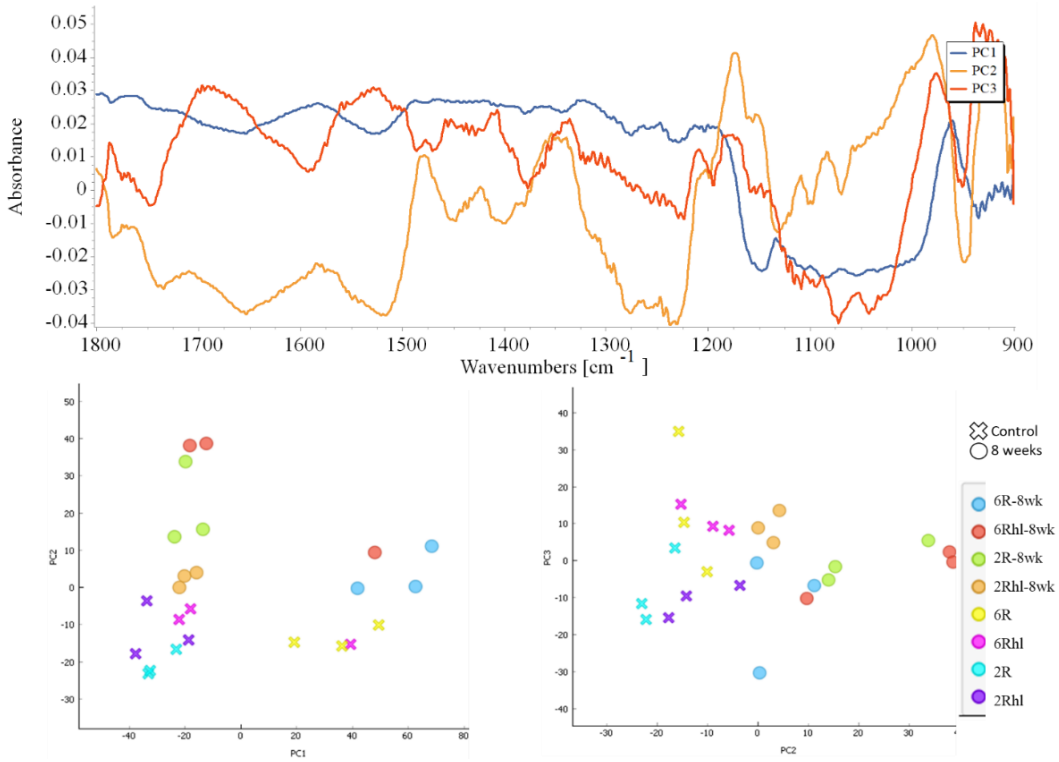

Figure 5.10 Top: PC data loading plot and bottom: PC score plots of control and 8-week stored samples of four barley varieties

5.1.6 Conclusion

The study's findings underscore the crucial significance of assessing the initial post-harvest quality of barley prior to its storage. While the adverse impact of unfavorable moisture conditions on barley storage is widely acknowledged, our study stands out for providing a comprehensive mapping of actual deterioration and the changes in barley microstructure through synchrotron X-ray techniques. This knowledge holds substantial promise in guiding the formulation and execution of storage strategies. The atlas of high resolution images developed in our study, encompassing the most prevalent malt and feed barley classes, serves as a foundational framework for the planning of post-harvest processing procedures for barley. A notable conclusion is that the presence of a hull cannot guarantee the protection of barley seeds if their structural integrity is already compromised. Moreover, our results emphasize that even sound hulless varieties may perform better in storage conditions. In our research, we successfully established a connection between microstructural changes and the corresponding nutritional and biochemical alterations resulting from spoilage over 8-week storage period. This comprehensive analysis allowed us to understand the intricate relationship between the physical changes in the grain's structure and the consequential shifts in its nutritional and biochemical composition during the storage period. These findings have practical implications for optimizing post-harvest storage practices in the barley industry, facilitating enhanced quality preservation and management. The future scope of our work is to train synchrotron data for development of machine learning algorithms for artificial intelligence (AI) segmentation of spoilage and identification of heathy barely for grain storage and malting industry.

5.1.7 Acknowledgment

The authors acknowledge the Netaji Subhash Chandra fellowship from the Indian Council of Agriculture Research via grant no. ICAR/2019 for the first author and the Natural Sciences and Engineering Research Council of Canada for supporting the student research via grant no. RGPIN-2018-04420 to Dr Jayas. Part or all of the research described in this paper was performed at the Canadian Light Source, a national research facility of the University of Saskatchewan, which is supported by the Canada Foundation for Innovation (CFI), the Natural Sciences and Engineering Research Council (NSERC), the National Research Council (NRC), the Canadian Institutes of Health Research (CIHR), the Government of Saskatchewan, and the University of Saskatchewan.

5.1.8 Authors' contributions

DSJ conceptualized the study, is the corresponding author, received funding, and contributed through editing, examination, and finalization of the manuscript drafts. All authors have read and approved the final manuscript. NSI and CK prepared an outline, the first draft, and the content of the whole paper based on the carried out experiment. MV, KT, JS, OM and VFB who are experts in synchrotron techniques at the Canadian light source provided technical inputs, and training, helped in data acquisition, and supported revision of the manuscript.

5.1.9 Competing interest statement

The authors declare that there are no competing interests.

5.1.10 Data availability statement

High-resolution imaging data are available on request to the corresponding author

5.1.11 References

1. Taner, A.; Muzaffer, A.; Fazil, D. *Barley: Post-harvest Operations*; 2004;

2. Canadian grain commision *Annual barley production 2022*; 2022;

3. CGC *Canadian Grain Commission Official Grain Grading Guide*; 2019; Libk. 1;.

4. Mills, A.; Ketterings, Q.; Verbeten, B.; Ganoe, K.; Sorrells, M. Harvest and Storage of Malting Barley Agronomy Fact Sheet Series 2014, 1–2.

5. Sychra, L.; Psota, V.; Mareček, J. Effect of long-term storage of malting barley on malt quality. *Monatsschrift fur Brauwiss.* 2001, *54*, 114–118.

6. Windes, S.; Bettenhausen, H.M.; Simaeys, K.R.V.; Clawson, J.; Fisk, S.; Heuberger, A.L.; Lim, J.; Queisser, S.H.; Shellhammer, T.H.; Hayes, P.M. Comprehensive Analysis of Different Contemporary Barley Genotypes Enhances and Expands the Scope of Barley Contributions to Beer Flavor. *J. Am. Soc. Brew. Chem.* 2021, *79*, 281–305, doi:10.1080/03610470.2020.1843964.

7. POLAT, H.E. Effects of Different Storage Conditions on the Nutritional Qualities of Barley and Maize. *Tarım Bilim. Derg.* 2015, *21*, 246, doi:10.15832/tbd.02887.

8. Krajčovič, T.; Psota, V.; Sachambula, L.; Mareček, J. Vplyv dlhodobého skladovania na kvalitu zrna sladovníckeho jačmeňa a sladu. *J. Cent. Eur. Agric.* 2016, *17*, 917–931, doi:10.5513/JCEA01/17.4.1791.

9. Yu, P.; Christensen, D.A.; Christensen, C.R.; Drew, M.D.; Rossnagel, B.G.; McKinnon, J.J. Use of synchrotron FTIR microspectroscopy to identify chemical differences in barley endosperm tissue in relation to rumen degradation characteristics. *Can. J. Anim. Sci.* 2004, *84*, 523–527, doi:10.4141/A03-102.

10. Narwal, S.; Gupta, O.P.; Pandey, V.; Kumar, D.; Ram, S. Effect of storage and processing conditions on nutrient composition of wheat and barley. In *Wheat and Barley Grain Biofortification*; 2020; or. 229–256 ISBN 9780128184448.

11. Lombi, E.; Smith, E.; Hansen, T.H.; Paterson, D.; De Jonge, M.D.; Howard, D.L.; Persson, D.P.; Husted, S.; Ryan, C.; Schjoerring, J.K. Megapixel imaging of (micro)nutrients in mature barley grains. *J. Exp. Bot.* 2011, *62*, 273–282, doi:10.1093/jxb/erq270.

12. Ochandio, D.; Cardoso, L.; Bartosik, R.; de la Torre, D.; Rodríguez, J.; Massigoge, J. Storage of canola in hermetic plastic bags. In Proceedings of the 10th International Working Conference on Stored Products Protection; 2010; Libk. 425, or. 323–330.

13. White, N.D.G.; Hulasare, R.B.; Jayas, D.S. Effects of storage conditions on quality loss of hull-less and hulled oats and barley. *Can. J. Plant Sci.* 1999, *79*, 475–482, doi:10.4141/P98-115.

14. Singh, T.; Garg, N.M.; Iyengar, S.R.S. Nondestructive identification of barley seeds variety using near-infrared hyperspectral imaging coupled with convolutional neural network. *J. Food Process Eng.* 2021, *44*, doi:10.1111/jfpe.13821.

15. Indore, N.S.; Karunakaran, C.; Jayas, D.S. Synchrotron tomography applications in agriculture and food sciences research: a review. *Plant Methods* 2022, *18*, 101, doi:10.1186/s13007-022-00932-9.

16. Sayed, T.S.; . F.Y.H.; . G.H.A. Resistance of Different Stored Wheat Varieties to Khapra Beetle, Trogoderma granarium (Everest) and Lesser Grain Borer, Rhizopertha dominica (Fabricus). *Pakistan J. Biol. Sci.* 2006, *9*, 1567–1571, doi:10.3923/pjbs.2006.1567.1571.

17. Singh, C.B.; Jayas, D.S.; Paliwal, J.; White, N.D.G. Fungal detection in wheat using near-infrared hyperspectral imaging. *Trans. ASABE* 2007, *50*, 2171–2176.

18. Senthilkumar, T.; Jayas, D.S.; White, N.D.G.; Fields, P.G.; Gräfenhan, T. Detection of fungal infection and Ochratoxin A contamination in stored wheat using near-infrared hyperspectral imaging. *J. Stored Prod. Res.* 2016, *65*, 30–39, doi:10.1016/j.jspr.2015.11.004.

19. Garbout, A.; Munkholm, L.J.; Hansen, S.B.; Petersen, B.M.; Munk, O.L.; Pajor, R. The use of PET/CT scanning technique for 3D visualization and quantification of real-time soil/plant interactions. *Plant Soil* 2012, *352*, 113–127, doi:10.1007/s11104-011-0983-8.

20. Rawson, S.D.; Maksimcuka, J.; Withers, P.J.; Cartmell, S.H. X-ray computed tomography in life sciences. *BMC Biol.* 2020, *18*.

21. Yashiro, W.; Voegeli, W.; Kudo, H. Exploring Frontiers of 4D X-ray Tomography. *Appl. Sci.* 2021, *11*, 8868, doi:10.3390/app11198868.

22. Karunakaran, C.; Lahlali, R.; Zhu, N.; Webb, A.M.; Schmidt, M.; Fransishyn, K.; Belev,

G.; Wysokinski, T.; Olson, J.; Cooper, D.M.L.; et al. Factors influencing real time internal structural visualization and dynamic process monitoring in plants using synchrotron-based phase contrast X-ray imaging. *Sci. Rep.* 2015, *5*, 12119, doi:10.1038/srep12119.

23. Olakanmi, S.J.; Jayas, D.S.; Paliwal, J. Applications of imaging systems for the assessment of quality characteristics of bread and other baked goods: A review. *Compr. Rev. Food Sci. Food Saf.* 2023, *22*, 1817–1838.

24. Bartosik, R.; Ochandio, D.; Cardoso, L.; De La Torre, D. Storage of Malting with Different Moisture Contents in Hermetic Silo-Bags. *Proceeding CAF 2012 9th Int. Conf. Control. Atmos. Fumigation Stored Prod.* 2012, 549–553.

25. Joseph, S. Moisture Measurement — Unground Grain and Seeds. *ASABE Stand.* 2017, *ASAE S352.*

26. Navanth S. Indore, Chithra Karunakaran, Digvir S. Jayas, Jarvis Stobbs, Miranda Vu, Kaiyang Tu, O.M. Characterization of spring and durum wheat during storage using non-destructive synchrotron phase contrast X-ray microtomography for reduction of post harvest losses. *Univ. Manitoba, Winnipeg, Manitoba, Canada. 2023, status (manuscript Submitt.* 2023.

27. Lahlali, R.; Karunakaran, C.; Wang, L.; Willick, I.; Schmidt, M.; Liu, X.; Borondics, F.; Forseille, L.; Fobert, P.R.; Tanino, K.; et al. Synchrotron based phase contrast X-ray imaging combined with FTIR spectroscopy reveals structural and biomolecular differences in spikelets play a significant role in resistance to Fusarium in wheat. *BMC Plant Biol.* 2015, *15*, 24, doi:10.1186/s12870-014-0357-5.

28. Faragó, T.; Gasilov, S.; Emslie, I.; Zuber, M.; Helfen, L.; Vogelgesang, M.; Baumbach, T. Tofu: a fast, versatile and user-friendly image processing toolkit for computed tomography. *J. Synchrotron Radiat.* 2022, *29*, 916–927, doi:10.1107/S160057752200282X.

29. Willmott, P. *An Introduction to Synchrotron Radiation*; Wiley, 2011; ISBN 9780470745793.

30. Cloetens, P.; Barrett, R.; Baruchel, J.; Guigay, J.P.; Schlenker, M. Phase objects in synchrotron radiation hard x-ray imaging. *J. Phys. D. Appl. Phys.* 1996, *29*, 133–146,

doi:10.1088/0022-3727/29/1/023.

31. Brar, G.S.; Karunakaran, C.; Bond, T.; Stobbs, J.; Liu, N.; Hucl, P.J.; Kutcher, H.R. Showcasing the application of synchrotron-based X-ray computed tomography in host-pathogen interactions: The role of wheat rachilla and rachis nodes in Type-II resistance to Fusarium graminearum. *Plant. Cell Environ.* 2019, *42*, 509–526, doi:10.1111/pce.13431.

32. Navnath S. Indore, Chithra Karunakarana, Digvir S. Jayasa, Viorica F Bondicib, Miranda VuKaiyang Tu, D.M. Mapping biochemical and nutritional changes in durum wheat due to spoilage during storage. *Univ. Manitoba, Winnipeg, Manitoba, Canada. 2023, status (manuscript Submitt.* 2023.

33. Lombi, E.; Scheckel, K.G.; Pallon, J.; Carey, A.M.; Zhu, Y.G.; Meharg, A.A. Speciation and distribution of arsenic and localization of nutrients in rice grains. *New Phytol.* 2009, *184*, 193–201, doi:10.1111/j.1469-8137.2009.02912.x.

34. Lombi, E.; Susini, J. Synchrotron-based techniques for plant and soil science: opportunities, challenges and future perspectives. *Plant Soil* 2009, *320*, 1–35, doi:10.1007/s11104-008-9876-x.

35. Solé, V.A.; Papillon, E.; Cotte, M.; Walter, P.; Susini, J. A multiplatform code for the analysis of energy-dispersive X-ray fluorescence spectra. *Spectrochim. Acta - Part B At. Spectrosc.* 2007, *62*, 63–68, doi:10.1016/j.sab.2006.12.002.

36. Karunakaran, C.; Vijayan, P.; Stobbs, J.; Bamrah, R.K.; Arganosa, G.; Warkentin, T.D. High throughput nutritional profiling of pea seeds using Fourier transform mid-infrared spectroscopy. *Food Chem.* 2020, *309*, 125585, doi:10.1016/j.foodchem.2019.125585.

37. Demšar, J.; Curk, T.; Erjavec, A.; Gorup, Č.; Hočevar, T.; Milutinovič, M.; Možina, M.; Polajnar, M.; Toplak, M.; Starič, A.; et al. Orange: Data mining toolbox in python. *J. Mach. Learn. Res.* 2013, *14*, 2349–2353.

38. Abass, A.B.; Ndunguru, G.; Mamiro, P.; Alenkhe, B.; Mlingi, N.; Bekunda, M. Post-harvest food losses in a maize-based farming system of semi-arid savannah area of Tanzania. *J. Stored Prod. Res.* 2014, *57*, 49–57, doi:10.1016/j.jspr.2013.12.004.

39. Le, T.D.Q.; Alvarado, C.; Girousse, C.; Legland, D.; Chateigner-Boutin, A.-L. Use of X-ray micro computed tomography imaging to analyze the morphology of wheat grain

through its development. *Plant Methods* 2019, *15*, 84, doi:10.1186/s13007-019-0468-y.

40. Zhang, T.; Sun, H.; Lv, Z.; Cui, L.; Mao, H.; Kopittke, P.M. Using Synchrotron-Based Approaches To Examine the Foliar Application of ZnSO 4 and ZnO Nanoparticles for Field-Grown Winter Wheat. *J. Agric. Food Chem.* 2018, *66*, 2572–2579, doi:10.1021/acs.jafc.7b04153.

41. Bamrah, R.K.; Vijayan, P.; Karunakaran, C.; Muir, D.; Hallin, E.; Stobbs, J.; Goetz, B.; Nickerson, M.; Tanino, K.; Warkentin, T.D. Evaluation of X-Ray Fluorescence Spectroscopy as a Tool for Nutrient Analysis of Pea Seeds. *Crop Sci.* 2019, *59*, 2689–2700, doi:10.2135/cropsci2019.01.0004.

42. Mazzolini, A.P.; Pallaghy, C.K.; Legge, G.J. f. Quantitative microanalysis of Mn, Zn and other elements in mature wheat seed. *New Phytol.* 1985, *100*, 483–509, doi:10.1111/j.1469-8137.1985.tb02796.x.

43. De Brier, N.; Gomand, S. V.; Donner, E.; Paterson, D.; Smolders, E.; Delcour, J.A.; Lombi, E. Element distribution and iron speciation in mature wheat grains (Triticum aestivum L.) using synchrotron X-ray fluorescence microscopy mapping and X-ray absorption near-edge structure (XANES) imaging. *Plant. Cell Environ.* 2016, *39*, 1835–1847, doi:10.1111/pce.12749.

44. Lombi, E.; Scheckel, K.G.; Kempson, I.M. In situ analysis of metal(loid)s in plants: State of the art and artefacts. *Environ. Exp. Bot.* 2011, *72*, 3–17, doi:10.1016/j.envexpbot.2010.04.005.

45. Ockenden, I.; Dorsch, J.A.; Reid, M.M.; Lin, L.; Grant, L.K.; Raboy, V.; Lott, J.N.A. Characterization of the storage of phosphorus, inositol phosphate and cations in grain tissues of four barley (Hordeum vulgare L.) low phytic acid genotypes. *Plant Sci.* 2004, *167*, 1131–1142, doi:10.1016/j.plantsci.2004.06.008.

46. Graham, R.; Webb, M. Micronutrients and disease resistance and tolerance in plants. In *Micronutrients in Agriculture*; 2018; or. 329–370 ISBN 9780891188780.

47. Dordas, C. Role of nutrients in controlling plant diseases in sustainable agriculture. A review. *Agron. Sustain. Dev.* 2008, *28*, 33–46.

48. Fones, H.; Preston, G.M. The impact of transition metals on bacterial plant disease. *FEMS Microbiol. Rev.* 2013, *37*, 495–519, doi:10.1111/1574-6976.12004.

49. Mendoza, F.; Verboven, P.; Mebatsion, H.K.; Kerckhofs, G.; Wevers, M.; Nicolaï, B. Three-dimensional pore space quantification of apple tissue using X-ray computed microtomography. *Planta* 2007, *226*, 559–570, doi:10.1007/s00425-007-0504-4.

50. Gupta, S.K.; Rai, A.K.; Kanwar, S.S.; Sharma, T.R. Comparative Analysis of Zinc Finger Proteins Involved in Plant Disease Resistance. *PLoS One* 2012, *7*, e42578, doi:10.1371/journal.pone.0042578.

51. Schindelin, J.; Arganda-Carreras, I.; Frise, E.; Kaynig, V.; Longair, M.; Pietzsch, T.; Preibisch, S.; Rueden, C.; Saalfeld, S.; Schmid, B.; et al. Fiji: An open-source platform for biological-image analysis. *Nat. Methods* 2012, *9*, 676–682.

52. Ambak, K.; Tadano, T.; Ambak, K. Effect of micronutrient application on the growth and occurrence of sterility in barley and rice in a Malaysian deep peat soil. *Soil Sci. Plant Nutr.* 1991, *37*, 715–724, doi:10.1080/00380768.1991.10416940.

53. Singh, C.B.; Jayas, D.S.; Paliwal, J.; White, N.D.G. Fungal Damage Detection in Wheat Using Short-Wave Near-Infrared Hyperspectral and Digital Colour Imaging. *Int. J. Food Prop.* 2012, *15*, 11–24, doi:10.1080/10942911003687223.

54. Saxton, R.; McDougal, O.M. Whey Protein Powder Analysis by Mid-Infrared Spectroscopy. *Foods* 2021, *10*, 1033, doi:10.3390/foods10051033.

55. Singh, C.B.; Jayas, D.S.; Borondics, F.; White, N.D.G. Synchrotron based infrared imaging study of compositional changes in stored wheat due to infection with Aspergillus glaucus. *J. Stored Prod. Res.* 2011, *47*, 372–377, doi:10.1016/j.jspr.2011.07.001.

56. Kaya-Celiker, H.; Mallikarjunan, P.K.; Kaaya, A. Mid-infrared spectroscopy for discrimination and classification of Aspergillus spp. contamination in peanuts. *Food Control* 2015, *52*, 103–111, doi:10.1016/j.foodcont.2014.12.013.

57. Grube, M.; Bekers, M.; Upite, D.; Kaminska, E. Infrared spectra of some fructans. *Spectrosc. An Int. J.* 2002, *16*, 289–296, doi:10.1155/2002/637587.

58. David moore Nutrition Available at: https://www.britannica.com/science/fungus/Form-and-function-of-fungi (eskuratua 29 abuztuak 2023).

59. Rosentrater, K.A. Biochemical, functional, and nutritive changes during storage. In *Storage of Cereal Grains and their Products*; 2022; or. 443–501 ISBN 9780128127582.

Chapter 6. SUMMARY AND CONCLUSIONS

Post-harvest losses during cereal grain storage pose significant concerns in both developing and developed countries, particularly where wheat and barley serve as staple food grains. Synchrotron X-ray imaging and spectroscopy techniques present promising tools for studying changes in garins during storage. Varieties within different classes exhibit distinct behaviors under storage, influencing their ultimate storage life. The study's hypothesis revolves around the idea that advanced imaging methods can trace changes in grain microstructural and nutritional properties caused by spoilage. To date, high-resolution imaging data for both dry and spoiled seeds are not available for any class of wheat or barley. Therefore, our initial attempt aimed to generate 3D data to enhance our understanding of seed structure and changes due to spoilage.

Building upon the results of the preliminary experiment, we conducted a characterization of varieties within the most common wheat classes (spring and durum). These varieties were stored for a short term of 5 wk at 17% moisture content. Both control (dry) and stored high-moisture seeds underwent analysis for structural and nutritional changes using synchrotron techniques: phase contrast micro-computed tomography, bulk X-ray fluorescence imaging, X-ray fluorescence imaging, and mid-infrared spectroscopy at the Canadian Light Source in Saskatoon, SK. During this study, wheat grains were also stored in a freezer (-18°C) for further scanning to investigate any additional changes in the structure of seeds due to freezing. The data acquisition parameters were standardized for SR-μCT (20 keV, 3.6μ resolution, and 5 cm propagation distance) and SR-XRF/XFI (15 keV, 5μ resolution, and 100 ms dwell time) and mid-IR (900–4000 cm^{-1} range and at 4 cm^{-1} resolution). From our preliminary experiment, we successfully developed a methodology for testing stored food grains (both wet and frozen) using synchrotron techniques. Image processing revealed changes in the microstructure of wheat with spoilage at the end of the 5-wk storage, and this structure remained unaltered after freezing of stored wheat.

The bulk XRF analysis highlighted the impact of storage time on variations in available nutrients. The SR-XRI demonstrated significant changes ($p<0.05$) in nutritional distributions at the micron scale in thin section maps within stored durum wheat seeds. Changes in nutritional features, including protein, lipids, and carbohydrates, due to spoilage during storage were determined using mid-infrared (mid-IR) spectroscopy. Among the durum wheat varieties, AAC Spitfire and CDC Defy exhibited the most substantial changes in both microstructure and nutritional composition compared to AAC Stronghold. In contrast, all spring wheat varieties

performed better with minimal quality changes than durum wheat. Notably, spring wheat outperformed durum wheat in short-term storage, with varieties Faller and Starbuck showing better performance than AAC Brandan based on microstructural and nutritional changes. This observation prompted further experiments, and we expanded our study to include more wheat and barley classes using the developed methodology.

In the second experiment, eight wheat varieties, each representing different western Canada wheat classes, and four barley varieties (two six-row and two two-row), each representing distinct western malt barley classes, were stored for 8 wk at 17% moisture content (wb). Data acquisition for both control (wheat, barley) and stored grains (wheat and barley at 8 wk) was conducted with the same standardized operational parameters for SR-µCT, SR-XFI, and mid-IR. The changes in microstructure within selected wheat classes allowed for the characterization of wheat. The results indicated that the following wheat classes—CNHR, CWRW, CWSP, and CPSW—performed better in storage compared to classes CWHWS, CPSR, CSWS, and CWES. Hulled barley varieties exhibited more deterioration in microstructure than hulless varieties, establishing a direct correlation between microstructural changes and alterations in nutritional content over time. Observations of changes due to spoilage within the grain structure informed the characterization of selected wheat and barley varieties based on alterations in grain structure, nutritional composition due to deterioration. The initial condition of the grain structure in control samples strongly influenced the storage life of wheat and barley during the short-term storage of 8 wk. The high-resolution information generated for selected wheat and barley varieties will be valuable in planning post-harvest storage. Additionally, these data could assist plant breeders in developing varieties that are less susceptible to spoilage, refining existing grain processing techniques, and formulating post-harvest recommendations for other crop varieties. Future work aims to develop a machine learning model for the identification and segmentation of spoiled components of seeds based on the acquired X-ray data for the eight wheat classes

Chapter 7. FUTURE WORK AND CONTRIBUTION TO THE RESEARCH KNOWLEDGE

7.1 Future work

There are several studies that could build on research reported in this thesis. For example,

- Machine learning models can be trained using the collected SR-μCT data of healthy and stored seeds for automated identification of spoilage and changes in microstructure.
- Other food grains such pulses, oil seeds can be tested using the developed methodology at a synchrotron facility.
- Perishable foods (e.g., valuable fruits and vegetables) could be analyzed using synchrotron tools to study affect of control atmosphere storage on their microstructure.
- Effects of long term storage (3-5 years) and different moisture levels (11%, 13%, and 15%) on structural changes in cereal grains can be characterized using developed methodology using a synchrotron facility.

7.2 Contribution to research knowledge

- The developed database of high-resolution images of dry and stored seeds in this study will be a guide for researchers who are engaged in grain storage studies.
- Grain managers will benefit from knowing how long their stored products can be safely stored depending on the variety in storage.
- Developed methodology in testing of food grains using synchrotron tools will be very useful in analysis of stored food.

Chapter 8. ANNEXURES

Annexure. A (CLS experiments)

1. **Canadian Light Source, Saskatoon**

2. **Storage Experiment at 17%mc (wb)**

3. **Sample preparation SR-µCT for BMIT beamline acquisition at CLS**

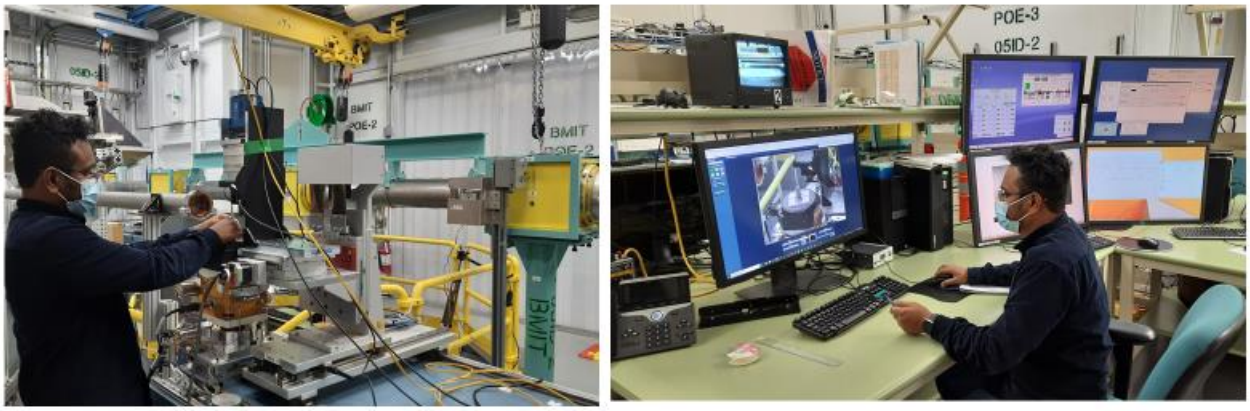

4. **Data acquisition wheat, barley using SR-µCT at CLS**

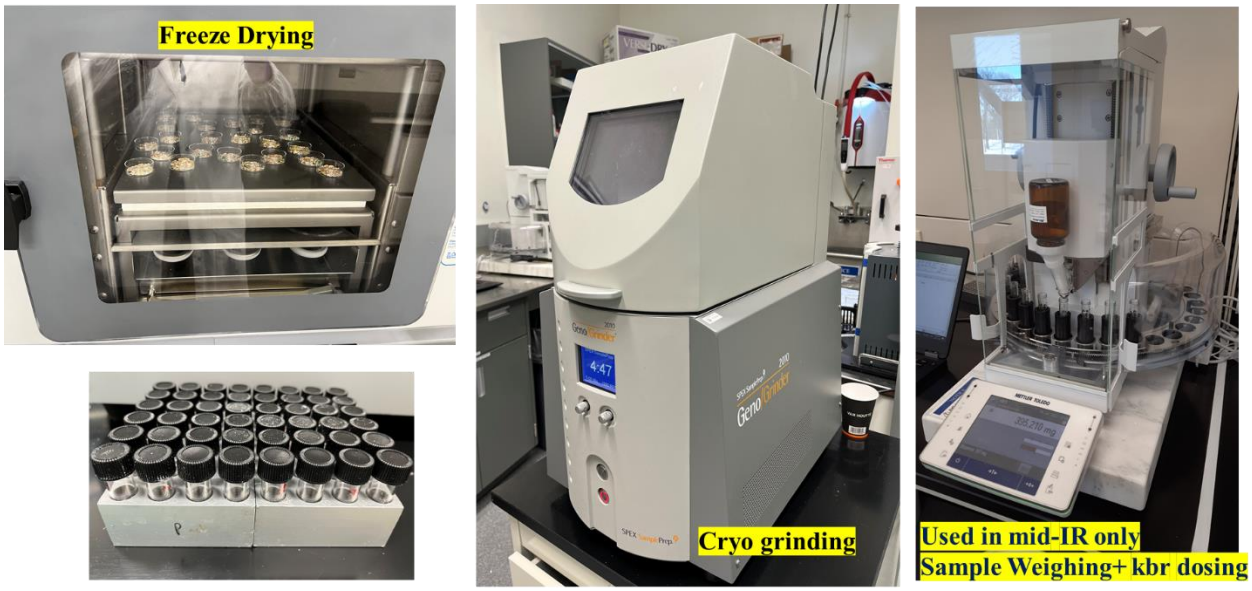

5. **mid-IR sample preparation step1 at CLS**

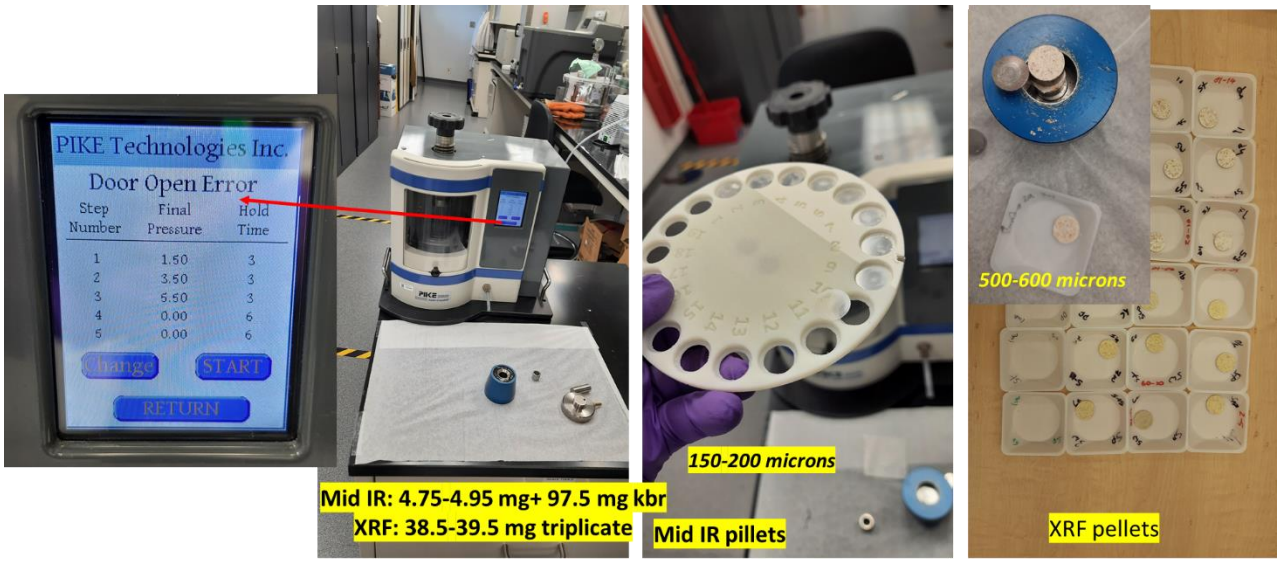

6. **mid-IR, SR-XRF sample preparation step2 at CLS**

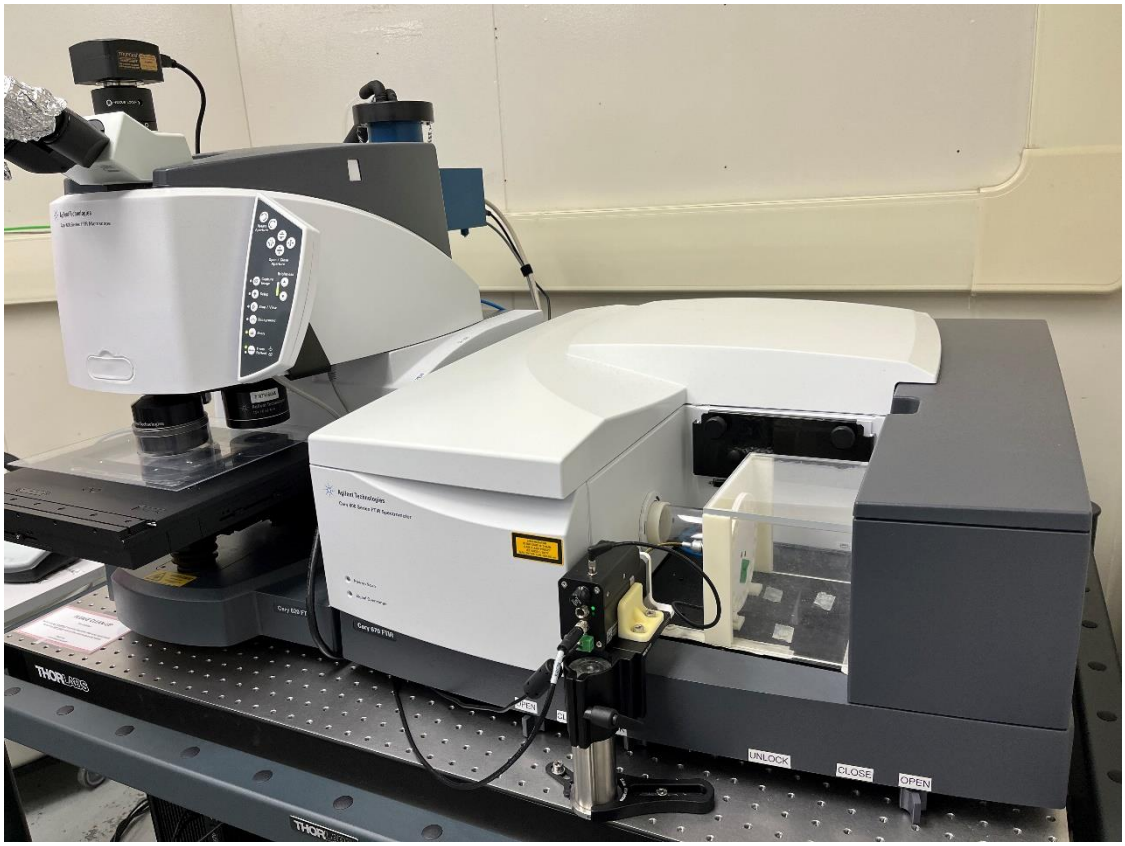

7. **mid-IR data acquisition at CLS**

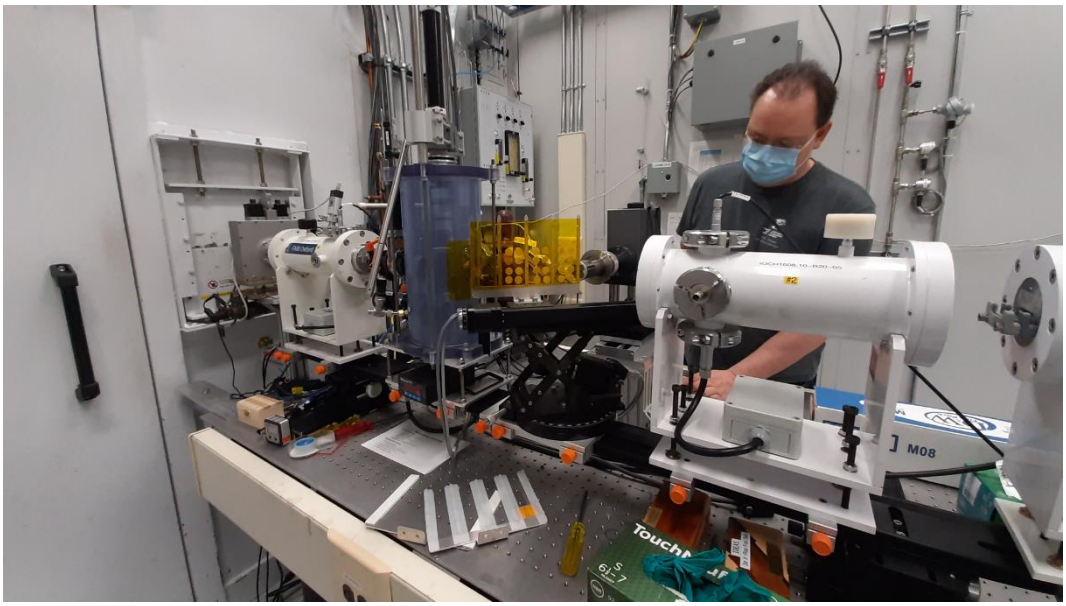

8. **SR-XRF data collection at IDEAS beamline, CLS**

9. **SR-XFI sample preparation for BIOXAS beamline acquisition**

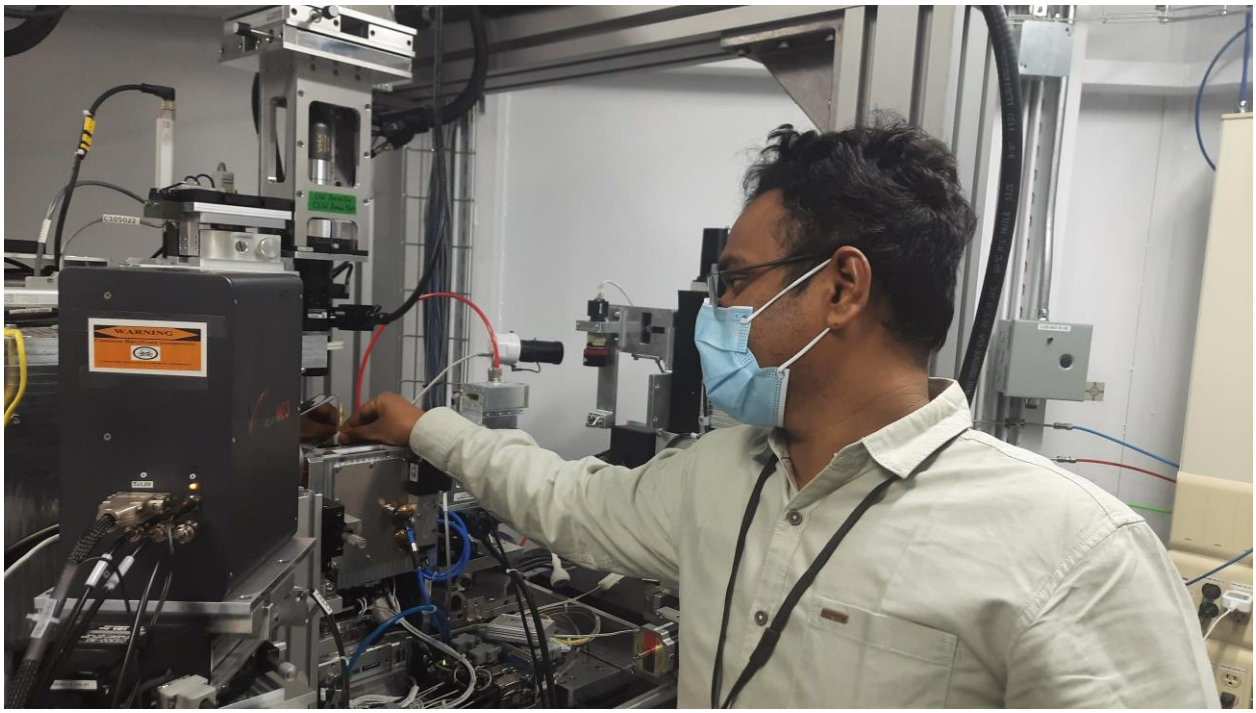

10. **SR-XFI data acquisition at BIOXAS beamline, CLS**

Annexure B (SR-XRF data of spring wheat and barley)

SR-XFI processed data of nutrient distribution in control and stored food grains

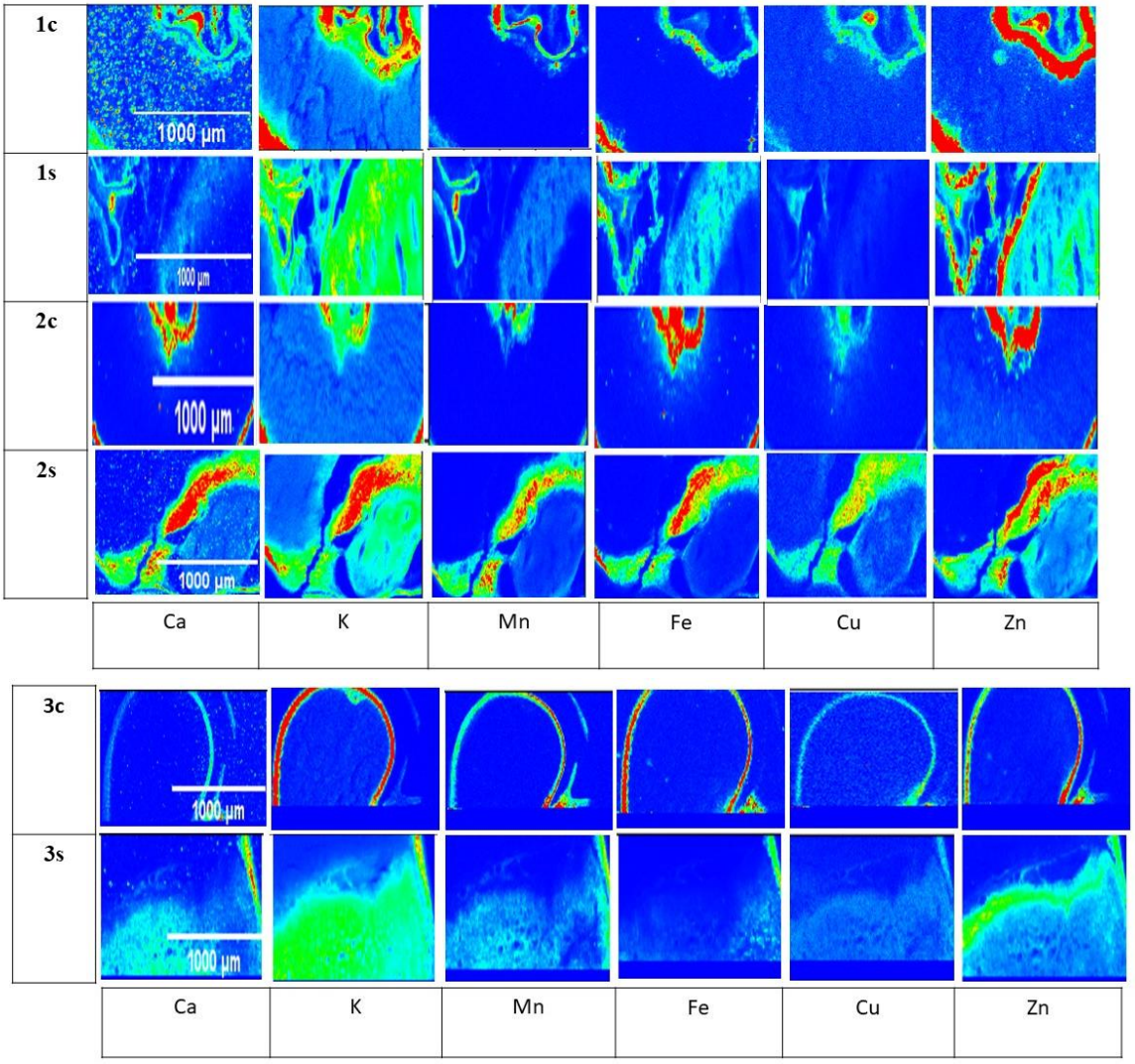

1. **Nutrient distribution in control (c) and 5 week(s) stored spring wheat (1: Faller, 2: AAC Starbuck and 3: AAC Brandon)**

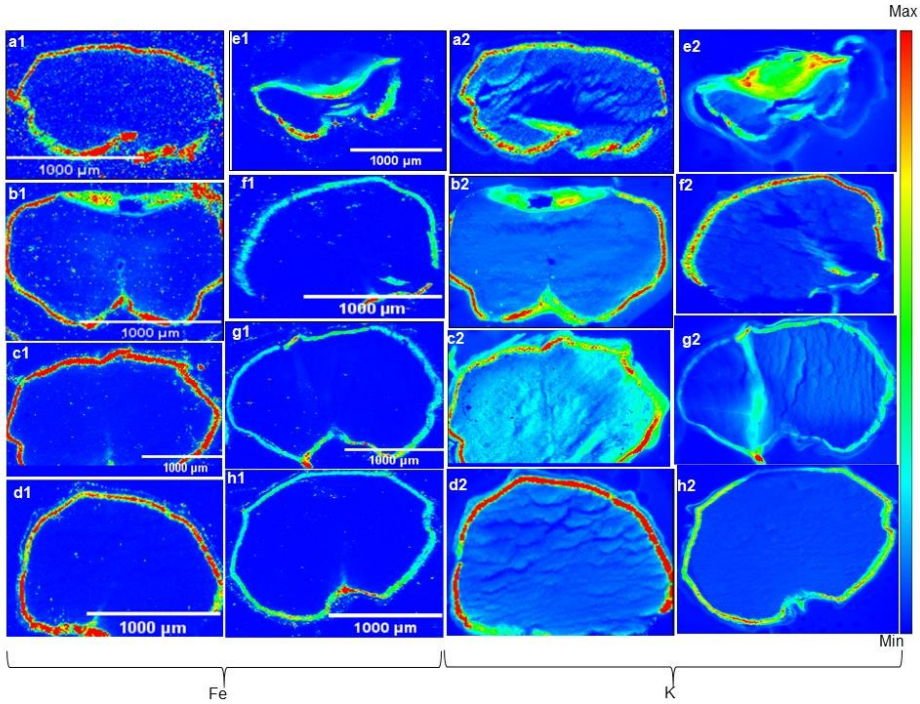

2. Left: SR-XFI images showing Fe distribution of barley control (a1:Esma, b1:AC Metacalf, c1: Tradition and d1: AB Cattlelac) and 8 weeks stored (e1:Esma, f1:AC Metacalf, g1: Tradition and h1: AB Cattlelac) samples. Right: SR-XFI images showing K distribution of barley control (a2:Esma, b2:AC Metacalf, c2: Tradition and d2: AB Cattlelac) and 8 weeks stored (e2:Esma, f2:AC Metacalf, g2: Tradition and h2: AB Cattlelac) samples

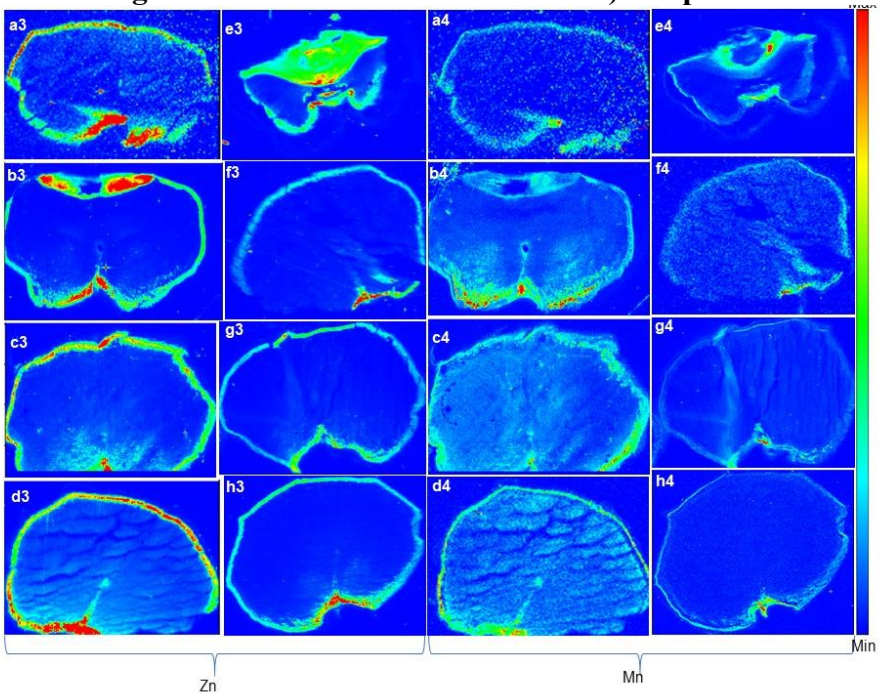

3.

3. Left: SR-XFI images showing Zn distribution of barley control (a3:Esma, b3:AC Metacalf, c3: Tradition and d3: AB Cattlelac) and 8 weeks stored (e3:Esma, f3:AC Metacalf, g3: Tradition and h3: AB Cattlelac) samples. Right: SR-XFI images showing Mn distribution of barley control (a4:Esma, b4:AC Metacalf, c4: Tradition and d4: AB Cattlelac) and 8 weeks stored (e4:Esma, f4:AC Metacalf, g4: Tradition and h4: AB Cattlelac) samples

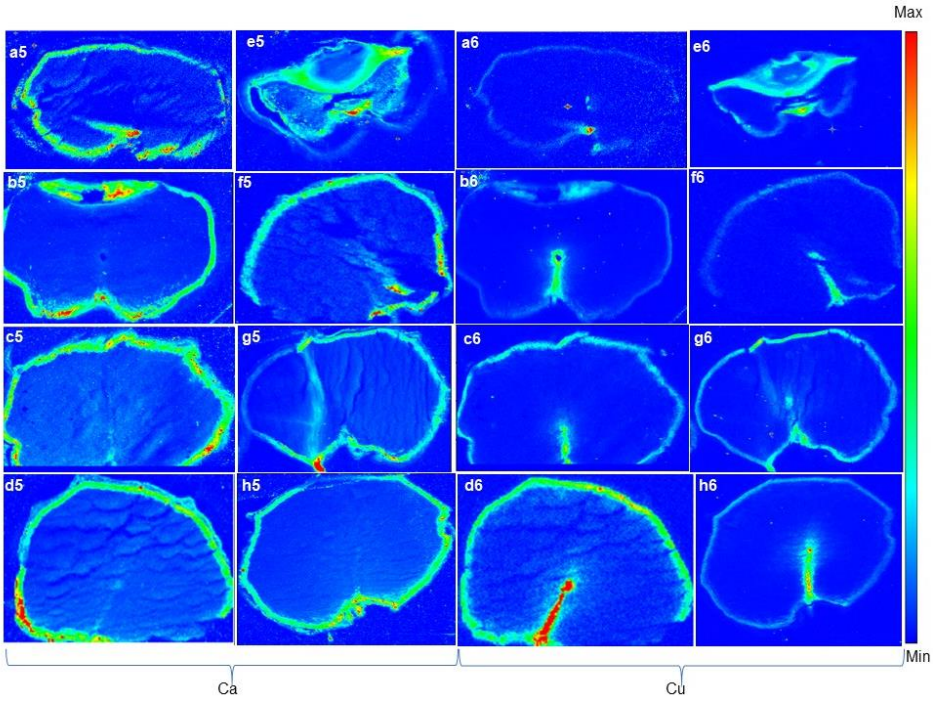

4. Left: SR-XFI images showing Fe distribution of barley control (a5:Esma, b5:AC Metacalf, c5: Tradition and d5: AB Cattlelac) and 8 weeks stored (e5:Esma, f5:AC Metacalf, g5: Tradition and h5: AB Cattlelac) samples. Right: SR-XFI images showing K distribution of barley control (a6:Esma, b6:AC Metacalf, c6: Tradition and d6: AB Cattlelac) and 8 weeks stored (e6:Esma, f6:AC Metacalf, g6 Tradition and h6: AB Cattlelac) samples

Annexure C (Statistical Analysis of SR-XRF data on nutrient counts)

1. Anova for Fe in AAC Spitfire

Anova: Single Factor						
SUMMARY						
Groups	*Count*	*Sum*	*Average*	*Variance*		
Column 1	9	3747698	416410.9	29408905		
Column 2	9	3375306	375034	33132379		
Column 3	9	3506189	389576.5	139577099		
Column 4	9	3720350	413372.3	66632088		
ANOVA						
Source of Variation	*SS*	*df*	*MS*	*F*	*P-value*	*F crit*
Between Groups	1.06E+10	3	3.52E+09	52.34118602	1.93E-12	2.90112
Within Groups	2.15E+09	32	67187618			
Total	1.27E+10	35				

2. Anova for Zn in AAC Spitfire

Anova: Single Factor						
SUMMARY						
Groups	*Count*	*Sum*	*Average*	*Variance*		
Column 1	8	109993.2	13749.15	3898245		
Column 2	8	126078.6	15759.83	1801468		
Column 3	8	101645.4	12705.67	2913165		
ANOVA						
ce of Varic	*SS*	*df*	*MS*	*F*	*P-value*	*F crit*
Between	38558767	2	19279383	6.71531	0.005564	3.4668
Within Gr	60290148	21	2870959			
Total	98848915	23				

3. **Anova for Mn in AAC Spitfire**

Anova: Single Factor						
SUMMARY						
Groups	*Count*	*Sum*	*Average*	*Variance*		
Column 1	8	39708.07	4963.509	329185.4		
Column 2	8	47316.19	5914.524	1118072		
Column 3	8	54967.34	6870.918	434115.9		
ANOVA						
ce of Varic	*SS*	*df*	*MS*	*F*	*P-value*	*F crit*
Between (	14552871	2	7276436	11.60286	0.000403	3.4668
Within Gr	13169612	21	627124.4			
Total	27722484	23				

4. **Anova for Ca of AAC Spitfire**

Anova: Single Factor						
SUMMARY						
Groups	*Count*	*Sum*	*Average*	*Variance*		
Column 1	8	78003.48	9750.435	1606829		
Column 2	8	79759.41	9969.926	1246789		
Column 3	8	73640.27	9205.034	381882.9		
ANOVA						
ce of Varic	*SS*	*df*	*MS*	*F*	*P-value*	*F crit*
Between (	2481865	2	1240933	1.150609	0.335604	3.4668
Within Gr	22648510	21	1078500			
Total	25130375	23				

5. **Anova fro Ca in CDC Defy**

Anova: Single Factor						
SUMMARY						
Groups	*Count*	*Sum*	*Average*	*Variance*		
Column 1	8	78003.48	9750.435	1606829		
Column 2	8	79759.41	9969.926	1246789		
Column 3	8	73640.27	9205.034	381882.9		
ANOVA						
ce of Varic	*SS*	*df*	*MS*	*F*	*P-value*	*F crit*
Between (	2481865	2	1240933	1.150609	0.335604	3.4668
Within Gr	22648510	21	1078500			
Total	25130375	23				

6. **Anova for Mn in CDC Defy**

Anova: Single Factor						
SUMMARY						
Groups	*Count*	*Sum*	*Average*	*Variance*		
Column 1	8	39708.07	4963.509	329185.4		
Column 2	8	47316.19	5914.524	1118072		
Column 3	8	54967.34	6870.918	434115.9		
ANOVA						
ce of Varic	*SS*	*df*	*MS*	*F*	*P-value*	*F crit*
Between (	14552871	2	7276436	11.60286	0.000403	3.4668
Within Gr	13169612	21	627124.4			
Total	27722484	23				

7. **Anova for Fe in CDC Defy**

Anova: Single Factor						
SUMMARY						
Groups	*Count*	*Sum*	*Average*	*Variance*		
Column 1	8	360	45	600		
Column 2	8	3331287	416410.9	33610178		
Column 3	8	3000272	375034	37865576		
ANOVA						
ce of Varic	*SS*	*df*	*MS*	*F*	*P-value*	*F crit*
Between (	8.42E+11	2	4.21E+11	17666.78	1.33E-34	3.4668
Within Gr	5E+08	21	23825451			
Total	8.42E+11	23				

8. **Anova for Zn in CDC Defy**

Anova: Single Factor						
SUMMARY						
Groups	*Count*	*Sum*	*Average*	*Variance*		
Column 1	8	109993.2	13749.15	3898245		
Column 2	8	126078.6	15759.83	1801468		
Column 3	8	101645.4	12705.67	2913165		
ANOVA						
ce of Varic	*SS*	*df*	*MS*	*F*	*P-value*	*F crit*
Between (	38558767	2	19279383	6.71531	0.005564	3.4668
Within Gr	60290148	21	2870959			
Total	98848915	23				

9. **Anova for Ca in AAC Stronghold**

Anova: Single Factor						
SUMMARY						
Groups	*Count*	*Sum*	*Average*	*Variance*		
Column 1	8	78003.48	9750.435	1606829		
Column 2	8	79759.41	9969.926	1246789		
Column 3	8	73640.27	9205.034	381882.9		
ANOVA						
ce of Varic	*SS*	*df*	*MS*	*F*	*P-value*	*F crit*
Between (	2481865	2	1240933	1.150609	0.335604	3.4668
Within Gr	22648510	21	1078500			
Total	25130375	23				

10. **Anova for Mn in AAC Stronghold**

Anova: Single Factor						
SUMMARY						
Groups	*Count*	*Sum*	*Average*	*Variance*		
Column 1	8	39708.07	4963.509	329185.4		
Column 2	8	47316.19	5914.524	1118072		
Column 3	8	54967.34	6870.918	434115.9		
ANOVA						
ce of Varic	*SS*	*df*	*MS*	*F*	*P-value*	*F crit*
Between (	14552871	2	7276436	11.60286	0.000403	3.4668
Within Gr	13169612	21	627124.4			
Total	27722484	23				

11. Anova for Fe in AAC Stronghold

Anova: Single Factor						
SUMMARY						
Groups	*Count*	*Sum*	*Average*	*Variance*		
Column 1	8	360	45	600		
Column 2	8	3331287	416410.9	33610178		
Column 3	8	3000272	375034	37865576		
ANOVA						
ce of Varia	*SS*	*df*	*MS*	*F*	*P-value*	*F crit*
Between	8.42E+11	2	4.21E+11	17666.78	1.33E-34	3.4668
Within Gr	5E+08	21	23825451			
Total	8.42E+11	23				

12. **Anova for Zn in AAC Stronghold**

Anova: Single Factor						
SUMMARY						
Groups	*Count*	*Sum*	*Average*	*Variance*		
Column 1	8	109993.2	13749.15	3898245		
Column 2	8	126078.6	15759.83	1801468		
Column 3	8	101645.4	12705.67	2913165		
ANOVA						
ce of Varia	*SS*	*df*	*MS*	*F*	*P-value*	*F crit*
Between	38558767	2	19279383	6.71531	0.005564	3.4668
Within Gr	60290148	21	2870959			
Total	98848915	23				